



HAL
open science

Laser cooling and manipulation of antimatter in the AEgIS experiment

Pauline Yzombard

► **To cite this version:**

Pauline Yzombard. Laser cooling and manipulation of antimatter in the AEGIS experiment. Atomic Physics [physics.atom-ph]. Université Paris Saclay (COMUE), 2016. English. NNT : 2016SACLS272 . tel-01446588

HAL Id: tel-01446588

<https://theses.hal.science/tel-01446588>

Submitted on 26 Jan 2017

HAL is a multi-disciplinary open access archive for the deposit and dissemination of scientific research documents, whether they are published or not. The documents may come from teaching and research institutions in France or abroad, or from public or private research centers.

L'archive ouverte pluridisciplinaire **HAL**, est destinée au dépôt et à la diffusion de documents scientifiques de niveau recherche, publiés ou non, émanant des établissements d'enseignement et de recherche français ou étrangers, des laboratoires publics ou privés.

NNT : 2016SACLS272

THÈSE DE DOCTORAT
DE
L'UNIVERSITÉ PARIS-SACLAY
PRÉPARÉE À
L'UNIVERSITÉ PARIS-SUD

AU SEIN DU LABORATOIRE AIMÉ COTTON,
EN COLLABORATION AVEC L'ORGANISATION EUROPÉENNE POUR LA
RECHERCHE NUCLÉAIRE (CERN)

ÉCOLE DOCTORALE N° 572
Ondes et Matières

Spécialité de doctorat : Physique quantique

Par

Mme Pauline Yzombard

Laser cooling and manipulation of antimatter
in the AEGIS experiment

Thèse présentée et soutenue à Orsay le 24 novembre 2016

Composition du Jury :

Dr. Lunney David	Directeur de recherche au Centre de Sciences Nucléaires et de Sciences de la Matière, CNRS, France	Président
Dr. Ulmer Stefan	Initiative researcher at the Ulmer Initiative Research Unit, RIKEN, Japan	Rapporteur
Dr. Karr Jean-Philippe	Maitre de conférence à l'Université d'Evry - Val d'Essonne, France	Rapporteur
Dr. Madsen Niels	Senior lecturer at the Swansea University, UK.	Examineur
Dr. Crivelli Paolo	Senior scientist at Laboratory of Positron & Positronium Physics - Switzerland	Examineur
Dr. Comparat Daniel	Directeur de recherche au laboratoire Aimé Cotton, CNRS, France	Directeur de thèse
Dr. Doser Michael	Senior research physicist at CERN, Switzerland	Invité

Laser cooling and manipulation of Antimatter
in the AEGIS experiment

Pauline Yzombard

Laboratoire Aimé Cotton, Campus d'Orsay, 91405 Orsay cedex, France

Acknowledgments - Remerciements

Faisant l'inventaire de toutes les personnes qui m'ont accompagnées lors de cette aventure et que j'aimerais tant remercier, j'ai pris la pleine mesure ma chance de vous avoir tout autour ! Commençons par mon cher directeur de thèse, Daniel, qui a eu la patience de répondre à ma dizaine d'e-mails angoissés quotidiens. J'aime à penser que nous avons accompli un beau travail ensemble. Un grand merci à Michael et à toute l'équipe cernoise d'AEgIS, qui m'ont accueillie sans condition: thanks a lot Stefan, thanks to you the cryogenics has no more secrets for me, grazie Seba per tutte le pause per il tè che abbiamo preso fuori ! How can I thank the AEgIS people without mentioning Ingrid, my dearest tea-breaker, Ine, BenJ, Ola, Lisa, Laura and Lillian, the famous positron dream-team crew. Grazie mille alla squadra laser e positroni italiana: Ruggero, Zeudi-cara, Gemma, Daniel K ! A little wink to IngMari, Olga, Sameed, Giancarlo, Nicola and Angela. Thanks to you guys, I spent three amazing years working with you in such a "challenging" (thank you Lillian) experiment, that made me become a better physicist and a better person I believe. As Seba likes saying: "what did you do today ? Well, I've saved the world and fixed my apparatus...".

En parlant de sauver le monde, je remercie absolument mes parents qui m'ont toujours soutenue jusque dans mes choix les plus saugrenus (étudier l'antimatière en Suisse ? Bien sûr ma chérie, fonce !). Et que dire de mon grand-frère et de sa constante présence ! Merci Julien pour toutes ces soirées jeux ensemble, relâcher la pression et poser le cerveau pour une heure ou deux sur un jeu vidéo, ça fait un tel bien ! Moi aussi je suis fière d'être ta soeur !

Enfin, un grand merci à tous mes amis, de tous bords. Les "supops", belle bande de physiciens/ingénieurs en devenir il y a trois ans, nous voici tous grands et face au choix existentiel de se trouver un "vrai" boulot, un autre

boulot, ici ou ailleurs ! Merci ma Louise, nos échanges acharnés d'e-mails ont été une vraie bouffée d'air, bisous à BenJ et son fidèle soutien pour l'anti-c*, bisous à voisine Aurélie, Sandra, binôme Delphine, Margaux, binôme Sophie, Cyrille, Sean&Aurore, Jerem et Clem', Marie-Aude, nos retrouvailles sont toujours aussi belles ! J'en profite pour embrasser aussi les amis du Sud, si bien nommés, Cynthi-puce et Seb, les années ne nous ont pas éloignées, loin de là! Et les nouveaux amis: Chloé& Stephan, Lucas & Céline, Simon, Marissa & Mat, merci pour ces soirées jeux, escapes games, et apéro cagoles !

As proper experimental physicists, we did try once to count the number of different "thank you" we learned in contact to the people of CERN, Seba and I. I think this is the proper time to repeat the experiment, without google-translate! Thanks, grazie, tuk (?!), danke schön, aligato, obrigado, spasiba, gracias, choukrane, xie-xie, merci pour tout !

Pauline

Contents

1	A Ph.D thesis in the AEGIS collaboration - about lasers and antimatter	2
I	Positronium physics and experiments	5
2	Positronium: an exotic atom	7
2.1	Positronium: an hydrogenoid atom	7
2.2	Positronium lifetimes: radiation process versus annihilation process	10
3	Positronium production in AEGIS	15
3.1	Positronium production	15
3.2	The positron system of AEGIS - setup description	17
3.2.1	The source and moderator	17
3.2.2	The first Surko trap	18
3.2.3	The accumulator	19
3.2.4	The transfer line and the buncher.	20
3.2.5	The test chamber	22
3.2.6	Ps detections	23
4	Positronium laser excitation	26
4.1	Ps laser excitations - latest results	26
4.2	Ps laser excitations - main interests for AEGIS experiment	27
4.3	The laser system in AEGIS - setup description	30
5	Experimental results of Ps laser excitation	37
5.1	The Ps n=3 laser excitation measurements	38
5.1.1	The signal diagnostics	38
5.1.2	The measurements settings	40
5.1.3	Results	41

5.1.4	A quick analysis of the n=3 excitation signal obtained	42
5.2	A Doppler scan of the Ps cloud spectral line	44
5.3	The saturation regime - verification measurements	46
5.4	Rydberg Ps excitation	47
5.5	Summary of the experimental results and short prospect . . .	48
6	Simulations analysis	50
6.1	The case of high saturation photoionization regime - a simple solution	52
6.2	High photoionization regime: studies of the Doppler Scan and UV saturation measurements	53
6.2.1	The geometrical coefficient η	54
6.2.2	The photoionization probability	55
6.3	The n=3 laser at resonance and at saturation - study of the photoionization saturation	56
II	A possible positronium laser cooling ? Theoretical and simulations studies	58
7	Ps Doppler laser cooling - theory	61
7.1	Laser cooling of an open two-level system	62
7.1.1	The rate equations	64
7.1.2	The excitation rate formula	64
7.1.3	The steady-state regime for short interaction time . . .	65
7.1.4	For long interaction times	66
7.2	The scattering rate	68
7.3	Toward the force resulting of the laser-atom interaction . . .	68
7.3.1	A possible laser broadening of for the narrow-line transition of the Positronium ?	71
7.4	The Ps laser cooling, which formalism ?	72
8	Positronium laser cooling - simulations	74
8.1	The simulation C++ code - the optical pumping code	76
8.1.1	The input files	76
8.1.2	The outputs	78
8.2	Doppler laser cooling of Ps - Some simulation results	79
8.2.1	In the absence of magnetic field	81
8.2.2	In the presence of a magnetic field	92
8.2.3	What is the effect of a 1D laser cooling on the velocities of the other directions.	98

8.2.4	What is the effect on the Ps positions of the 1D cooling along the z axis ?	98
8.3	Conclusion and prospective	100
9	The Orsay laser system for the Doppler laser cooling of Ps	104
9.1	Description of the current system	104
9.1.1	The red-laser beam	109
9.1.2	The 243-nm beam	109
9.2	Stretching the UV pulse	111
9.2.1	The fiber setup	112
9.2.2	Loss cavity using beam splitter	116
9.2.3	The loss cavity setup using polarization cube	118
9.2.4	Current situation of the Orsay laser	122
10	Another way to focus of the Ps cloud? The dipolar force interaction	123
10.1	The dipolar force interaction principle	123
10.2	The dipolar force on a single atom	129
10.3	Some results	130
10.4	The dipolar force's effect on the Gaussian distributions of Ps cloud	133
11	Short summary of the Ps studies and prospective	139
III	Antiprotons manipulations and cooling studies	141
12	The AEgIS main apparatus - the traps description and plasma behaviors	144
12.1	The choice of Penning-Malmberg traps	145
12.1.1	The ideal Penning trap	145
12.1.2	The cylindrical-shape Penning trap alternative	146
12.1.3	The Penning-Malmberg trap	148
12.1.4	The AEgIS apparatus	149
12.2	The 4.5 T Penning-Malmberg trap - the catching system	150
12.3	The 1 T Penning-Malmberg trap	151
13	The 2014 and 2015 beamtimes - some results about the cooling and compression of the \bar{p} plasma	154
13.1	Electron cooling and rotating walls techniques	156
13.2	The diagnostics	157
13.3	Results on \bar{p} plasma compression	159

13.3.1	Procedure 0: loading and cooling of electrons - Study: RW applied on electron plasma only.	159
13.3.2	Procedure 1: catching and cooling of antiprotons - Study: centrifugal separation vs heating plasmas by RW drive.	161
13.3.3	Procedure 2: a second faster RW applied once the an- tiprotons are cooled.	165
13.3.4	Procedure 3: a third RW stage, with a reduced number of electrons	168
13.3.5	Procedure 4: toward a fourth RW stage and higher compressions of e^- and \bar{p}	170
13.4	Summary	171
14	Toward a sympathetic cooling of antiprotons - the laser cool- ing of molecular anions	173
14.1	A possible laser cooling of anions to sympathetically cool an- tiprotons in AEgIS	176
14.2	The C_2^- molecule	177
14.3	The first scheme: Doppler cooling over $X \leftrightarrow B$ transition . . .	179
14.3.1	The 3D optical molasses	179
14.3.2	In a Paul trap	182
14.4	The second scheme: Sisyphus cooling over $X \leftrightarrow A$ transition .	184
14.4.1	The simplest scheme with 3 lasers	187
14.4.2	With repumping lasers on the vibrational state $X(v''=1)$	188
14.5	Conclusion	189
15	Conclusion and perspective	191
A	Hydrogenoid atoms: scaling relations between Hydrogen and Positronium atom	193
A.1	General description	193
A.1.1	The positronium model	195
A.2	The time independent Schrödinger equation	195
A.2.1	For a reduced particle μ	195
A.2.2	The 1D-Schrödinger equation	197
A.2.3	Scaling relation between Ps and H atoms	198
A.3	Scaling relations - prospective	199
B	Photoionization probability for a 3-level system	200
B.1	An exact solution	200
B.2	The high saturation hypothesis to simplify the formula	201

B.3	Approximations formula - determination of the validity conditions	201
B.4	Verification of the approximation's validity made for our measurements analysis	202
B.5	The geometrical factor η approximation	205
C	Derivation of the internal energies of an hydrogenoid atom	209
C.1	Q.E.D correction	209
C.2	Zeeman effect	211
C.3	Stark and Motional Stark effects	211
C.4	The dipole strength of an optical transition	213
D	Laser cooling on a broad-transition - the radiation pressure force	214
D.0.1	The low saturation regime - $s \ll 1$	216

Chapter 1

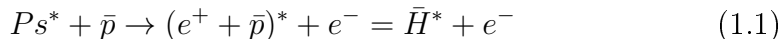
A Ph.D thesis in the AEgIS collaboration - about lasers and antimatter

Since its prediction by Dirac at the beginning of the past century and its first experimental discovery in 1933 by Anderson [1], antimatter has generated great interest and triggered multiple studies, among which experimental tests on the QED theory [2], the Charge, Parity and Time Reversal (CPT) theorem or the Weak Equivalence Principle (WEP). The WEP states that any body in a gravitational field experiences the same acceleration, independent of its own composition. Several experiments have been carried out and have verified the WEP at 10^{-13} accuracy for ordinary matter [3]. But the question is still open for antimatter. Some experiments [4, 5] and theoretical discussions such as [6] infer that the WEP should hold for antimatter. However, this statement relies on theoretical assumptions and indirect arguments, and some attempts to model a quantum gravity theory tend to predict a possible violation of the WEP for antimatter [7]. That's why further tests of the WEP are still required. In order to try to answer the debate, one promising possibility is to perform a direct measurement of the effect of gravity on antimatter.

As the unique source of low energy antiprotons in the world, the Antiproton Decelerator (AD) facility at CERN has provided bunches of tens of millions cold antiprotons (5.3 MeV \bar{p}) for more than a decade. In 2002, the first cold antihydrogen atoms were produced [8, 9]. Since then, a trapping technique has been developed to catch small numbers of \bar{H} for several minutes [10]. These advances have opened paths for systematic studies of antimatter properties, such as atomic spectroscopy [11] or gravity tests [12].

Like the GBAR experiment [13] or the recent ALPHA-g project [14], the AEGIS collaboration [15] - Antihydrogen Experiment: Gravity, Interferometry, Spectroscopy - wants to investigate the effect of gravity on antimatter. More specifically, AEGIS aims to measure the deflection of a cold antihydrogen beam under Earth's gravitational field in order to perform a direct test of the WEP.

The AEGIS collaboration plans to form antihydrogen atoms using a charge-exchange process between trapped antiprotons and a Rydberg⁰ excited positronium (Ps*) cloud:



The creation of antihydrogen via Ps charge-exchange has already been realized by the ATRAP collaboration [16] in 2004. In their system, the excitation of Ps toward a Rydberg state was performed using Rydberg cesium atoms Cs*. The Cs* excited by laser collide with the e⁺ cloud, and form Ps atoms into Rydberg states. Contrary to the double charge exchange processes used by ATRAP, AEGIS rather plans to directly laser excite the positronium cloud, in order to be able to control the Rydberg states of the Ps atoms.

I started my mission in AEGIS as a master student of the laboratoire Aimé Cotton, for studying the feasibility of laser cooling the positronium, in order to enhance the antihydrogen formation via charge exchange. I continued this project within my Ph.D project, where it was decided that I would work full-time at CERN in order to supervise the laser systems, and would take an active part in the daily experimental life of AEGIS.

Following the objectives I had to address during this Ph.D, this thesis is divided in three parts:

- Part I deals with the experimental results we obtained on the positronium atom. This first part opens with physics properties and definition of the Ps atom, in Chap. 2. Then, the first observation of the laser excitation of the Ps n=3 level, plus the demonstration of an efficient two-photon excitation path to reach the Ps Rydberg states are shown in Chap. 5. The description of the experimental setups used -positron system (Chap. 3) and laser system (Chap. 4)- as well as simulations to analyze our results are also presented (Chap. 6).

⁰A Rydberg atom is an excited atom with one or more electrons that have a very high principal quantum number (n). In this work, we will consider that the electronic level $n \geq 15$ is a Rydberg state.

- Part II is dedicated to theoretical studies and simulations of possible laser cooling of Ps. Doppler laser cooling is considered in Chap. 8, and some theory discussions about the feasibility of such a cooling are mentioned in Chap. 7. In order to perform the first experimental trials, an appropriate laser system needs to be developed. The Chap 9 deals with the technical challenges to be tackled and the possible solutions we have considered to improve the dye-laser system I installed at CERN, that presents suitable wavelengths for Doppler cooling. Finally, another laser manipulation of the Ps cloud is studied, using the Dipolar force (Chap. 10). A small summary of the studies and experimental work performed on the Ps atom is given in Chap. 11 and opens the path to the third part on antiproton physics.
- Part III is devoted to the work I took part regarding the manipulations of antiprotons. The trapping system of AEgIS, where the catching, cooling and compression of antiproton plasma take place, is reviewed in Chap. 12. Some results of the beam-time of 2014 and 2015 are given in Chap. 13. Good compression is reachable with our trapping system which leads to a better stability of the confined \bar{p} plasma and thus to better antihydrogen formation. However, cold antiprotons (~ 100 mK) are still required to enhance drastically the charge exchange cross section [15, 17] and form a cold beam of antihydrogen, crucial for precise gravity test. That's why finally, the idea of using laser cooled molecular anions to sympathetically cool the antiprotons is discussed in Chap. 14, where the theoretical studies and simulations are shown. The conclusion and prospective of this Ph.D work are discussed in Chap. 15

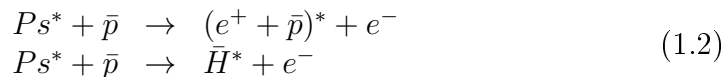
From these studies and experimental work, we published three articles [18, 19, 20]. Chapters 14, 5 and 3 respectively deal with the details of these publications.

Part I

Positronium physics and
experiments

The positronium (Ps) is a purely leptonic hydrogenoid atom formed by an electron (e^-) and its antiparticle, a positron (e^+) bound together with a binding energy of 6.8 eV. It is the lightest atom known, and it was experimentally discovered in 1951 by Deutsch [21].

As said in the introduction, Ps atom plays a major role in the AEGIS experiment since we plan to use Rydberg excited positronium to create anti-hydrogen, via a charge-exchange process with trapped antiprotons:



The study of the Ps formation (emission cone, creation rate, temperature [22], etc.) as well as its spectroscopic properties [23, 24] is not only crucial for the success of the AEGIS collaboration, but also of great interests for many physics studies, like QED tests [2, 25]. Indeed, the purely leptonic property of the positronium atom removes the corrections due to the nucleus (no quarks involved) and allows a direct measurement of the QED corrections. Positronium atoms are also an important tool for applied research, notably in porous condensed matter [26].

In the following chapters, we will first present a quick review of the Ps physics theory (chap.2), before describing the AEGIS experimental setup for Ps formation (chap.3) and Ps laser excitation (chap.4). We will then present some of the latest results we obtained (chap.5), and discuss in the second part of this thesis, a possible laser cooling of Ps (Chap. 7).

Chapter 2

Positronium: an exotic atom

As Positronium binds a matter particle and its antimatter counterpart, this metastable atom has some interesting properties, and a short lifetime. Ps has two ground-states, corresponding to different configurations of spins orientations of the electron and positron. The singlet state, with a total spin equal to zero, is called para-positronium (p-Ps). It has a short lifetime of 125 ps in vacuum and annihilates in 2γ emission. The triplet state or ortho-positronium (o-Ps) corresponds to a total spin number equal to 1 and has a longer lifetime of 142 ns in vacuum. It annihilates in 3γ emission.

2.1 Positronium: an hydrogenoid atom

As positronium is an hydrogen-like atom, its physics is very well-known and can be easily scaled from the Hydrogen physics. Indeed, in the reduced-mass framework, the reduced masses of a Hydrogen and a Ps are given by:

$$\mu^{(H)} = m_e \quad (2.1)$$

$$\mu^{(Ps)} = 2 \times m_e \quad (2.2)$$

$$\boxed{\mu^{(Ps)} = 2 \times \mu^{(H)}} \quad (2.3)$$

where m_e is the mass of an electron (or of a positron).

Resulting from the factor 2 between the reduced masses of the two systems, one can easily derive⁴ the following relations:

- Bohr radius

$$a_0^{(Ps)} = 2 \times a_0^{(H)} \quad (2.4)$$

⁴A more detailed study is given in the Appendix A.

- Hartree energy

$$E_{Ha}^{(Ps)} = \frac{1}{2} E_{Ha}^{(H)} \quad (2.5)$$

- Internal energy

$$E_n^{(Ps)} = \frac{1}{2} E_n^{(H)} \quad (2.6)$$

- Wave function

$$\psi^{(Ps)}(E_{n,l,m}^{(Ps)}, r, \theta, \phi) = \frac{1}{2\sqrt{2}} \psi^{(H)}(2 E_{n,l,m}^{(H)}, \frac{1}{2} r, \theta, \phi) \quad (2.7)$$

- electric dipole

$$d_{n_1, n_2}^{(Ps)} = 2 \times d_{n_1, n_2}^{(H)} \quad (2.8)$$

where the dipole electric (matrix element) is given by:

$$\begin{aligned} d_{n_1, n_2}^{(\mu)} &= \langle \psi_{n_1}^{(\mu)} | q_e r | \psi_{n_2}^{(\mu)} \rangle \\ &= \int \psi^{(\mu)}(E_{n_1, l_1, m_1}^{(\mu)}, r, \theta, \phi) \times (q_e r) \times \psi^{(\mu)}(E_{n_2, l_2, m_2}^{(\mu)}, r, \theta, \phi) r^2 dr d\theta d\phi \end{aligned} \quad (2.9)$$

- spontaneous rate between $|n, l, m\rangle$ and $|n', l', m'\rangle$ states.

$$\Gamma^{(Ps)} = \frac{1}{2} \Gamma^{(H)} \quad (2.10)$$

For instance, the last relation (2.10) can be derived using the proportionality relation $\Gamma \propto d^2 \Delta E^3$, where ΔE is the energy difference between the two states $|n, l, m\rangle$ and $|n', l', m'\rangle$.

These scaling relations make it possible to quickly calculate the internal energy structures of Ps, in zero field (cf. Fig 2.1). For example, the internal energy of the transition between the triplet ground state of Ps and its first triplet excited state ($n=2, l=1$) is characterized by a wavelength of 243.1 nm ; that is the double of the well-known wavelength of the Lyman alpha transition for Hydrogen ($\lambda_{Lyman\alpha} = 121.6$ nm). This assessment opens some great possibilities concerning the laser excitation studies, since the current technologies provide more easily intense beams in the range of 243 nm than in the UV-C range.

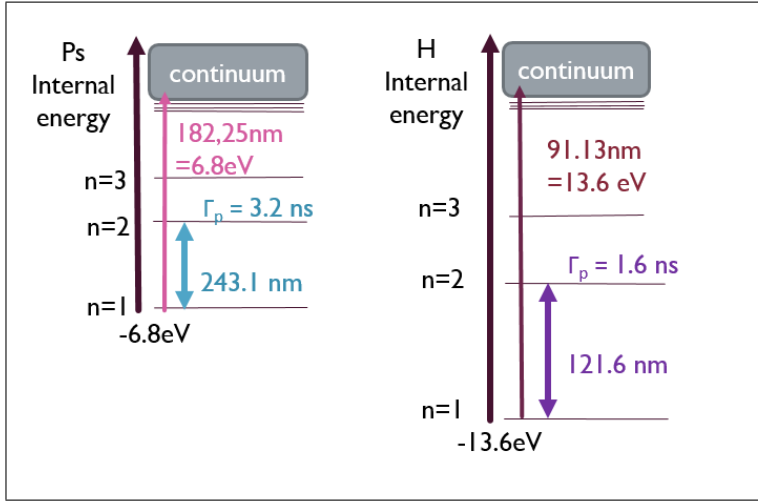


Figure 2.1: Ps and H internal energies sketches - scaling relations illustrated here. Note that no fine nor hyperfine structures are drawn. The spontaneous emission of the n=2 triplet (P) state is indicated by Γ_p

An important remark is that this scaling approach is only valid for the electrostatic interaction. When considering the fine - hyperfine structures of H and Ps, the sub-level splitting differs not only in scale but also in general structure. For the hydrogen atom, the spin-orbit coupling dominates and gives the fine structure, whereas the spin(μ_{e^-})-spin(μ_p) interaction is much smaller and provides the hyperfine splitting. For positronium, the large magnetic moment of the positron ($\mu_{e^+} = \mu_{e^-} = 657\mu_p$) leads to a bigger spin-spin interaction, comparable to the spin-orbit interaction. In addition, as mentioned in [27], "the electron-positron annihilation mechanism, acting virtually, causes spin-dependent fine-structure shifts of the same order as those caused by magnetic spin-spin and spin-orbit interactions."

In Fig 2.2, a comparison of the n=1 and n=2 hyperfine structures of hydrogen and positronium is presented. For Ps, the distinction between fine and hyperfine structures is not as well defined as for the hydrogen.

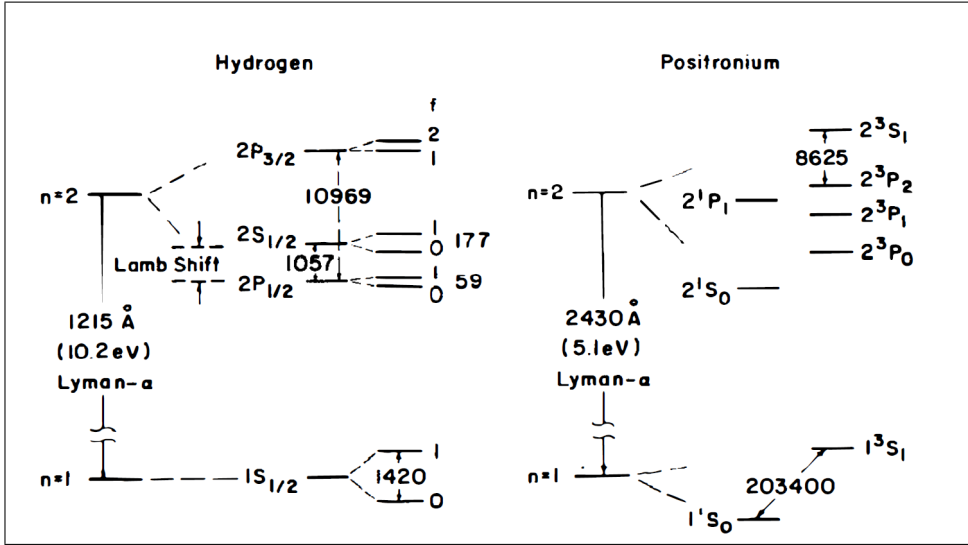


Figure 2.2: Zoom on the ground and first excited states' hyperfine structures, for hydrogen and positronium atoms. The scaling considerations only work for the electrostatic interaction framework ; once the spin-orbit and spin-spin interactions are taken into account, the unique nature of Ps leads to a different internal structure than for hydrogen. Figure taken from [27], energy level differences are given in MHz.

2.2 Positronium lifetimes: radiation process versus annihilation process

In this section, we want to explore the Ps lifetimes, for ground and excited states. Indeed, the positronium is a meta-stable atom, of whose ground states annihilate in 0.125 ns (p-Ps) or 142 ns (o-Ps) in vacuum. The p-Ps annihilates in 2γ , whereas the o-Ps tends to annihilate in a 3γ process.

By laser excitation, the lifetime of Ps can be drastically increased. In Table 2.1 are given some of the relevant radiation lifetimes (spontaneous lifetimes) and annihilation times for Ps ground states, first and second excited states and Rydberg states. It is worth noting that the radiative lifetime scales with n^3 . Ps internal states are noted as: $n^{2s+1}\ell$, where n is the principal quantum number, $s = s_{e^+} + s_{e^-}$ the total spin, and ℓ the orbital momentum.

states	annihilation lifetime	radiation lifetime
1 ¹ S	0.125 ps	-
1 ³ S	142 ns	-
2 ¹ S	1 ns	243.1 ms
2 ¹ P	3.3 ms	3.19 ns
2 ³ S	1.1 μ s	243.1 ms
2 ³ P	$\geq 100 \mu$ s	3.19 ns
3 ¹ S	-	3.36 ns
3 ¹ P	400 μ s	10.54 ns
3 ¹ D	$> 400 \mu$ s	-
3 ³ S	3.7 μ s	-
3 ³ P	11 ms	10.54 ns (<i>toward 1³S</i>) and 30.92 ns (<i>toward 2³S</i>)
3 ³ D	> 11 ms	30.92 ns (<i>toward 2³P</i>)
(n ≥ 3) ¹ S	$\propto \frac{n^3}{\alpha^3}$	$\propto \frac{n^3}{\alpha^3}$
(n ≥ 3) ³ S	$\propto \frac{n^3}{\alpha^4}$	$\propto \frac{n^3}{\alpha^3}$

Table 2.1: lifetimes of Ps, considering annihilation and radiation processes [27, 28]

The annihilation first order rates for $\ell=0$ (S states) states are given by [27]:

$$\begin{aligned} \Gamma_{2\gamma}(n^1S) &\sim f_{RYD} \frac{\alpha^3}{n^3} = \frac{1}{\tau_{S,2\gamma}} \\ \Gamma_{3\gamma}(n^3S) &\sim f_{RYD} \frac{\alpha^4}{n^3} = \frac{1}{\tau_{S,3\gamma}} \end{aligned} \quad (2.11)$$

Where α is the fine-structure constant, and f_{RYD} such as $h f_{RYD} = h c R_\infty$, where R_∞ is the Rydberg constant.

And the first order annihilation rates for $\ell=1$ states (P states) are proportional to:

$$\begin{aligned}\Gamma_{2\gamma}(n^1P) &\sim f_{RYD} \frac{\alpha^5}{n^3} = \frac{1}{\tau_{P,2\gamma}} \\ \Gamma_{3\gamma}(n^3P) &\sim f_{RYD} \frac{\alpha^6}{n^3} \ln(\alpha) = \frac{1}{\tau_{P,3\gamma}}\end{aligned}\tag{2.12}$$

In a semi-classical approach ([28]), the radiative mean-lifetimes for a given state with the final state unspecified (for $\ell > 0$) can be approximated thanks to the correspondence principle, that gives the following proportionality relation:

$$\Gamma_{spont}(n, \ell) \sim 2\pi f_{RYD} \frac{\alpha^3}{n^3} (l(l+1))\tag{2.13}$$

We would like to comment on these equations. As shown in equations (2.12) and (2.13) for P states, the radiative process appears to be faster (in α^{-3}) than the annihilation process (in α^{-5}). This observation works even better for higher ℓ states, since the overlap of positron and electron wavefunctions decreases when ℓ increases. That leads to a lower probability for having both e^+ and e^- in the same orbit, and consequently the annihilation time should increase with ℓ .

That's why in general, excited Ps are more likely to deexcite than to annihilate as it is illustrated in Fig 2.3. Referring to the Table 2.1, the reader can note that this behavior is under some particular exceptions. For instance, the 2^3S state is more likely to first annihilate than to decay toward the ground states, since the radiation transition is not allowed ($\Delta\ell \neq 1$). The 2^3S state is considered in that case as "meta-stable" with a lifetime 1.1 μs .

For further details regarding the annihilation process, the reader could refer to [27], chap 2.3. Concerning the Ps deexcitation, the reader could consult [28, 29]. A summary of the lifetimes and annihilation times for the $n=1$, $n=2$ and $n=3$ of the Ps atom is summarized in Fig. 2.4.

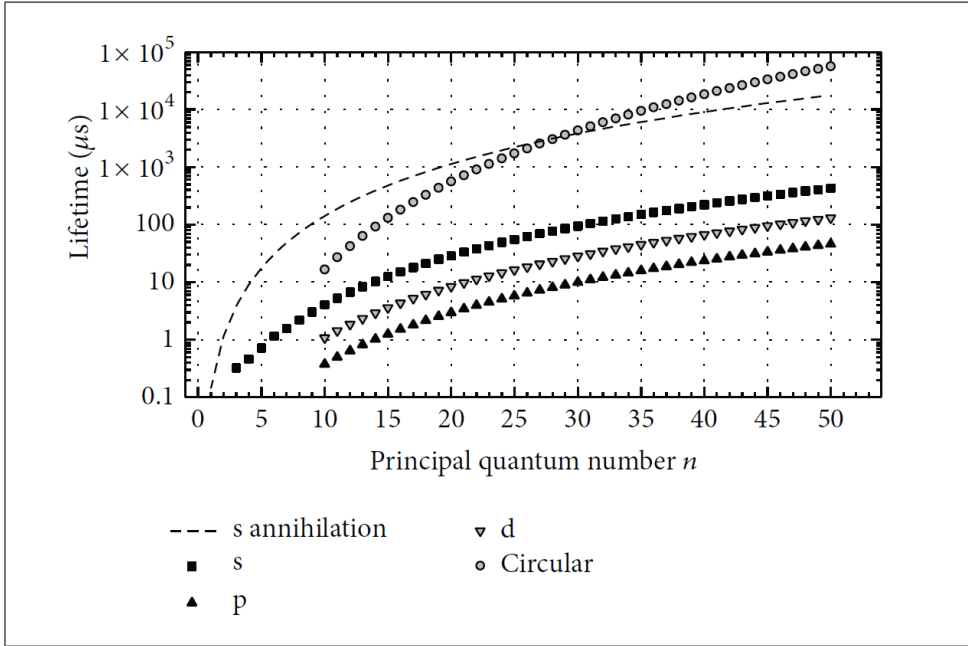


Figure 2.3: Radiative lifetime of Ps states, as a function of the principal quantum number n . *Graph taken from [13], Fig.9.* For excited Ps states ($n > 2$), the radiation process over all the sub-levels (over all ℓ) dominates the annihilation, and Ps will first deexcite before annihilating in the ground state.

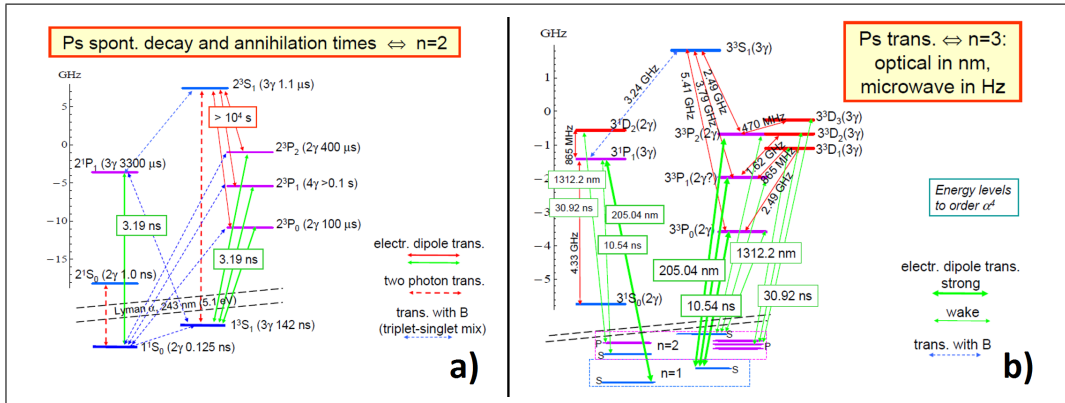


Figure 2.4: Zoom on the internal $n=1$, $n=2$ and $n=3$ levels of the Ps atom. The radiative and annihilation lifetimes of the states, as well as the wavelengths of the transition are indicated.

Chapter 3

Positronium production in AEGIS

Since the AEGIS experiment aims to create antihydrogen via charge-exchange between a Rydberg⁰ excited Ps* and an antiproton, one of the major efforts of our collaboration was to build a dedicated positron system to form Ps, excite and study it.

Here, we will present first the basics of the Ps production, and then we will give a quick review of the positron system, its main characteristics and challenges. For a more detailed description, the reader could refer to [20].

3.1 Positronium production

In metal and semi-conductors, the density of free electrons is too high for any Ps formation in bulks, the implanted positrons just annihilate after a short diffusion path inside the medium. Insulator, in the contrary, has a low enough electron density to form Ps. In particular, when implanting into silica bulks, a conversion efficiency up to 72% has been demonstrated [30].

In order to form Ps in AEGIS, a bunch of positrons is implanted on a silica-based target, with a kinetic energy in the range of few keV (see Fig.3.1). Such targets are synthesized, using a Silicon wafer electro-chemically etched in order to form nano-channels (of about 5 - 15nm diameters) inside. The surface of these nano-channels is oxidized to form a thin layer of silica.

In silicon, positrons have a quite long diffusion length before annihilation (few hundreds of nm). That allows the e^+ to release energy and diffuse toward the silica layers where Ps can be formed and emitted into the nano-channels.

⁰We remind that a Rydberg atom is an excited atom with one or more electrons that have a very high principal quantum number (n).

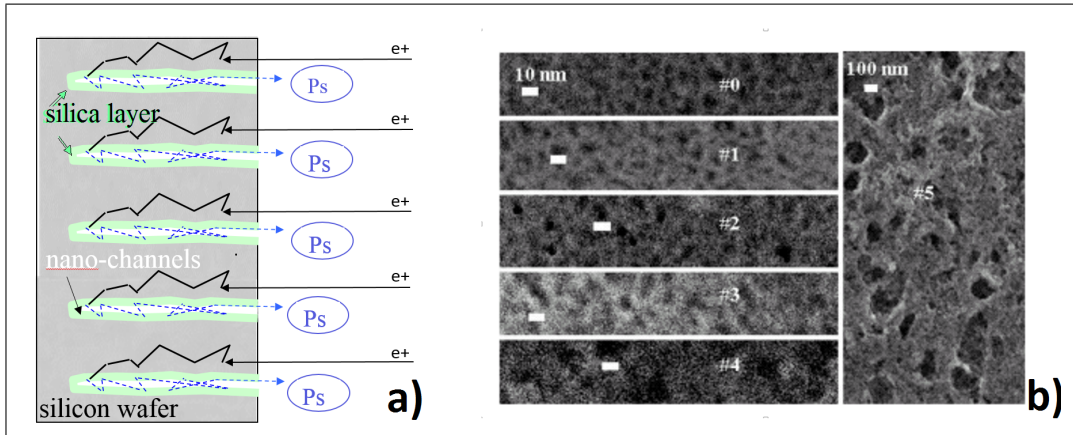


Figure 3.1: Positronium formation: a) Sketch of a silica-based target (transverse cross-section). The incoming e^+ is implanted in the Silicon wafer, diffuses and reaches the Silica layer where Ps is created. Ps then reaches the surface after several collisions with the nano-channels' walls. b) top view images of some silica-based targets used in AEGIS - These pictures are obtained by scanning electron microscope (SEM) technique, that reveals the nano-channels structure. *Pictures taken from [31]*

The converted Ps atoms collide with the nano-channel's walls and loss energy, some of them annihilate during the process. In our samples, up to 50% of the implanted positrons are converted to o-Ps that can reach the surface and be emitted into the vacuum. By varying the implantation energy, one changes the depth impact of the e^+ into the target, and consequently, the efficiency of the thermalization of the Ps by collision with the nano-channels' walls.

In order to form efficiently o-Ps into vacuum, the positron cloud has to be implanted at keV energy range into the nano-channel silica target convertor. We need then to be able to bunch the e^+ cloud at the suitable energy, and in the mean time, being able to both focus spatially (full width tens of maximum <5 mm) and temporally (FWHM <10 ns) the positrons on the target. The following section 3.2 gives a quick overview of the positron system conceived to provide positron bunches optimized for the o-Ps production with our target convertors.

3.2 The positron system of AEGIS - setup description

To produce positrons, the AEGIS experiment uses a ^{22}Na radioactive source¹, that emits β^+ radiation with a half-life of 2.6 years. In March 2012, AEGIS bought a ^{22}Na 21mCi β^+ radioactive source. Since the radioactive source efficiency decreased down to 11mCi in 2015, a new 50mCi e^+ source was ordered and installed in June 2016, that provides about 4 times more positrons. We will start here to first give a quick description of each different part of the so-called positron system of AEGIS, from the source to the vacuum test chamber (see the schematic in fig 3.2), before getting into the positronium production.

3.2.1 The source and moderator

As the radioactive source emits positrons at high energy, with a broad energy spectrum, a *moderator* is used to slow down fast positrons at the exit of the source, with an efficiency of a few percent. The moderator consists of a thin solid film of Neon deposited directly on the surface of the source and its holder. For growing it, a Ne gas is injected into the source chamber, and freezes on the source holder, set at 7 K via a closed Liquid Helium (LHe) cooling circuit.

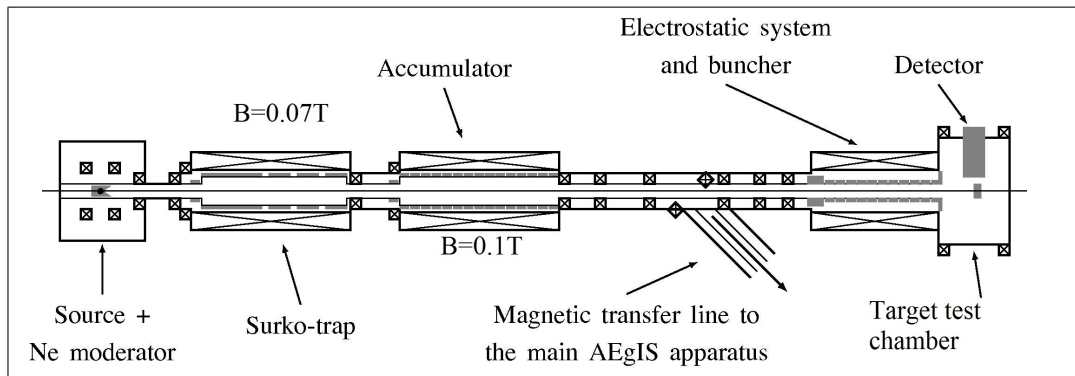


Figure 3.2: Sketch of the AEGIS positrons system. [20]

¹Another way to produce e^+ is to bombard high energy electrons on a dense target, that can be converted in a pair of ($e^- - e^+$).

3.2.2 The first Surko trap

Continuously emitted positrons are first stacked into a Surko-like trap, then into a second trap, called the "accumulator", which typically enable to reach up to 10^8 positrons in a bunch. Named after C.M.Surko and coworkers who first invented this type of trap [32, 33], a Surko trap is a Penning-Malmberg trap using a buffer gas to cool down the positrons. Different stages composed a Surko trap, each stage has a lower electrode potential than the previous one, as well as a lower buffer gas pressure. Our Surko trap has 3 stacking stages (see fig 3.3). As positrons come into the trap in the first stage, they loose energy through inelastic collisions with gas molecules and get colder. This first cooling has to be efficient, that's why the buffer gas pressure is quite high ($\simeq 10^{-4}$ mbar), as a consequence, the lifetime of positrons is shortened to few hundreds of milliseconds. Cooler positrons then fall into a second deeper stage, they can't escape back, and get colder. Then they fall into a third lower potential well, and get stack.

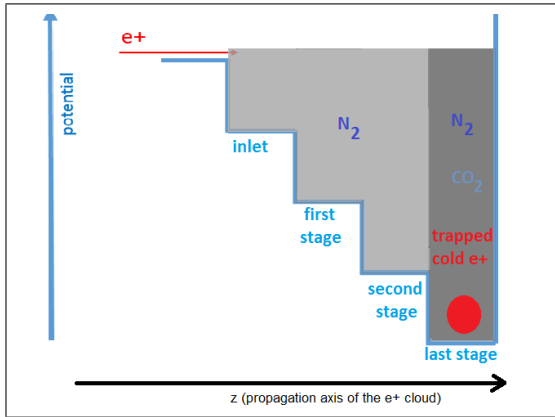


Figure 3.3: Principle of a Surko trap: continuously emitted e^+ enter by the inlet electrode, collide with buffer gas, get cooled and finally accumulate in the last stage, where rotating wall (RW) compression is applied to them.

In the AEGIS system in 2015, with the 11mCi source, the Surko trap provides a pulse of around $3 \times 10^4 e^+$, every 0.15 s. The magnetic radial confinement is done with a 0.07 T magnetic field, and the three stages are shaped with 6 electrodes. A rotating wall² (RW) drive to compress the positron plasma is applied on the last stage. The buffer gas is a mixture of N_2 gas (up to 10^{-4} mbar, injected into the whole trap to first cool fast

positrons), and CO₂ gas (which is injected only in the third stage directly through the sectorized electrode, in order to compensate the heating from the RW).

3.2.3 The accumulator

The so-called accumulator trap is also a Penning-Malmberg trap, using only CO₂ gas to compensate the heating from RW and thus to compress positrons. In comparison to the first Surko trap, the accumulator has a lower gas pressure (6×10^{-8} mbar), with a confinement magnetic field of 0.1 T. Consequently, the e⁺ lifetime is of the order of minutes, rather than milliseconds for the Surko trap. 21 electrodes shape a harmonic potential well, improving the storage time of e⁺ and thus a better cooling process (adiabatic decay of e⁺ into deeper regions of the trap) than for a stairs-like potential. RW is applied on the middle electrode. By raising up and down the inlet electrode (see Fig.3.4), this second trap can be filled several times, stacking e⁺ pulses from the first Surko trap every 0.15 s. The maximum storage time is around 9 min. In normal working conditions with the 11mCi source (year 2015), 1000 pulses are stacked in the accumulator to reach up to 7×10^7 e⁺ in less than 3 min. Then, the potential well is reshaped to a linear slope in order to dump the e⁺ plasma, with an ejecting energy that can be adjusted between 50 eV and 500 eV. In order to be efficiently transferred to the "main" apparatus, the positrons need to be accelerated up to 300eV, to avoid to be back-reflected by the 4.5T magnetic field of the Penning trap. We note that raising a potential to give them an acceleration of 50eV to 500eV leads to a typical temporal spread of the cloud of about 15 - 20 ns. Opening the accumulator trap, without accelerating the positrons would lead to a e⁺ cloud of only few eV energy, with a big energy spread. This is not desirable for a good transport, compression and acceleration, that is necessary to implant focused positrons with the proper energy in the target converter of the test chamber. . To work in the test chamber (Fig. 3.6, the e⁺ plasma is dumped with 100 eV energy from the accumulator (see fig 3.4) into the "buncher", the accelerating electrodes (see section below). In this context, the term "positron plasma" will refer to a compressed cloud of positrons, with a typical number in the range of $10^6 - 10^8$ positrons.

²The RW technique is also called Radial Compression Using Rotating Electric fields. This consists of applying a rotating electric field in order to couple it with the plasma to inject angular momentum. "These fields produce a torque on the plasma, thereby compressing the plasma radially in a non-destructive manner" [34] Chap. 4.5.

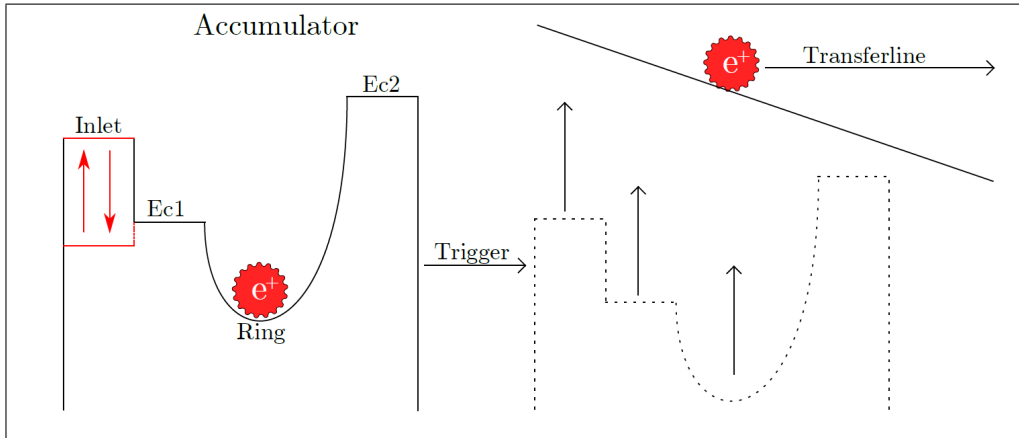


Figure 3.4: Accumulator: principle of the dumping process. Positrons are accumulated up to $10^8 e^+$ in the center of an harmonically-shaped trap, where a RW compression is applied (left figure). In order to dump, the electrodes' potential is raised to form a linear slope to bunch the e^+ plasma, with an adjustable kicking energy of few tens of eV (right figure). *Figure taken from [35]*

3.2.4 The transfer line and the buncher.

As seen previously, the AEgIS experiment aims to produce \overline{H} via a charge-exchange process between a Rydberg excited Ps and a trapped \overline{p} (see Eq. 1.2). For a matter of space, the experimental zone is organized in different floors or layers, see Fig.3.5. On the first floor, the \overline{p} are delivered from the AD thanks to several focusing and bending magnets. We will name this part the AD-6 arm. The two main Penning-Malmberg traps (referred as 4.5 Tesla and 1 Tesla traps) are settled in the prolongation of the incoming \overline{p} line.

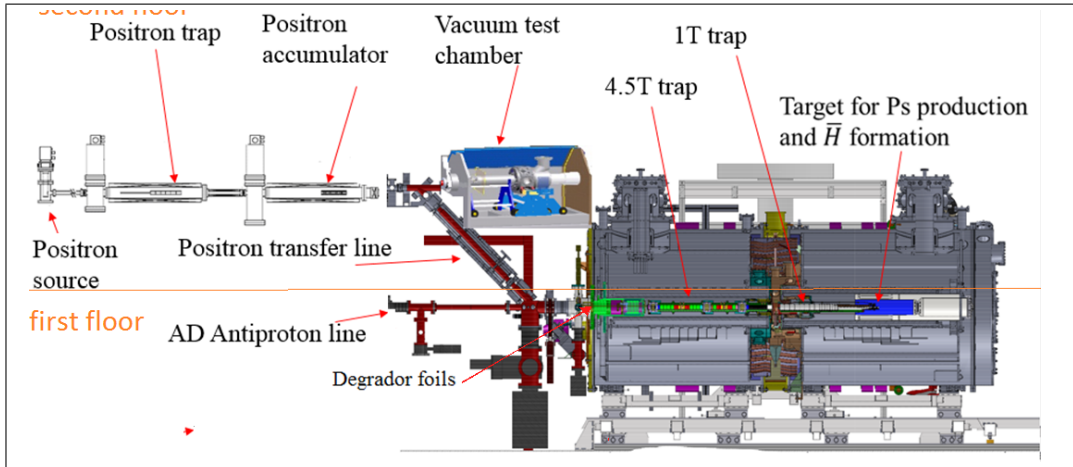


Figure 3.5: Sketch of the AEGIS zone, in front view. In the first floor, the AD arm provides antiprotons that are trapped into the main apparatus (first in the 4.5 Tesla trap and then into the 1 Tesla trap). On the second floor, the positron system is installed. A transfer line has been built to transport e^+ from the accumulator traps into the main traps.

On top of the AD arm, the positrons system (source and traps) is set-up. A dedicated transfer line to inject e^+ from the second floor accumulator trap to the 4.5 T trap has been developed (see Fig.3.5). At the exit of the accumulator, the positrons move in a bunch of ~ 20 ns and ~ 20 cm spread (FWHM). They are then magnetically transported by the use of 7 solenoids. Some small correction coils have been installed too.

In order to study more easily the e^+ and Ps physics, a **test chamber** at room temperature has been built on the second floor. For some of the intended physics studies, like spectroscopy measurements, the region of the test chamber has to be as magnetic-field-free as possible. For other studies, a magnetically induced quenching between o-Ps and p-Ps would be needed. Thus, the chamber has been designed to implant positrons in a target held in a magnetic field tunable from less than 2 Gauss up to 300 Gauss.

In order to inject the e^+ inside this test chamber, 28 electrodes generate the final electrostatic transport, as shown in Fig.3.6(no more magnetic field guiding). A special device has been conceived to reshape the temporal spread of the e^+ beam, and to give an adequate implantation energy [20]. It is called the "buncher" (see Fig. 3.2), and is made of the 25 last transferring electrodes of 1.6 cm each, for a total length of 40 cm.

The first electrode is made of μ -metal, that acts as a magnetic field terminator to reduce the field from 85 G (the transport magnetic field value immediately before the injection in the electrostatic system) to 2 G within 5 mm. The μ -metal electrode, set at -800 V, the second electrode (-2100 V) and the following 25 electrodes of the buncher form two lenses focusing the positrons into the middle of the buncher itself.

With its 40 cm long, this system is long enough to contain the whole positron pulse which. Indeed, at the buncher entrance, the e^+ pulse width is estimated to be about 20 cm [20]. When the positron pulse is arrived, a parabolic potential is raised between the first and the last electrode in order to compress the pulse in time (from 20 - 30 ns to about 7 ns) and space (few mm, depending for instance of the electro-magnetic conditions inside the test chamber). It also allows to accelerate the e^+ bunch, from an energy of 100 eV to the required implantation energy, typically 3.5 keV (up to 7 keV).

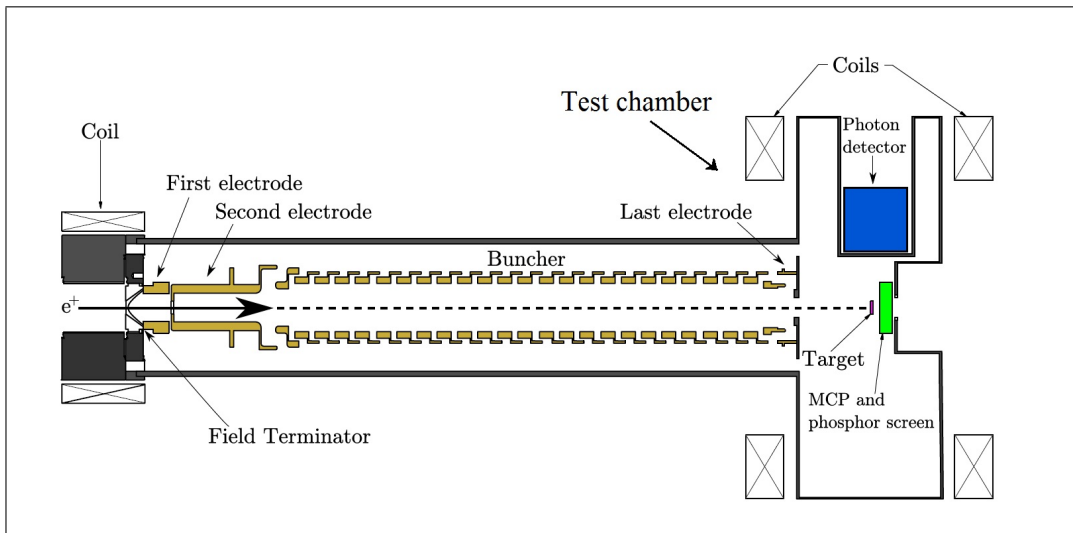


Figure 3.6: Transfer line (Buncher) and the test chamber sketch. *Figure taken from [35]*

3.2.5 The test chamber

The final stage of the e^+ system is the aforementioned test chamber, where the e^+ beam is implanted with a kinetic energy of few keV into a nano-channeled silica target (See Fig. 3.6). An "actuator" holder, consisting of a movable mount with several slots on it, that makes possible the installation

of 5 target samples the same time. This system gives the possibility to test different targets by moving the actuator position, without having to break the chamber's vacuum for changing from one target to another one. For centering the incoming beam, one of the 5 slots of the actuator is left empty to let the e^+ beam pass through it, and annihilate on a micro-channel plate (MCP) with phosphor screen, that is placed just behind the target holder. A PbWO_4 detector is set-up as close as possible on the top of the target (~ 4 cm) in order to maximize the annihilation counts registered. This crystal is a fast detector able to quickly acquire annihilation gammas ; for a single photon, the answer of this PbWO_4 gives a signal with a FWHM less than 4 ns.

These detectors provide both a spatial diagnostic to measure the e^+ beam size (MCP) and an annihilation detection to monitor the amount of e^+ hitting the target area (PbWO_4). It is estimated that 30 -40 % of positrons released from the accumulator hit the sample in a spot of < 4 mm FWTM³ . The others are lost mainly because of the small entrance of the Buncher, that is at the switching point from magnetic to electrostatics transport. Indeed, the e^+ beam expands when passing from magnetic to electrostatic confinement, causing losses. The incoming e^+ are efficiently converted into partially thermalized o-Ps ; up to $\sim 35\%$ of the 3.3 keV e^+ are converted into o-Ps. The calibration of the efficiency of conversion of the targets used in AEGIS has been realized in a previous work by the Trento group, led by Sebastiano Mariazzi and Roberto Brusa [22] by integrating the o-Ps signal.

3.2.6 Ps detections

A widely used method to probe positron behavior in diverse media and detect positronium formation is the **positron annihilation lifetime spectroscopy** (PALS) technique. Based on the principle that positrons or positronium atoms will annihilate through interaction with electrons in materials, the released annihilation gamma rays are detected. The positrons are continuously emitted by a radioactive source and implanted in the target with a precisely defined timing, using electrical choppers. This is the start signal.

The detection of the gamma rays resulting from the annihilation with the material gives the stop signal. By integrating many signals, the lifetime spectrum of positrons is obtained. The Ps formation can be detected since o-Ps usually has a much longer lifetime than positrons, therefore the gamma rays coming from their annihilation hit the detector after the prompt peak coming from e^+ annihilation.

³Full width at tenth maximum

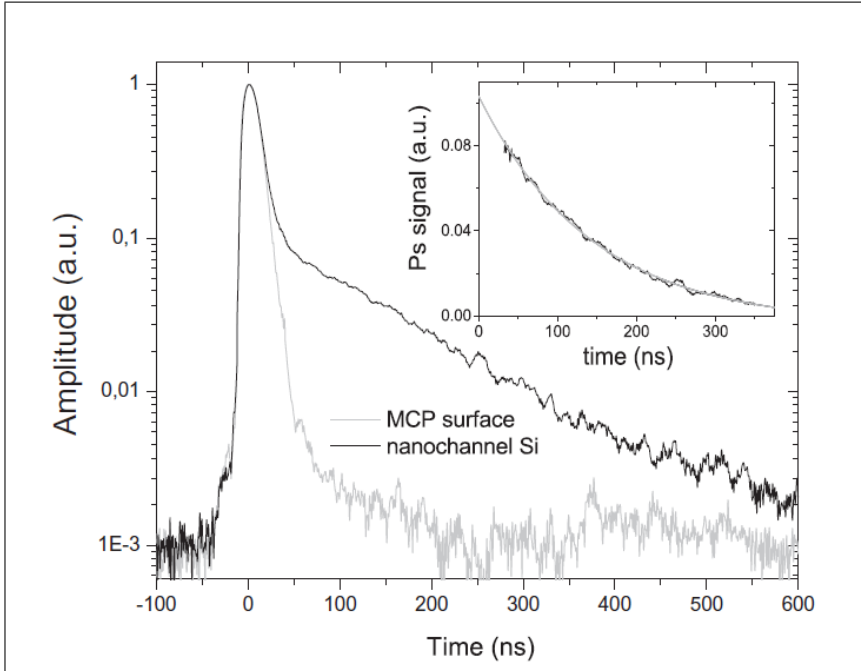


Figure 3.7: Typical SSPALS[36] spectra measurements in AEGIS. The gray curve shows the e^+ prompt peak annihilation on the MCP (no Ps formation). The black curve shows the signal of the e^+ implantation on a silica-based target and the Ps formation. After the prompt peak of e^+ , a long tail is recorded corresponding to the annihilation of o-Ps in vacuum, with an expected lifetime of 142 ns. In the top right window image of the figure, a zoom of the long tail annihilation signal is fitted by a decreasing exponential and gives a $\tau \sim 140$ ns. The long lifetime tail signal is evidence of Ps formation and emission in vacuum. Each curve is an average of 10 SSPALS signals. *Figure taken from [20].*

An alternative way to measure Ps formation, used in AEGIS, is the single-shot **positron annihilation lifetime spectroscopy** (SSPALS) technique [36]. In contrary to the PALS, this technique consists in implanting simultaneously many e^+ . Fast detectors are required in order not to saturate the signal by the numerous annihilation gamma rays obtained in one implantation shot. In this process, the long lifetime spectrum of Ps can be measured in one bunch of positrons. Fig 3.7 shows typical signals of e^+ implantation and Ps formation inside the test chamber of AEGIS.

An example of the calibration of the efficiency of a typical positron-positronium target converter we use is shown in Fig. 3.8. This works comes from previous studies of the positron crew in AEGIS [22]. We estimate that around 35 % of positrons implanted with an energy of 3.3 keV are formed as o-Ps. Then, using a Ps diffusion model, we can estimate that from 3×10^7 e^+ , 4×10^6 o-Ps are emitted into vacuum [22], meaning an efficiency of about 13%. An example of the calibration of the efficiency of a typical positron-positronium target converter we use is shown in Fig. 3.8. This works comes from previous studies of the positron crew in AEGIS [22]. We estimate that around 35 % of positrons implanted with an energy of 3.3 keV are formed as o-Ps. Then, using a Ps diffusion model, we can estimate that from 3×10^7 e^+ , 4×10^6 o-Ps are emitted into vacuum [22], meaning an efficiency of about 13%.

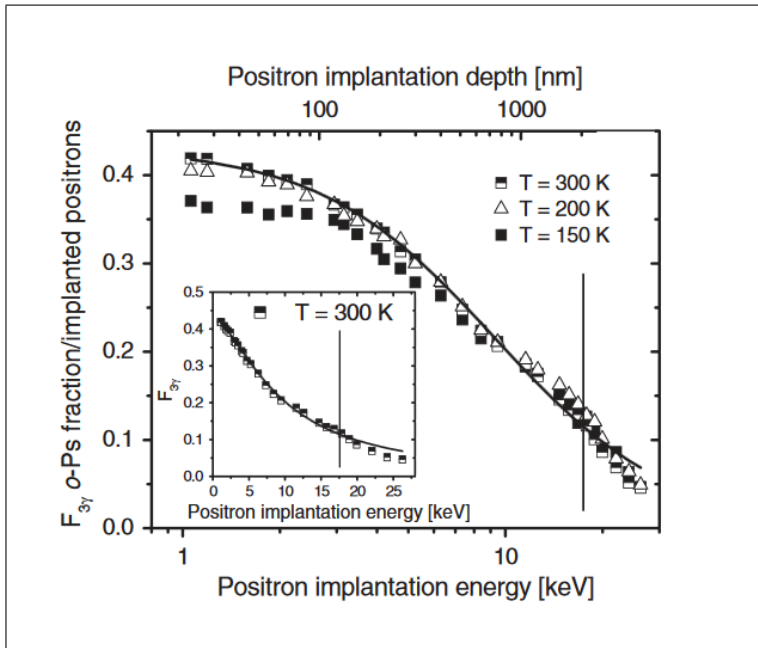


Figure 3.8: The fraction $F_{3\gamma}(E)$ of implanted positrons forming o-Ps that annihilate in a 3γ process is shown as a function of the implantation energy E of the positrons. This works has been realized in [22], for three different temperatures of the target converter. For 3.3keV, the converted fraction is about 35 %.

Chapter 4

Positronium laser excitation

4.1 Ps laser excitations - latest results

Since its discovery in 1951, the study of positronium physics - and in particular the spectroscopy - has become a great tool to perform tests on bound-states QED theory, since Ps is free of hadronic effects that disturb QED calculations.

The first laser excited state of Ps has been observed by S. Chu and A. P. Mills, Jr. [37] in 1982, via a two-photon absorption technique to perform the $1^3S \rightarrow 2^3S$ optical transition. Following this work, in 1990, K P Ziocck, C.D. Dermer and coworkers developed a UV pulsed laser system to saturate the transition $1^3S \rightarrow 2^3P$ ($\lambda_0 = 243$ nm) [38] and produce a large fraction of excited Ps. They also first demonstrated in 1990 the Rydberg excitation of Ps, using a two-photon process via $1^3S \rightarrow 2^3P \rightarrow n=\text{Rydberg}$ states [39].

In 2012, A.P. Mills and coworkers exploited the same optical path to produce Rydberg positronium [40] with an overall efficiency of 25 %. More recently, the Cassidy's group worked on developing a technique to select Ps* Rydberg states via the Stark effect [41], that leads to the possibility of manipulating long-lifetime Ps*, using the huge electric-dipole momentum of Rydberg states to control their motion. This technique is of great interest to create a beam of long-lifetime Ps, to perform free-fall gravity test on Ps [42]. In the last chapter (chap.II) of this part, we will also present another technique we believe could lead to a great control of Ps motion and lifetime, thanks to Doppler laser cooling.

4.2 Ps laser excitations - main interests for AEGIS experiment

As seen in Chap.1, in order to form a cold beam of antihydrogen, AEGIS plans to use the charge-exchange process between an antiproton and a Rydberg positronium, following the reaction:



There are mainly three benefits in using this technique rather than the standard mixing process in nested traps⁴ :

- In the AEGIS charge-exchange scheme, the Ps cloud is generated via conversion of a pulsed e^+ plasma implanted on a Silica-based target. Consequently, the \bar{H} formation is pulsed, which is primordial for a time of flight measurement as planned in AEGIS.
- This method forms \bar{H} with a narrow and well-defined n-state distribution, in comparison to the mixing process [43]. Indeed, the created \bar{H} has a similar binding energy than the internal energy of the Ps^* implied in the reaction [17].
- Besides, colder antihydrogen atoms are expected to be formed via charge-exchange than via mixing formation. In the mixing process, the two plasmas of \bar{p} and e^+ merge and consequently get some heat during the process. Unlike in the charge exchange formation, where the \bar{p} plasma can be merely held at rest. Since the formed \bar{H} momentum is dominated by the \bar{p} one, this reaction potentially leads to form cold \bar{H} , with an antiproton plasma kept at 100mK. For further details, the reader could refer to [44], chap 2.3.

In order to increase the formation rate of antihydrogen by charge exchange, the positronium cloud is excited to Rydberg states. The Ps geometrical cross section scales as $\sigma_{Ps,n} = a_0^2 n^4$ for an excited Ps, where n is the principal quantum number.

Although a quantum calculation is necessary to obtain the collisional cross section when the positronium is in a low-n state, for a high-n state of positronium, a classical trajectories Monte Carlo approach can be used [15, 17]. This

⁴This process consists of a 3-body recombination, between two positrons and an antiproton. The two plasmas are trapped into a nested trap (M-shape trap). During the antihydrogen formation, the inner-potential walls of the trap are lowered in order to let the two plasmas interact.

collision model leads to the following conclusion: the rate of \bar{H} produced via charge exchange with a Ps^* scales with the collisional cross section σ_C . This cross section is proportional to the Ps geometrical one (σ_{Ps}) and also depends on the relative velocity between antiprotons and positronium (see [15] chap 4.).

The AEGIS proposal plans on using 100mK confined antiprotons to form efficiently antihydrogen. However, as explained in more details in Part III, the caught antiproton are cooled (via electron and adiabatic cooling) down to few tens of Kelvin. Briefly, the antiprotons delivered by the AD facility have an energy of 5.3 MeV, that is slowed down to few 10 keV after passage through thin degrader foils (tens of μm). Our apparatus allows us to catch the fraction of \bar{p} at 9 keV, and we use the so-called "electron cooling" technique (see Chap. 13.1) to cool them far below few eV. The e^- cooling that consists of sympathetically cooling the antiprotons with the electrons that have thermalized by synchrotron radiation with the environment. This limits the minimum temperature reachable to be close to the room temperature (at the Helium liquid temperature, 4.2 K). That explains why we have investigated techniques to obtain cooler \bar{p} plasmas.

Assuming that the antiprotons are cooled down to 100mK, the cross section of the charge exchange process reaction increases when the relative velocity $k_v = \frac{v_{PsCM}}{v_{e^+}}$ of the center of mass velocity of the Ps and the positron orbits decreases, as shown in Fig. 4.1.

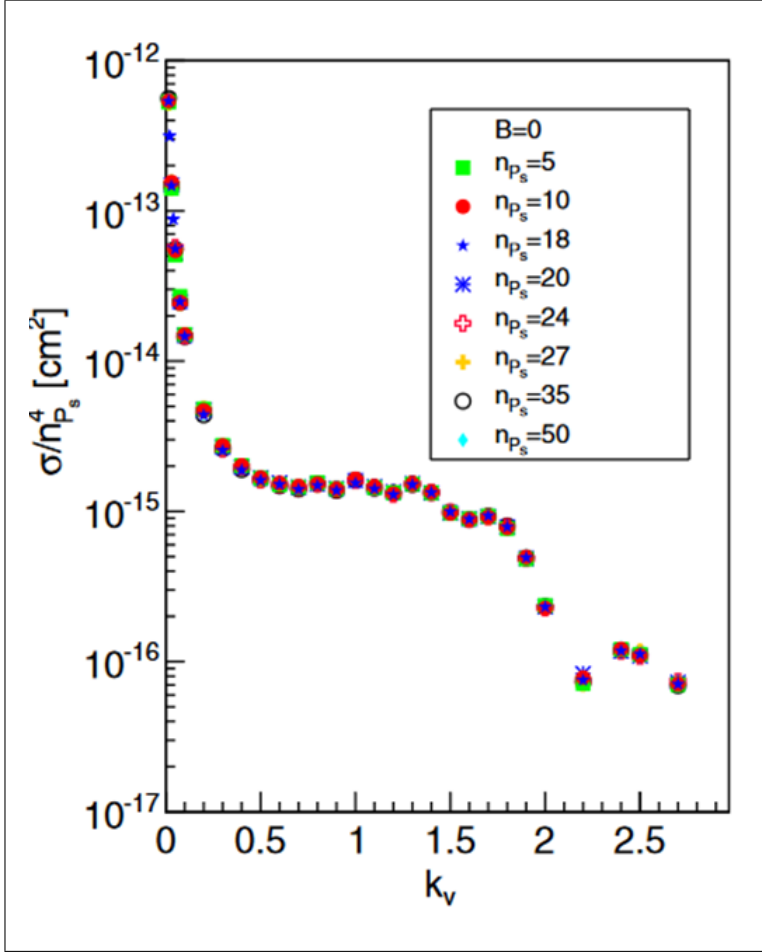


Figure 4.1: Charge-exchange cross section σ divided by $n_{p_s}^4$, as a function of k_v , the ratio of the positronium center of mass's velocity and the orbit velocity of the positron. For $k_v \leq 1$, the cross section increases drastically. Calculations performed in [17].

We will deal with the particular issue of cooling antiprotons in Chap. 14.

As mentioned previously, the cross section of the reaction of charge exchange scales in n^4 , where n is the first quantum number of the Ps internal state, translating then the excitation level of the Ps [17]. AEGIS aims to excite Ps around $n=15$ to $n=20$, in order to drastically improve the \bar{H} formation rate. A higher excitation would lead to an even better enhancement of the antihydrogen production rate, but it is not feasible in the AEGIS ap-

paratus. Indeed for $n \geq 20$, Ps^* is ionized due to the huge motional Stark effect in a 1 T magnetic field. More information about this limiting process can be found in [45].

Another benefit to the Rydberg excitation is that the Ps lifetime is drastically prolonged, as seen in the section 2.2. In the 1 T trap's production region, the distance between the target convertor to produce Ps and the \bar{p} trapped plasma is about 2 cm (see Fig. 4.2). The excitation of the Ps cloud toward Rydberg states allow them to fly by this 2 cm distance without self-annihilating and then reach the antiproton region where the charge-exchange process can occur to form antihydrogen.

4.3 The laser system in AEgIS - setup description

We will now describe the dedicated AEgIS laser system for excitation to Rydberg states, before presenting some experimental results of laser excitations inside the test chamber.

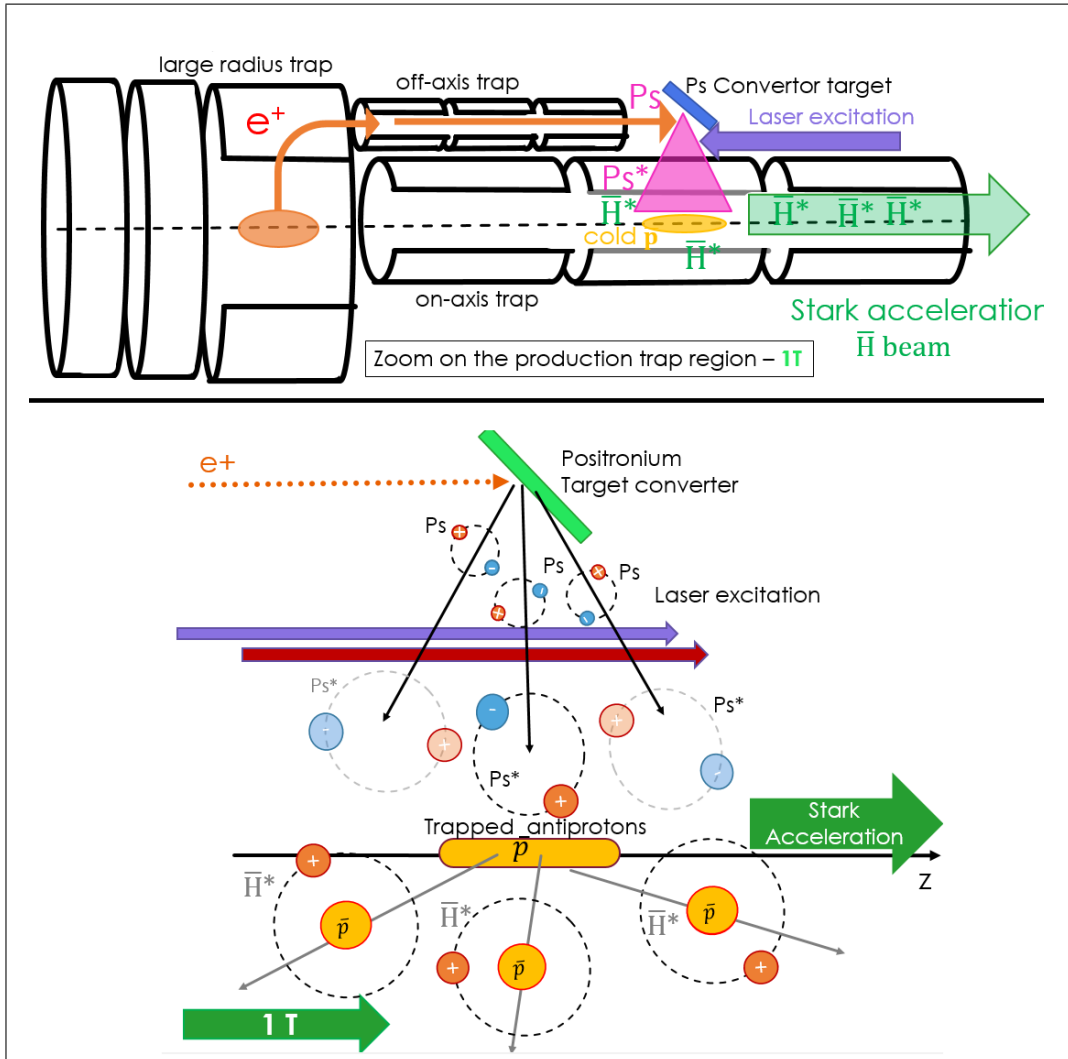


Figure 4.2: Schematics of the inside of the 1 T trap. Top: the \bar{p} plasma is trapped on axis, whereas the positrons are loaded by cyclotron excitation motion into the off-axis trap. The production Silica-based target is placed off-axis, at about 2 cm distance from the on-axis \bar{p} trap. Bottom: the \bar{H} production is triggered by the implantation of the pulsed positron plasma into the target. A Ps cloud is created, laser excited to Rydberg states and travels to the \bar{p} plasma to form \bar{H}^* via charge-exchange $Ps^* + \bar{p} \leftarrow e^- + \bar{H}^*$.

In order to reach Rydberg states for Ps in presence of 1 T magnetic field, a dedicated broadband laser system has been conceived and built by the Milano

group of our collaboration (INFN, Milano University) [46]. The maintenance of this laser system to perform Ps excitation inside the test chamber has been part of my work at CERN.

As mentioned previously, the production of Rydberg positronium has been first demonstrated by Ziock and coworkers in 1990 [39], using a two photon excitation process, via the optical path $1^3S \leftarrow 2^3S \leftarrow n$ Rydberg. This technique has been also exploited in 2012 by Cassidy and Mills [40] that excited 25 % of the produced Ps toward Rydberg states.

The Milano group of AEGIS has preferred designing and building a laser system to reach Rydberg levels using the $n=3$ level as the intermediate step, as illustrated in Fig. 4.3. The excitation from $n=3$ to Rydberg states was expected to be more efficient and to require less laser intensity than from $n=2$ level [45], which is interesting when laser excitation has to be done in a cryogenic environment as in the AEGIS apparatus. Conceiving such a laser system at VUV wavelength with broad lines represented by itself a challenging project, regarding the laser technologies. This was another motivation for our collaboration to choose this optical path for the two photon excitation.

Moreover, exciting Ps toward $n=3$ level hadn't been performed so far ; and for instance, the excited Ps($n=3$) can decay toward the $n=2$ metastable state (the S triplet state) with a branching ratio of $\approx 13\%$ [46, 47]. Being able to obtain a long-living Ps beam in a single defined state is a key ingredient for interferometry and gravity measurements, since the precision of the interferometry measurement scales in T^2 , where T is the time of interaction [48]. For example, the group of Cassidy plans to realize a gravity interferometer using Rydberg states [42]. Producing a beam of Ps in the metastable $n=2$ state could open ways to Ps gravity measurements too.

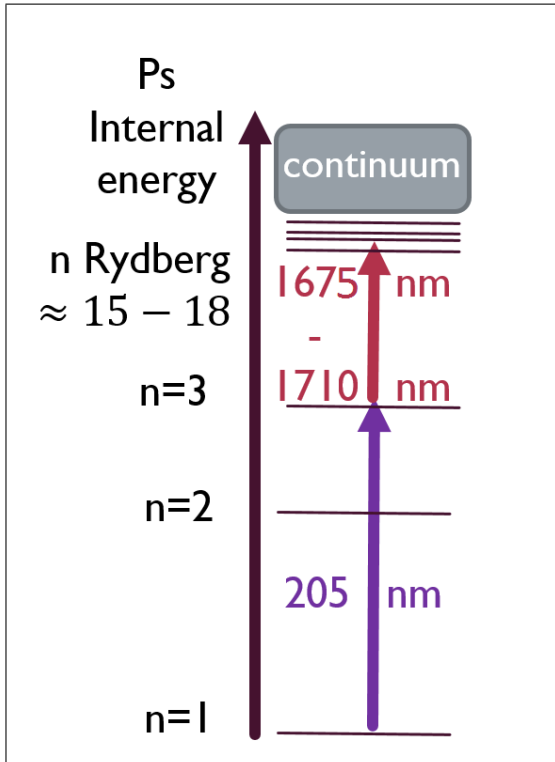


Figure 4.3: Internal Ps energy scheme with the Milano laser system transitions. The purpose of this laser system is to perform Rydberg excitation in 1 T magnetic field and cryogenic environment. It has been developed to have a broad spectral linewidth of $\sigma_{rms} = 2 \pi \cdot 48 \text{ GHz}$ (spectral bandwidth measured FWHM = $110 \text{ GHz} = 2 \sqrt{2 \ln(2)} \sigma_{rms}$).

The main laser pump in the AEGIS apparatus is a Q-Switched Nd:YAG laser from Eskpla that provides three wavelengths: 1064 nm (100 mJ), 532 nm (150 mJ) and 266 nm (15 mJ). A fourth exit delivers a pulse of 1064 nm + 532 nm (150mJ). The repetition rate is 10Hz, for a pulse length $t_{1064nm} = 6 - 8 \text{ ns}$; depending on the supply settings of the flash-lamp which pumps the Nd:YAG crystal. Fig.4.4 shows the two different optical lines that generate the required 205 nm and $\sim 1700 \text{ nm}$ beams. Here is given a short description:

- *The UV (205nm) line: $n=1 \leftrightarrow n=3$ transition*
 In order to generate the 205nm beam, a non linear BBO (Barium borate) crystal is used to sum two incoming beams of 266nm and 894nm. This crystal is named frequency "sum" crystal in our apparatus. Although the 266 nm is directly provided by the Nd:YAG pump, the 894

nm has to be generated first. A PPKTP⁵ crystal is used to convert the 532 nm light (pump) into 894 nm (signal) and 1313 nm (idler). We refer to this PPKTP crystal as an OPG crystal, for Optical Parametric Generator. The 894 nm beam is then amplified through two BBO crystals, named OPA (optical parametric amplifiers). The visible damage threshold is higher for BBO than KTP crystal, allowing the use of an intense 532 nm pump beam to amplify. At the end of the line, around 10 mJ of 894 nm is created, collimated and injected with 10 mJ of 266 nm inside the sum crystal. A beam of around 130 μ J of 205 nm is generated, with a pulse of 1.5 ns. Between the sum crystal and the test chamber, the 205 nm has to travel in air through more than 4 m. As a consequence, more than 55 % of the beam energy is lost during the path, due to absorbing optics (the specially coated mirrors we used still absorb around 5 % each) and absorption during the travel in air. The UV absorption process in air is interesting and quite complex we believe: VUV at 200 nm dissociates oxygen molecules (O_2), that recombine into ozone molecules (O_3). This ozone molecules are created along the UV paths, and drastically absorb the UV light at 200 nm. We measured an absorption of about 10 % along 1 m of propagation. Typically, 60 μ J of 205 nm is sent through the test chamber to excite Ps, with 6 mm x 8 mm of waists. We can remark that even with this absorption, by focusing the laser spot over 6mmx8mm, the transition $n=1 \leftrightarrow n=3$ is saturated. Experimental checks of this saturation have been performed and are presented in Chap. 5.

- *The IR (1675 - 1710nm) line $n=3 \leftrightarrow n=Rydberg$ transition:*

The 1064nm beam is converted via two KTP crystals to generate the $n=3 \leftrightarrow n=15-20$, corresponding to wavelengths in a range of 1708nm - 1678nm, with an idler beam of 2907nm - 2821nm. Indeed, as mentioned in Sec. 4.2, the presence of the 1T magnetic field in the production trap region limits the Rydberg states of the Ps that we can reach: for $n \geq 20$, the Ps* are ionized due to the huge motional Stark effect induced in 1 T magnetic field [45]. We then aim to only excite Ps between $n=15-20$.

The adequate beam is first generated via an OPG crystal, then amplified through an OPA. Unlike the previous situation, the KTP crystal has a higher damage threshold for IR (2.5 GW/cm² for the KTP_(1064nm,10ns)) than BBO (500 MW.cm⁻² for the BBO_(1064nm,10ns)).

⁵PPKTP is used for Periodically Poled Potassium Titanyl Phosphate. Our crystal has an inversion polarization period of 10 μ m over 3 cm.

After the OPA stage, up to 4 mJ at 1675nm -1710nm can be reached. The tuning of the wavelength is done by monitoring the temperature of the OPG crystal. This 4 mJ has to be compared to the saturation energy of these transitions $n=20$ is typically around $250 \mu\text{J}\cdot\text{cm}^{-2}$, for a full-mixing of the manifolds in 1 T magnetic field. More details are given in [46], Chap. 3.3.

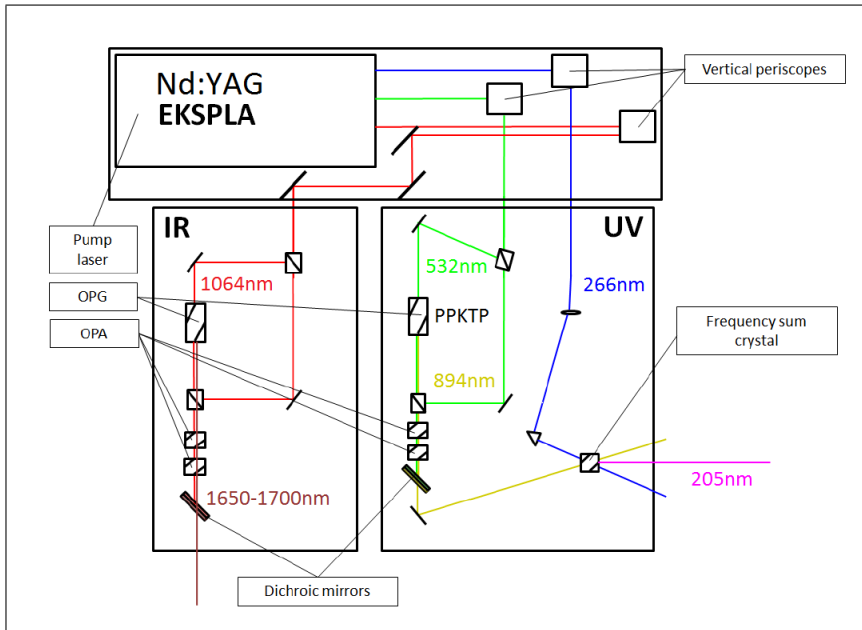


Figure 4.4: Schematic of Milano laser apparatus with the different optical line to generate the 205 and 1650 - 1700nm beams. Schematic taken from [49].

As the laser system is implemented directly in the experimental zone, and not in a separated laser chamber with temperature control and white-room standards, this system needs to be frequently readjusted. Besides, the flash-lamp characteristics change on a month-scale, leading to a different pumping of the Nd:YAG crystal and thus, to different emission parameters for the pump beams (changes in energy, beam size and beam divergence). The spot sizes and beam divergence are crucial for this system in order to optimize the non linear processes, without burning the crystals. A couple of telescopes is judiciously set along the different generation lines to adapt the beam char-

acteristics to the nominal required values.

Usually, the time-scale for a measurement of Ps laser excitation is a couple of weeks. The laser system is realigned from scratch before we start the measurements. This typically takes few days. However, the calibration and optimization of the lasers are daily checked before starting the data taking: spatial alignment, wavelengths, spot sizes, power delivered, etc.

Chapter 5

Experimental results of Ps laser excitation

In this chapter, I will present the latest results of Ps excitation we performed in AEGIS. These are the first observation of the $n=3$ excited state of Ps, and the demonstration of an efficient Rydberg excitation path using the $n=3$ level as the intermediate state. These measurements have been performed in the vacuum test chamber (see Fig. 5.1) between April and June 2015, and are the collective results of

- **the positron system's crew** - mainly constituted at that time by Sebastiano Mariazzi, the expert responsible for the positron system at CERN, by Roberto Brusa and Giancarlo Nebia leaders respectively of the Trento and Padova groups, by Benjamin Rienacker, Ph.D student of the CERN group, and by the technical students Ola K. Forslund, Lisa Marx, Laura Resch and Ine B. Larsen,
- **and the laser group** - namely Ruggero Caravita, Ph.D student of the INFN Genova group, Fiodor Serrentino and Marco Prevedelli, also from the Genova group, Zeudi Mazotta, Ph.D student of the INFN Milano lab and her supervisor Simone Cialdi, Daniel Comparat and I from the laboratoire Aime Cotton, CNRS.

A PRA article has been published [19]. As for the measurements themselves, where I worked on optimizing and aligning the laser system with the positron system, I took an active part in the redaction of this collaboration article and several corrections and exchanges with the editors and referees.

To be able to laser excite the Ps cloud, one main requirement was to synchronize the e^+ implantation in the target (that gives the starting time of the

Ps formation) with the laser pulses, in order to overlap spatially and temporally the Ps and laser beams. The synchronization was done via a custom field-programmable gate array (FPGA) based synchronization device, giving a time resolution of 2 ns and a jitter of less than 600 ps. The time delay between the prompt positron annihilation peak and the laser pulses was set to 16 ns as an optimal value. This delay was determined after several measurements for different timings around a theoretical value, given by the expected escape time of Ps from the target. This expected value was calculated thanks to a Monte Carlo code developed by Zeudi Mazzotta, that derives the propagation of the Ps cloud for a isotropic emission, taken into account the initial temperature of the Ps and its initial size. The geometry of the test chamber is implemented as well as the detector positions and efficiency given by the solid angles of detection. This code gives the laser excitation efficiency of Ps as function of the spatial and temporal localizations of the laser in regard of the Ps cloud, and provides us the theoretical optimum time and position to send the lasers inside the test chamber and enhance the excitation signal detected.

5.1 The Ps n=3 laser excitation measurements

Our first goal was to perform the $n=1 \leftrightarrow n=3$ excitation. As we have seen previously, until then, only the first excited state $n = 2$ and the Rydberg levels $n = 10 - 31$ Ps have been experimentally observed [38, 37, 40, 41].

5.1.1 The signal diagnostics

Two methods of diagnostics have been used to measure the excitation signal:

- The magnetic quenching-based measurement.

In presence of a magnetic field the 3^3P sub-states with $m = 0, \pm 1$ (excluding $3^3P_{1,m=0}$ ⁶) are mixed with the 3^1P sub-states, and can decay toward the 1^1S state, subsequently annihilating with a lifetime of 125 ps into two γ rays [46].

In a SSPALS signal (as in Fig. 3.7), this phenomenon results in a quick rise of annihilation counts just after the laser excitation, then in

⁶We note the internal state of Ps, with the hyperfine structure splitting $|n, l, s, j, m\rangle$ as: $n^{2s+1}\ell_{j,m}$, where n is the main quantum number, l the orbital momentum, s the total spin, $j = l + s$ the total angular momentum, and m its projection over the quantization axis. We use the associated letters to define the value of l as: $l = 0 \Leftrightarrow \ell=S$, $l = 1 \Leftrightarrow \ell=P$, $l = 2 \Leftrightarrow \ell=D$, etc.

a decrease of the annihilation counts coming from the long lifetime o-Ps remaining, that forms the long tail of the signal. Since we laser excite really close in time after to the prompt e^+ peak signal, the small rise due to Ps quenching is lost in the prompt peak counts; thus the signal observed is simply the decrease in annihilation counts for the long tail.

- The photoionization. The 1064nm beam is used to photoionize the Ps 3^3P excited states. As for the quenching process, this technique results in a decrease of the o-Ps population since the photoionization dissociates the positronium atoms, the free positrons are quickly accelerated in few ns toward the last negative electrode of our set-up, where they annihilate.

As a diagnostic, we define the fraction $S(\%)$ of quenched or ionized o-Ps atoms as the difference of areas of the SSPALS spectra with and without lasers, normalized to area without laser. For this first measurement, the areas are taken in the region between 250 ns and 450 ns from the prompt peak:

$$S = \frac{(f_{off} - f_{on})}{f_{off}} \quad (5.1)$$

where f_{off} is the area defined by the SSPALS signal, without laser, and f_{on} the one, with laser shot. The integration time window for the S fraction of $n=3$ excited Ps is indicated in the Fig. 5.2 b) that delimits the areas f_{on} and f_{off} between the two vertical lines. This time window has been arbitrary chosen to correspond to the o-Ps emission signal into vacuum (exponential decrease of the number of o-Ps, with a lifetime of 142 ns in vacuum, translated by a $3-\gamma$ emission), before the arrival of the fast Ps atoms on the walls of the test chamber, that enhances the annihilate rate recorded in the SSPALS curves.

Note that all SSPALS curves are normalized to 1, regarding the maximum prompt peak value. This normalization is done to limit variations of the experimental conditions from one measurement set to another. Indeed, the measurements presented here have been recorded over weeks time, but the stability of the positron system is of order of hours. The moderator efficiency decreases of a 7% per hour during the first 7 hours and then around 7% per day in normal conditions. Typically during the measurements records, we grew a new moderator twice a day to keep a good efficiency of positrons production and accumulations. The normalization makes significant the comparison between SSPALS curves registered from one day to

another with different moderators states that lead to different numbers of positrons, since both the positron prompt peak and the number of Ps produced are proportional to the number of implanted positrons.

For the first measurements performed to excite and detect the $n=3$ state, the S parameter definition is independent of the chosen time window. Indeed, the excitation toward $n=3$ and photoionization of the Ps cloud is translated by the immediate dissociation of the excited o-Ps. The increase of annihilation counts caused by the photoionization of the addressed o-Ps is lost in the e^+ prompt peak annihilation signal. The signal measured in the long-tail part of the SSPALS curves is then only due to annihilation in vacuum of the o-Ps, in both case of lasers ON or OFF. That's why the S parameter that is a ratio of two integrals defined by the exponential decay of o-Ps in vacuum is independent of the time windows chosen for those measurements.

As a matter of test, we double-checked the S values obtained for a different time window (from 230ns to 450ns instead of 250ns to 450ns), and the values calculated were matching each other within the error-bar range as shown in Fig. 5.5, in the section 5.2. Indeed, the S parameter is defined as a relative change of the areas below the SSPALS spectra with laser on (f_{on}) and off (f_{off}). If the time window is changed, the area f_{on} and f_{off} are different but their normalized difference should stay constant.

5.1.2 The measurements settings

Our excitation measurements have been performed in the test chamber at room temperature. The implanted e^+ energy was 3.3keV, with a beam size of $\text{FWTM}^7 < 4$ mm. The magnetic field was set at 250 G, and the electric field experienced by the formed o-Ps was 600V/cm, generated by the last transfer electrode.

For the first measurement, the excitation laser was set at theoretical resonance ($\lambda_L = 205.05$ nm), with an energy of $60\mu\text{J}$ measured in front of the test chamber viewport, and a spot size of $6\text{mm} \times 8\text{mm}$ (FWHM). The test chamber viewport is made in fused silica, with a measured transmission efficiency of around 90% for the 205nm. In fig.5.1 is presented the schematic of the vacuum test chamber: the incoming laser beams are shot through the viewport, perpendicularly to the positrons beam (Z axis), and excite the Ps emitted from the target, in the transverse direction (Y direction). The laser was aligned as close as possible from the target production region, in order

⁷Full width at tenth maximum

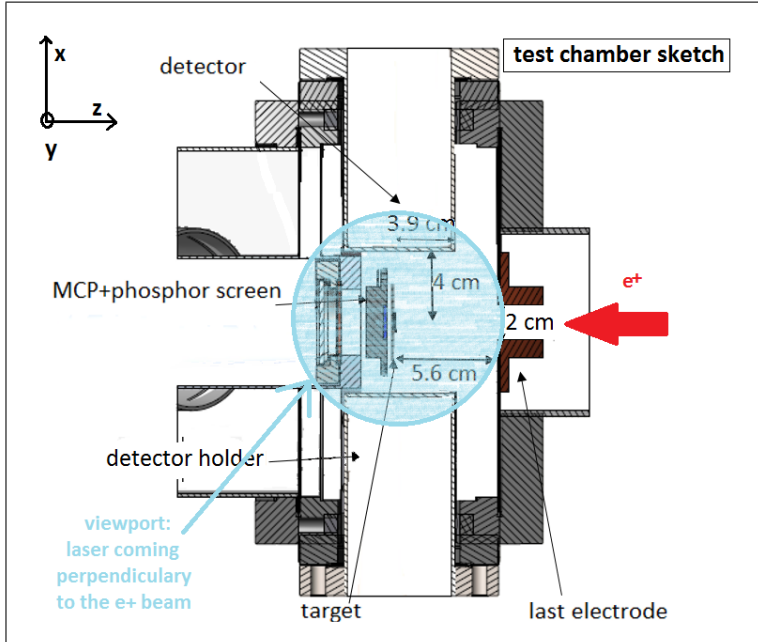


Figure 5.1: test chamber schematic. The e^+ comes from $-z$ direction to be implanted on the target, where Ps are emitted in a supposedly isotropic cone. Laser beams are sent in the y axis through the viewport as close as possible to the target to excite the exiting Ps .

to cover geometrically all the o-Ps exiting the converter. The Ps cloud is supposed to have the same exiting beam radius than the e^+ implanted beam. In order to protect the nano-porous silica-based target from any damage due to the laser radiation, a small mechanical shadow has been installed on the target holder to mask the target to prevent that any laser light hits directly the target. Specially, we want to avoid any formation of paramagnetic centers into the target, induced by the UV light, as studied in [50]

5.1.3 Results

In Fig.5.2 are presented our experimental results. In the left image (5.2 a) is shown a typical signal obtained for the quenching measurement type. A signal $S_{quenching} = 3.6 \pm 1.2 \%$ has been recorded for the magnetic quenching measurements, for an average of 11 single SSPALS shots.

We then wanted to confirm the $n=3$ excitation using a second intense laser

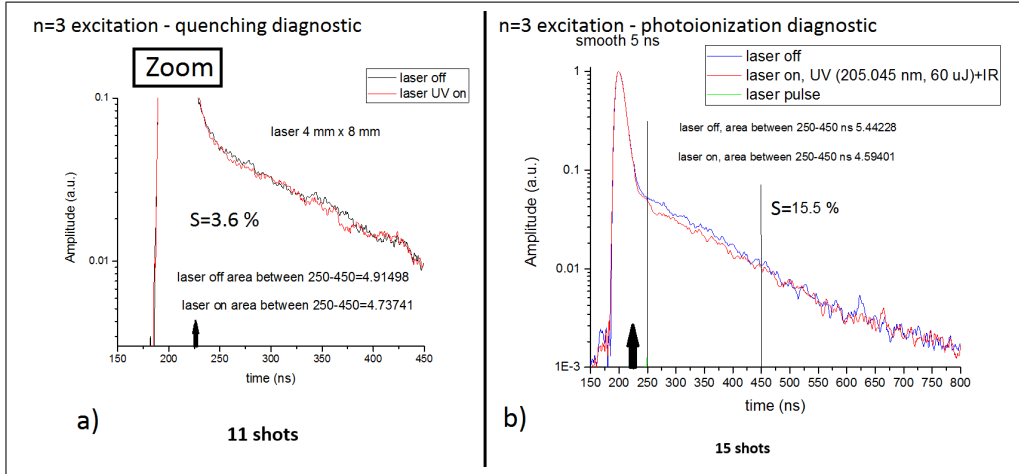


Figure 5.2: Ps laser excitation to $n=3$ state. The black arrow indicates the time when the laser is sent. Fig a). Quenching result: $S \approx 3.6 \%$. average of 11 single shots. Fig. b). Photoionization result: a signal of $S \approx 15.5 \%$ has been measured, for an average of 15 single shots. The S parameter values have been calculated for a time window between 250ns and 450ns.

beam to photoionize the excited o-Ps. For this purpose, the 1064nm beam was used with a high energy (50 mJ) and a big spot (FWHM ≈ 12 mm), synchronized and aligned in order to cover the UV beam in the target region. This measurement gives at resonance a signal $S_{photoionization} = 15.5 \pm 1.1 \%$, for an average of 15 single SSPALS shots (see Fig. 5.2 b)).

5.1.4 A quick analysis of the $n=3$ excitation signal obtained

In order to predict the excitation laser efficiency, a C++ code was used to perform the numerical diagonalization of the full interaction Hamiltonian in electric and magnetic fields and to calculate the generalized Einstein's coefficients [46]. These coefficients were fed into a rate equation solver to calculate the transition probabilities, as a function of the laser excitation intensity, bandwidth and electro-magnetic fields environment. This code was first written in a Mathematica program by Fabio Villa, before being improved by Ruggero Caravita that translated the code into a faster version in C++. During my master thesis studies, I spent a great part of my time working

on this code and the theory behind: the matter-light interaction, for an hydrogenic atom in electro-magnetic fields, with all the energetic corrections applied (QED, Zeeman, Stark, Quadratic Stark effects). For more information about the calculations performed by this code, the reader could refer to [46, 51].

For a theoretical point of view, at resonance and with perfect temporal and geometrical overlaps between Ps cloud and lasers, one should expect 100 % excitation+ionization efficiency in the high saturation regime. The photoionization measurement has been performed in high saturation regime for the 1064nm laser beam, and consequently any $n=3$ excited Ps is quasi-instantaneously disassociated.

Considering the magnetic and electrical fields of the experiment, our simulation code gives a theoretical value for the quenching efficiency $f_{quenched} = 17 \%$, and an excitation+ionization efficiency of $f_{photoionized} = 93 \%$ with perfect temporal and geometrical overlaps between Ps cloud and lasers.

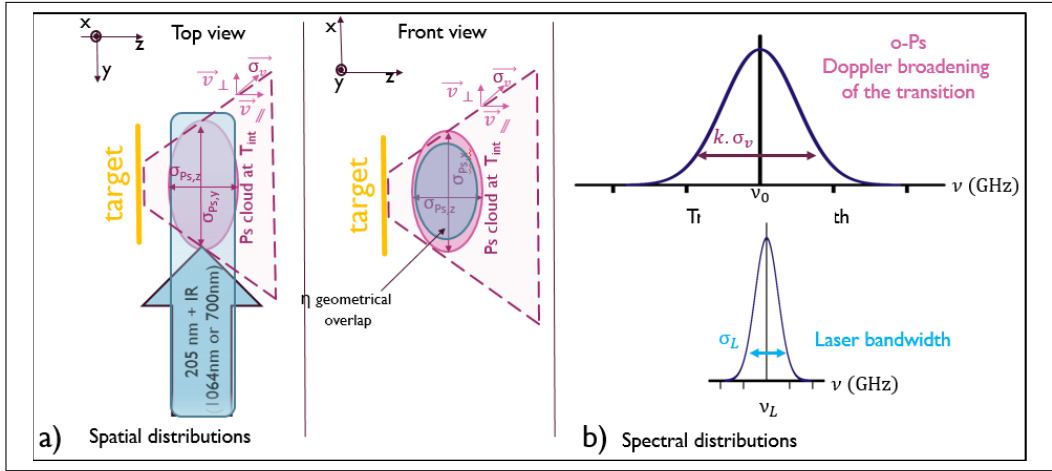


Figure 5.3: Ps laser excitation in the test chamber: schematics of the spatial and spectral distributions of the lasers and Ps cloud. Fig. a) indicates the directions of propagation of the lasers (along $+y$) and the Ps cloud (toward $+z$), with the geometrical overlap η , both in top and front views inside the test chamber. Fig. b) shows the two spectral distributions of the lasers and the transition line, broadened by the Doppler effect.

In our experimental setup, sketched in Fig. 5.3, one of the main limitations for reaching a higher excitation signal is due to the laser spectral width, that covers partially the Doppler profile of Ps emitted from a room-temperature target and limit the velocity range of atoms at resonance. A second limitation is the limited geometrical overlap of the laser spot on the Ps cloud. With the 3.3keV e^+ implantation energy, the mean velocity of partially thermalized o-Ps is expected to be of the order of 10^5 m.s $^{-1}$, giving a Doppler broadening $k\sigma_v \approx 2\pi \times 470$ GHz, with $k = \frac{2\pi}{\lambda_L}$ the wavevector norm, when the laser bandwidth is measured to be $\sigma_L = 2\pi$ (48 GHz).

Further analysis is developed in the Chap. 6. Nevertheless, a quick look on the results obtained shows that the ratio between purely quenched signal and quenching+photoionization signal remains in the same order for theoretical predictions and measured values. For a number of $n=3$ excited atoms $N_{excited} = 15.5\%$ of the total produced Ps, the expected quenched fraction is then $S_{theo,quenching} = N_{excited} \times f_{quenched} = 15.5\% \times 17\% = 2.6\%$, that is in reasonable agreement with the experimental value measured $S_{quenching} = 3.6 \pm 1.2\%$.

5.2 A Doppler scan of the Ps cloud spectral line

We then performed a scan in frequency of the 205nm exciting beam, for a photoionization 1064nm beam constant at 50 mJ. We kept the UV energy constant at $60\mu J$, with the same FWHM = 6mm \times 8mm spot size. Fig. 5.4 shows the fraction of excited Ps, for different detunings of the UV laser ($\delta = \omega_0 - \omega_L$, where ω_0 is the transition frequency, and ω_L the laser frequency). Doing so gives the linewidth of the $1^3S - 3^3P$ Ps transition, with a Doppler broadening of the line measured to be about $\sigma_{Doppler} = 470$ GHz.

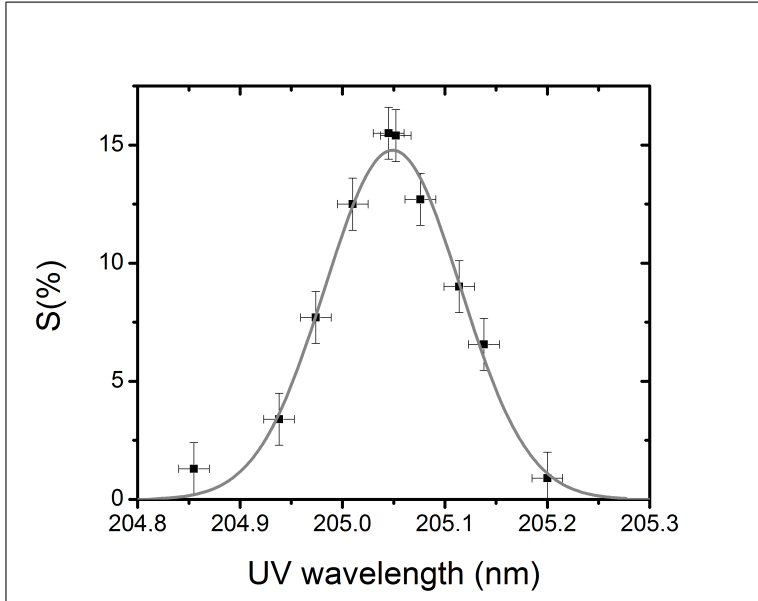


Figure 5.4: The linewidth of the $1^3S \leftrightarrow 3^3P$ transition, obtained by scanning the frequency of the UV laser, for a constant energy of $56 \mu\text{J}$. The photoionization laser was set 50mJ , in the high saturation regime. Each point is then given by 15 SSPALS shots and the continuous curve is the result of a fit process described in Chap.6.

Fitting a Gaussian to the resulting points gives the central value of the $3P$ excitation line at $205.05 \pm 0.02 \text{ nm}$. The value predicted by theory is 205.0474 nm [46]. The simulations performed to analyze the data are described in the following chapter 6.

Finally, in order to double check the independence of the time-window chosen to analyze our SSPALS signals, we performed a second data extraction of the $S(\%)$ parameter, using as a time window $t=230\text{ns}$ to 450ns , instead of 250ns to 450ns . The results are presented in Fig. 5.5, and shows that the S parameters calculated with the new time window (in red) are consistent with the value calculated with the time window 200ns width (black points).

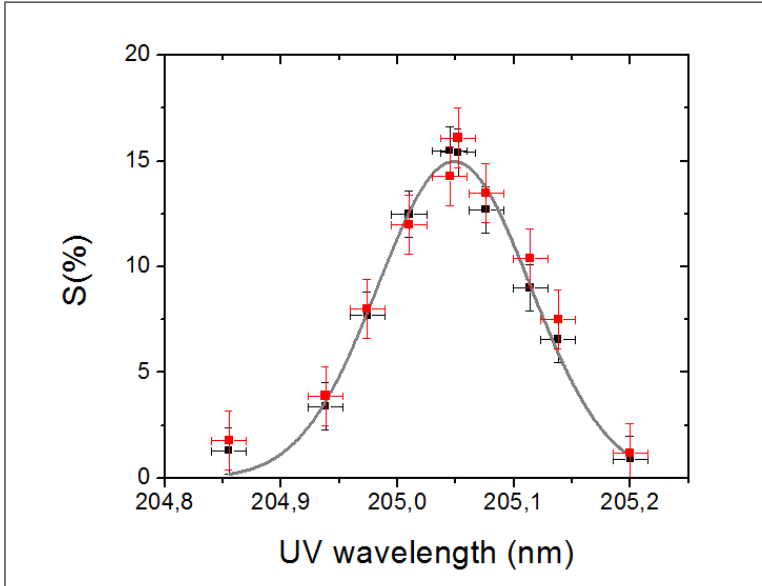


Figure 5.5: To demonstrate that the signal $S(\%)$ is independent of the time window we selected, we present here the linewidth of the $1^3S \leftrightarrow 3^3P$ transition, with the data points analyzed for a time window 250 ns to 450 ns (black points), and for a second time window from 230 ns to 450 ns (red points). The $S(\%)$ values calculated for the two different time windows are within the error bars, and thus consistent each other.

5.3 The saturation regime - verification measurements

In order to verify if the previous laser settings actually saturate the transition, we performed several measurements for different laser intensities, for both the 205nm (at photoionization beam intensity fixed 50mJ) and for the 1064nm (at UV beam intensity fixed $60\mu\text{J}$). The results are presented in Fig. 5.6. The 1S-3P transition appears only slightly saturated, while the 3P-continuum is strongly saturated, meaning that any $n=3$ atom is dissociated (photoionized) as soon as they get excited. These considerations are discussed in more details in the following chapter Chap.6 of the data analysis and in appendix B.

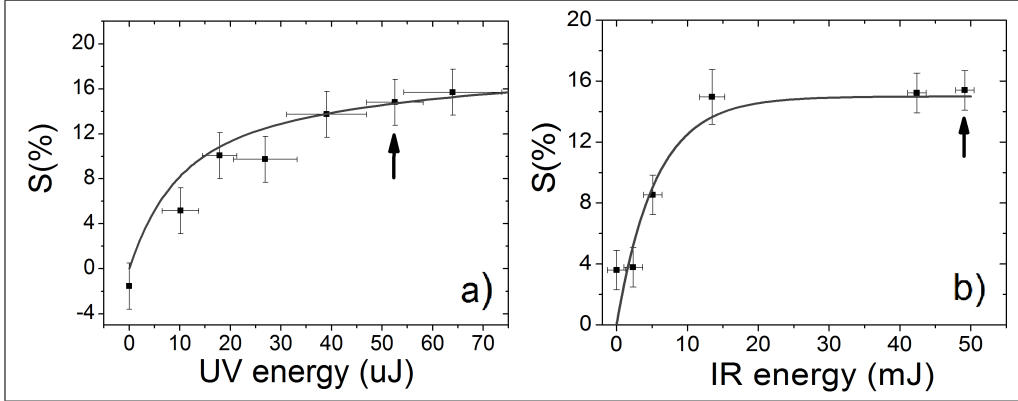


Figure 5.6: Saturation measurements: S parameter as a function of a). UV 205nm energy (IR energy = 50 mJ) and b). IR 1064nm energy (UV energy = 60 μ J). Arrows mark the laser energies used for the measurements presented in Fig. 5.2. The continuous lines are fits of the 3 levels rate equation model -see Chap.6

5.4 Rydberg Ps excitation

Once the $n=3$ excitation performed and characterized, we demonstrated for the first time the Ps excitation toward Rydberg states via the 3^3P intermediate state. These measurements were performed using the 205 nm beam at resonance, with 60 μ J, and varying the wavelength of the dedicated IR 1675 nm-1720 nm laser for addressing the $n=3 \leftrightarrow n$ Rydberg.

In case of Rydberg excitation, long lifetime Ps^* can reach the walls of the vacuum chamber where they annihilate. The most distant walls of the test chamber seen by Ps are between 4 and 6 cm away from the production target, as illustrated in Fig. 5.1. For a Ps cloud produced at a mean velocity of 10^5 m.s $^{-1}$, these distances correspond to a journey time of 400 - 600 ns before Ps^* annihilation. Consequently, the SSPALS spectra signal of Ps^* excitation is a decrease of annihilation immediately after the laser shot and an increase at later times when Ps^* annihilate on the walls, as shown in the Fig. 5.7 a).

We then varied the λ_{IR} from 1715 nm to 1685 nm, and scanned the different Rydberg states resonant transition from $n = 15$ to $n \approx 18$, as plotted in Fig. 5.7 b). Because of the presence of magnetic and electric fields that broaden and mix the lines, the different Rydberg states start to be hardly distinguishable for $n > 16$. A theoretical spectrum plotted in Fig. 5.7b) was

obtained with our code of the full-Hamiltonian diagonalization in external fields. For these measurement scans, the S parameter has been defined on an arbitrary time window between 350 ns and 600 ns, and gives another indirect proof of the efficient laser excitation of the $n = 3$ states.

Note that because of the combination of both the annihilation phenomena in vacuum and in the inner walls of the test chamber at the long times, the ratio of the integrals of the SSPALS curves is dependent of the time window chosen. Consequently in this case, the S parameter only gives a qualitative diagnostics of the excitation toward Rydberg.

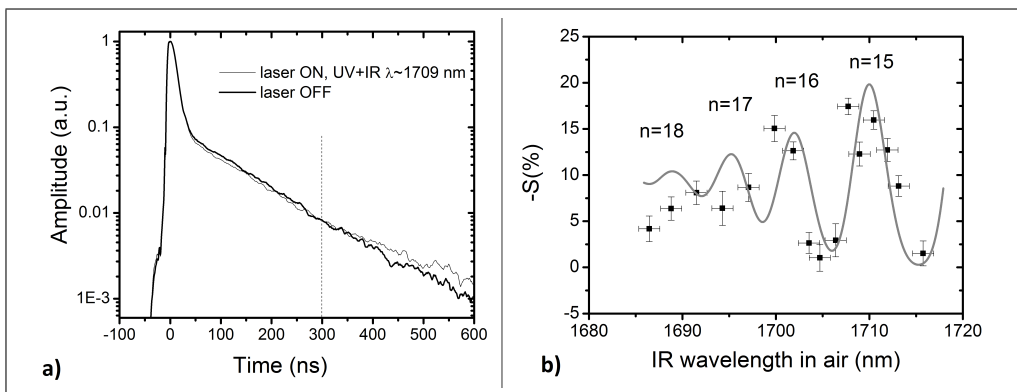


Figure 5.7: Fig a) Rydberg excitation SSPALS signal, for $\lambda_{IR} = 1709$ nm, corresponding to the transition $n=3 \leftrightarrow n=15$. 205 nm beam is set at resonance. Fig. b) Scan of the Rydberg transitions: the different S parameters data are plot as a function of the IR wavelength in the range $n = 15 - 18$, compared with a theoretical linear spectrum. The electro-magnetic field conditions are 600V/cm and 250G, implying a mixing of the lines. For $n \geq 16$ it becomes difficult to distinguish from the different Rydberg states.

5.5 Summary of the experimental results and short prospect

In this chapter, the recent measurements of the laser excitation of Ps have been presented, showing the first observation of the $n=3$ laser excited Ps as well as the Rydberg $n=15-16$ Ps levels reached via the $n=3$ level as the intermediate step. These results have been obtained in the test chamber, at room temperature and for 250 G and 600 V/cm environment and with an implantation energy of 3.3 keV for the e^+ bunch. A next step for AEGIS is to

perform the same laser excitations in the cryogenic and high magnetic field environment of main apparatus, that is planned for the beamtime of 2016.

In addition to this, the measurements carried out into the test chamber still continue to be performed in parallel of the work in the main traps. A clear signal of the $n=2$ metastable Ps, via spontaneous decay from the $n=3$ excited state is under study, as well as the transverse Doppler profile of the emitted o-Ps for different energies of positron implantation. The characterization of the transverse energy of the Ps cloud, via the Doppler profile measurements are of importance to obtain information about the o-Ps emission. We want to know if the emission can be directional or if o-Ps are emitted without any privileged direction (2π steradian emission). This information will be primordial to refine the estimation calculations of the number of o-Ps* that will be able to reach the antiproton plasma in the production trap. Moreover, the demonstration of the efficient production of a meta-stable Ps beam (the 2^3S) will open paths for a physics studies on long-living Ps, that is also interesting for us and more widely for the scientific community. For instance, this could help the realization of the Ps interferometry to perform a gravity test (see [13]).

Further experiments are foreseen be to tested in the next months and years, like the Doppler cooling of Ps. We will discuss the feasibility and the interest in Chap. 8.

Chapter 6

Simulations analysis

To analyze these results, I improved a simple 3-level rate equation model first developed by Daniel Comparat. The absorption, stimulated and spontaneous emissions, and ionization are taken into account in order to calculate the population evolution of the 3 states: N_0 is the population of the ground state (1^3S), N_1 is the intermediate state (3^3S) one and N_2 gives the number of photoionized atoms, or for our model, the population of a "continuum state". In Fig 6.1 is presented a scheme of our model with the different interesting parameters.

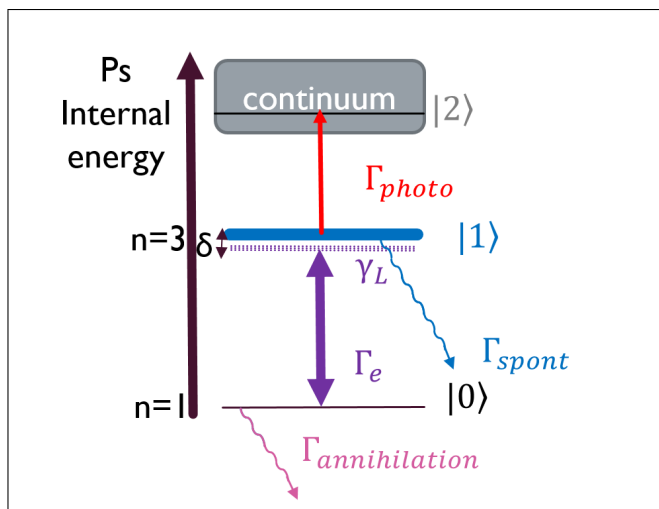


Figure 6.1: Schematic of the 3 level system used to model the photoionization rate and thus the expected signal to be measured.

For most of our measurements the photoionization process was in the saturation regime, we consequently considered that the ionization occurs before any spontaneous decay from the intermediate $n=3$ state, in other words $\Gamma_{photo} \gg \Gamma_{spont} = \frac{1}{10ns}$. This hypothesis will be checked at the end of this chapter, specially for the photoionization saturation measurements where the IR energy has been varied. Besides, the annihilation rate from the $n=3$ triplet state is much longer than the spontaneous decay ($\tau_{annih,n=3,s=1} \geq 400 \mu s$, cf Table. 2.1), and has been neglected too.

Since the interaction time was defined by the laser pulses of 4-5 ns for the IR photoionization beam and 1.5 - 2 ns for the UV light, we also neglect the annihilation process of the ground state in vacuum, which has a much longer characteristic time of 142 ns for o-Ps than the interaction time ($T_{int} \sim t_{pulse}$).

The o-Ps cloud emitted in the AEGIS test chamber has to travel between 4 and 6 cm to reach the closest walls of the chamber where they annihilate (see Fig. 5.1). For a mean velocity of 10^5 m.s^{-1} (given by a Boltzmann distribution of the Ps cloud with a temperature around 1000 - 1500 K), this implies a traveling time of 300 ns before the first o-Ps can annihilate. We also neglect this annihilation process since the laser is shot between 12 ns and 16 ns after the e^+ implantation in the target, meaning right after the o-Ps are emitted. Therefore, we consider that the $|0\rangle$ ground state is stable during the laser interaction process.

As consequences, the spontaneous emission rate can be neglected compared to the photoionization process, as well as the annihilation rate compared to laser interaction duration, and we obtain the following rate equations:

$$\begin{cases} \frac{dN_0}{dt} = \Gamma_e(N_1 - N_0) \\ \frac{dN_1}{dt} = -\Gamma_e(N_1 - N_0) - \Gamma_p N_1 \\ \frac{dN_2}{dt} = \Gamma_p N_1 \end{cases} \quad (6.1)$$

where $\Gamma_{photoionization} = \Gamma_p$ the photoionization rate and Γ_e the, stimulated excitation rate, and N_i the population of the state $|i\rangle$.

An exact solution for the rate equations 6.1 is derived in the appendix B. We consider a constant power of the lasers during the interaction, that leads to the probability of photoionization:

$$\begin{aligned}
P_{photo}(T_{int}) &= \frac{N_2(T)}{N} \\
&= \left(1 - \frac{1}{2\sqrt{4\Gamma_e^2 + \Gamma_p^2}} \exp\left(-\frac{1}{2}(2\Gamma_e + \Gamma_p + \sqrt{4\Gamma_e^2 + \Gamma_p^2})T_{int}\right)\right) \\
&\quad \times \left\{ (2\Gamma_e + \Gamma_p + \sqrt{4\Gamma_e^2 + \Gamma_p^2}) \exp(\sqrt{4\Gamma_e^2 + \Gamma_p^2}T_{int}) \right. \\
&\quad \left. + (2\Gamma_e + \Gamma_p - \sqrt{4\Gamma_e^2 + \Gamma_p^2}) \right\}
\end{aligned} \tag{6.2}$$

With T_{int} the interaction time of the laser excitation+photoionization.

This result can be simplified under some conditions that are discussed in the appendix B. Anyhow, we would like now to introduce an intuitive solution in case of the high saturation regime for the photoionization process. We will then verify its compatibility with our conditions.

6.1 The case of high saturation photoionization regime - a simple solution

Our experimental settings give a photoionization rate of:

$$\begin{aligned}
\Gamma_p &= \sigma_{photo,n=3,theo} \frac{I_{IR}}{h\nu_{IR}} = \sigma_{photo,n=3,theo} \times \frac{E_{IR}}{t_{pulse,IR} \pi w_{IR}^2} \times \frac{\lambda_{IR}}{hc} \\
&= 3.48 \times 10^{-17} \text{ cm}^2 \times \frac{50 \text{ mJ}}{4 \text{ ns} \pi \left(\frac{8 \text{ mm}}{2\sqrt{2\ln(2)}}\right)^2} \times \frac{1064 \text{ nm}}{hc} \\
&= 6.42 \times 10^9 \text{ s}^{-1}
\end{aligned} \tag{6.3}$$

Where E_{IR} and $t_{pulse,IR}$ are respectively the energy and the pulse duration of the IR photoionization beam, with a wavelength $\lambda_{IR} = 1064 \text{ nm}$), and $\sigma_{photo,n=3,theo}$ is the theoretical value of the photoionization cross section from the $n=3$ triplet state of Ps, taken from [46, 45]. The IR beam is considered to be top-hat shaped, with w_{IR} is the radius. The interaction time T_{int} is limited by the laser pulse, so $T_{int} = t_{pulse,IR}$

For an interaction time of 4 ns corresponding to the IR photoionization FWHM pulse time, we obtain a ratio $\Gamma_p \times T_{int} \approx 25 \gg 1$, corresponding to the high saturation regime case.

If the photoionization time $t = 1/\Gamma_p$ is much faster than the interaction time T_{int} , we can consider that the change in population toward the continuum state occurs instantaneous compared to the total time of excitation T_{int} , i.e. $\forall t \leq T_{int}, N_1(t) \approx 0$. This statement could be physically understood as the following: once a Ps gets excited toward the $n=3$ state, it is immediately photoionized. Thus, the first rate equation is simplified in:

$$\frac{dN_0}{dt} = -\Gamma_e N_0$$

By integrating over the total interaction time T_{int} , we obtain the ground state population $N_0(T_{int}) = N_{tot} \exp(-\Gamma_e T_{int})$. Since we considered a closed system, the number of photoionized atoms after T is:

$$N_2 = N_{tot} - N_0 - N_1 \approx N_{tot}(1 - \exp(-\Gamma_e T_{int})) \quad (6.4)$$

We then approximate the probability of photoionization after a time T_{int} with:

$$\boxed{P_{photo,approx}(T_{int}) \approx 1 - \exp(-\Gamma_e T_{int})} \quad (6.5)$$

Eq. 6.5 means that the probability to photoionize the Ps cloud is only given by the excitation rate toward the $n=3$ state and the excitation time interaction. This is derived under the hypothesis of a strong saturation regime for the photoionization laser.

The validity conditions for a good agreement of this approximation with the exact solution of N_2 are discussed in the appendix B. It is shown that we can consider that the simple solution (Eq.6.5) can be applied for any measurement done with the photoionization laser at saturation energies we had.

6.2 High photoionization regime: studies of the Doppler Scan and UV saturation measurements

In this section, in order to extract the transverse temperature of the Ps cloud, we want to fit the Doppler scan measurements. Fitting the UV saturation measurements will allow us to extract the value of the dipole strength of the transition. In both cases, the photoionization was set to be in the strong saturation regime, meaning that the Eq. 6.5 can be used. To determine the

photoionization probability $P_{photo,approx}(T_{int})$, we then need to determine the excitation rate formula.

In the appendix B, the excitation rate Γ_e is derived considering that the excitation laser which performs the $1^3S \leftrightarrow 3^3P$ transition (~ 110 GHz) is much larger than the natural linewidth of the transition (~ 0.1 GHz) and the hyperfine splitting (< 4 GHz for the 3^3P , see Fig. 2.4). This leads to:

$$\Gamma_e(\delta, \Omega, \sigma_L) = \frac{\Omega(r)^2 \pi}{2} \frac{1}{\sqrt{2\pi\sigma_L^2}} \exp\left(-\frac{\delta^2}{2\sigma_L^2}\right) \quad (6.6)$$

where $\Omega(r)$ is the Rabi frequency of the laser-matter coupling such as $|\hbar\Omega(r)| = |dE_L(r)|$, where d is the electrical dipole strength of the transition (matrix element) and E_L the laser amplitude (electric wave). We also define σ_L the rms value of the laser bandwidth, and $\delta_0 = \omega_0 - \omega_L$ the laser detuning compared to the transition energy $\hbar\omega_0$ for an atom at rest. For an atom at a velocity \mathbf{v} , the detuning δ is then taken to be $\delta = \delta_0 - \mathbf{k}_L \cdot \mathbf{v}$

6.2.1 The geometrical coefficient η

In general, the probability of photoionization $P_{photo,approx} = 1 - \exp(-\Gamma_e T_{int})$ depends on the spatial distribution of the laser $I(\mathbf{r})$, since Γ_e the excitation rate toward $n=3$ state is a function of the Rabi frequency $\Omega(r)$ of the light-matter interaction.

In case of a low saturation regime for the $n=1 \leftrightarrow n=3$ transition, the photoionization probability can be approximated by

$$P_{photo,approx}(\Omega(r)) \sim \Gamma_e(\Omega(r)) T_{int}.$$

Therefore, the total photoionization probability $P_{photo,approx,tot}$ is the result of the 3D integral of the excitation rate times the spatial distribution of the Ps cloud. It is shown in Appendix B Sec. B.5 that the probability of photoionization $P_{photo,approx,tot} = P_{photo,approx}(\Omega_0) \times \eta$, where η is a geometrical factor of overlap between the lasers and Ps cloud distributions and Ω_0 is the peak value of the Rabi frequency.

In the Appendix. B, Eq. B.22, η has been derived to be:

$$\eta_{theo} = \frac{\sigma_{r,L}^2}{\sigma_{r,Ps}^2 + \sigma_{r,L}^2} \quad (6.7)$$

Where $\sigma_{r,L}$ and $\sigma_{r,Ps}$ are respectively the rms values of the spatial Gaussian distributions of the laser and the Ps cloud, both taken in the interaction plane $\{x, z\}$ (plane transverse to the lasers' propagation direction). The situation is illustrated in Fig. 5.3 a), with the notations given.

For simplification, we use the approximated probability of photoionization $P_{photo,approx,tot} = P_{photo,approx}(\Omega_0) \times \eta$, not only for the weak saturation case, but also for generic saturation regimes. In a sens, the efficiency reduction due to the spatial variation of the laser intensity in the tails is taken into account in the global geometrical coefficient η .

We then introduce a coefficient $\eta \leq 1$ that contains all the spatial dependencies of the problem (See Fig. 5.3 a)):

- The spatial overlap between the laser beams and the Ps cloud.
- The excitation efficiency's spatial dependance ($\Gamma_e(r)$) that comes from the spatial variation of the laser intensity $I(r)$.

6.2.2 The photoionization probability

In order to fit the Doppler scan measurements, we want to find an expression of the photoionization probability that takes into account the Ps velocity and the laser detuning. Both lasers to perform the $n=1 \leftrightarrow n=3$ and the $n=3 \rightarrow$ continuum transitions are at saturation. Since the photoionization laser is powerful enough to imply a strong saturation the transition to the continuum, the photoionization probability can be approximated by Eq. (6.5). This equation provides an approximation of the photoionization probability, for a given velocity v of the Ps atom and for a given laser detuning δ of the 205nm beam.

We assume that the Ps velocity distribution is a Gaussian distribution, with a mean temperature $T(K)$. The integrated photoionization probability over the Ps velocity spectrum is thus given by:

$$P(t, \delta) = \eta \int_{-\infty}^{+\infty} P_{photo,approx}(t, \delta, v) \sqrt{\frac{1}{2\pi\sigma_v^2}} e^{-\frac{v^2}{2\sigma_v^2}} dv \quad (6.8)$$

where $\sigma_v = \sqrt{k_B T/m}$ is the standard deviation of the velocity along the laser propagation axis, for a Ps cloud at a temperature T .

The formula 6.8 was used to fit the data in Fig.5.4 and Fig.5.6 a). We found a Rabi frequency $\Omega_{fit} \approx 5.5 \times 10^{10} \text{ s}^{-1} \pm 1.1 \times 10^{10} \text{ s}^{-1}$ that gives a dipole strength of $d_{fit} = 1.76 \pm 0.59$ Debye, in good agreement with the theoretical value of 1.65 Debye, derived from the equation:

$$d \approx \sqrt{\Gamma_s 3 h 4\pi\epsilon_0 \frac{\lambda_0^3}{64\pi^4}} \quad (6.9)$$

Since the lineshape of Fig.5.4 is almost entirely dominated by the thermal distribution of the Ps, the fit also gives information about the Ps cloud's transverse temperature. We obtained a standard deviation of o-Ps velocity in the transverse direction $\sigma_v \approx 10^5 \text{ m/s}$, or a temperature $\mathbf{T} = \mathbf{1300} \pm \mathbf{200K}$.

From the fit, the geometrical overlap coefficient η has been determined to be $\eta_{fit} = 80 \%$. The implanted e^+ cloud has a full width tens of maximum (FWTM) of $4 \text{ mm} \times 5 \text{ mm}$, meaning a variance value of $\sigma_{int} = \frac{FWTM}{2\sqrt{2 \text{Log}[2]}}$. We assume the Ps cloud is emitted out of the target surface with the same initial size than the e^+ cloud spread, and that it propagates with a mean velocity of $\sigma_v = 10^5 \text{ m.s}^{-1}$.

The laser interaction happens with a delay of $t_{delay}=16 \text{ ns}$. The spatial spread of the Ps cloud at the time of the laser interaction is then $\sigma_{r,Ps} = \sqrt{\sigma_{init,x}^2 + t_{delay}^2 \times \sigma_v^2} \times \sqrt{\sigma_{init,z}^2 + t_{delay}^2 \times \sigma_v^2}$. We found a variance of the Ps cloud $\sigma_{r,Ps} = 2.7 \text{ mm}$. Finally, for a laser waist of $6 \text{ mm} \times 8 \text{ mm}$, we found a theoretical $\eta_{theo} = 62\%$, in good agreement with the fit value of 80%, regarding the accuracy of the measurements.

6.3 The n=3 laser at resonance and at saturation - study of the photoionization saturation

In this last section, we want to analyze the photoionization saturation measurements we did (see Sec. 5.3 and Fig. 5.6 b)). For this, we set the UV laser at resonance ($\delta=0$) and saturation ($E_{UV} = 56\mu\text{J}$), that fixes the coupling efficiency, i.e. Ω that we previously fit to be $\Omega_{fit} = 5.37 \times 10^9 \text{ s}^{-1}$. We thus obtain:

$$\Gamma_e(\delta = 0, \Omega_{fit}) = 6.04 \cdot 10^9 \text{ s}^{-1} \quad (6.10)$$

Since we want to analyze the photoionization probability at resonance, for various photoionization energies, we use the probability formula given in Eq.6.2. This formula is valid under the condition $\Gamma_p \gg \Gamma_{spont}$, its validity is checked in the next paragraph.

The fit curve is plotted in the Fig. 5.6.b). For a high saturation energy of $E_{IR}=60$ mJ, the photoionization rate parameter is fitted to be $\Gamma_{p,fit}(60\text{mJ}) = 5 \cdot 10^9 \text{ s}^{-1}$. This value allows us to extract a photoionization cross section value:

$$\sigma_{photo,fit} = \Gamma_{p,fit} \times \frac{hc \times t_{int} \times \pi w^2}{\lambda_0 E_{IR}} = 3.1 \times 10^{-17} \text{ cm}^2 \quad (6.11)$$

That is in a good agreement with the theoretical one $\sigma_{photo} = 3.48 \times 10^{-17} \text{ cm}^{-1}$.

Validity of the hypothesis

With the fit cross section's value we obtained, we can now check the validity of our hypothesis. For deriving the Eq.6.2 that gives the photoionization probability for various energies of the UV and IR lasers, we did the approximation: $\Gamma_p \gg \Gamma_{spont}$. This inequality remains valid for the low IR energy measurements we did, with: $\Gamma_p(5.6\text{mJ}) \approx 5 \times 10^8 \gg \Gamma_{spont} = \frac{1}{10 \text{ ns}} = 1 \times 10^8$. For the measurement performed at the lowest IR photoionization energy of 2.9 mJ, the photoionization rate is still higher than the spontaneous decay ($\Gamma_p(2.9\text{mJ}) \approx 2.5 \times 10^8 \approx 2.5 \times \Gamma_{spont}$), we consider this case to be at the limit of validity of our model, and should not be taken into account for fitting the curve Fig. 5.6.

Part II

A possible positronium laser
cooling ? Theoretical and
simulations studies

In the AEgIS scheme (cf Fig. 6.2 a)), two main parameters can drastically increase the charge exchange formation efficiency:

- The \bar{p} plasma temperature. As shown in the AEgIS proposal ([15]), cold antiproton plasma is required to have an efficient charge transfer with the weakly-bound positron from the Ps^* . In the chapter 14, I explain in more details the strategy we started to develop to sympathetic cool trapped antiprotons, using laser cooled molecular anions. One of the big issue to perform laser cooling of molecules is to find a closed cycle of absorptions/emissions of photons. A promising candidate seems to be the C_2^- molecule, and I present later some simulation results for the different laser cooling schemes that are encouraging. In the AEgIS proposal, we aim to cool the \bar{p} plasma down to ≈ 100 mK.
- The overlapping of the trapped \bar{p} plasma and the Ps cloud. In the current geometry of our apparatus, Ps beam is formed at a distance 2 cm from the antiproton plasma region, most of the created Ps atoms don't reach the \bar{p} plasma, as shown in Fig. 6.2 a).

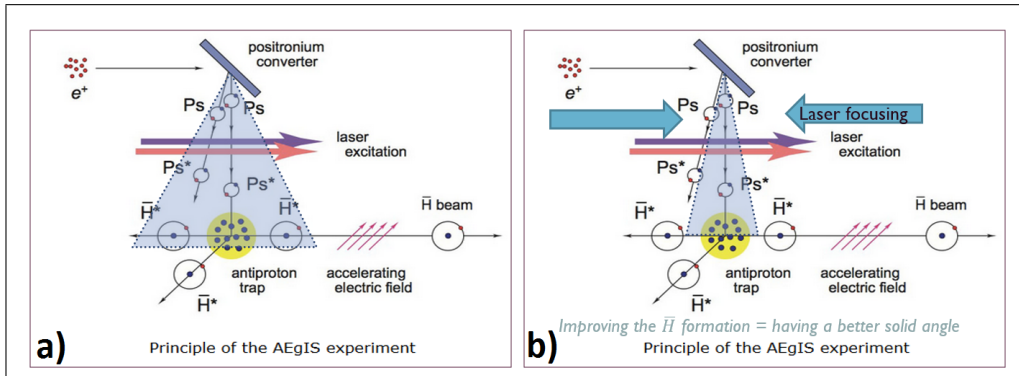


Figure 6.2: The AEgIS $\bar{\text{H}}$ formation schematic: in gray, the emission cone of Ps cloud sketched. Fig a) shows a wide emission. Most of the formed Ps atoms don't reach the antiproton plasma and are consequently lost for the charge exchange process. Fig b) shows a more collimated Ps cloud thanks to some laser interaction.

During my thesis, I investigated several laser-matter interaction schemes in order to try to collimate the Ps atoms before Rydberg excitation, as shown in Fig. 6.2. the collimation of the Ps cloud would significantly increase the

solid angle of overlaps between \bar{p} and Ps^* .

To do so, I studied the possibility:

- to use a Doppler laser cooling to reduce the transverse velocity of the Ps cloud and focus the Ps emission. I develop the basics theory in Chap. 7 and present some simulations results in 8. The Chap. 9, the current status of the laser setup to perform the first laser cooling trial is described.
- to use the dipolar force of a highly detuned and intense laser to act as a focusing lens on the Ps cloud and collimate it. This will be seen in Chap. 10.

Chapter 7

Ps Doppler laser cooling - theory

It is common to model the Doppler laser cooling by a two-level atomic system in interaction with a monochromatic laser acting on a broad-line transition. This simple model works particularly well for alkaline atoms, like for sodium atoms, on which the first optical molasses has been performed in 1985 by S. Chu and coworkers at the Bell Labs. Or, for instance, for rubidium on which the first BEC was observed [52]. The limits of validity of such a theory imply that the transition linewidth has to be greater than the recoil energy of a single absorbed photon and than the laser bandwidth.

The case of the positronium differs for two main reasons:

- The really small mass of the Ps atom ($m_{Ps} = 2 \times m_{e^-} \ll m_H$) implies a huge recoil energy for each photon absorbed. For the transition $n=1 \leftrightarrow n=2$, the energy recoil of the 243 nm photon ($E_r = \frac{\hbar^2 k_L^2}{2 m_{Ps}}$) is 200 times more important than the natural linewidth equivalent energy $\hbar \Gamma_{spont}$. The Doppler cooling on the first transition of the Ps is then a case of a narrow-line transition cooling, and the model of a broad-line transition has to be carefully checked and adapted.
- Ideally, to address a maximum of emitted Ps, the huge Doppler broadening would have to be covered by the spectrally broad exciting lasers, and consequently, the approximation of the monochromatic laser is no more valid. For a Ps cloud at 1000 K, the Doppler broadening is about 400 GHz wide, much larger than the spontaneous rate $\Gamma_{spont} = 1/142 ns = 7 \times 10^6 s^{-1}$, meaning a spontaneous frequency of about 1 MHz.

For all these reasons, the study of the Doppler cooling of the Ps atom has to be performed with care. The possibility of a Ps laser cooling has been first

studied by [53]. Later in 2000 - 2002, the group of K. Wada, M. Kajita and coworkers [54, 55] experimentally proceeded to the first trials. Even if the experiment was not successful, theoretical and simulations studies have been performed to model the cooling efficiency over the first transition $n=1 \leftrightarrow n=2$ (with a typo of a factor 2π in their paper). A recent work [56] proposed a combine scheme to reach the BEC, taken into account thermalization with the nano-channels of the target convertor, and Ps-Ps scattering process in addition of the Doppler laser cooling.

During my thesis, I studied the possibility to laser cool the Ps atom on the transition $1^3S_1 \leftrightarrow 2^3P_2$. The theoretical particularities of such laser cooling are discussed in the following sections. In Sec. 7.1. I remind briefly the 2-level system model in order to derive the rate equations and define properly the parameters of interests for a Doppler cooling, as the scattering rate 7.2. In a second time in Sec. 7.3, I deal with the force resulting from the laser-matter interaction. Here, a distinction between broad-line and narrow-line transitions has to be done. In the last Sec. 7.4, I briefly conclude this theory section for the Ps case. The explanations derived here lead to the simulations results I present in Chap. 8.

7.1 Laser cooling of an open two-level system

Here is considered a two-level system atom coupled with an external electro-magnetic field, as illustrated in the Fig. 7.1. We study this usual model with two refinements:

- the 2-level system is considered to be open, in order to be able to simulate the annihilation and photoionization processes
- the laser is not considered monochromatic, but has a large spectral bandwidth $\sigma_L \gg \Gamma_s$

The excitation rate between the two states is noted Γ_e , and we introduce the rates Γ_1 and Γ_2 that are the decay rates from the level $|1\rangle$ and $|2\rangle$ toward all the other energies levels but the two considered states $|1\rangle$ and $|2\rangle$. For instance, for the laser cooling of the o-Ps over the first transition, $|1\rangle$ would be the ground state and Γ_1 the annihilation rate $\Gamma_1 = \frac{1}{142 ns}$.

We want here to remind the well-known results of the populations evolution in a quasi steady-state regime, as well as the important definitions such as the saturation parameter, saturation intensity or photon scattering rate.

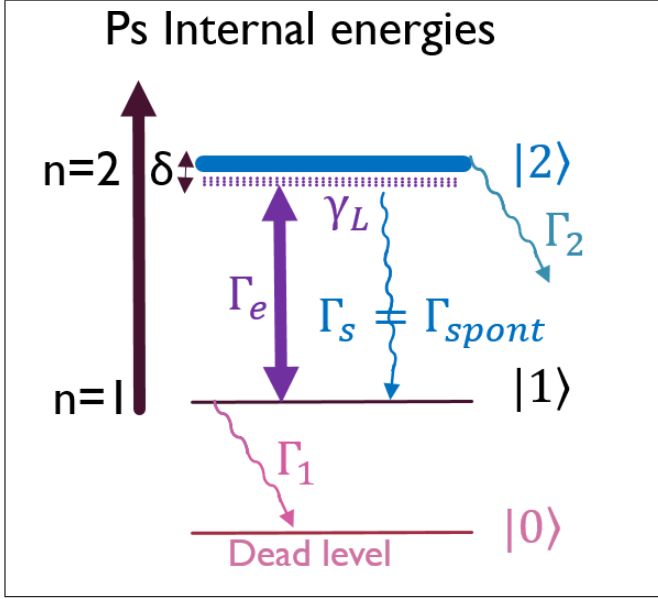


Figure 7.1: The opened 2-level system scheme. Γ_1 and Γ_2 are the leak rates from the levels $|1\rangle$ and $|2\rangle$ to all the other levels. In case of the Ps, Γ_1 can be associated to the annihilation rate, that would mimic the annihilation toward a fictive "dead" level $|0\rangle$

We define the density matrix ρ that gives both information about the population and coherence of the system:

$$\hat{\rho} = \begin{pmatrix} \rho_{11} & \rho_{12} \\ \rho_{21} & \rho_{22} \end{pmatrix} \quad (7.1)$$

such as $\rho_{ii} = N_i$ is the population of the level $|i\rangle$, and $\rho_{12} = \rho_{21}^*$ the coherence between the two levels.

The coupling with the laser is given by the Rabi frequency $\Omega = \frac{d E_L \exp(i\psi_L)}{\hbar}$, where d is the electric dipole strength of the transition, E_L the amplitude of the laser wave and ψ_L the phase of the laser.

We introduce Γ_{tot} that is the decoherence relaxation rate of the coupling. It takes into account the contributions from the spontaneous emission (coupling with the vacuum states of the electro-magnetic field), from the optical relaxations toward other levels (Γ_1 and Γ_2) and the decoherence induced by the rms laser bandwidth (σ_L): $\Gamma_{tot} = \Gamma_s + \sigma_L + \Gamma_1 + \Gamma_2$.

7.1.1 The rate equations

Since we want to model the cooling of the Ps atoms with a large Doppler broadening, the laser bandwidth σ_L has to be in the order of the hundreds of GHz, much larger than the natural linewidth of the transition ($\frac{1}{3.2 \text{ ns}} = 0.3$ MHz). That leads us to study the case of a fast decoherence of the coupling, that is similar to assume: $\frac{d\rho_{12}}{dt} = 0$.

In the semi-classical framework, the dynamic of the incoherent laser-matter interaction can thus be modeled using the framework of the rate equations [57]:

$$\begin{cases} \frac{d\rho_{11}}{dt} = (\Gamma_s + \Gamma_e) \rho_{22} - (\Gamma_e + \Gamma_1) \rho_{11} \\ \frac{d\rho_{22}}{dt} = -(\Gamma_s + \Gamma_2 + \Gamma_e) \rho_{22} + \Gamma_e \rho_{11} \end{cases} \quad (7.2)$$

where Γ_e is the excitation rate, that gives the laser coupling efficiency.

7.1.2 The excitation rate formula

In order to calculate the dynamics of the laser interaction, it is then primordial to derive the excitation rate.

The excitation rate is proportional to the convolution of the laser spectrum $I_L(\omega)$ and the Lorentzian natural bandwidth ($L_s = \frac{\Gamma_s}{2\pi(\omega - \omega_0)^2 + \Gamma_s^2}$), as explained in Appendix B of [58]⁸

$$\Gamma_e = \frac{\pi d^2}{\hbar^2 \epsilon_0 c} I_L(\omega) \otimes L_s(\omega) \quad (7.3)$$

- If we consider a Lorentzian laser spectrum, the excitation rate can be analytically calculated:

$$\Gamma_e = \frac{\Omega^2}{\delta_0^2 + \Gamma_{tot}^2/4} \times \frac{\Gamma_s}{2} \quad (7.4)$$

⁸I corrected a missing factor \hbar^2

where $\delta_0 = \omega_0 - \omega_L$, the detuning of the laser regarding the atomic transition angular frequency ω_0 .

- In the scenario of Ps laser cooling, it is interesting to study the case of a Gaussian laser much larger than the natural linewidth of the transition, that can be approximated by a Dirac function in $\omega = \omega_0$. The excitation rate becomes:

$$\Gamma_e = \frac{\Omega^2}{2} \frac{\pi}{\sqrt{2\pi\sigma_L^2}} e^{-\frac{\delta_0^2}{2\sigma_L^2}} \quad (7.5)$$

7.1.3 The steady-state regime for short interaction time

We want to simulate the laser cooling of Ps over the transition $1^3S \leftrightarrow 2^3P$. We then consider $\Gamma_2 = 0$, neglecting the photoionization process. For interaction times shorter than the annihilation lifetime, we can consider $\tau_{annih} = 1/\Gamma_1 \gg T_{int}$ that leads to close the 2-level system. We obtained the well-known steady-states solutions of the rate equations (7.2), for $\Gamma_1 = \Gamma_2 = 0$:

$$\begin{cases} \rho_{22,st} &= \frac{1}{2} \frac{s}{1+s} \\ \rho_{11,st} &= 1 - \rho_{22,st} \end{cases} \quad (7.6)$$

where we define the saturation parameter $s = 2 \frac{\Gamma_e}{\Gamma_s}$.

At the resonance $\delta_0 = \omega_0 - \omega_L = 0$, we note the saturation parameter $s(\delta_0 = 0) = s_0$, and we can define the saturation intensity for a monochromatic laser I_{sat} as:

$$s_0 = \frac{I_L}{I_{sat}} \quad (7.7)$$

Remark: For high saturation case, $s \gg 1$, we obtain $N_2 \approx N_1 \approx \frac{N_{tot}}{2}$ that is the maximum number of possibly excited atoms for a closed 2-level system. Thus, the saturation intensity for $s=1$ can be seen as the laser intensity needed to excite at resonance half of the number of atoms one could excite for an infinite intensity.

In case of a Lorentzian laser, the s parameter can be also expressed as:

$$\begin{aligned}
s(\delta_0) &= \frac{2|\Omega|^2}{\Gamma_{tot}^2 + 4\delta_0^2} \frac{\Gamma_{tot}}{\Gamma_s} \\
s_0 &= s(0) = \frac{2|\Omega|^2}{\Gamma_{tot}\Gamma_s}
\end{aligned} \tag{7.8}$$

For a monochromatic Lorentzian laser then: $s_0 = \frac{2\Omega^2}{\Gamma_s^2}$

Using the expression of the dipole seen in Eq (6.9), we obtained the well-known expression:

$$\boxed{I_{sat} = \frac{1}{6} \hbar c \left(\frac{2\pi}{\lambda_0}\right)^3 \frac{\Gamma_s}{2\pi}} \tag{7.9}$$

For the Ps atom, the saturation intensity of the transition $n=1 \leftrightarrow n=2$ excited by a monochromatic laser is then $I_{sat} = 0.45 \text{ W.cm}^{-2}$.

For a non-monochromatic laser as the case studied here, the saturation intensity depends on the laser bandwidth and is defined by:

$$\boxed{I_{sat,L} = I_{sat} \times \frac{\Gamma_{tot}}{\Gamma_s}} \tag{7.10}$$

For a laser bandwidth of $\sigma_L = 2\pi 100 \text{ GHz}$ and $\Gamma_{tot} = \sigma_L + \Gamma_s \approx \sigma_L$, we obtain a saturation intensity of $I_{sat,L} = 910 \text{ W.cm}^{-2}$.

7.1.4 For long interaction times

Because we want to be able to perform an efficient laser cooling on Ps, longer interaction times should be studied as well, typically of the order of the Ps lifetime. The approximation consisting in neglecting the annihilation decay rate is no more valid for times $T_{int} \sim \tau_{annih}$. The laser interaction between two levels with finite lifetime is treated in details in [59]. Chap. 2.4. where the population evolution over times is given. No more steady-states can be reached, since for infinite time all the atoms would have flee out of the open system.

For our simulations, we decided to treat the annihilation of Ps over time as the decay toward a fictive third level "dead". The simplest way to model this situation is then to consider a closed 3-level system, where the $n=1$ o-Ps ground state is modeled as a meta-stable state, and the "dead" fictive level

is the ground state, named $|0\rangle$. We keep $\Gamma_2 = 0$, Γ_1 is then the decay rate from the ground state $|1\rangle$ to the dead level $|0\rangle$. The rate equations become:

$$\begin{cases} \frac{d\rho_{22}}{dt} = -(\Gamma_s + \Gamma_e) \rho_{22} + \Gamma_e \rho_{11} \\ \frac{d\rho_{11}}{dt} = (\Gamma_s + \Gamma_e) \rho_{22} - (\Gamma_e + \Gamma_1) \rho_{11} \\ \frac{d\rho_{00}}{dt} = \Gamma_1 \rho_{11} \end{cases} \quad (7.11)$$

In the case of the laser excitation of Ps, the annihilation lifetime of the ground state $|1\rangle$ is much longer than the lifetime of the excited state $|2\rangle$: $\tau_{annih} = 142 \text{ ns} \gg 1/\Gamma_s = 3.2 \text{ ns}$.

As a consequence, the evolution of the dead level $|0\rangle$ is much slower than the evolution of the ground $|1\rangle$ and excited $|2\rangle$ states. Over the characteristic evolution step Δt that defines the typical time for the level $|1\rangle$ and $|2\rangle$ to change, the population of the dead level can be considered constant. We define the interaction time $T_{int} = N \times \Delta t$, where N would be the number of absorptions and emissions of photon that lead to a population changes in ρ_{11} and ρ_{22} .

Thus, quasi-steady states can be calculated between T_{int} and $T_{int} + \Delta t$, and leads to $\left. \frac{\Delta \rho_{11, st}}{\Delta t} \right|_{T_{int}} = 0$ and $\left. \frac{\Delta \rho_{22, st}}{\Delta t} \right|_{T_{int}} = 0$:

$$\begin{cases} \rho_{22, st} = \frac{1}{2} \frac{s}{1+s} (1 - \rho_{00}) \\ \rho_{11, st} = \frac{1}{2} \frac{s+2}{s+1} (1 - \rho_{00}) \\ \rho_{00} = \exp(-\Gamma_1 \rho_{11, st} T_{int}) \end{cases} \quad (7.12)$$

For short interaction time $T_{int} \ll \tau_{annih} = \frac{1}{\Gamma_1}$, $\rho_{00} \approx 0$, that leads back the usual steady-state solutions for a closed 2-level system seen previously (Eq. 7.6).

This derivation confirms that we can use the usual formula of the saturation parameter s and the saturation fluence I_{sat} when we study the Ps laser excitation, even for a long excitation time. For instance, this is of great interest to determine the good parameters to choose to simulate the laser cooling, as the laser power, detuning and bandwidth.

7.2 The scattering rate

At the end, the rate equations formalism allows to calculate the population evolution of an atomic system in interaction with a laser. In order to model the cooling effect of this interaction, the interesting parameter to express is the photon scattering rate.

$$\begin{aligned}\Gamma_{scat} &= \Gamma_s \rho_{22} \\ \Gamma_{scat} &= \Gamma_e \times (\rho_{11,st} - \rho_{22,st})\end{aligned}\tag{7.13}$$

The expression of the excitation rate Γ_e depends on the model of the laser spectrum chosen, as seen previously in Sec. 7.1.2.

This scattering rate gives the cooling efficiency of the interaction. In order to determine the cooling process on an atom in motion, we can calculate over time the changes in impulsion due to photon absorbed ($\hbar \vec{k}_L$) and scattered⁹, based on the rate equations.

We used this principle to simulate a possible laser cooling on the Ps, that we will discuss on the following chapter 8.

7.3 Toward the force resulting of the laser-atom interaction

In order to find the adapted parameters for the cooling simulations, it was useful to determine the force resulting of the laser interaction with the atom in motion. Taking into account the velocity \mathbf{v} of the atom in the previous formula is rather simple if we replace the laser frequency ω_L by the one seen by the atom $\omega_L - \mathbf{k}_L \cdot \mathbf{v}$. The detuning becomes thus $\delta_0 = \omega_0 - \omega_L \rightarrow \delta = \delta_0 - \mathbf{k} \cdot \mathbf{v}$ and for a Lorentzian laser, $s(v) = \frac{2\Omega^2}{4(\delta_0 - \mathbf{k}_L \cdot \mathbf{v})^2 + \Gamma_{tot}^2} \frac{\Gamma_{tot}}{\Gamma_s}$.

To model the laser interaction resulting force, a distinction has to be done between broad-line transition and the narrow-line transition:

⁹The spontaneous emission is not isotropic and depends if deexcitation goes toward a σ_{\pm} or a π transition. For a π transition ($\Delta m = 0$), the spontaneous emission's density of probability is $\rho_{\pi}(\theta) = \sin^2(\theta)$; whereas for σ_{\pm} transition ($|\Delta m| = 1$), the density of probability of emission is $\rho_{\sigma_{\pm}} = \frac{1 + \cos(\theta)^2}{2}$. Here, θ is the co-latitude $\theta \in [0, \pi]$ in the spherical coordinates. More details are given in my master thesis [51], Append. C.

In the following, we call an optical transition "broad" when the recoil energy due to the absorption or emission of a photon is much smaller than the natural linewidth of the transition ($\hbar\Gamma_s \gg E_{recoil}$). In this situation, the Brownian motion formalism can be applied to derive the average force felt by the atom in interaction with a classical electromagnetic laser wave [60]. This force is called the radiation pressure force, and can be seen as a friction force of coefficient α , such as $\vec{F} = -\alpha\vec{v}$ for the low velocities and low saturation regime. Physically, this force can be understood as the pressure of the photons applied on the atom. The laser cooling over a broad-line transition leads to a velocity distribution evolution that decreases exponentially $\vec{v}(t) = \vec{v}_0 \exp(-\alpha t)$.

As seen in the introduction of this chapter, this case models most of the laser cooling processes, mainly over alkali atoms. In Fig. 7.2, a) is shown a typical radiative force generated by two counter-propagating lasers in interaction with an atom in motion ; the capture range and force strength are determined by the laser detuning, intensity and bandwidth. More details are given in Appendix D. The minimum temperature reachable with the Doppler cooling over a broad-line transition is given by the Doppler energy:

$$T_{min} = \frac{E_{Doppler}}{k_B} = \frac{\hbar\Gamma_s}{k_B} \quad (7.14)$$

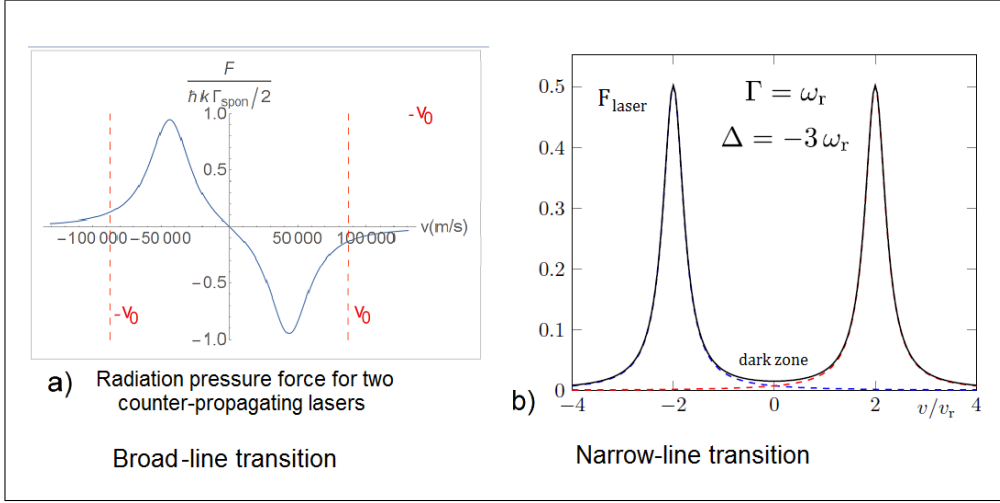


Figure 7.2: Illustration of the force resulting from the laser-matter interaction and the scattering rate, for respectively the two transitions cases. a) In case of a broad-line transition ($\hbar\Gamma_s \gg E_{recoil}$), the averaged radiative force can be derived. The force strength and capture range are determined by the laser intensity, detuning and bandwidth. Here, the force is obtained for two counter-propagating lasers, with a power $P_L = 5000$ W, a rms bandwidth $\sigma_L = 100$ GHz, and a detuning $\delta = \pm \frac{k_0 v_0}{2}$, where $k_0 = \frac{2\pi}{\lambda_0}$ is the wavevector

of the transition and $v_0 = \sqrt{\frac{k_B T}{m_{Ps}}}$ is the mean velocity of the Ps cloud at the temperature $T = 1000$ K. b) Case of a narrow-line transition ($E_{recoil} \geq \hbar\Gamma_s$): The resulting scattering rate of 2 counter-propagating monochromatic lasers is plotted. The optimum photon scattering power (equivalent to the cooling efficiency) can be derived and is obtained for a detuning of $\delta = -3\omega_r$, where ω_r is the angular frequency of the photon energy recoil such as $E_{recoil} = \hbar\omega_r$. Figure taken from [60], where the complete derivation of this force can be found.

In the case of the light positronium atom, the transition over the triplet states $n=1 \leftrightarrow n=2$ belongs to a **narrow-line transition case**, where the recoil energy for a 243 nm photon is $E_{recoil} \approx 200 \times \hbar\Gamma_s$. From this situation, the force resulting of the laser interaction is more complex to derive. As shown in [60] the velocity distribution evolves in $\frac{1}{v^{-\beta}}$, where β is a positive damping coefficient. This is a much smoother evolution than in the

case of the broad-line transition, where the velocity distribution exponentially evolves (for $s \ll 1$, $m \vec{a} = \vec{F} \sim \alpha \vec{v}$) as seen previously.

The coefficient β can be calculated and is found to be $\beta = 2 \frac{|\delta|}{\omega_{recoil}}$, where $E_{recoil} = \hbar \omega_{recoil}$. In order to define a normalizable kinetic energy, the laser detuning must be chosen $\delta > \frac{3}{2} \omega_{recoil}$. Numerical simulations of the force of two counter-propagating monochromatic lasers give an optimum cooling efficiency for $\sigma_L \approx \omega_{recoil}$ and $\delta \approx 3 \omega_{recoil}$ [60]. As illustrated in Fig. 7.2 b), where the scattering power of the force is plotted, this detuning is a good compromise between the velocity capture range of the lasers and the range of atoms in "dark".

The minimum temperature reachable with the Doppler cooling over a narrow-line transition is given by the recoil energy:

$$T_{min} = \frac{E_{recoil}}{k_B} = \frac{(\hbar k_L)^2}{2 k_B m} \quad (7.15)$$

For the Ps over the transition $n=1 \leftrightarrow n=2$, we found $T_{min}=0.15$ K.

7.3.1 A possible laser broadening of for the narrow-line transition of the Positronium ?

In some cases, the laser intensity is powerful enough to broaden consequently the transition line, and a situation of a broad transition can be recovered. For intense "monochromatic" lasers, the linewidth of the transition is not more characterized by Γ_s but by an effective term

$$\Gamma_{s,eff} = \Gamma_s \sqrt{1 + I/I_{sat,L}} = \Gamma_s \sqrt{1 + \left(\frac{2\Omega^2}{\Gamma_s^3}\right) \times \Gamma_{tot}} \quad (7.16)$$

For a non-monochromatic laser, the broadening of the transition is given by: $\Gamma_{s,eff,L} = \Gamma_s \sqrt{1 + \frac{I}{I_{sat,L}}}$.

Consequently, if the broadening of the line is large enough to fulfill the condition of validity of the Brownian motion approach:

$$\boxed{\hbar \Gamma_{s,eff} \gg E_r (\geq \hbar \Gamma_s) \quad \text{or (non monochromatic)} \quad \hbar \Gamma_{s,eff,L} \gg E_r (\geq \hbar \Gamma_s)} \quad (7.17)$$

then, the friction force model can be applied. For the laser cooling on Ps we want to attempt, the characteristic values are given in Table 7.1.

Γ_s	ω_r	$\Gamma_{s,eff}$	$\Gamma_{s,eff,L}$
$\frac{1}{\tau_{lifetime}}$	$\hbar \frac{k_L^2}{2m_{Ps}}$	$\Gamma_s \sqrt{1 + I/I_{sat}}$	$\Gamma_s \sqrt{1 + I/I_{sat,L}}$
0,3 GHz	19 GHz	52 GHz	3 GHz

Table 7.1: This table summarizes some interesting parameters to determine if the laser cooling of Ps can be approximated by the cooling over a broad-line, enlarged by intense laser. We took a laser power $P = 5000$ W, equivalent of $500 \mu\text{J}$ over 100 ns, and $\sigma_L = 100$ GHz. It appears that for our large and intense laser, the condition Eq. 7.17 is not fulfilled, and the approach of the friction force formalism can't be strictly applied.

Since we want to perform a Doppler cooling with broadband lasers, the condition $\omega_r \leq \Gamma_{s,eff,L}$ to recover a situation of broad-line transition is not fulfilled. The Brownian motion approach and the radiation pressure force can't be use for a good modeling of the Ps cooling.

Nevertheless, the radiation pressure force gives a good empirical explanation of the effect of laser interaction on the atom in general. That's why in a preliminary approach, we decided to use the well-known expression of the radiation pressure force to determine some rough estimations of the parameters of interest to maximize the laser cooling efficiency, namely: the laser power, detuning and spectral bandwidth. The radiation pressure force for two counter-propagating lasers in low saturation is given by:

$$\langle \vec{F}_{rad} \rangle = \hbar k_L \frac{\Gamma_s}{2} \left(\frac{s_1}{s_1 + 1} - \frac{s_2}{s_2 + 1} \right) \quad (7.18)$$

where s_1 and s_2 are the saturation parameters of the two counter-propagating lasers. This force expression was used to the plot the Fig. 7.2 a).

7.4 The Ps laser cooling, which formalism ?

In this chapter, we have seen that the laser cooling of Ps differs from the usual Doppler laser cooling. Although the rate equations formalism is still valid, the annihilation process needs to be taken into account. This modifies the well-known steady-state solutions for a closed two-level system in interaction with a non-monochromatic laser. The table 7.1 summarizes some

characteristics lifetimes of the Ps atom.

We have also reminded that the radiation pressure force model is only valid for broad-line transition (when $\hbar\Gamma_s \gg E_{recoil}$), and leads to exponential changes in the velocity distribution. In the contrary, for narrow-line transition as for the Ps case, the effect of the laser interaction on the atom is more complex to derive, and appears to be smoother with velocity changes in $|v|^{-\beta}$.

Nevertheless, the laser cooling of positronium can be properly simulated within the rate equations formalism: the effect of the Doppler cooling on the atoms can be derived by calculating the changes in impulsion due to absorbed and scattered photons over time using the rate equations. We used this formalism to numerically simulate Ps laser cooling on a C++ code and I propose to discuss about our simulation results in the next chapter 8.

Chapter 8

Positronium laser cooling - simulations

As we have seen previously, the positronium is a metastable atom with a short lifetime in vacuum of 142 ns for the ground state o-Ps. One of the greatest challenges is then to be able to efficiently cool o-Ps in few tens of nanoseconds. The typical Doppler laser cooling times for alkali atoms rather scale in the order of tens of microseconds. However, the positronium is the lightest atom possible. The energy recoil of one emitted photon is consequently much more important than for usual atoms, with a mass at least of the order of the proton mass. This statement implies that every scattered photon removes a large amount of energy from the Ps atom, and a consequent laser cooling on o-Ps should be feasible in scales on tens of ns, over the transition $n=1 \leftrightarrow n=2$.

The 2^3P Ps states have a decay time of 3.19 ns, and a much longer annihilation lifetime ($> 100 \mu s$), see Table. 2.1. The annihilation for the $n=2$ level can easily be neglected in comparison to its decay time. Without magnetic field, the transition wavelength λ_0 between $1^3S \leftrightarrow 2^3P$ is at 243.01 nm, leading to a recoil velocity of $\Delta v = 1500 \text{ m.s}^{-1}$ that can be translated in kinetic energy by $\Delta E_K = 1/2 m_{Ps} \Delta v^2 = k_B 0.15 \text{ K}$. Potentially, only few cycles of absorption/spontaneous emissions are needed to change consequently the Ps velocities: an initial temperature of the Ps cloud of 1000 K (Boltzmann distribution) means a velocity spread of 90 km/s. In a first simple calculation, the huge energy recoil removed for each spontaneous scattered photons implies that only $\frac{80 \times 10^5}{1500} = 60$ cooling cycles, in an interaction time of $t_{int} = 60 \times 3.2 \text{ ns} \times 2 \approx 380 \text{ ns}$, would lead to the drastically decrease of the 1D temperature of the Ps cloud, down to the Doppler limit.

Besides, for a 100 GHz broadband laser, the saturation intensity is 5800 W/cm², meaning an energy of 580 μJ for a pulse of 100 ns and a waist of about 8 mm (for a Gaussian laser $I_L = \frac{2 P_L}{\pi w^2}$). These values are quite realistic to obtain, if generated with pulsed lasers. Since the first quick derivations of a Doppler laser cooling tend to indicate its feasibility, we started to study it in more details.

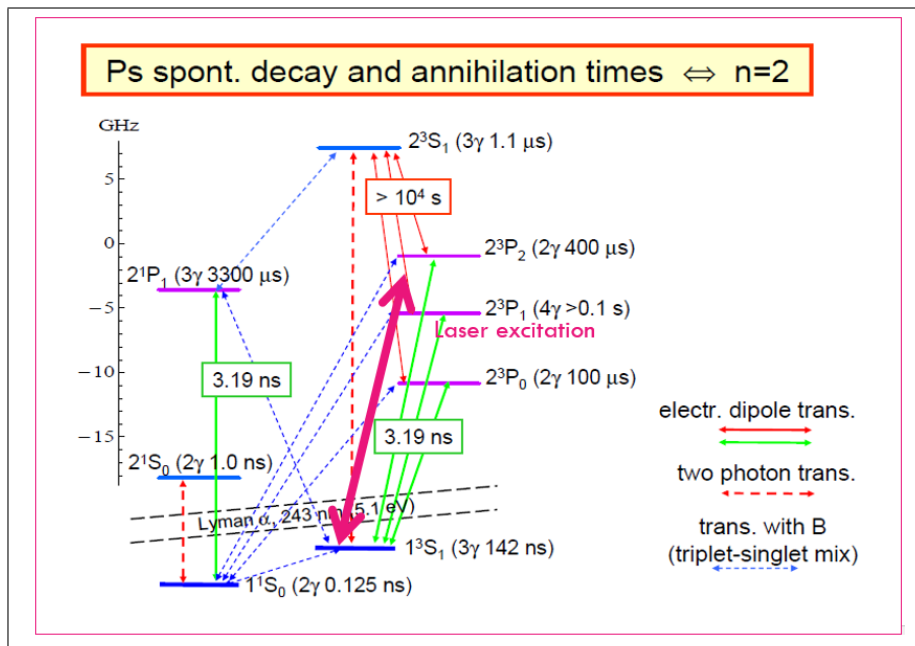


Figure 8.1: Ps n=1, n=2 hyperfine structures, with the transition strengths indicated on the arrows and the annihilation time in parenthesis. The pink double arrow indicates the cooling transition chosen.

I simulated laser cooling of Ps for different situations: in one-dimension (1D) and three-dimension (3D), in free space and for a 1 T magnetic environment. Before presenting the results, I would like first to explain briefly the C++ code used, as well as the Ps internal levels structures that we had to model for the simulations at 0 T and 1 T environment, see Fig. 8.1.

8.1 The simulation C++ code - the optical pumping code

The C++ program developed by Daniel Comparat is called the "optical pumping code" in the following. It uses the rate equations for spontaneous, absorption and stimulated emissions. It derives laser excitation and motion under external forces (scattering + dipolar + magnetic + electric + gravity) and take into account N-body Colom's interactions and Lorentz forces, in case of charged particles. The momentum recoil is also implemented. I used this code to simulate not only the Ps laser cooling, but also the possible laser cooling of the molecular anion C_2^- in traps. I present our studies on this matter in the Part III Chap. 14.

The algorithm and details of calculations can be found on the appendix of [57]. Here, I simply present the main results of our study on Ps atoms.

During the simulations, I mainly worked on debugging the code and I implemented some modifications concerning the initial thermalization of the atom cloud, as well as the non isotropic spontaneous emission, see App. C of my master thesis [51]. I also generated the Ps atoms input files for both 0 T and 1 T cases.

8.1.1 The input files

The code reads two types of input files:

- a "levels file" that expresses the different internal energy states of the particle considered.

A state is defined by its quantum numbers, including the projection of total angular momentum along the magnetic axis M , and an arbitrary number to name the level. To identify a state, the code also needs its energy at zero electrical-magnetic field. In order to calculate the energy shift due to the presence of an electric or a magnetic field, the "levels file" also gives coefficients to compute the linear and quadratic changes in energy.

In case of Ps, we had to implement different types of internal states:

- The usual quantum states, identified in the basis $|n, l, s, j, m\rangle$.

For instance, the o-Ps ground states 1^3S_1 are then $n=1, s=1, l=0, m=0, \pm 1$.

- The "dead levels" to model the annihilation of Ps. These fictive levels have been created to model the annihilation as a spontaneous decay toward quantum states. In Sec. 7.1.4, this principle has been treated for the simple case of the opened 2-level system on which we close the losses due to the annihilation by adding a fictive third level "dead".
- The "continuum levels" to simulate a possible photoionization. In order to mimic the continuum, we decided to also create fictive states defined at the energy of photoionization. The atoms that reach this kind of level can't be re-emitted (no spontaneous or stimulated emission).
- a "lines file" provides the information about the transitions between the different internal levels. For transition between two usual quantified states (or between a usual state and a dead level), the strength of the transition is given by the electrical dipole squared, in Debye². For transition between a quantified state and a "continuum" state, the strength is given by the cross section of photoionization¹¹, in cm².

In order to simulate the Doppler laser cooling on Ps, my work was first to generate such input files. Because we wanted to investigate the cooling only over the transition $n=1 \leftrightarrow n=2$, I focused on the creation of the level files for the 4 states of the $n=1$ level and the 16 states of the $n=2$ level, and the associated lines files, for both cases of no magnetic field and a 1 T field.

To do so, I wrote a Mathematica code based on the work of the former AEgIS Ph.D student Fabio Villa [46].

By performing the diagonalization of the full-Hamiltonian of the system, this code calculates the internal energies of an hydrogenoid atom, with the QED corrections, Zeeman and Stark effects, as well as the dipole strengths for each transitions, with or without magnetic fields. More details can be found in the Appen. C.

In addition to these two input files, the code reads a global parameter file, where different variables can be defined, such as the type of particles,

¹¹The derivation of the photoionization cross section of the $n=2$ Ps was made thanks to a Mathematica code provided by Fabio Villa ([46]) and Fabrizio Castelli (from the Milano-INFN group of AEgIS), based on the Gordon formula ([61, 62]) that I adapted.

the initial temperature of the particles clouds (Boltzmann distribution), its dimensions, positions in regard of the lasers, its initial velocities, and the electro-magnetic environment that can simulate trapping.

In this file are also defined the lasers properties: number of lasers, along one, two or the three dimensions of space, the direction, the type of spectral distribution (Lorentzian or Gaussian), the laser frequencies, power, waists, bandwidths and polarization. This parameter file allows the user of the code to easily play on the parameters of the simulations.

8.1.2 The outputs

For each particle, the internal state (the population of the internal energy states) and the external state (position, velocity, kinetic energy) are the output of the code.

Although well defined for a Boltzmann distribution of the atoms velocities, the meaning of the notion of temperature is not really conserved during the Ps laser cooling. However we define $T_{1D,i}$ the "fictive" temperature along the axis i , for a mesoscopic number of $N \geq 1$ particles as:

$$\frac{1}{N} \sum_{j \leq N} \frac{1}{2} \times m \times (\bar{v}_i - v_{i,j})^2 = \frac{1}{2} \times k_B T_{1D,i} \quad (8.1)$$

where $v_{i,j}$ is the velocity along the axis i of the particle j , m its mass, \bar{v}_i is the averaged velocity $\bar{v}_i = \frac{1}{N} \sum_{j \leq N} v_{i,j}$ along the direction i . The 3D temperature is then defined as the rms value of the 1D temperatures of the three directions of space $T_{3D} = \sqrt{\frac{1}{3} \sum_{i \in x,y,z} T_{1D,i}^2}$.

The output files can provide information of each single particle, but also statistics of the cloud: averaged temperature over 1 axis or the 3 axis (3D mean temperature), averaged velocities, kinetic and potential energies, average positions and the corresponding standard deviations.

These statistics are calculated over 50% of the particles within the core of the cloud; meaning we removed the 25% of the most extreme particles on both sides of the mean velocity. This selection has been done to remove any particle with weird orbit or extreme velocities. This is specially useful for the studies of trapped particles, like for our work on the C_2^- molecules, presented in the Chap. 14.

In the following simulation results for Ps, we will present the 3D temperature $T_{3D,50\%}$ and 1D $T_{1D,50\%}$ that are the average temperature calculated over 50% of the most centered particles. To simplify the notations we will write $T_{nD,50\%} = T_{nD}$. Because the Doppler broadening of the Ps cloud is huge, the laser cooling will affect only a fraction of the Ps atoms. As mentioned previously, the definition of temperature is not really conserved during the Ps laser cooling. By selecting the 50% atoms in the core of the distribution, we emphasize the laser interaction effects on the atoms selected.

8.2 Doppler laser cooling of Ps - Some simulation results

During my thesis, I spent time to optimize the laser cooling efficiency, both in free field condition and for a 1 T field. The quantification axis associated to the magnetic field has been set along the z axis. In AEGIS, the target convertor in the test chamber is typically at room temperature. The energy implantation of the positrons determined the depth into the nano-channels in which the Ps are formed. Once bound, the Ps collides with the nano-channels' walls to reach the surface and the Ps cloud tends to partially-thermalize with the target. The implantation energy and the temperature of the target convertor are then of importance to control the temperature of the emitted Ps cloud. We can mention that in AEGIS, for a target at room temperature, the "slow" fraction of Ps is emitted for a mean temperature around 1000 K, depending of the energy implantation of the incoming positrons [63, 31]. The "slow" Ps atoms are partially-thermalized via phonon emission during the collisions with the nano-channels of the target. Besides, preliminary studies have been carried out on targets cooled down at cryogenic temperature and show that the slow fraction of Ps can reach cooler temperatures of few hundreds of Kelvin.

In our simulations, the Ps cloud can expand in all the direction of space. This situation is an approximation of the real situation of Ps creation in AEGIS, where the Ps are emitted from the target convertor with a privileged direction among the +z axis, and can't propagate along -z where the target stops them.

The initial conditions of the Ps cloud and laser spots are illustrated in Fig. 8.2: the laser spots are centered in the position of space (0,0,0), and the Ps cloud is set at the position (0,0,-2mm), meaning we model the target

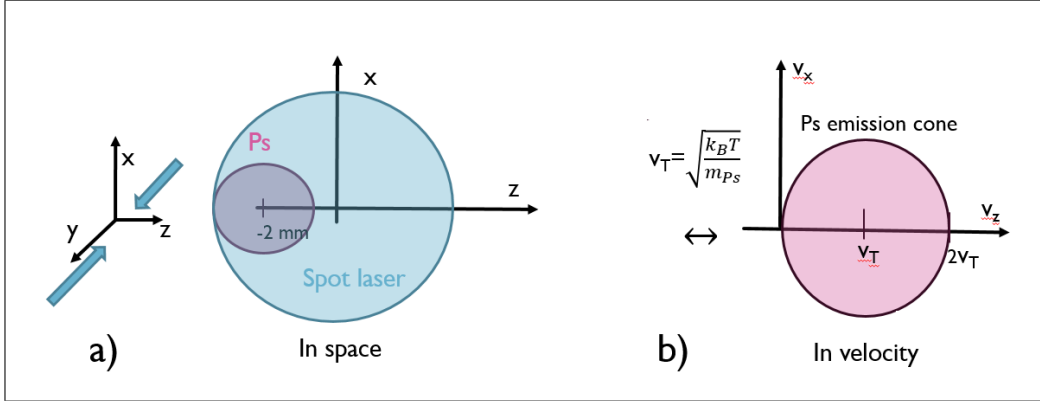


Figure 8.2: Illustration of the simulations initial conditions of the Ps cloud (positions and velocity distributions) and the laser beams, in free field environment. a) shows the spacial positions of the Ps cloud and laser beams, in case of a 1D laser cooling. b) shows the initial velocity distribution of the Ps cloud. To model the cone of Ps emitted with a privileged direction toward $+z$, an initial velocity kick has been added to the random velocity of each particle, given by its Maxwellian velocity distribution at a temperature T .

converter to be placed at -2 mm along the z axis.

To model the cone of emitted Ps that has a privileged propagation direction toward $+z$, an initial velocity kick on the z direction is added to the initial random 3D velocity of each particle. This velocity kick v_T is chosen to be the equivalent velocity of the fixed initial temperature T of the cloud, meaning $v_T = \sqrt{\frac{k_B T}{m_{Ps}}}$, see Fig. 8.2 b).

note that in all our simulations, we consider that the Ps atoms are all emitted at the same time ($t=0$). We model the space distribution as a Gaussian, but the time distribution is a Dirac function. This approximation doesn't show the reality of the Ps emission in AEGIS: the positron cloud implemented in the nano-channel target has a temporal spread of few ns. Its temporal width is reduced via the buncher device (see Chap. 3). The emission of o-Ps lasts some ns, the fast Ps atoms are emitted within the first ns after the e^+ implantation (no many collisions with the nano-channels), but the slow fraction of the Ps are emitted later, after having partially thermalized with the walls of the target.

Anyhow, since we want to laser cool only the slow fraction of the emitted Ps, we send the laser beams after a delayed time, long enough for all the Ps atoms to be formed and emitted. If the laser spots are big enough, they cover all the slow positronium atoms. In this case, we can model the laser interaction with the whole Ps cloud, as if the Ps atoms would have been generated instantaneously.

Typically, the laser cooling was simulated for a cloud of 400 particles in interaction with 2 or 6 counter-propagating lasers, modeling 1D or 3D optical molasses. For the initialization of the simulations, the velocity and position of each particle are randomly chosen along the Gaussian distributions set by:

- the temperature T that defines the Maxwellian velocity density distribution $p(\vec{v}) = \left(\frac{m}{2k_B T}\right)^{3/2} \exp\left(-\frac{m\vec{v}^2}{2k_B T}\right)$
- the 3D rms value $\sigma_{r,Ps}$ of the Gaussian spatial distribution $n(\vec{r}) = \frac{1}{(2\pi\sigma_{r,Ps}^2)^{3/2}} e^{-\frac{r^2}{2\sigma_{r,Ps}^2}}$

The initial spatial cloud of the Ps has usually been set at $\sigma_{r,Ps} = 3$ mm, and the lasers waists at 7 mm.

8.2.1 In the absence of magnetic field

In this section, are presented some results of the simulations of the Doppler laser cooling of Ps in the absence of magnetic field. More than proving the possibility of such cooling in relatively short interaction times, which has already been done in the literature [53], these simulations were important to determine the optimum parameters for the lasers, in order to prepare an experimental trial in AEGIS.

We first present a typical result of 1D Doppler cooling, obtained for the two counter-propagating lasers detuned at -2.5 cm^{-1} ($\sim 75 \text{ GHz}$), meaning a wavelength at resonance at 243.036 nm (over a transition at 243.021 nm in absence of magnetic field), with a power of 5000 W each, and a spectral bandwidth of 50 GHz. In other words, the Ps atoms at resonance with the laser have a velocity around $18\,200 \text{ m.s}^{-1} \pm 12\,150 \text{ m.s}^{-1}$.

Experimentally, to be able to diagnose the cooling effect on the Ps cloud, one solution is to probe the velocity distribution of the cloud with a second

narrow-band laser that will be referred as the "probe" laser. The probing has to be done at different times during the cooling process to diagnose the evolution of the Ps velocities during the laser interaction. For each probing time, a frequency scan of the probe laser has to be done to reconstruct the Doppler profile of the transition in an histogram of the Ps velocities. That's why the histogram of velocities of Ps appears to be a good diagnostics of the cooling.

In Fig. 8.3 are presented several histograms of the Ps velocities after different times of the laser interaction, with a simulated initial cloud of 2000 particles. The $t=0$ ns histogram gives the velocity distributions of the cloud at its initial temperature of 1000 K. Then, the cloud is probed at 20 ns and 50 ns. The velocity range at resonance with the cooling laser is slowly depleted, and the number of Ps in zero-velocity range increases, demonstrating then the cooling effect.

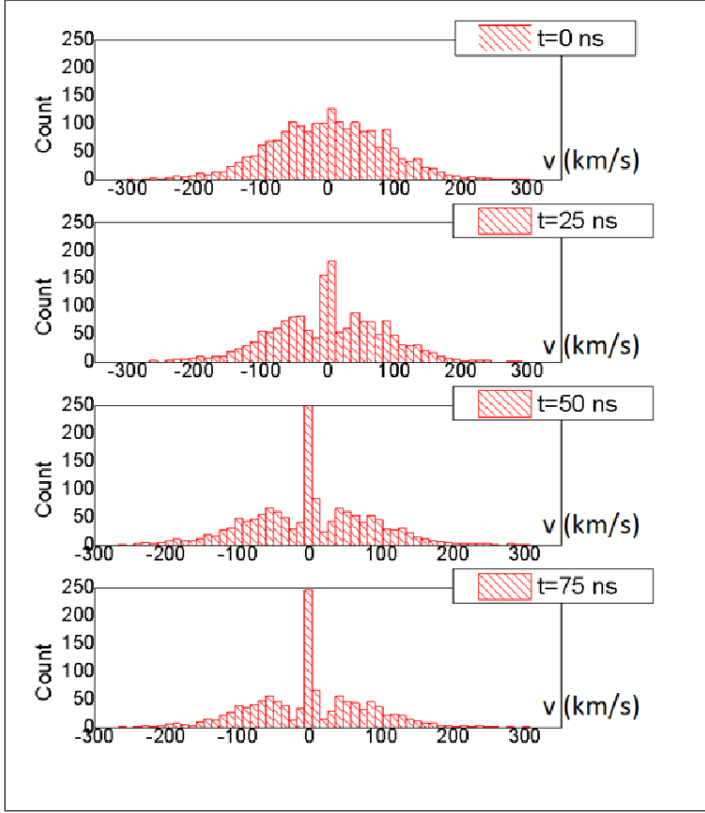


Figure 8.3: Velocity distributions of the Ps cloud, probed over time during 1D laser interaction. During the laser cooling, the velocity range addressed by lasers is depopulated, and the number of Ps atoms at low velocity increases.

In order to obtain the optimized results, different scans of the cooling parameters have been run: the laser power, bandwidth and detuning. For instance, the detuning determines the central velocity at resonance $v_{res} \approx 18200 \text{ m.s}^{-1}$ for a Ps atom, given by the formula:

$$\begin{aligned}
 \omega_0 - \omega_L - k.v &= 0 \\
 v_{res} &= \frac{\omega_0 - \omega_L}{k} \\
 v_{res} &= \frac{2\pi c 100 \times \delta [cm^{-1}]}{k}
 \end{aligned} \tag{8.2}$$

The laser bandwidth σ_L determines the window of velocities Δv_{res} around v_{res} that are still at resonance with the laser. Then, varying the laser bandwidth σ_L changes the width of the velocity range Δv_{res} . The expression of

Δv_{res} is obtained from Eq. (8.2):

$$\begin{aligned}\Delta(\omega_0 - \omega_L) &= k \Delta v_{res} \\ \Delta\omega_L = 2\pi \sigma_L &= k \Delta v_{res} \\ \Delta v_{res} &= \frac{2\pi 10^9 \sigma_L [GHz]}{k}\end{aligned}\tag{8.3}$$

From the laser power, the Rabi frequency ($|\Omega| = \frac{d E_L}{\hbar}$) is derived, which determines the speed or efficiency of the cooling; with d the electric dipole of the transition and E_L the wave amplitude of the laser.

In the figures 8.4, 8.5, 8.6, the histograms of the evolution of the velocity distribution are presented for different values of the laser power (P_L), laser detuning δ and laser bandwidth σ_L . The Ps cloud has been generated at 1000 K, for 2000 particles. The Doppler broadening of the cloud is therefore about 360 GHz.

For the laser power scan given in Fig. 8.4, the laser powers of 1000 W, 5000 W and 10 000 W correspond to respectively to a moderate saturation regime ($s_0=2.8$), high-saturation regime ($s_0=14$) and strong-saturation regime ($s_0=28$). This saturation parameter has been calculated using the expression of the Eq. (7.7); the laser intensity I_L has been derived for a laser waist of 7 mm and the saturation intensity for $\sigma_L = 50$ GHz is $I_{sat,L} = 456$ W.cm⁻².

We can note from histograms $t=50$ ns and $t=75$ ns, that the case of 10 000 W shows two peaks into the zero-velocity ranges, whereas the 5000 W histograms show a single peak. Although the central peak of the 5000 W histogram appears higher than one of the two peaks of the 10 000 W histogram, the sum of the two peaks of the 10 000 W histogram actually give a higher number of Ps in the velocity-range, than for the 5000 W case. Thus, in case of highly saturated transition ($P_L=10$ 000 W), the number of cooled Ps seems to be higher.

However, for the case $P_L = 10$ 000 W, the presence of these two peaks in the low-velocity range seems to indicate that the Ps cloud couldn't reach a temperature as cold as in the case of the mid-saturation regime (5000 W), where just a single peak in the low-velocity range appears. This can probably be explained by the broadening of the transition line due to the high laser intensity.

Finally we can note that for a power of $P_L=1000$ W, the cooling appears to be slow and not complete in 75 ns. For a fast and efficient cooling, $P_L \geq 5000$ W seems a good value.

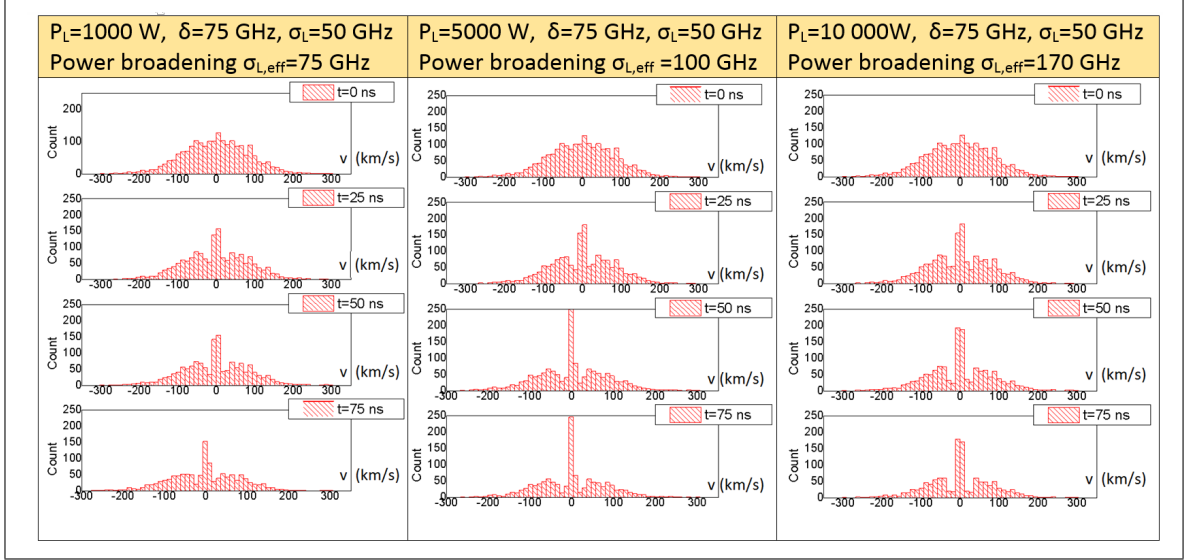


Figure 8.4: Scan of the laser power P_L . The detuning δ and the spectral bandwidth σ_L have been fixed at $\delta = -2.5\text{cm}^{-1} \sim 75$ GHz and $\sigma_L=50$ GHz. a) $P_L = 1000$ W, b) $P_L = 5000$ W, c) $P_L = 10\,000$ W.

The scan of the laser linewidth is given in Fig. 8.5. As for the histograms in Fig. 8.4, the lasers are detuned $2.5\text{ cm}^{-1} = 75$ GHz.¹²

The scan performed in the Fig. 8.5 gives the cooling behavior for different linewidths of the laser: $\sigma_L = 50$ GHz means an excitation window of $\Delta v_{res} = 12\,150\text{ m.s}^{-1}$ around v_{res} , $\sigma_L = 100$ GHz $\leftrightarrow \Delta v_{res} = 24\,300\text{ m.s}^{-1}$ and $\sigma_L = 200$ GHz $\leftrightarrow \Delta v_{res} = 48\,600\text{ m.s}^{-1}$. In the histograms for $\sigma_L = 50$ GHz and $\sigma_L = 100$ GHz, the depletion of the atoms around v_{res} is clearly visible after 75 ns of cooling ; whereas for the broader laser bandwidth case (200 GHz), the velocities at resonance for the two counter-propagating lasers overlap. In this case, even if the number of Ps atoms in the low-velocities window increases, there is no clear hole formation around v_{res} .

¹²the unity of the frequency detuning δ is given in cm^{-1} with $\delta[\text{cm}^{-1}] = \frac{\omega_0 - \omega_L}{100 \times 2\pi c}$.

We can note that for $T = 1000$ K, the Doppler broadening is about 360 GHz, whereas the laser is detuned to be resonant at a frequency centered around 75 GHz. The capture range of the laser, given by σ_L , varies here for the scan. The common setting for a Doppler cooling over a broad-transition is usually to choose $\delta \approx \Gamma_{doppler} = \frac{k_L v_0}{2\pi}$. However, as seen previously in Chap. 7 the case of the Ps is special because of the huge photon recoil generated on such a light atom. That's why the bandwidth needs to be adjusted in order to avoid any heating on the slow atoms. Indeed, if the lasers are too large and not enough detuned, the atom in motion will also be at resonance with the laser propagating in the same direction, compensating the cooling effect of the counter-propagating laser. This limits the minimum temperature reachable during the laser cooling.

From the simulations, it seems that the case Fig. 8.5 b) where $\sigma_L = 100$ GHz $\approx \frac{1}{3} \frac{k_L v_0}{2\pi}$ is a good compromise for a relatively fast cooling with a good capture range around the detuned frequency 75 GHz, and without heating the slow atoms. The case $\sigma_L = 200$ GHz addresses faster Ps atoms, but the minimum temperature reachable might be higher.

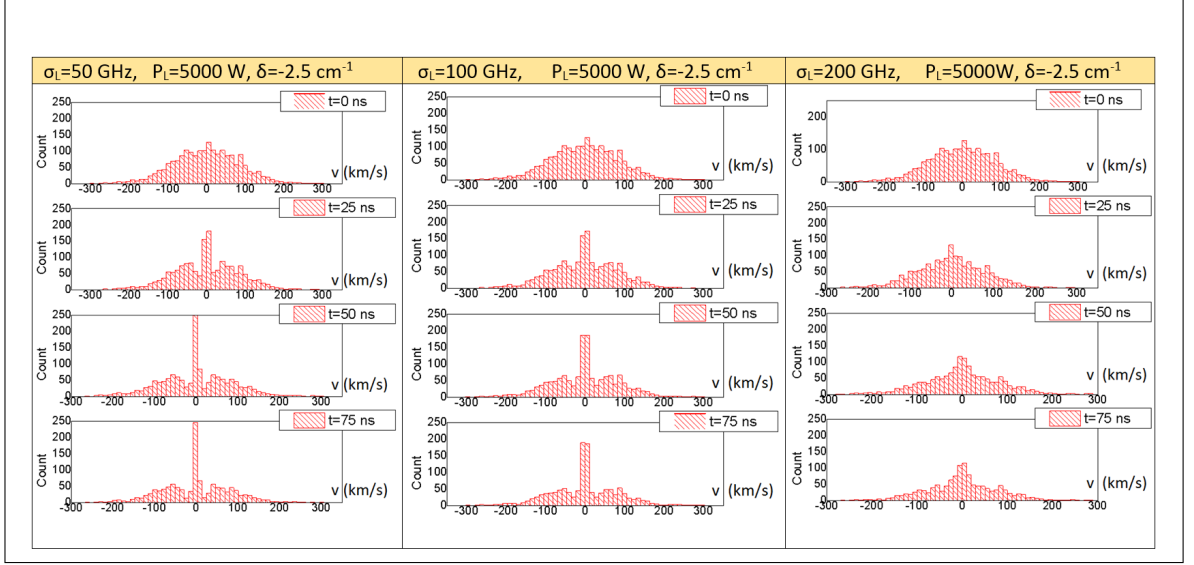


Figure 8.5: Scan of the laser linewidth σ_L . The detuning δ and the power P_L have been fixed at 75 GHz and 5000 W. a) $\sigma_L = 50$ GHz, b) $\sigma_L = 100$ GHz, c) $\sigma_L = 200$ GHz.

From the laser power scan of Fig. 8.4, we can note that increasing the laser power to reach the strong saturated regime ($P_L=10\,000$ W) leads to a similar cooling effect than when the laser bandwidth is increased from 50 GHz to 100 GHz (Fig. 8.5). This illustrates the broadening of the line due to the intense laser that over-saturate the transition ($s_0(10\,000\text{ W})=4.5$).

The last scan - presented in Fig. 8.6 - is performed over the laser detuning δ . The capture range $\Delta v = 12\,150\text{ m.s}^{-1}$ is fixed by the laser bandwidth at 50 GHz - see Eq. (8.3). The first column a) is for a detuning $\delta = 75$ GHz, corresponding to a central velocity at resonance of $v_{res} = 18\,200\text{ m.s}^{-1}$. The central peak increases over time, showing that the number of cooled Ps grows.

The second column b), the detuning is set at $\delta = 120$ GHz ($\sim 4\text{ cm}^{-1}$) corresponding to a central velocity at resonance of $v_{res} = 29\,140\text{ m.s}^{-1}$. The depletion of the atoms with their velocities at resonance is clearly moved toward higher velocity. The number of cooled atoms increases and several central peaks in the histogram are formed: the low velocity atoms are spread along a larger range (four central peaks). Indeed, the atoms within the low velocities ranges around 5000 m.s^{-1} are not at resonance with the laser (dark

zone) and thus not cooled as in the previous case a).

Finally in c), the cooling interaction sets for $\delta = 180$ GHz (~ 6 cm $^{-1}$) $\leftrightarrow v_{res} = 43700$ m.s $^{-1}$ is presented in the last column. We can see the up-rising of two peaks at around 25 000 m.s $^{-1}$, meaning that the detuning is too strong, and the atoms are only slowed down to around the range of 25 000 m.s $^{-1}$, but cannot be cooled down to lower velocity (out of resonance). Indeed, the atoms at lower velocities are in the "dark" zone of the photon scattering rate (cooling efficiency low is no photon scattered), as illustrated in Fig. 7.2 b).

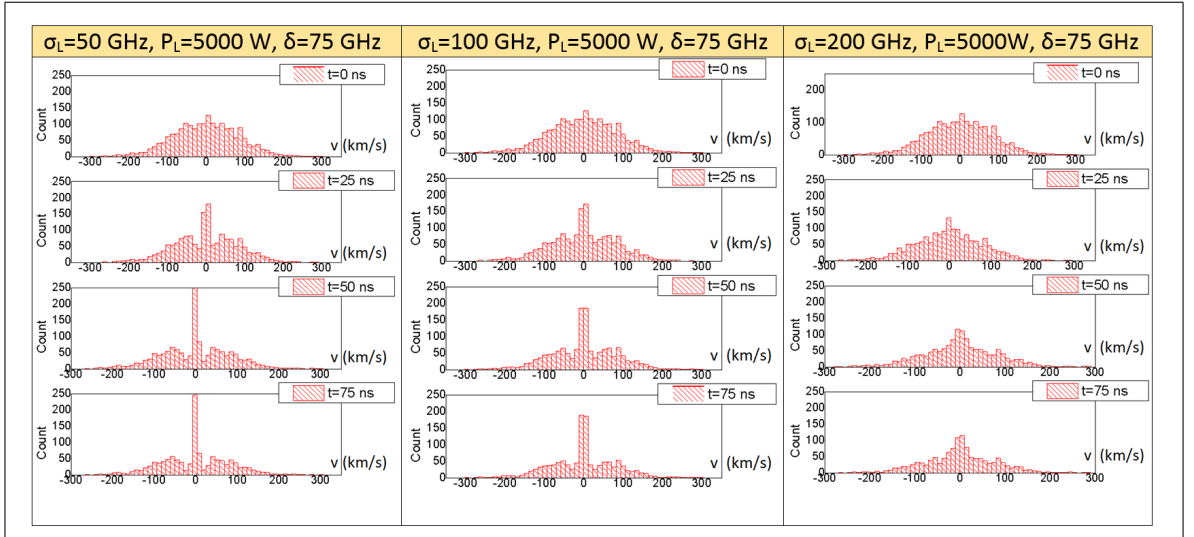


Figure 8.6: Scan of the detuning δ . The power P_L and the laser linewidth σ_L are fixed at 5000 W and 50 GHz. a) $\delta=75$ GHz, b) $\delta=120$ GHz, c) $\delta=180$ GHz

The detuning then needs to be adjusted to find a compromise between addressing the fast atoms ($\delta \approx \Gamma_{Doppler} \approx 10$ cm $^{-1} \sim 300$ GHz) for an efficient and fast cooling, but also having an effect on the slow Ps to reach even lower temperature ($\delta \approx 75$ GHz). In order to keep the atoms at resonance with the laser during the whole cooling process, both the detuning and the bandwidth should be smoothly decreased. A possible solution might be to perform a temporal sweep of the laser detuning: starting from a high detuning to cool the fast atoms, the frequency at resonance and the laser power

are adapted during the cooling interaction to affect the slower Ps atoms as well. A sweep in the laser linewidth would also increase the cooling efficiency.

At the end, thanks to these parameters scans, the optimum values for the lasers detuning, power and bandwidth can be roughly determined, for different initial parameters of the Ps cloud (temperature and size). The choice of the laser parameters requires to answer to some compromises. First, the lasers have to excite fast atoms (being highly detuned and broad spectrally) without heating the moderately slow atoms (narrower bandwidth) or having the slow atoms in a dark zone (not too much detuned). Because the Doppler effect on the Ps atom is so important - a broadening of 360 GHz for a cloud at 1000 K - the frequency sweep could appear to be a good solution. However, in practice the sweep of the bandwidth and the frequency over a such wide range of frequencies could be hard to implement.

Besides, a second compromise has to be found regarding the laser intensity. Because the atoms of Ps are so light, they escape quickly from the laser interaction area. This speaks in favor of generating big laser spots to have time to perform the cooling, and as a consequence, for a fixed laser power, this will lead to less intense lasers. But at the opposite, the Ps annihilation ($\tau_{lifetime\ Ps\ under\ interaction} = 2 \times 142\ ns$) process has to be tackled, and requires an efficient cooling, so intense lasers. This consideration adds complexity to the cooling experimental setup and choice of the parameters: large laser spots are required versus intense lasers needed for a fast cooling.

3D cooling and effect on the Ps cloud temperature ?

Once the scans of the laser parameters performed for the velocity distributions, I looked into the temperature evolution of the Ps cloud. The cooling was simulated either in 1D case (2 counter-propagating laser along z) or 3D configuration (6 lasers). The temperatures T_{1D} and T_{3D} used here have been defined previously in Sec. 8.1.2, in order to characterize the efficiency of the laser cooling on the core of the excited atoms. As the initial temperature of the Ps cloud is an important parameter for the cooling efficiency, I mainly studied 3 cases:

- The partially-thermalized situation: where the slow o-Ps atoms have a typical temperature of 1000 K, emitted from a target converter at room temperature.
- The cryostat situation: the target is attached to a cryostat, and the initial temperature of the o-Ps cloud is set at 100 K.

- And an intermediate case, where the initial temperature of the cloud is set at 500 K.

The simulations presented here in Fig. 8.7 are the results of the optimization of the laser cooling parameters, obtained by some scans of the values.

In the results presented in Fig. 8.7, the blue solid curves represent the temperature evolutions, both for the 1D (first column) and 3D (second column) laser cooling situations with different initial temperatures ; the population evolution over time is plotted in red dots, the decrease is due to annihilation in vacuum. The dashed-dotted green line represents the fraction of the Ps atoms that escape from the laser interaction region (referred as "Numbers Ps out from the interaction area" in Fig. 8.7). In other words, this is the percentage of the atoms that leave the laser waist region and are lost for the cooling process, compared to the initial number of atoms generated in the cloud. This region is simply defined as the volume defined by the laser waists in the three directions of space.

In these simulations, the power of each laser has been set at 5000 W, that appears to be a good compromise between a high efficient laser cooling and a power reachable experimentally (5000W over 100 ns is $500\mu J$). The detuning and laser bandwidth has been adapted for each initial temperature using the formula of Eq. (8.2) and Eq. (8.3).

Starting from an initial temperature of 1000 K, the Ps cloud can be cooled in 100 ns down to around 500 K (see Fig. 8.7, first row). However, we can note that the laser cooling of fast Ps appears to be limited: at such high kinetic energy, fast Ps atoms escape from the laser interaction space in tens of ns and are lost for the cooling (green dashed curves).

In Fig. 8.7, the second row starts with a Ps cloud at $T_{initial} = 500$ K and reaches about 150 K for the 1D case, and above 200 K for the 3D case in 100 ns. The third simulation starts with a Ps cloud at $T_{initial} = 100$ K and leads to a final temperature of few Kelvin after hundred ns, and we note that less and less atoms escape from the interaction laser area.

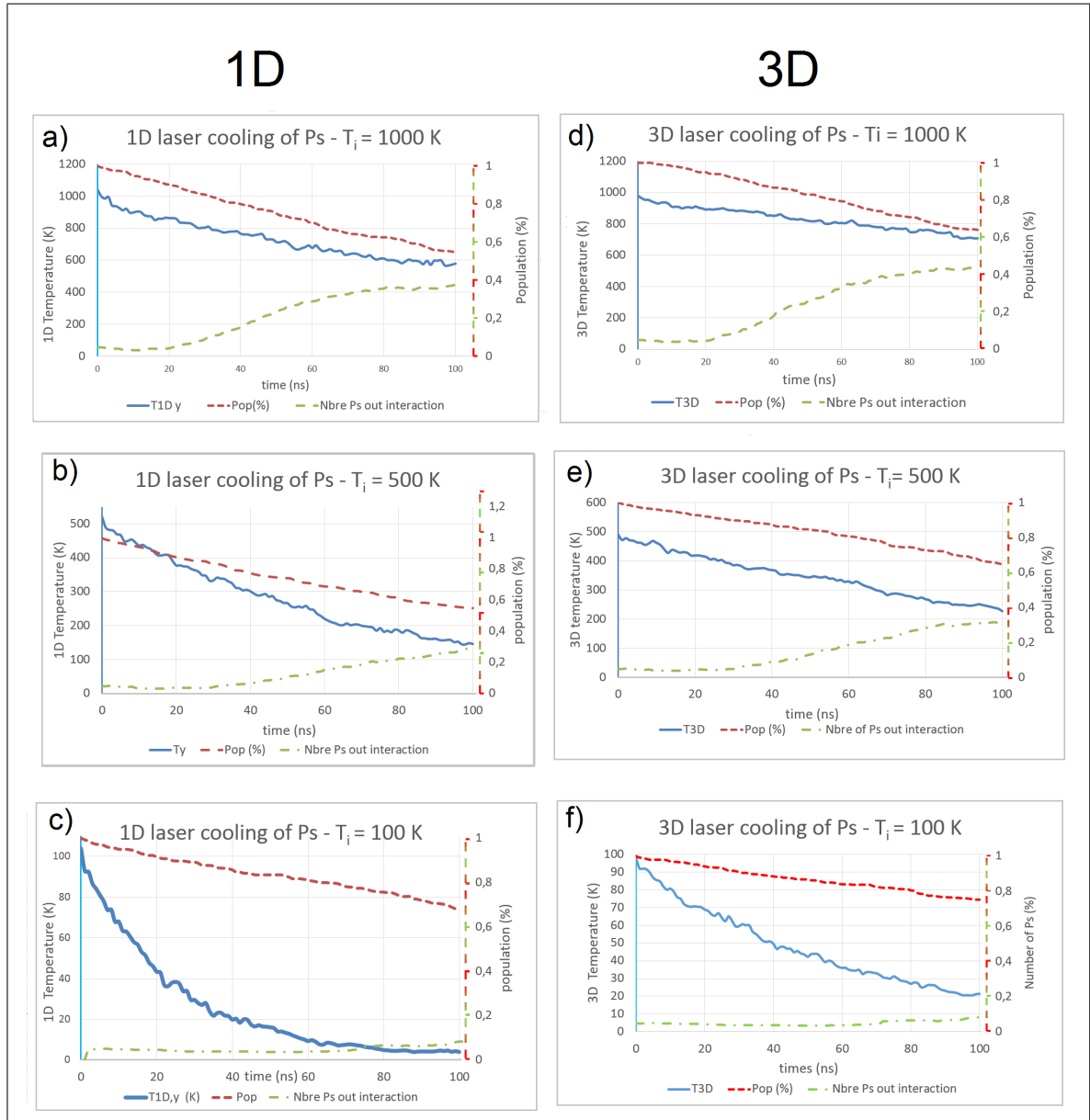


Figure 8.7: Simulations results of Doppler 1D and 3D laser cooling in a free field environment. The temperatures evolution ($T_{1D,y}$ and T_{3D}) of a cloud of 400 Ps are given for a laser interaction of 100 ns, with different initial temperature. Row 1). The initial temperature is set at 1000 K, the laser detuning is 300 GHz ($\sim 10 \text{ cm}^{-1}$), and the laser bandwidth rms value is 500 GHz. Row 2). The initial temperature is set at 500 K, the laser detuning is 190 GHz ($\sim -6.33 \text{ cm}^{-1}$), and the laser bandwidth rms value is 200 GHz. Row 3). The initial temperature is set at 100 K, the laser detuning is at 84 GHz ($\sim -2.8 \text{ cm}^{-1}$), and the laser bandwidth rms value is 100 GHz. For all the simulations, the power of each laser was set at 5000 W.

A frequency sweep ?

Starting from an initial temperature of 1000 K, a sweep in laser frequency would be needed to be able to cool further down the Ps. As seen in Sec. 8.2.1, the laser needs to be strongly detuned to excite fast atoms, but in that case the slower Ps are not addressed by the cooling lasers. We could consider the three previous simulations in a row to roughly model a frequency sweep of the cooling lasers. If we only consider the Ps lost by annihilation, we can see that after an interaction time of 300 ns, about 30 % of the initial Ps haven't yet annihilated and are cooled down to few kelvins, in both 1D and 3D cases. Indeed, the laser interaction tends to extend the Ps cloud's lifetime: at the strongly saturated steady state regime, 50% of the Ps are in the $n=2$ level with an infinite lifetime ($\tau_{annih,n=2} > 100\mu s$). The overall lifetime is then $2 \times \tau_{annih,n=1} = 286$ ns, instead of the 142 ns lifetime in vacuum for ground-state o-Ps without laser excitation. However, since the fast Ps atoms tend to escape from the laser area, the number of Ps atoms in initial conditions of the following simulations ($T_i = 500$ K and $T_i = 100$ K) have to be readjusted in order to consider these simulations as the result of a smooth sweep of the laser parameters.

From these simulations, we can see that in the first 100 ns, the Ps cloud be cooled from 1000 K to 500 K; then adjusting the laser for a further cooling for an additional 100 ns, the temperature could decreased to 100 K. A last step of cooling with adapted parameters would decrease the temperature to few K, for an additional 100 ns.

8.2.2 In the presence of a magnetic field

In this section, I studied the particular case of the laser cooling for Ps formed in the AEgIS apparatus, meaning for a fixed value of the magnetic field at 1 T, and for a cryogenic environment of a few K. The Fig. 8.8 presents a schematic of the situation modeled here: the Ps are emitted in a preferential propagation direction along the -y axis, and the magnetic field is along +z.

The presence of the magnetic field couples the 2^1P and $2^3P_{m=0,\pm 1}$ states, except for the $2^3P_{0,m=0}$. In a 1T magnetic field, the Zeeman mixing between the singlet ground state $1^1S_0, m=0$ and the triplet ground state $1^3S_1, m=0$ has also to be taken into account, and induces the fast annihilation of the triplet¹³ $m=0$.

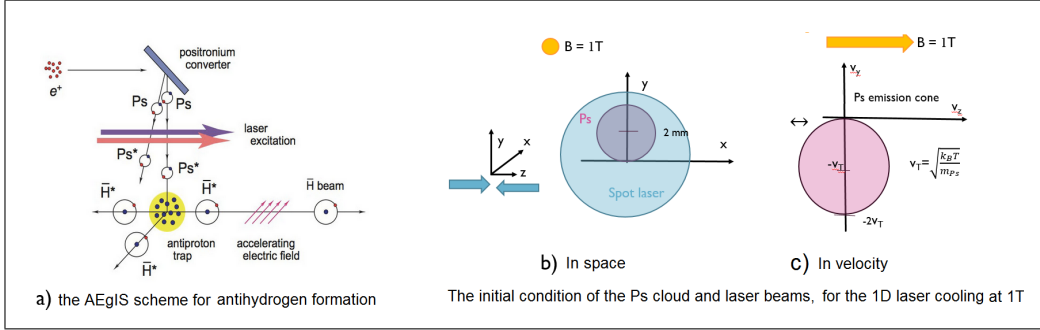


Figure 8.8: a) Scheme of the antihydrogen formation in AEGIS. b) and c) Illustration of the simulations initial conditions of the Ps cloud (positions and velocity distributions) and the laser beams, in case of a 1T magnetic environment. b) shows the spacial positions of the Ps cloud and laser beams, in case of a 1D laser cooling along the z axis. c) shows the initial velocity distribution of the Ps cloud. To model the cone of Ps emitted with a privileged direction toward -y, an initial velocity kick has been added to the random velocity of each particle, given by its Maxwellian velocity distribution at a temperature T.

In case of an optical pumping on the $1^3S_1 \leftrightarrow 2^3P$ transition with a linear laser polarization, mixed states can be excited and consequently decayed into the p-Ps ground state 1^1S where they instantaneously annihilate. This is the quenching process, already mentioned in Sec. 5.1. To perform a laser cooling, several photon absorption/emission cycles ($\sim \frac{10^5 m.s^{-1}}{1500 m.s^{-1}} \sim 70$) have to occur in order to substantially remove energy. For each photon absorbed, the excited Ps has a certain probability to quench and annihilate, depending of the magnetic field. Any laser cooling cycling on mixed triplet-singlet states will allow the Ps to deexcite toward the singlet ground state, with a lifetime

¹³The Zeeman effect leads to a mixing between the two ground states with $m=0$. In the perturbed new basis for a magnetic field of 1T, the eigen states that express the mixing are: $|1\rangle = 0.99|n=1, l=0, s=0, j=0, m=0\rangle + 0.13|n=1, l=0, s=1, j=1, m=0\rangle$ and $|3\rangle = 0.12|n=1, l=0, s=0, j=0, m=0\rangle + 0.99|n=1, l=0, s=1, j=1, m=0\rangle$. The lifetime of the mainly-triplet ground state $|3\rangle$ is given by $\tau_{annihil} = \frac{1}{0.99^2 \frac{1}{142 ns} + 0.13^2 \frac{1}{0.125 ps}} = 7 ns$, whereas the mainly-singlet state $|1\rangle$ becomes 127 ps. The triplet ground states with $m=\pm 1$ stay pure states.

in the 1 T field of 127 ps. Therefore the laser cooling will lead to the annihilation of the Ps cloud in few tens of ns.

To reproduce at best this situation of the antihydrogen formation in the AEGIS setup (see 8.8 a), the simulation initial parameters of the Ps cloud and laser beams have been modified, as illustrated in Fig. 8.8 b) and c): for each single particle, an initial velocity kick is added on the y component as $v_{y,0} = -v_0$, and the Ps initial position is set at (0, +2 mm, 0), meaning a target convertor located 2 mm distance from the laser beam centers (0,0,0).

1D cooling with linear laser polarizations

In a first stage, to verify the theoretical enhancement of the Ps annihilation, I simulated the 1D laser cooling on the z axis, with a linear polarization of the lasers, for a cloud of 600 Ps initially at 100 K. The Fig. 8.9 shows both the 1D mean temperature (blue curve) and the number of Ps (dashed red curve) evolution over time. Although the laser cooling still works, only 15 % of the Ps are still there after a laser interaction of 100 ns. This has to be put into perspective with the case of no laser interaction, where after a flight in vacuum of 100 ns, 50 % of the o-Ps atoms remains. Thus, for lasers propagating along the quantification axis (magnetic field direction), with linear polarizations, the laser interaction results in both cooling the Ps cloud and enhancing the Ps annihilation.

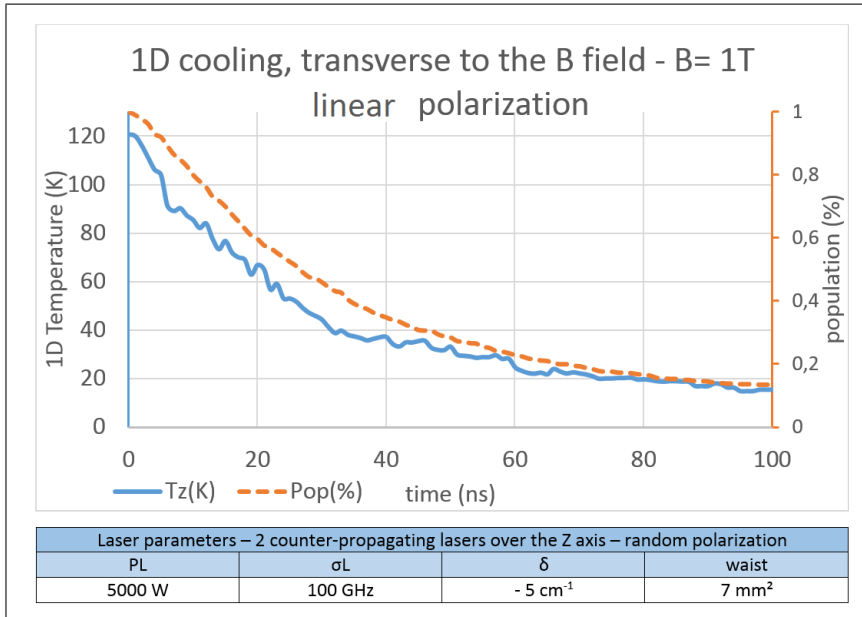


Figure 8.9: 1D laser cooling of a Ps cloud, in presence of a 1T magnetic field. The blue curve presents the temperature evolution over time, the dashed red curve shows the population evolution. After a laser interaction of 100 ns, less than 15% of the Ps remains.

Control of the laser polarization to limit the annihilation decay

When studying in details the Zeeman mixing of the Ps states, it appears that some triplet states are not mixed with singlet states, as for instance the level 2^3P_2 , $m=\pm 2$ that remains purely triplet. Indeed, the Zeeman effect couples only states with the same configuration of the total quantum momentum projection over the quantum axis m , as mentioned in the Appendix C.

If the photon absorptions and emission cycles only occur on optical transitions between pure triplet states, the laser cooling could be realized without enhancing the annihilation rate.

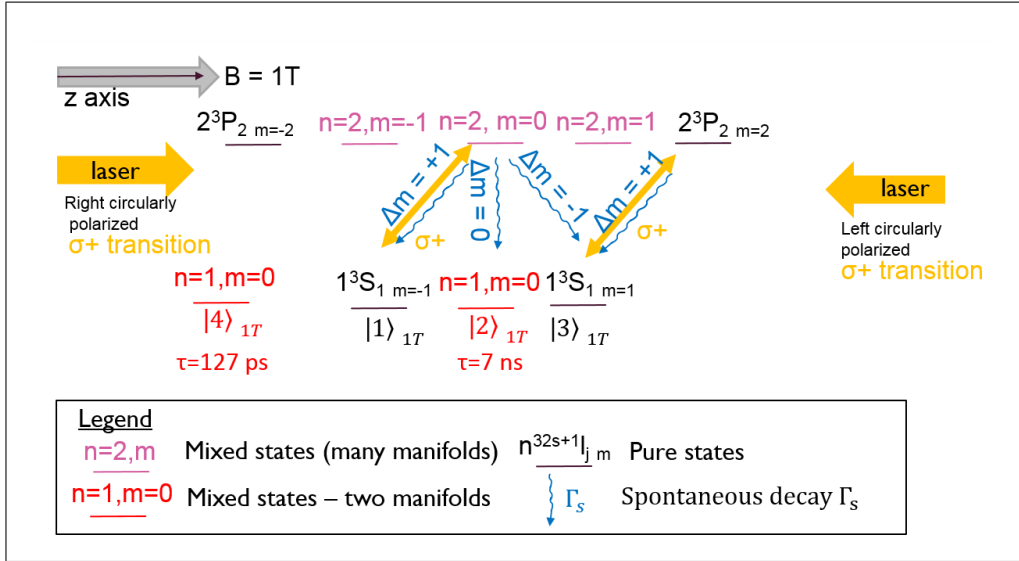


Figure 8.10: The σ^+ -excitation cycling scheme. The magnetic field is along the z axis, as the two-counter propagating lasers direction. The laser polarizations are chosen to only allow the σ^+ transitions leading to a laser cooling that cycles only over the pure states $|1^3S_1, m = 1\rangle \leftrightarrow |2^3P_2, m = 2\rangle$ that don't mix even in presence of magnetic field - this is the optical pumping process.

Thanks to the Pauli selection rules¹³, the laser cooling over the transition $1^3S_1, m=1 \xleftrightarrow{\sigma^+} 2^3P_2, m=2$ (or $1^3S_1, m=-1 \xleftrightarrow{\sigma^-} 2^3P_2, m=-2$) appears to be a closed cycle between only pure states. The principle of this cooling scheme is illustrated in the Fig. 8.10.

I then simulated the 1D laser cooling following the σ^+ excitation cycling scheme, by selecting the polarization of the lasers as indicated in Fig. 8.10. The result is shown in Fig. 8.11: after 100 ns of cooling, about 50% of the Ps remains, compared to the 15% remaining atoms for a laser cooling without

¹³We remind here that if the propagating wavevector k_L is aligned with the quantification axis of the atom (parallel to the magnetic field), then the laser polarization can be associated to the transition polarization: a right circular polarized laser - propagating along the quantification axis - will induce a σ^+ transition ($\Delta m = m_{excited} - m_{ground} = +1$), whereas a left circular polarized beam will lead to a σ^- transition ($\Delta m = -1$). A linear laser polarization along the quantification axis will π excite the atom ($\Delta m = 0$). As a consequence, the laser polarization can lead to a selection of the excited states, according to the Pauli selections rules

polarization control. We can conclude that forcing the excitation over σ_+ transitions, in order to cycle over only pure states limits the decay toward singlet ground states and makes possible the 1D laser cooling of Ps in presence of magnetic field.

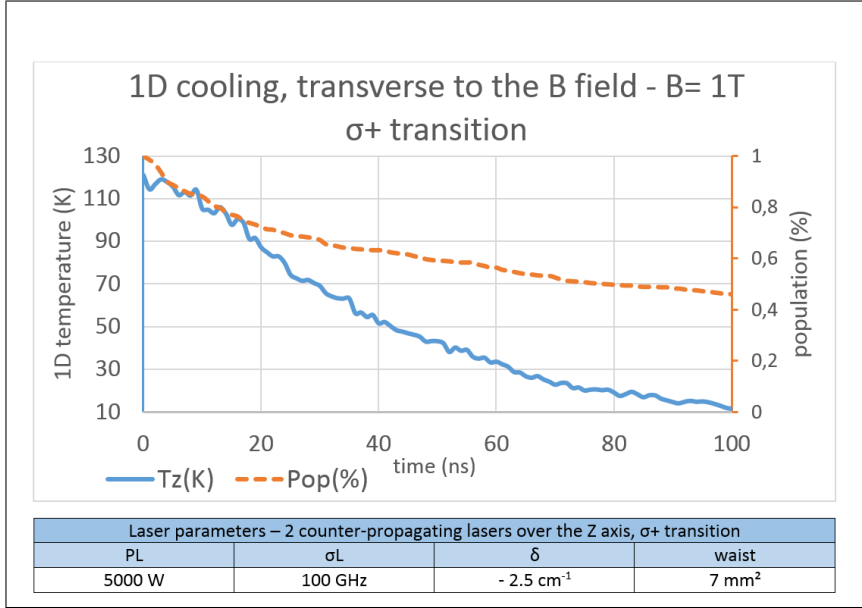


Figure 8.11: 1D laser cooling of a Ps cloud, in presence of a 1T magnetic field, cycling on only pure states. The polarization of the 2 counter-propagating lasers has been chosen to only excite σ_+ transitions. The blue curve presents the temperature evolution over time, the dashed red curve shows the population evolution. After a laser interaction of 100 ns, about 50% of the Ps are still alive. This optical excitation scheme limits the decay toward singlet ground states and makes possible the 1D laser cooling of Ps in presence of magnetic field.

However, we can state that the remaining number of Ps in the case of the σ_+ excitations cycling scheme is still lower than for the 1D laser cooling in absence of magnetic field, as seen in Sec. 8.2.1. This is explained by the initialization of the internal states of the Ps cloud generated for the simulations. I consider that the Ps formed by the target convertor and emitted in vacuum are distributed over the pure triplet states, $m=-1,1$, and the mixed state $|2\rangle$ $m=0$ that has the longer lifetime ($\tau_{|2\rangle} = 7$ ns). We consider that

the $|4\rangle$ mixed state $m=0$, with an annihilation lifetime of 127 ns can't reach the surface to be emitted. As a consequence in the simulations, only a third of the atoms (those generated in the $m = +1$ triplet ground state) are directly excited in a closed optical cycle where they can't decay toward the fast annihilation ground state $|4\rangle$. For the other atoms, the optical pumping process requires several excitations and decays before populating fully the pure-states ; during the process, the annihilation rate is still a bit enhanced.

8.2.3 What is the effect of a 1D laser cooling on the velocities of the other directions.

So far, we have discussed about the possibility to laser cool the Ps cloud in 1D along the transverse velocity, i.e. along the z axis (quantized axis), see Fig. 8.8 b). However, one could remark that the cooling over one direction comes from the spontaneous emission of a photon, scattered randomly in 3D.

As reminded in Fig. 8.8 b), we want to maximize the overlap between the trapped antiprotons and the Ps cloud, thus the heat mechanism due to the cooling along the z axis has to be negligible along the x -axis. This point is important to be verified.

Using the simulations described above, I then studied the behavior of the 1D transverse temperature along x , with and without laser cooling along the z axis. In presence of laser cooling, it appears that for a Ps cloud initially at 100 K, the increase of $T_{1D,x}$ is not appreciable. Indeed, the velocity increase in x seems to be smoothed by the temperature fluctuations we observe, due to the annihilation of the Ps atoms: the atoms which decay to the "dead" level that simulates the annihilation process are removed from the atom data set used to calculate the 1D temperature. At the end, the random process of the simulated annihilation leads to small fluctuations in the temperature of the Ps cloud, that covers the heating from the photon scattering. In the contrary, the laser cooling along the z axis is efficient enough to bring the $T_{1D,z}$ down to 5-10 K in 100 ns.

8.2.4 What is the effect on the Ps positions of the 1D cooling along the z axis ?

All the studies mentioned above are motivated because we want to maximize the number of Ps atoms reaching the antiproton plasma inside the production trap (in a 1T magnetic field environment). This aims to increase

the efficiency of the formation of antihydrogen via charge-exchange process. The idea of laser cooling the transverse temperature along the z -axis is then to increase the solid angle of the Ps cloud with the antiprotons.

In this last section, I looked into the effect of the 1D laser cooling on the Ps positions. More specifically, I aimed to specified the number of Ps atoms that stay "focused" in a cloud of less then 5 mm size during their travel toward the antiprotons (propagation along the y axis, see Fig. 8.8 b)). I counted then the numbers of Ps inside $|x, z| < 5$ mm with and without laser cooling, and probed for different times. The results are presented in Fig. 8.12. I chose a size of 5 mm that would correspond to a typical length of the antiproton plasma, in the z direction (axial confinement).

	No laser	1D cooling along z
propagation	$ z < 5\text{mm}$	$ z < 5\text{mm}$
t= 0 ns	100 %	100%
t= 100 ns	23%	31%
t=300 ns	2%	5%

	No laser	1D cooling along y
propagation	$ x < 5\text{mm}$	$ x < 5\text{mm}$
t= 0 ns	100%	100%
t= 100 ns	21%	25%
t=300 ns	2%	2%

Figure 8.12: Table which gives the number of Ps atoms that stay inside a cloud of $|x, z| < 5$ mm size, with or without laser interaction. The upper table presents the number of Ps for the transverse z direction, where the 1D cooling is applied. The lower table gives the number of Ps for the other transverse direction x . In these simulations, a cloud of 2000 Ps is emitted toward the antiproton plasma at a temperature of 100 K, along the y propagation axis. The annihilation of the o-Ps in vacuum is taken into account.

In the tables of Fig. 8.12, we can see that the number of Ps inside $|x| < 5$ mm doesn't change much during the cooling over the z direction, in comparison to the case without laser. This is a confirmation that the heating due to the scattered photon is negligible, as mentioned in Sec. 8.2.3 just above.

However, in the cooled direction z , it appears that only a factor 2 in the number of Ps that stayed inside $|z| < 5$ mm can be won. This limited improvement is mostly due to the annihilation process: the laser cooling takes time, in the order of the o-Ps lifetime (142 ns). During the laser cooling, most of the Ps annihilate and don't reach the antiproton plasma. This problem was initially thought to be resolved by exciting the o-Ps toward the Rydberg states $n=15-20$, that is impossible during the laser cooling.

If we only consider the impact of the collimation of the 1D laser cooling on the Ps cloud, this analysis seems to indicate that the 1D cooling over the z -axis is not preferable compared to the solution of a direct excitation of the Ps cloud to Rydberg state.

8.3 Conclusion and prospective

We have seen in this chapter that laser cooling of Ps should be realizable for reasonable short interaction times, and for both 0 T and 1 T magnetic field environments. For instance, if we consider a Ps cloud with an initial temperature of 1000 K, an efficient cooling would be given by lasers set at 5000 W, detuned around 300 GHz ($\sim 10 \text{ cm}^{-1}$) for a bandwidth of 200 GHz ; in 100 ns the 1D and 3D temperatures can be expected to have decreased around 500 K.

The presence of magnetic field limits the possibility of a 3D laser cooling because of the Zeeman mixing of singlet and triplet states. Indeed, the selection of pure-states cycles we just presented is only possible for lasers aligned with the magnetic axis direction. Thus, the laser cooling of Ps in presence of magnetic field appears to be feasible only in 1D, and parallel to the B field. We can remark the laser cooling scheme in 1T is not efficient in 3D. Indeed, the lasers need to be parallel to the quantification axis to be able to only excite on the pure states ($\sigma\pm$ transitions), in order to avoid to enhance the annihilation of the cloud by exciting mixed triplet-singlet states.

A proof of principle of this laser cooling will be important for us, that's why I spent a great part of my thesis to develop a laser system that could

achieve this cooling scheme. The next chapter gives more details about this laser system and its current status.

To conclude these studies, I would like to mention here another idea to improve the laser cooling of Ps. First studied by [53], the challenge was to try to present a solution to avoid to heat the slow atoms when the lasers are broad to excite the fast atoms one. The idea was to find a way without using the frequency sweep trick that appears to be experimental complex for such a wide range of frequencies. We can note that for all the simulations presented in this chapter, we used a Gaussian spectral shape for the lasers. Because of the symmetry of the spectrum shape, if the lasers are too broad, the slow atoms can be at resonance with both lasers and then absorb photons from both lasers, that limit the cooling effect and can even lead to some heating.

Nevertheless, the spectrum of the laser could be shaped to generate a better cooling, by cutting the symmetry of the spectrum. For instance, if we consider a top-hat spectrum laser, we could model it to excite a wide range of velocities from high velocities ($\approx 300 \text{ km.s}^{-1} \approx 3v_0$) to medium velocity ranges ($\approx 1/2v_0$), and cut its spectrum at the low frequencies to avoid to excite the low velocities.

Shaping the frequency spectrum of the cooling laser, the group of Liang and Dermer found a sub-doppler temperature limit for their cooling scheme [53]. The shaping of the laser spectrum would open paths to new studies and simulations. This refinement would be important in order to access to temperature below few Kelvin.

Anyhow, in AEgIS, we are interested in collimating the Ps cloud to increase the number of Ps that reach the antiprotons trapped plasma and for the moment, we don't aim to cool the Ps below the Doppler limit. A diminution of the transverse temperature of hundreds of Kelvin should be enough to provide a visible impact on the divergence of the incoming Ps cloud, but the annihilation process enter in competition and reduces the numbers of Ps finally reaching the antiprotons. The excitation to Rydberg state of the Ps cloud, directly after the emission in order to block the annihilation could appear to be preferable.

However, in order to open the discussion, I would like to point out that the cooling of the Ps has a huge impact of the cross-section of charge-exchange process. As calculated in [17] and shown in Fig. 8.13 b), the cross section increases drastically when the Ps velocity (center of mass) decreases. At 1K, for the o-Ps $n=16$, the cross section is about 10^{-13} cm^2 , instead of few

10^{-15} cm^2 for 100 K (pink arrows) ! This will be in favor of performing the laser cooling of Ps along the y direction (reduction of the Ps center of mass velocity), as illustrated in Fig. 8.13 a). In this schematic, the pink arrows indicate the two counter-propagating lasers that perform the 1D laser cooling at 1T along z . One idea could be to slightly tilt the laser directions (red arrows) to couple the cooling to z and y , and reduce the CM velocity of the o-Ps. .

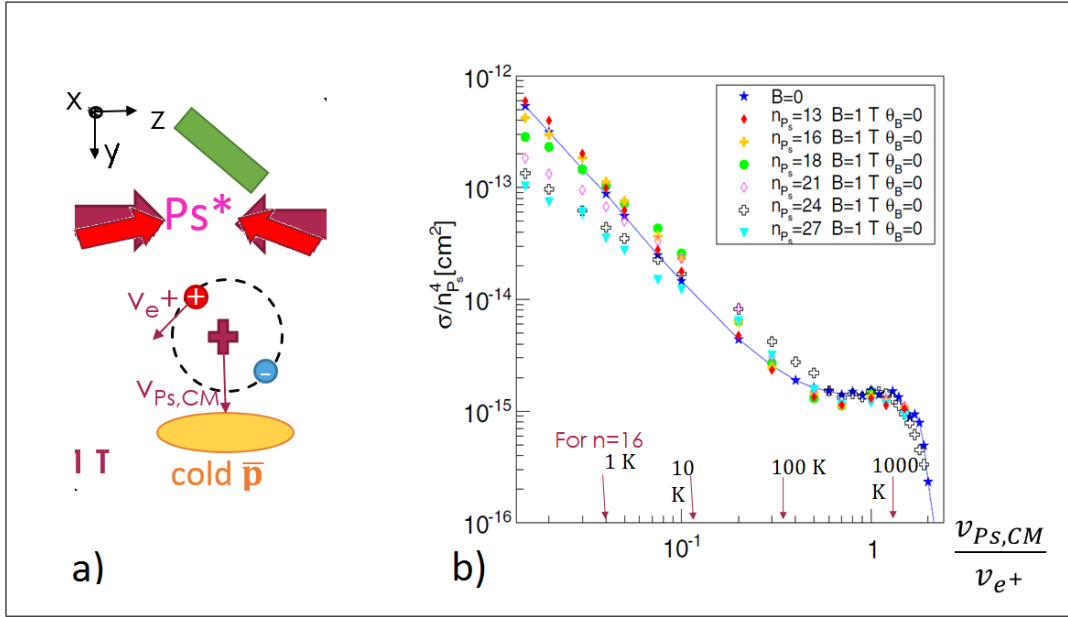


Figure 8.13: a) A drawing presenting the 1D laser cooling situation inside the production trap (1T field). The center of mass (CM) velocity of the o-Ps $v_{CM,Ps}$ and the positron velocity v_{e^+} are represented. The pink arrows indicate the two z counter-propagating lasers performing the cooling ; the red ones are a suggestion to couple the cooling of the transverse z direction with the direction of propagation y , in order to reduce the Ps CM velocity. b) The cross-section of the charge exchange process, for different n -states of the o-Ps, is plotted in function of the relative velocity of the CM and the positron orbital velocity, for $B=0$ T and $B=1$ T. For the o-Ps($n=16$), the corresponding ratio $\frac{v_{CM,Ps}}{v_{e^+}}$ is indicated by the pink arrows, for several equivalent temperatures $T = \frac{m_{Ps} \times v_{CM,Ps}^2}{kB}$ of 1000 K, 100 K, 10 K and 1 K. The cross-section increases when the velocity of the CM decreases.

This would require more developed studies to quantify any potential gain: in one hand, the laser cooling down to 1K of Ps atom increases by a fact 100 the cross section of the charge-exchange process. In the other hand, during the laser cooling, the annihilation of the o-Ps decreases the number of Ps reaching the antiprotons to few percents (in 300 ns). The quenching effect should obviously not be forgotten too. The question remains opened to find the best compromise of the two situations.

Chapter 9

The Orsay laser system for the Doppler laser cooling of Ps

Started with my master thesis, and continued during my Ph.D, I was in charge of installing a second laser system of AEgIS, to perform the excitation of Ps toward Rydberg states using the optical path: $n=1 \leftrightarrow n=2 \leftrightarrow n=\text{Rydberg}$. Compared to the Milano laser system that uses the optical path $n = 1 \leftrightarrow n = 3 \leftrightarrow n = \text{Rydberg}$, and has been conceived to be broadband enough to cover the huge Zeeman splitting induced in the 1 T field environment of the AEgIS trap (see Chap. 4 Sec. 4.3), the idea of this new system was to develop a narrow-band laser system to perform spectroscopy on Ps and possibly a laser cooling, in absence of magnetic field inside the test chamber. Indeed, using the transition $n=1 \leftrightarrow n=2$ will allow us to perform laser cooling of Ps.

This new laser system is referred as the Orsay-laser system, and we plan to use it to carry out the first trials of Ps laser cooling on the transition $n = 1 \leftrightarrow n = 2$ beginning of 2017. In this chapter, I will briefly describe the system and how it has been incorporated in the AEgIS zone (Sec. 9.1); before explaining the main limitations of this laser for the Doppler cooling and the ideas we studied to solve it in Sec. 9.2.

9.1 Description of the current system

Until January 2016, the Orsay laser system was composed of two dye-lasers, pumped with the Ekspla Nd-YAG pump common to the Milano system (see Sec. 4.3). In absence of any electro-magnetic field, a 243.023 nm beam is needed to perform the $n=1 \leftrightarrow n=2$ transition of Ps. In addition,

we also have developed a tunable red laser with wavelengths from 736 nm to 745 nm to excite Ps from the first excited state $n=2$ to Rydberg ($n= 15 - 20$), and then Rydberg spectroscopy in absence of magnetic field in the test chamber.

Because of the restrictive space of the AEgIS zone, the second laser system has to be added in a second floor, above the Milano-laser table. The Fig. 9.1 shows a scheme of the so-called laser hut in AEgIS, that is a 4 meter squared space, placed in the back of the trap magnets, and delimited by two black curtains. When working on the lasers, the curtains are closed and prevent the access of the back of our zone. Part of my work was to supervise the installation of this second floor and a removable walking platform that allows the laser user to work at 2-m height. I also spent time to comply the quite restrictive safety requirements of CERN to get the authorization to work with class 4 lasers on two floors (with periscopes to connect the two laser systems).

Working on the laser systems in AEgIS is complex mainly because of the really confined space and the necessity to work at height on a platform that isn't specially recommended for lasers works. Besides, the vibrations due to other workers in the zone make the optimization of the laser quite challenging - our laser systems are not isolated in a laser hut apart from the experimental zone, as it is the case for the other experiments in the AD hall. No air temperature control is present in the AEgIS laser hut, that is also critical for the stability of the systems. Finally, because the access to the back of our experimental zone can only be done by crossing the laser hut or climbing over the two vessels of the trap magnets, the works on the lasers have to be strictly planned in order not to disturb the other workers.

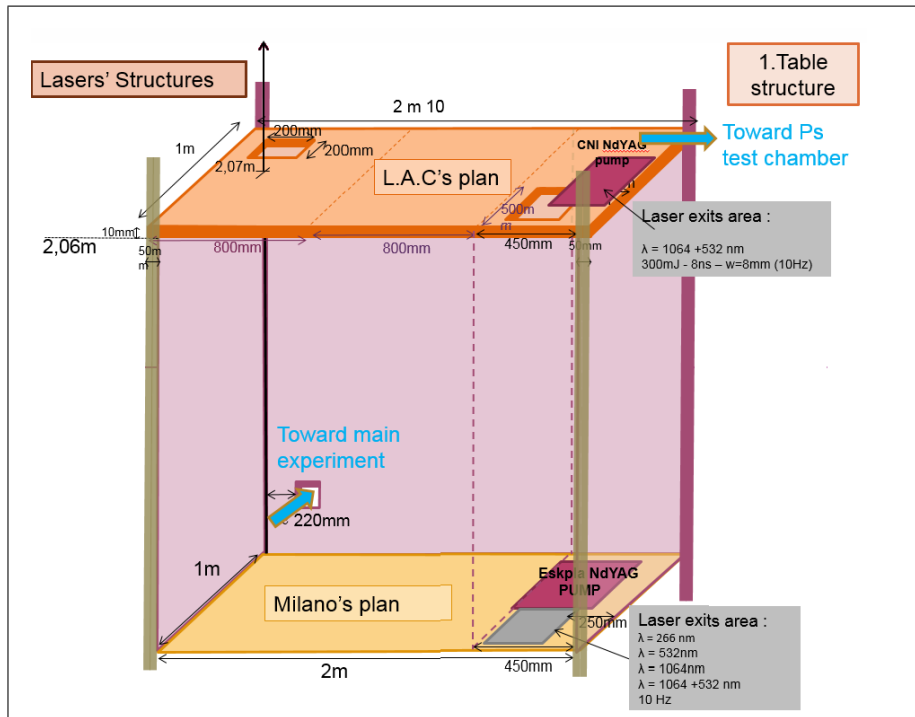


Figure 9.1: Scheme of the AEGIS laser hut. The two laser-systems are divided in two floors. The Milano system is on the first floor, and the Orsay-laser system is placed above, at 2 m altitude. In order to work on the second table, a removable platform has been built to allow the laser user to stand up at the proper height.

Since February 2016, a new Nd-YAG pump from the CNI company has been ordered by my laboratory and installed in the upper laser table, as indicated in Fig. 9.1. More powerful than the Ekspla one, it delivers 250 mJ of 532 nm, in an 8-ns pulse (top-hat), and this allows the two laser systems to be independently pumped and used in parallel.

The Orsay-laser system is based on dye-laser technologies. Fig. 9.2 a) shows the principle of our dye-laser cavity. The dye powder is diluted into some solvents (ethanol and methanol) and circulates into a transparent cell, and plays the role of the active medium of the laser. Despite the inconvenient of using flammable toxic products¹⁴, using dye-laser has some benefits:

¹⁴During my thesis, I took care of the safety issues regarding the chemicals used in AEGIS. Dye-powders are registered as toxic, and diluted in ethanol, flammable. Assur-

- As the active medium of the laser, an excited (pumped) dye typically fluoresces over a large spectrum, with a bandwidth of about 20-30 nm. By introducing a grating into the laser cavity, this huge fluorescence spectrum is diffracted over a large cone of angles. The edge mirror of the cavity reflects a fraction of the wavelengths diffracted by the grating, and thus selects only one wavelength that circulates into the cavity and generates the laser beam. The dye-laser can be tuned over the width of the fluorescence spectrum (about 20-30 nm) by adjusting the angle of reflection of the edge mirror that selects the wavelength matching the laser cavity.
- This kind of laser setup tends to generate quite narrow-band lasers. When the fluorescence spot covers N lines of grating, the bandwidth $\Delta\nu$ of the laser at a central frequency ν is given by: $\frac{\Delta\nu}{\nu} \approx \frac{1}{N}$. In our case, we use a 1 cm long grating with 2400 lines/mm, meaning a selection in frequency of the fluorescence spectrum of the excited dye medium of $F = \frac{\Delta\nu_{486\text{ nm}}}{\nu} \approx 4 \cdot 10^{-5}$. In other words, the laser bandwidth is then $\delta\nu = \nu \times F \approx 25$ GHz.

ing the safety of the uses of such products at CERN, as well as the storage and stock-management were part of my work.

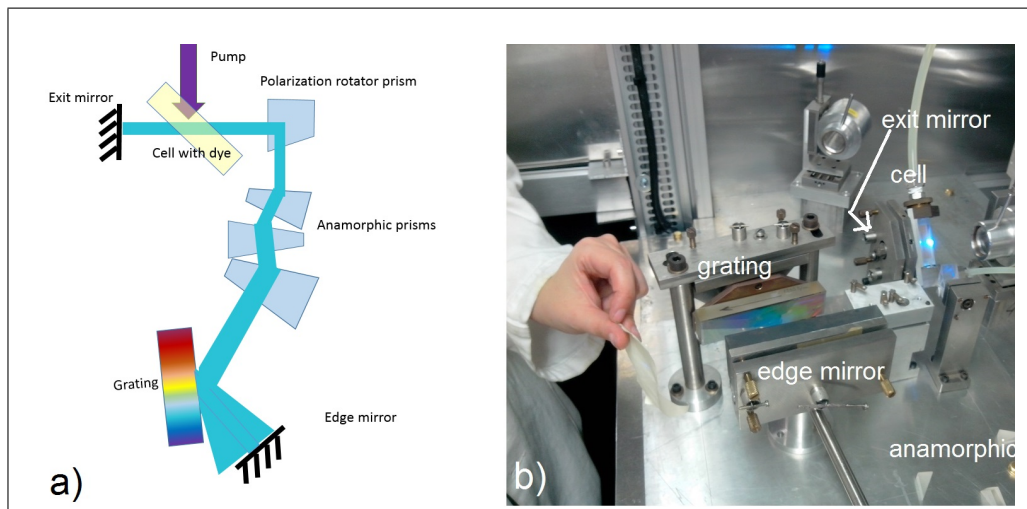


Figure 9.2: Dye laser cavity - schematic and picture. a) the schematic of the cavity of a dye-laser. The grating allows to generate a narrow-band laser, and adjusting the angle of reflexion of the edge mirror allows to select the wavelength. b) Picture of the home-made dye laser cavity, that was used to produce the red laser for the transition $n=2 \leftrightarrow n = \text{Rydberg}$.

The Fig. 9.3 a) shows a schematic of the Orsay table, where the two dye-lasers were first installed and pumped by the Ekspla NdYAG source until beginning of 2016 - Fig. b): the second laser has been removed to free some space, and the CNI YAG pumped has been installed. The BBO crystals are used to generate the third harmonic of the YAG (355 nm) and to double the 486 nm generated by the Continuum dye-laser, and produce the 243 nm beam.

9.1.1 The red-laser beam

To generate the 740-nm beam, we use the oxazyn-dye diluted in ethanol, pumped with the second harmonic of YAG (532 nm). This laser is a home-made dye laser, from the Laboratoire Aimé Cotton that hadn't been used for years, and I had to reinstall it from scratch, piece by piece at CERN. The Fig. 9.2 is a picture of the cavity of this home-made dye laser. We can see the cell where the dye is circulating, the edge-mirror (the exit mirror is hidden), the anamorphic prisms that expand the fluorescence spot to cover all the grating surface. With about 40 mJ of 532 nm, about 3 mJ of red beam could be produced. This laser is installed on an aluminum plate in order to be able to easily remove and reinstall it. It has been removed beginning of 2016 to free space.

9.1.2 The 243-nm beam

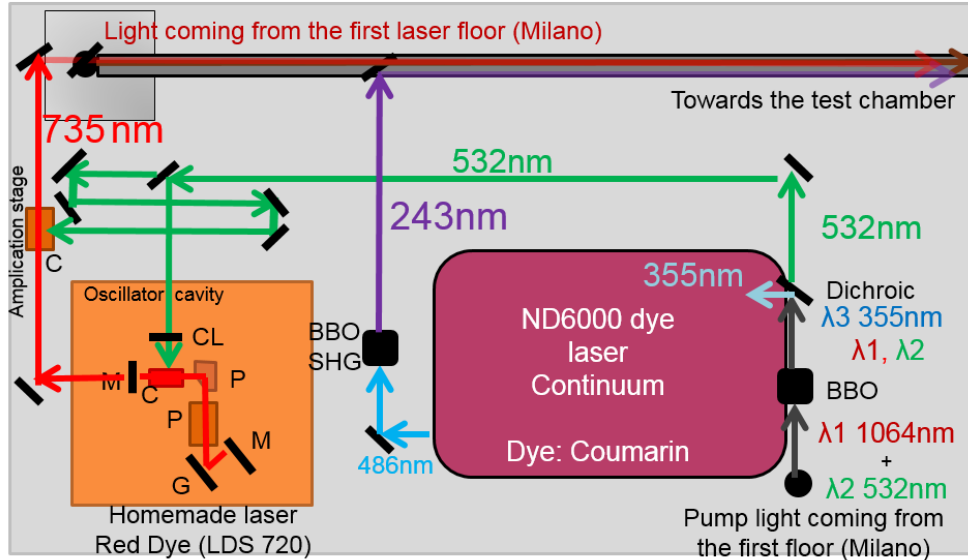
In order to generate the 243-nm UV beam, we first generate a 486-nm laser from a Coumarin-dye laser, pumped by the third harmonic of the pump YAG (355-nm beam). Then, the 486-nm light is frequency-doubled using a non linear BBO crystal of 5 mm × 5 mm × 5 mm size. The dye-laser setup used here is an industrial Continuum laser ND4600. With 35 mJ of pump 355 nm, up to 2.5 mJ of blue light (486 nm) is produced, and converted up to 600 μJ of 243 nm. Because its intrinsic nature of dye laser (multi-modes), the UV energy fluctuates shot by shot by about 15%.

The 243-nm beam to laser cool Ps atoms?

As explained in the previous chapters 7 and 8, we want to perform laser cooling of Ps using the 243-nm beam. The simulations tend to indicate that the UV pulse needs to last some tens of ns. Unfortunately, the two NdYAG pumps we own in AEgIS, based on Q-switched technologies, provide respectively laser pulses for the 1064 nm of 5-6 ns for the Ekspla source, and 8 ns pulses for the CNI pump.

The Ekspla pump provides quasi Gaussian pulses. The non linear process for the second harmonic generation (SHG) acts on the temporal Gaussian pulse by shortening the generated pulse as: $t_{SHG} = \frac{t_{pump}}{2}$. Then, the 243-nm beam pumped by the Ekspla pump leads to a pulse of about 2 ns (FWHM). Whereas the CNI laser delivers top-hat spectral pulses. The SHG pulse from

The second laser system's floor 2013 – January 2016



Legend:

CL: cylindrical lens
M: mirror

P: prism
G: grating

SHG: second harmonic generation
C: cell where the dye circulates

The second laser system's floor from January 2016

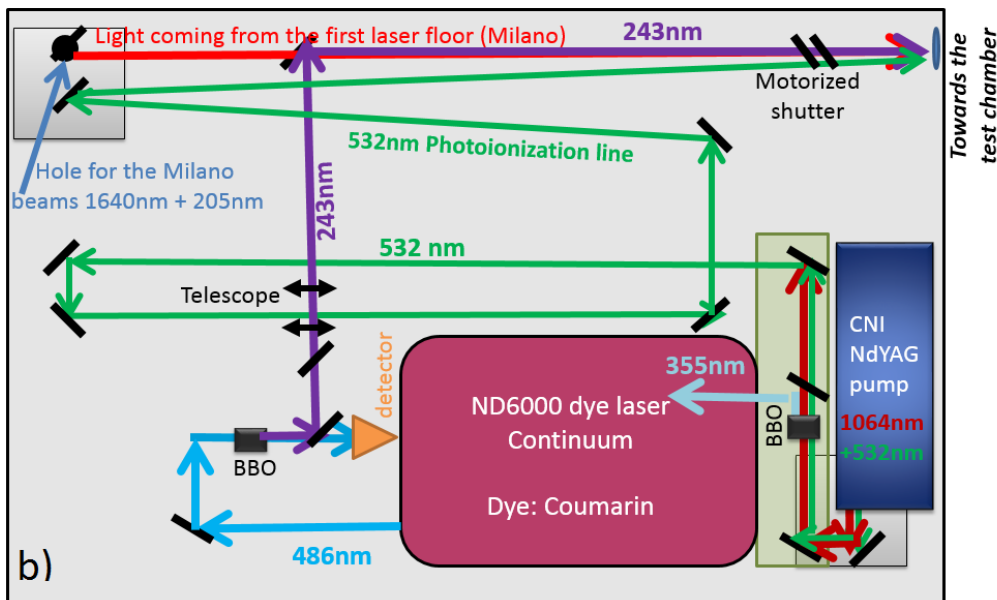


Figure 9.3: Schemes of the Orsay table, for the two different periods of time. a) until beginning of 2016, the Orsay-system was composed of two dye-lasers, that generated the wavelengths for performing the Ps Rydberg excitation using the transitions $n=1 \leftrightarrow n=2 \leftrightarrow n=\text{Rydberg}$. b) Since February 2016, a new NdYAG pump from the CNI company has been installed, and the home-made red dye laser has been removed to free some space.

a top-hat spectral profile keep the same pulse width. Thus, the CNI laser leads to a 243 nm beam of rather 8 ns (FWHM). This is still too short to see any measurable laser cooling effect on Ps. The UV pulse needs then to be lengthened. That's why the red dye-laser has been removed to be able to carry-out some trials to stretch the UV pulse. I will explain now different ideas we studied to lengthen the 243-nm laser.

9.2 Stretching the UV pulse

We first studied the possibility to buy a commercial laser that would match the requirements of generating a long pulse (≥ 100 ns), high power and tunable bandwidth at 243 nm. We found that the commercial solution based on the Alexandrite ($\text{Cr}^{3+}:\text{BeAl}_2\text{O}_4$) crystal from LightAge company was very promising. Its main characteristics are:

- Tunable outputs:
 - 720-735 nm, can be extended to 720-800 nm, for the fundamental harmonic.
 - higher harmonics possibly tunable too: 360-400 nm, 240-270 nm, 190-200 nm
- A long pulse duration: the nominal Q-switched pulse duration is 100 ns and can varied from below 30 ns to 200 ns.
- An adjustable spectral bandwidth. The spectral linewidth is <30 MHz for the fundamental and can be modified from Fourier-Transform limited pulse to very large bandwidth (>100 GHz) based on different CW laser seeders inside the cavity.
- Nice stability of the laser frequency: output wavelength stability of <300 MHz/day. Frequency chirp corrected to be less than 50 MHz.
- And finally, good energy generated. We can expect a pulse of an energy greater or equal to 1 mJ for the 243-265 nm beam.

This laser will match perfectly the requirements for an efficient laser cooling of the Ps cloud, for the "modest" sum of ≈ 200 k€.

Among the other possible choices we looked for, we could mention:

- Using the Cr:LiSAF based laser as developed in [64]. But this would lead to intense laser development with no guarantee to reach a large laser power.

- Using a long (>100 ns) pump (like the Hawk-HP from quantronix lasers or the Mesa-355-40M from Continuum company or the Evolution 527 nm from Coherent Inc) to pump the Orsay laser system to produce the 243 nm. This may lead to some issues during the pumping of the dye (thermal effect). Furthermore the dye fluorescence is a non linear process and needs intense pump to be efficient. This technique could also be limited because of a weak laser power generated.
- Considering a continuous-wave (cw) pulse-amplified laser, such as the one developed in the ASACUSA experiment at CERN [65]. In a similar way, the injection seeded pulsed (Ti:Sa) lasers produce 729 nm beam that can then be tripled to form 243 nm. In a very recent publication studying the cooling of Positronium for Bose-Einstein Condensation (BEC) [56], they suggested such a complex laser with frequency tripling with an injection seeded pulsed Ti:Sa, and a sophisticated spectral modification by Electro-Optics Modulator. Here again this would lead to a non-negligible laser development for us.

In absence of any funding, we tried to find cheap solutions. The obvious one would be to lengthen the pulse generated by the dye-laser system (Orsay system) currently installed in AEgIS. We studied mainly two setups:

- dividing physically the mother pulse into several secondary pulses. Each secondary pulse travels different paths, with the length adapted to cause additional temporal delay. At the end, the secondary pulses are recombined with their time delays into a single final pulse. To do so, we studied the possibility of using fibers.
- entering the mother pulse into a loss-cavity. One of the mirror of the cavity has a low transmission percentage (typically 10 to 40 % transmission), for each turn into the cavity, a secondary pulse is emitted. We studied mainly two setups for this loss-cavity, also called stretching cavity in literature [66].

9.2.1 The fiber setup

The concept of this fiber setup is illustrated in Fig. 9.4 a). First, we had to contact and discuss with companies to determine which kind of fiber divider is technically realizable for UV beam, in order to minimize the losses during the injection. I investigated different combinations to divide the pulse into N secondary pulses. Fig. 9.4 b) shows the fiber divider we used in AEgIS to carry out the first trials - this divider is not UV-resistant, and can't be use

as a long-term solution.

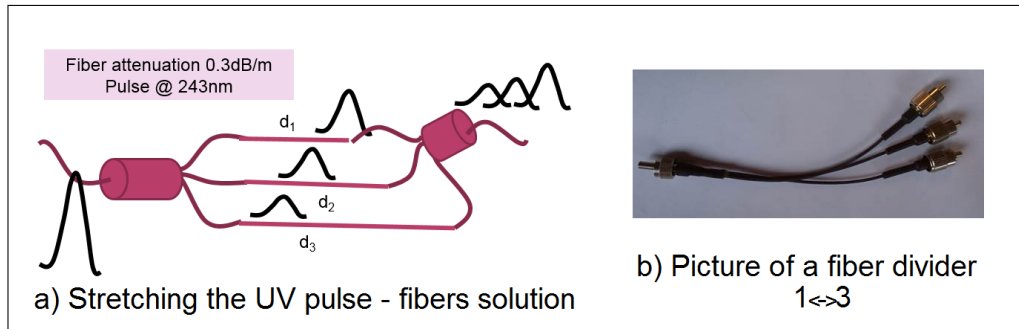


Figure 9.4: The fibers solution to stretch the UV pulse. a) the schematic of the principle is drawn here. The mother pulse is divided into 3 secondary pulses. Each sister-pulse travels into one of the 3 paths with different lengths ($d_1 < d_2 < d_3$), leading to different time delays for each path. The UV beam is absorbed by the fused-silica solarization resistant fibers with an attenuation factor of 0.3dB/m. This implies that the secondary pulses are more and more attenuated as they propagate in longer lengths of fiber. b) the picture of a fiber divider 1 toward 3 that we have in AEGIS, not adapted for UV. The coupling is not optimized for this device, and the losses are about 50 % for visible light. Since these dividers haven't been conceived to be UV-resistant and minimize the UV absorption, the losses for the 243nm were considerable: only few percents of the incoming pulse exited at the end of each secondary fiber. We used two of these dividers to obtain the results shown in Fig. 9.5 a).

The Fig. 9.6 gives a table of three different configurations studied, with the combined pulse results: shape, temporal stretching and final total energy. The losses come from two sources: the geometrical overlap between the mother fiber with a big core ($600 \mu\text{J}$ for the simulations) toward the N secondary fibers of varying core size, and the attenuation during the pulse propagation into the fibers. Indeed, the UV beam at 243 nm is absorbed by the fused-silica solarization resistant fibers with an attenuation factor of 0.3dB/m. The effect is not negligible, specially for the long delayed secondary pulses that propagate along a great path into the fiber. This attenuation explains the progressive decreases of the intensity of secondary pulses.

According to the simulations, it appears that the division of 1 pulse into 5 secondary pulses is a good compromise to optimize the areas overlaps of the fibers. For the mother fiber of a core of $600\mu\text{m}$, the division into 5 fibers of $200\mu\text{m}$ is technically realizable, and will induce geometrical losses of only 30 %.

For an initial pulse at 243 nm of $I_0 = 600\mu\text{J}$ and a pulse of $\text{FWHM} = 8\text{ ns}$, we obtain a combined pulse of $260\mu\text{J}$ in 90 ns duration, meaning a power of 2900 W or an intensity of $5800\text{ W/cm}^2 \approx I_{sat,L,100\text{ GHz}}$ for a waist radius of 4 mm . This configuration seems adequate for the cooling purpose.

However, we are here limited by the fiber technology. We contacted several companies to ask the possibilities of conceiving such dividers, that could hold the $600\mu\text{J}$ of UV pulsed beam without melting. We are still in discussion with the IDIL French company to solve the melting issue. Using the two fibers dividers we had at CERN (shown in Fig. 9.4 b)), in 2015, we did a first test to lengthen the pulse, as presented in Fig. 9.5. At that time, the laser pump used was the NdYAG Ekspla pump, with an initial pulse duration of about $6\text{-}8\text{ ns}$, that produced an UV pulse of about 2 ns . The fiber lengths of 3 m , 5 m and 10 m to delay the secondary pulses were not adapted to delay the pulses in order to make them overlap. The refractive index of the fiber core for the UV is about $n_{fiber}=1.45$, the propagation of the light over 1 m leads then to a time delay of: $\Delta t = 1\text{ m} \frac{1.45}{c} \approx 5\text{ ns}$ for the pulse.

With the new CNI NdYAG pump, the 243 nm beam has a pulse length of about 8 ns , the delays induce by 3 m , 5 m and 10 m are respectively 15 ns , 25 ns and 50 ns . In the Fig. 9.5 a), the secondary pulses are separated in time since their mother pulse was 2 ns (FWHM) and the fibers too long for such short pulses; whereas the sisters pulses coming from the 8 ns mother pulse generated by the CNI pump should overlap using the same fibers (3 m , 5 m and 10 m).

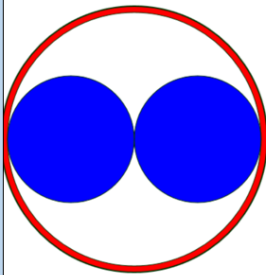
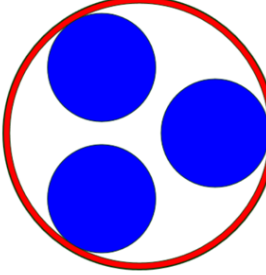
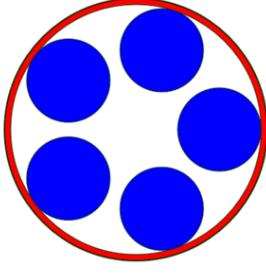
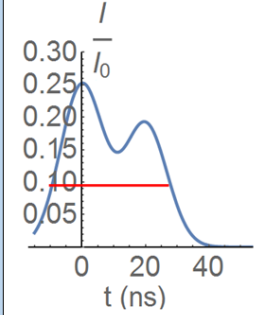
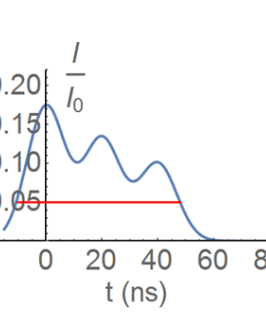
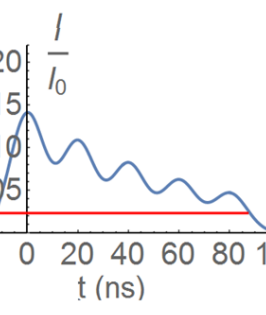
Initial mother pulse: Gaussian pulse of maximum energy I_0 and FWHM = 8 ns			
	Divider 1 ↔ 2	Divider 1 ↔ 3	Divider 1 ↔ 5
mother fibre core	600 μm	600 μm	600 μm
Sister fibre core	300 μm	250 μm	200 μm
Occupied area			
Geometrical Losses (overlaps)	50 %	48 %	30 %
Stretching			
Attenuation per UV fibre	0.3 dB/m		
Fibre lengths	2 fibers of 1 cm and 4 m lengths	3 fibers of 1cm, 4 m, and 8 m lengths	5 fibers of 1 cm, 4 m, 8 m, 12 m, and 16 m lengths
Final pulse energy	0.43 I_0	0.40 I_0	0.43 I_0
Final pulse duration (*)	37 ns	58 ns	89 ns
(*) (half of the maximum of the last peak)			

Figure 9.6: Fiber divider solutions: Simulations results for 3 different configurations. The initial UV pulse has a FWHM of 8 ns. The solution using the dividers 1 ↔ 5 seems to be a good configuration, where the geometrical overlap is maximized and the initial pulse of 8 ns is lengthened to about 90 ns with only 60 % total losses. These losses are due both to the attenuation into the fibers and the geometrical overlaps of the mother fiber's core with the secondary fibers' core. For an initial pulse of $I_0 = 600 \mu\text{m}$, we obtain a combined pulse of 260 μJ in 90 ns duration, meaning a power of 2900 W or an intensity of $5800 \text{ W}/\text{cm}^2 \approx I_{\text{sat},L,100 \text{ GHz}}$ for a radius waist of 4 mm.

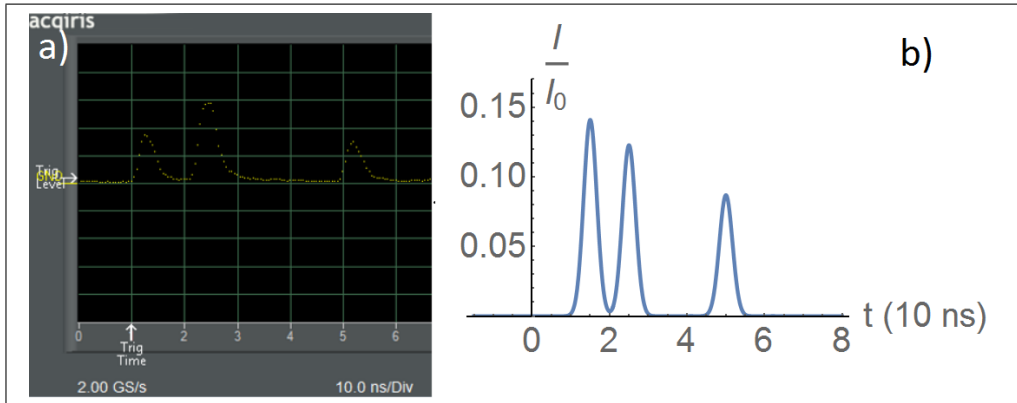


Figure 9.5: Test on the fibers solution to lengthen the UV pulse. The initial pulse duration is about 2 ns. a) The secondary pulses recorded on an oscilloscope card Agilent 1 GHz. b) the simulation expected result for the lengths of the fibers (3 m, 5 m and 10 m). The fibers lengths have to be adapted to overlap the pulses, and new fiber dividers $1 \leftrightarrow 3$ or $1 \leftrightarrow 5$ have to be purchased since the ones used that are not UV resistant. The simulations are made considering that the coupling from the mother fiber into the 3 sister fibers is the same for each sister fiber. The attenuation of the peaks in the simulation is only due to the absorption into the fibers. However, the experimental result in a) shows experimentally that the coupling is not equal for each sister fiber, that's why the second pulse is higher than the first one.

9.2.2 Loss cavity using beam splitter

In parallel to the fibers solution, we studied then the loss cavity setup, also referred as the "stretching cavity". In Fig. 9.7 is presented the typical schematic of a such cavity.¹⁵

¹⁵We only studied squared-shape cavity instead of triangle-shape or other kind of setups (see [66]) since we want to limit the reflectivity losses of the commercial UV mirrors that are typically optimized for a 45° reflexion.

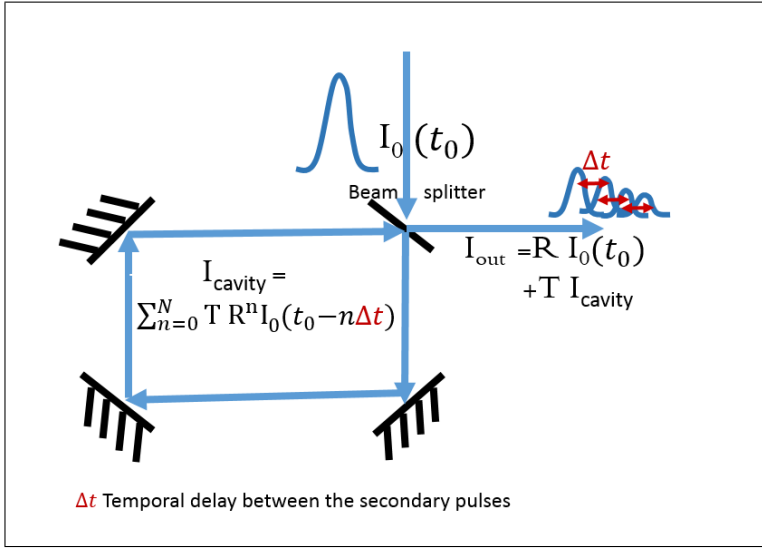


Figure 9.7: Schematic of the loss cavity setup. The incoming beam I_0 enters into the loss cavity through the beam splitter. Partially reflected ($R\%$) and transmitted ($T\%$), the inner-cavity beam undergoes N turns before leaving completely the cavity. At each turn $n \leq N$, a secondary pulse is emitted. The final pulse formula is given by $I_{out}(t) = R I_0(t) + \sum_{0 \leq n \leq N} T^2 R^n I_0(t_0 - n \Delta t)$. By adjusting the length of the cavity, we can adjust the delay Δt between each secondary pulse emitted.

The optimization of this setup was then to determine the proper ratio reflectivity over transmission (R/T) to generate secondary pulses of the same order of magnitude. Fig. 9.8 shows different configurations for the transmission and reflection parameters of the beam splitter. For all the different configurations, the number of secondary pulses with similar intensity appears to be limited. There is a simple reason for this: in order to have a great number of secondary pulses, most of the energy of the mother pulse has to enter into the cavity, implying R small. But then, after the first turn, the first secondary pulse emitted will be highly intense since $T = 1 - R$ is high. Then, most of the energy has left the cavity after just one turn. Coefficient such as $R \approx 35\%$ seems to be a good compromise and the mother pulse of FWHM=8 ns can be stretched up to 50 ns.

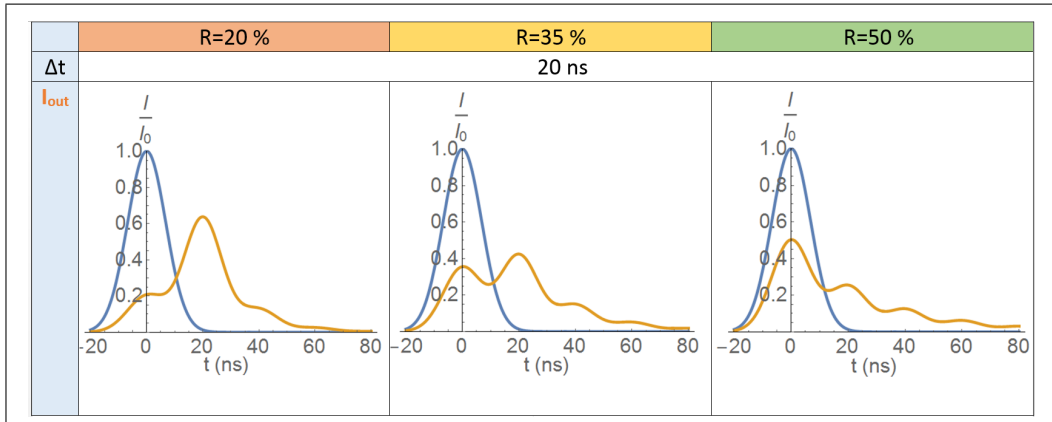


Figure 9.8: Simulations results for the loss cavity setup, varying the reflexion/transmission ratio. In blue is plotted the mother pulse, of FWHM = 8 ns, in orange is the stretched beam, made of the secondary pulses. A good compromise for having similar intensity secondary pulses seems to be $R \approx 35\%$. In this case, the pulse can be lengthened to 50 ns.

At the end, if we consider that we want to produce only secondary pulses with comparable intensity, the number of secondary pulses that can be emitted from the stretching cavity appears to be limited. Indeed, the final stretched pulse has to be intense to excite the transition $n=1 \leftrightarrow n=2$ over all its duration, otherwise the stretching will be ineffective. The solution $R=35\%$ (shown in Fig. 9.8, mid column, seems a good compromise.

However, even if the stretching capacity of this loss cavity setup appears to be smaller than for the fibers solution, this system has the great benefit of limiting the energy losses. For UV excimer mirror at 99.9 % reflectivity, the energies losses are negligible after few turns into the cavity compared to the 0.3dB/m of the fiber attenuation (see Sec. 9.2.1). Besides, according to the previous simulations of laser cooling (See Chap. 8), generating a UV pulse of 50 ns should be enough to see an effect on slow positronium atoms. This technique seems promising then.

9.2.3 The loss cavity setup using polarization cube

For studying the last stretching solution, I supervised the work of an under-graduated student Grace Kerber, from the Boston students exchange program. Grace studies at the Gustavus Adolphus College, in Minnesota,

USA, and she worked in AEGIS for 4 months between March to June 2016.

With Grace, we then looked for an idea to improve the loss-cavity setup and find a solution to increase the number of secondary pulses with comparable intensity. We thought of using polarization cube instead of a simple beam splitter. The scheme of principle is presented in Fig. 9.9. The polarization cube transmits horizontal polarized light, and reflects vertical polarization. By projecting the inner-cavity pulses into a combination of vertical and horizontal polarization, we can select the among of light transmitted at each turn. A waveplate $\lambda/2$ can be used to polarize the light into a combination of vertical ($a\%$) and horizontal ($b\%=1- a\%$) polarization.

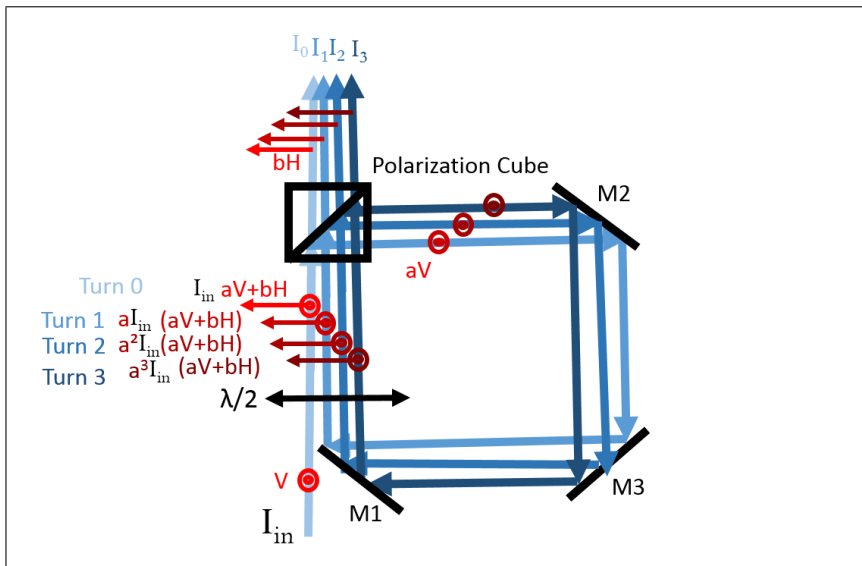


Figure 9.9: The loss-cavity setup, using a polarization cube. In order to enter the cavity, the first mirror (M1) is barely missed. A waveplate $\lambda/2$ is placed into the cavity to select the percentage of light vertically polarized a (that will be reflected in the cavity) and the percentage b of horizontally polarized light (that will be transmitted). The exiting pulse is then given by the formula: $I_{out}(t) = \sum_{n \geq 0}^N I_{in}(t - n\Delta t) \times b a^n = \sum_{n \geq 0} I_n(t)$.

In order to enter into the cavity, the first mirror (M1) has to be barely missed, and the light enters the cavity with a small angle. This angle will lead to the displacement of the pulse's after each turn, until the beam gets

out of the mirrors. This will limit the numbers of pulses we can possibly have inside the cavity.

Grace wrote a code in Matlab to simulate this setup, and tried to find the best setting parameters to maximize the number of secondary pulses. In Fig. 9.10 is presented some of the results. a) shows the paths of three rays that delimit the incoming UV pulse. In order to represent the laser beam, with a possible divergence, she chose to plot three different optical rays: the red and black lines determine the edge of the beam (contours), and the green line is the central ray. This trick allows to illustrate the divergence of the beam and the possible issues after several turns into the cavity. The beam enters with a slight angle (mirror slightly missed to let enter the mother pulse), the edge rays are tilt from the central path (case of a non collimated beam), and for each reflexion on the 45° mirrors of the cavity, they accumulate a bigger angle with respect to the normal of the mirrors. As a consequence, the direction of reflexion for the central ray and the edges rays differs a lot after a few turns inside the cavity. This creates different spot locations at the Ps target region for the each secondary pulse, as shown in Fig 9.10 a).

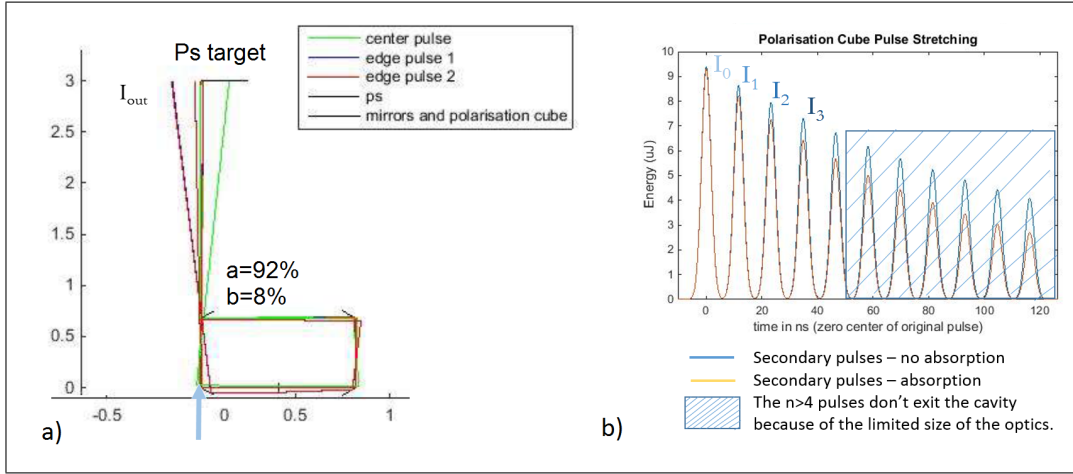


Figure 9.10: Some simulations result performed by Grace Kerber, for $a=92\%$, $b=1-a=8\%$, a cavity length of 3.2 m and an initial pulse of FWHM = 4 ns. a) shows the paths of three rays that delimit the incoming UV pulse - the red and black lines determine the edge of the beam, and the green line is the central path. This illustrates the effect of divergence on the beam after several turns into the cavity. The secondary pulse spots are spatially separated at the Ps target region. b) presents the exiting pulse $I_{out}(t) = \sum I_n(t)$. The secondary pulses I_n don't overlap temporally in purpose, to extend even more the exiting pulse.

The Fig. 9.10 b) plot presents the exiting pulse I_{out} , where the secondary pulses (I_0, I_1, I_2 , etc.) don't temporally overlap in purpose.

In order to increase even more the laser interaction time, we thought it could be interesting to perform some tests with temporally separated pulses. Indeed, the typical cooling cycle over $n=1 \leftrightarrow n=2$ transition of Ps is about $2 \times \tau_{spont} = 6.4$ ns. If the laser excitation is made of several pulses of FWHM ≈ 8 ns spaced of few ns as shown in Fig. 9.10 b), this temporal spacing will give the time for the excited atom to decay toward ground state, before getting excited by the following pulse. The cooling efficiency shouldn't be too much disturbed. The optical pumping code (c++ code) used for the simulations in Chap. 8 should be adapted a bit, before being able to make the simulations with a temporal laser pulse made of several separated pulses.

One of the main limitations of this setup still remains the possible number of turns we can expect to reach, entering with a small angle into the cavity. Some tricks can be played introducing a correcting converging lens. Grace

also implemented in her code the possibility to add one convergence lens inside the cavity to try to correct the divergence of the beam. The first results seem to indicate that the focal length of the lens should be of the order of the cavity length to be able to compensate the divergence at each turn. The best position to place the lens seems to be right before the first mirror M1. Anyhow, the preliminary simulation results of Grace indicate that it will be difficult to generate more than 4 turns, for standard optics sizes (1 inch diameter). Besides, the fact that all the secondary pulses don't spatial overlap neither could be a big limitation of this scheme. Further studies are needed to be able to select one or the other stretching solution.

9.2.4 Current situation of the Orsay laser

For now, the optimization of the Orsay system with the new source is going on, as well as the implementation of new safety requirements due to the installation of a second class 4 laser pump in the zone. Specially, this new source has to be interlocked with the existing synchronization system used for the Milano system. Moreover, the non linear crystal used to produce the second harmonic of the 1064 nm YAG has to be replaced because of some damage at the delivery, that is slowing down the laser work in the zone. We also ordered a bigger BBO crystal to generate even more the third harmonic of the YAG to pump the Coumarin laser dye. We hope to be able to generate up to 800 μ J of 243nm with an optimized system.

Olga Khalidova is a new post-doc of AEgIS who started in March 2016. Together we continue testing the different stretching solutions, to be ready for the beginning of 2017. We have ordered both the beam splitter and a UV polarization cube to try to set-up the cavity loss solution in the following months.

Chapter 10

Another way to focus of the Ps cloud? The dipolar force interaction

During my Ph.D, I also studied the possibility to collimate the Ps beam using the dipolar force. A strongly detuned and intense laser creates a local potential well that either attracts or repulses the atoms in interaction with it, depending of the detuning sign.

The dipolar force can lead to the deceleration of the particles in interaction with the created well. In 2010, Barker's group produced a stationary molecular beam thanks to the interaction with an optical lattice [67] using the dipolar interaction. Our idea was to investigate the possibility to use the dipolar force to focus the Ps cloud, using the attraction/repulsion property of this interaction.

In the following chapter, I will briefly present the dipolar force effect on the phase-space of the atom, and I will give some simulation results, before discussing the possibility of a practical realization. It is beyond the purpose of this chapter to deal with the theory to derive the dipolar force; for instance, the reader could refer to [68] for more detail.

10.1 The dipolar force interaction principle

The dipolar force derives from the laser dipolar potential U_{dip} such as:

$$\vec{F} = -\vec{\nabla}U_{dip}(\vec{r}) \quad (10.1)$$

Where the dipolar potential can be expressed - for a strong detuning and

low saturation - as $U_{dip}(\vec{r}) = \pm \frac{\hbar\Omega(\vec{r})^2}{4\delta} \propto \frac{I(\vec{r})}{\delta}$, with $\delta = \omega_L - \omega_0$ the detuning of the transition and \vec{r} the position of the particle inside the laser spot. More generally, the dipolar potential can be derived as $U_{dip} = \frac{\hbar\delta}{2} \ln(1 + s(r))$ (See [68]), where the s parameter refers to the saturation parameter defined previously in Eq. (7.7).

It appears that the more intense the laser is, the deeper the potential well is, allowing to capture fast atoms. However, the laser also need to be strongly detuned in order to avoid to absorb and scatter any photon.

In Fig. 10.1, a simple scheme of the dressed atom picture illustrates the dipolar force effects of a blue detuned laser between a transition $|f\rangle \leftrightarrow |e\rangle$ of an atom. The dipolar force acting on the atom over the transition $|f\rangle \leftrightarrow |e\rangle$ depends on the sign of the detuning. During the interaction, the states $|f\rangle$ (lower level) and $|e\rangle$ (upper level) are mixed, and form new states $|+\rangle$ and $|-\rangle$ that are usually called the dressed atom states. A red-detuned intense laser creates a potential well that attracts the atoms (low-field seeker) in the $|-\rangle$ state, and a blue-detuned laser tends to expel the atoms (high-field seeker) in the $|-\rangle$ state. The dipolar force has the opposite effect on the $|+\rangle$ state. If strongly detuned, we can identify $|f\rangle \approx |-\rangle$ and $|e\rangle \approx |+\rangle$.

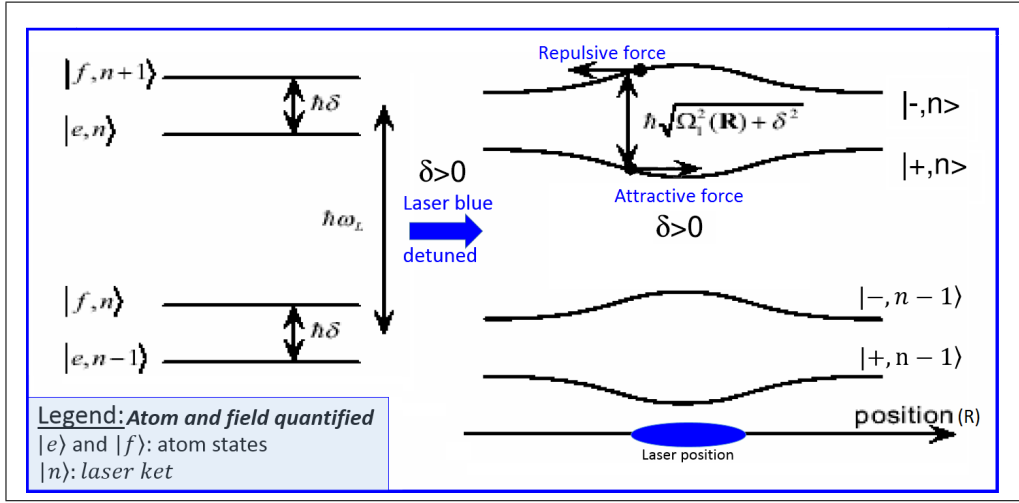


Figure 10.1: The dipolar force's effect over the transition $|f\rangle \leftrightarrow |e\rangle$ is illustrated in the dressed-atom picture, for a blue detuned laser. Both the atom and the laser field are quantized. The states $|f\rangle$ and $|e\rangle$ are mixed and form the coupled states $|+\rangle$ and $|-\rangle$, usually called the dressed-atom states. Inside the laser spot, the atoms either see an attractive potential ($|+\rangle \approx |e\rangle$) or a repulsive one ($|-\rangle \approx |f\rangle$). *Illustration taken from [68]*

As mentioned previously, our idea here is to use the dipolar force to focus the Ps cloud, using the attraction/repulsion property of this interaction. In Fig. 10.2 is sketched the interaction scheme (top figure) and the dipolar force effect on the atoms in phase-space picture (bottom figure). The dipolar effect is illustrated within the harmonic approximation (see below).

In the Fig. 10.2 top-figure, the Ps cloud is emitted at a time t_0 , freely travels during a time t_{10} , before interacting with the laser during a time t_{21} . After the laser interaction, the Ps cloud continues its free-flight during a time t_{32} . In the case of an attractive force, the laser interaction induces a rotation of the position and velocity distribution in the phase-space of the atoms, as shown in Fig. 10.2 bottom figure. By precisely tuning the interaction time, we can play on the rotation effects, and then the atom cloud can be focused in a certain point of space after the interaction and a free flight.

The studies I performed aimed to determine the ideal interaction time to focus the Ps cloud, depending on parameters such as its initial temperature

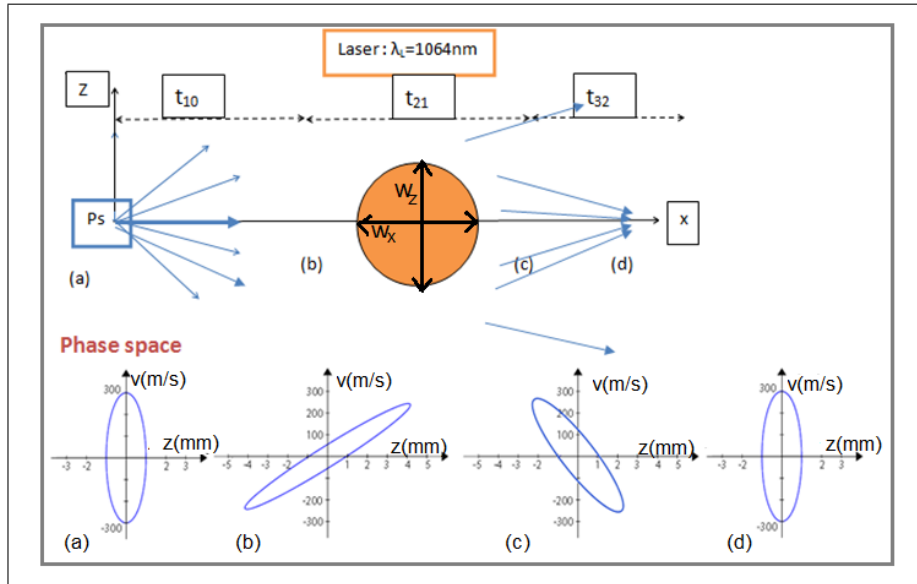


Figure 10.2: The dipolar force focusing principle. In the top image, the Ps cloud is emitted (a), where it travels during a time t_{10} free from any interaction, before interacting (b) with the laser, for a time t_{21} . Leaving the interaction region (c), the Ps cloud continues its free-flight during a time t_{32} until reaching the target point (d), where we want to focus the Ps atoms. The laser interaction with a strongly detuned and intense laser creates a potential well felt by the atoms, that induces a rotation on the phase-space distribution of the atoms, as illustrated in the bottom figure. The phase-space distribution of the Ps cloud is shown for the different positions (a), (b), (c) and (d), before and after the interaction. We consider here the dipolar force within the harmonic approximation.

and size.

In order to be able to use the dipolar force with the laser system already available at CERN, I only studied one scheme using the NdYAG wavelength 1064 nm that is the most powerful laser we have. Using a highly intense laser is mandatory to create a deep potential well and increase the capture range on the atoms in interaction. Moreover, as illustrated in Fig. 10.3, the YAG laser pump appears to be ideally detuned to interact on the transition $n = 2 \leftrightarrow n = 3$ of the Ps (corresponding wavelength $\lambda_{32} = 1312\text{nm}$).

Beforehand, the Ps cloud would required to be excited to the $n=3$ state, in order to make the dipolar force attractive on the transition $n = 2 \leftrightarrow n = 3$. In our simple model, we neglect the spontaneous decays from the $n=3$ states, compared to the time of interaction. The spontaneous decays from the Ps $n=3$ are: $\Gamma_{s,3\leftrightarrow 2} = \frac{1}{30.92 \text{ ns}}$ and $\Gamma_{s,3\leftrightarrow 1} = \frac{1}{10 \text{ ns}}$. So, in a first approach, for small interaction times of 2 or 3 ns, this approximation can still be applied.

In our scheme, if a Ps excited in $n=3$ absorbs a photon to go to $n=2$ and deexcites toward the ground state, it will be lost for the dipolar interaction on the transition $n = 3 \leftrightarrow n = 2$. The laser needs then to be far from resonance. In other words, the scattering rate has to be negligible:

$$\begin{aligned} \Gamma_{scatt} &= \frac{\Gamma_s U_{dip}}{\hbar \delta} \\ \Gamma_{scatt} &= \frac{\Omega^2 \Gamma_s}{4 \delta^2} \end{aligned} \quad (10.2)$$

Thus, to be neglected, we need $\Gamma_{scatt} \sim \frac{I}{\delta^2} \ll \frac{1}{t_{interaction}}$, meaning the dipolar force is strong for $\delta \gg \Gamma_s, \Omega$. That's why the 1064 nm laser appears to be suitable for our purposes: intense and strongly detuned from the transition. For our YAG pulsed laser of 350 mJ, 15 ns and waists of $w = \sqrt{5 \text{ mm} \times 0.1 \text{ mm}}$, we derive a scattering rate of: $\Gamma_{scatt} = \frac{1}{2.7 \mu s}$ ¹⁶.

¹⁶To derive the scattering rate, the Rabi frequency of the interaction needs to be calculated. From the theoretical spontaneous decay $\Gamma_{s,2\leftrightarrow 3} = \frac{1}{30.92 \text{ ns}}$, we can derive the dipole strength of the transition $n=2 \leftrightarrow n=3$: $d_{23} = \sqrt{\frac{\hbar \Gamma_{s,2\leftrightarrow 3} 3\pi \epsilon_0}{k_0^3}} \approx 15$ Debye. Then, for a YAG pulse laser of 350 mJ, over 15 ns and a waist of $w = \sqrt{5 \text{ mm} \times 0.1 \text{ mm}}$, we obtain

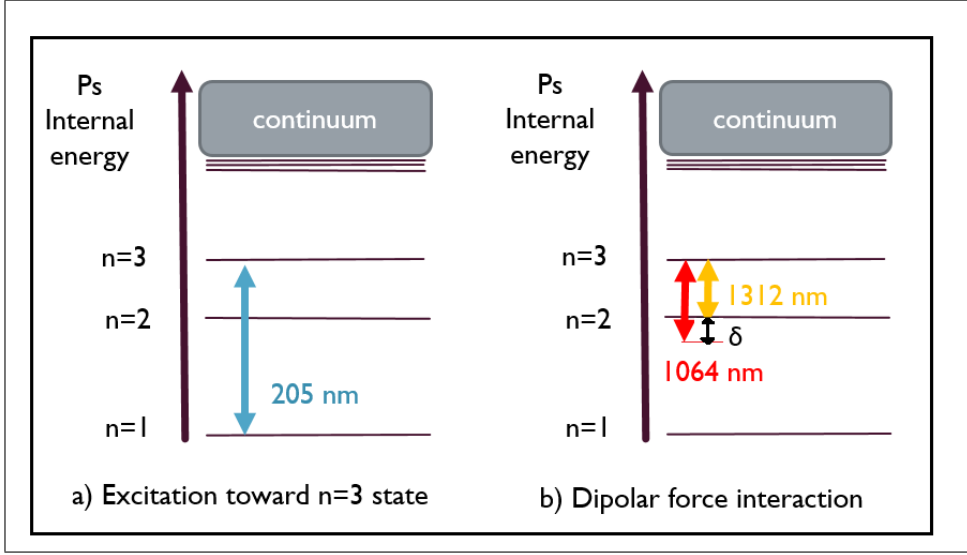


Figure 10.3: Schemes of principle to use the dipolar force on Ps atom: a) First, the Ps atom has to be in the $n=3$ excited state. b) Once the atoms are in $n=3$, they will experience a blue-detuned dipolar force (attractive force) on the transition $n = 3 \leftrightarrow n = 2$.

Typically in the following, we consider interaction times of the order of 2 ns or 3 ns, thus $\Gamma_{interaction} = \frac{1}{t_{interaction}} \approx \frac{1}{2 \text{ ns}} = 0.5 \text{ GHz} \gg \Gamma_{scat} = \frac{1}{2.7 \mu\text{s}}$.

For the simulations, I consider that the Ps cloud is emitted toward the x direction, and the laser is shined along the y axis (focusing of the z component). The laser interaction will affect the Ps cloud position and velocity on the transverse $\{x, 0, z\}$ plane, as illustrated in Fig. 10.2.

the Rabi frequency value:

$$\Omega = \frac{d_{23} E_L}{\hbar} = \frac{d_{23}}{\hbar} \sqrt{\frac{2 I_L}{\epsilon_0 c}} \approx 7 \times 10^{13} \text{ s}^{-1} \quad (10.3)$$

Using Eq. (10.2), this leads to the scattering rate: $\Gamma_{scatt} = \frac{1}{2.7 \mu\text{s}}$

10.2 The dipolar force on a single atom

In case of the dipolar force, the laser-matter interaction's impact on the classical position and velocity of the atom can be easily pictured by the phase-space vector $Z(t) = \begin{pmatrix} z(t) \\ v_z(t) \end{pmatrix}$, where $z(t)$ is the particle position, and $v_z(t)$ its velocity along the z axis. The atom propagating in a free-flight during a time t_{prop} is given by the matrix:

$$M_{free} = \begin{pmatrix} 1 & t_{prop} \\ 0 & 1 \end{pmatrix} \quad (10.4)$$

The laser-matter interaction with the dipolar force during a time t_{int} leads to a rotation in the phase-space distribution of the atom and its phase-space vector is multiplied by the matrix:

$$M_{int.dip.} = \begin{pmatrix} \cos(\omega_{trap} t_{int}) & \frac{\sin(\omega_{trap} t_{int})}{\omega_{trap}} \\ -\omega_{trap} \times \sin(\omega_{trap} t_{int}) & \cos(\omega_{trap} t_{int}) \end{pmatrix} \quad (10.5)$$

Where ω_{trap} is the angular frequency of the dipolar trap.

We consider here that the laser is stationary ($I(t)$ constant), and we model within the harmonic well approximation: the cold atoms oscillate in the center of the dipolar well, the Gaussian laser effect can be approximated by: $\exp(-\frac{r^2}{2\sigma_L^2}) = 1 - \frac{r^2}{2\sigma_L^2}$. In other words, the atoms in interaction feel an harmonic potential with the angular frequency ω_{trap} and experience a rotation of their phase-space distributions - see Fig. 10.2.

In a harmonic trap, the particle oscillates at a defined frequency of ω_{trap} :

$$\omega_{trap} = 2\pi \frac{1}{\pi w_L} \sqrt{\frac{U_{dip}}{m_{Ps}}} \quad (10.6)$$

where w_L is the laser waist

In the matrix formalism, it is easy to calculate the classical path of several particles in interaction with a laser. The total interaction matrix, resulting of a free-flight of the atom during a time t_{10} , followed by the laser interaction during t_{21} and finishing by a free flight until the target region, during t_{32} is then:

$$M_{tot} = M_{free,t_{32}} \times M_{int,t_{21}} \times M_{free,t_{10}} \quad (10.7)$$

The classical path evolution of an atom is then derived by:

$$\boxed{Z(t) = \begin{pmatrix} z(t) \\ v_z(t) \end{pmatrix} = M_{tot} Z_0} \quad (10.8)$$

I wrote a Mathematica code to solve and plot the path of several particles, for different interaction times. The dipolar trap parameters (depth and angular frequency) are also derived in the code.

10.3 Some results

The main limitation of this focusing principle comes from the laser intensity needed to induce a deep enough potential well to catch Ps at few tens of Kelvin. The maximum temperature captured by the trap is defined by:

$$T_{max} = \frac{U_{dip}}{k_B} = \hbar \delta \ln \left(1 + \frac{I/I_{sat}}{1 + 4 \frac{\delta^2}{\Gamma_s^2}} \right) \times \frac{1}{2 k_B} \quad (10.9)$$

We define the mean velocity of the Ps cloud by, $v_0 = \sqrt{\frac{k_B T}{m_{Ps}}}$ where T is the initial temperature of the Ps cloud. Here we can give some typical values reachable with our system: for a laser intensity of 3 GW/cm², meaning a pulse laser of 450mJ over 10 ns, focused on asymmetric waist $w_L = \sqrt{5 \text{ mm} \times 0.2 \text{ mm}}$, the maximum temperature of capture for the Ps is about 30 K corresponding to a mean velocity caught of $v_{0, trapped} = 15 \text{ km.s}^{-1}$. The oscillation frequency of the rotation in the potential well is then $\omega_{trap} \approx 2\pi \cdot 4.7 \text{ MHz}$.

As reminded in Fig. 10.4 a), we want here to determine the optimum times of free-flights and laser interaction that the Ps cloud should experience to be more focused when reaching the trapped antiproton region - located at about 3 cm from the Ps cloud's formation. To do so in the simulations, the first free-flight time t_{10} can be tuned, as well as the interaction time t_{21} . Since the antiproton target region is fixed at a 2 cm distance from the Ps convertor target, the last free-flight time t_{32} is fixed by the other two times.

In the simulations, I first modeled the Ps beam evolution over time by tracing the paths of 15 atoms that illustrate some typical atoms trajectories of the global cloud. These atoms are generated for 3 different positions in space, with 5 different initial velocities. Fig. 10.4 b) shows the initial rays that model the Ps cloud, for a temperature of 30 K. The Ps cloud size is considered to be initially 2 mm wide, thus I only take into account 3 extreme positions generated at $\{0 \text{ mm}, -1 \text{ mm}\}_{x,z}$, $\{0 \text{ mm}, 0 \text{ mm}\}$ and $\{0 \text{ mm}, +1 \text{ mm}\}$. For each point, five different paths are plotted with five different velocities that define the limits of the Ps cone of emission: $\vec{v} = v_0\vec{e}_x \pm 2v_0\vec{e}_z$, $\vec{v} = v_0\vec{e}_x \pm v_0\vec{e}_z$ and $\vec{v} = v_0\vec{e}_x$.

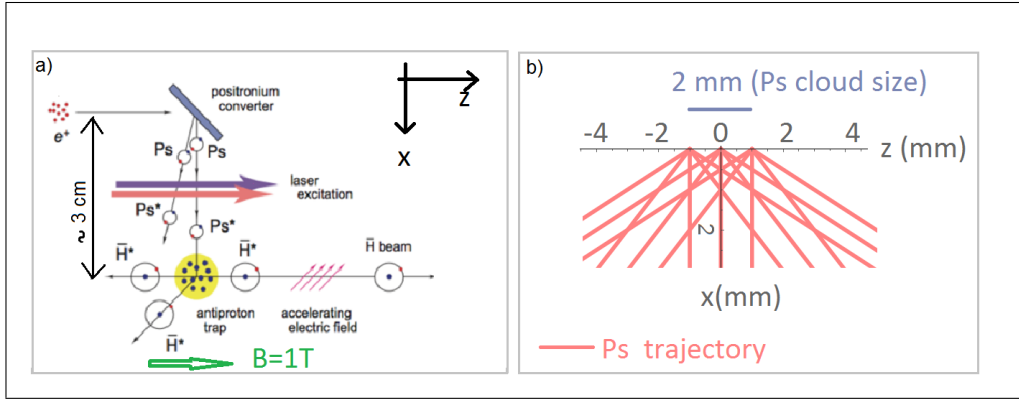


Figure 10.4: The initial conditions for the Ps focusing, using the dipolar force. a) is a reminder of the AEGIS schematic for the antihydrogen production. Between the Ps converter target and the antiproton trap, the Positronium cloud has to travel about 2 cm distance. b) shows the 15 initial paths that define the Ps cloud in the Mathematica code. Initially, the Ps cloud is supposed to be 2 mm wide along the z axis, with an initial temperature T. The temperature gives the mean velocity v_0 that fixes the emission cone, given two extreme atoms' paths with the initial velocity $\vec{v} = v_0\vec{e}_x \pm 2v_0\vec{e}_z$. We consider that the atoms are emitted at the same time (no spread in x).

The simulation purpose was then to determine a set of entangled parameters:

- For a fixed temperature of the atoms, the ideal interaction time is determined to focus their path in the antiproton trapped region, as illustrated in Fig. 10.5 a). The new NdYAG laser we have at CERN has a pulse time of about 15 ns. In order to select an interaction time

smaller than this value, we can for instance squeeze the laser dimensions to reduce the crossing time. The interaction time is defined to be the minimal value between the laser pulse time ($t_{pulse,laser} = 15$ ns) and the Ps atoms crossing time ($t_{cross} = \frac{w_x}{v_0}$).

- But squeezing the laser spot also modifies the trap depth and then the maximal temperature of capture. Thus, faster Ps atoms would feel the dipolar trapping force and the interaction time has to be adapted to focus them at the antiproton position.

In Fig. 10.5 are presented some typical results. In order to initialize the atom paths, as shown in Fig. 10.4 b), the initial velocity v_0 has been taken to correspond to a fictive temperature $T = 30$ K, $v_0 = \sqrt{\frac{k_B T}{m_{Ps}}} \approx 15$ km.s⁻¹. These 30 K correspond to the maximum capture depth of the dipolar trap generated by a laser energy of 350 mJ, over 15 ns and for a waist of $w_L = \sqrt{w_x \times w_z} = \sqrt{0.1\text{ mm} \times 5\text{ mm}}$. I considered the laser interaction was delimited by its waist sizes w_x and w_z (the effect of the tails are not taken into account into this simple simulation). This value of 30 K is an arbitrary temperature, chosen to be in the order of the lowest temperatures that the thermalized o-Ps emitted in vacuum can reach, for the target we use (with nano-channels of 6 - 8 nm size) and in the case where the target is cooled to cryogenic temperatures.

During a free-flight over a distance of 3 cm - corresponding to an over-estimation of the distance to reach the trapped antiproton area - the Ps cloud expands to 12 cm ; as shown by the red dashed paths in the simulations. We define the Ps cloud extremities by the two extreme atom paths, that gives the final size in the \bar{p} target.

In the column 1, a scan of the interaction time $t_{21} = t_{int}$ is presented. The distance between the positronium target convertor and the laser is fixed and corresponds to the free-flight distance $x_{10} = 2$ mm. The interaction time is crucial to be able to focus the atoms in the target region. If the Ps cloud is focused on 1.1 cm in the target region for the (b) situation, the (c) situation gives a focusing of about 2 cm whereas the interaction time only differs of 0.5 ns.

In the column 2 are shown the results of a scan of the free-flight distance x_{10} for a fixed interaction time of $t_{int} = 4$ ns. The distance of free flight before

laser interaction is also important: a variation of 1 mm in position drastically changes the focusing result. Besides, for a too long free-flight before the laser interaction (see (e) and (f) cases), the Ps cloud extends too much and the laser spot doesn't overlap it completely anymore. In the simulations, this is visible on the Ps trajectory at the edges of the cloud that don't interact with the laser and are not deflected (the effect of the laser tails is not taken into account since we consider only a harmonic potential well of interaction, approximation valid at the center of the laser spot) .

For these basic simulations, the best parameters seem to be for the b) situation with $t_{int} = 4.5$ ns and $x_{10} = 2$ mm. Under this laser interaction, the Ps cloud's size is focused down to 1.1 cm in the antiproton target region.

In Fig. 10.5, the graph a) appears to be a good configuration to concentrate the Ps beam on the antiproton region in a spot of 1.1 cm spread ; whereas without laser interaction, the Ps cloud would have expended to 12 cm after the 3 cm of free- flight (red dashed line).

These results are encouraging, but the capture range of the dipolar trap is too small for the Ps actually produced in the test chamber of AEGIS: only a small fraction of the Ps emitted could feel the rotating effect of the dipolar force. Besides, this simulation only takes into account the paths of some atoms with fixed initial position and velocity, and doesn't take into account the spread distribution of the Ps cloud, in both velocity and position. To refine more, I also studied the influence of the dipolar force on the Gaussian distributions of the emitted Ps cloud.

10.4 The dipolar force's effect on the Gaussian distributions of Ps cloud

So far, we have only considered point sources: each path represents one Ps atom, and we simulated the path of 15 atoms that roughly delimit the Ps emission cone's extremities. But the Ps cloud can also be modeled as a spread source.

The emitted Ps cloud can be associated to the random variable $Z(t)$, such as at the emission time $t=0$, $Z(t=0)=Z_0$ follows a 2D normal distribution $\mathcal{N}(\mu_0, \Sigma_0)$ with:

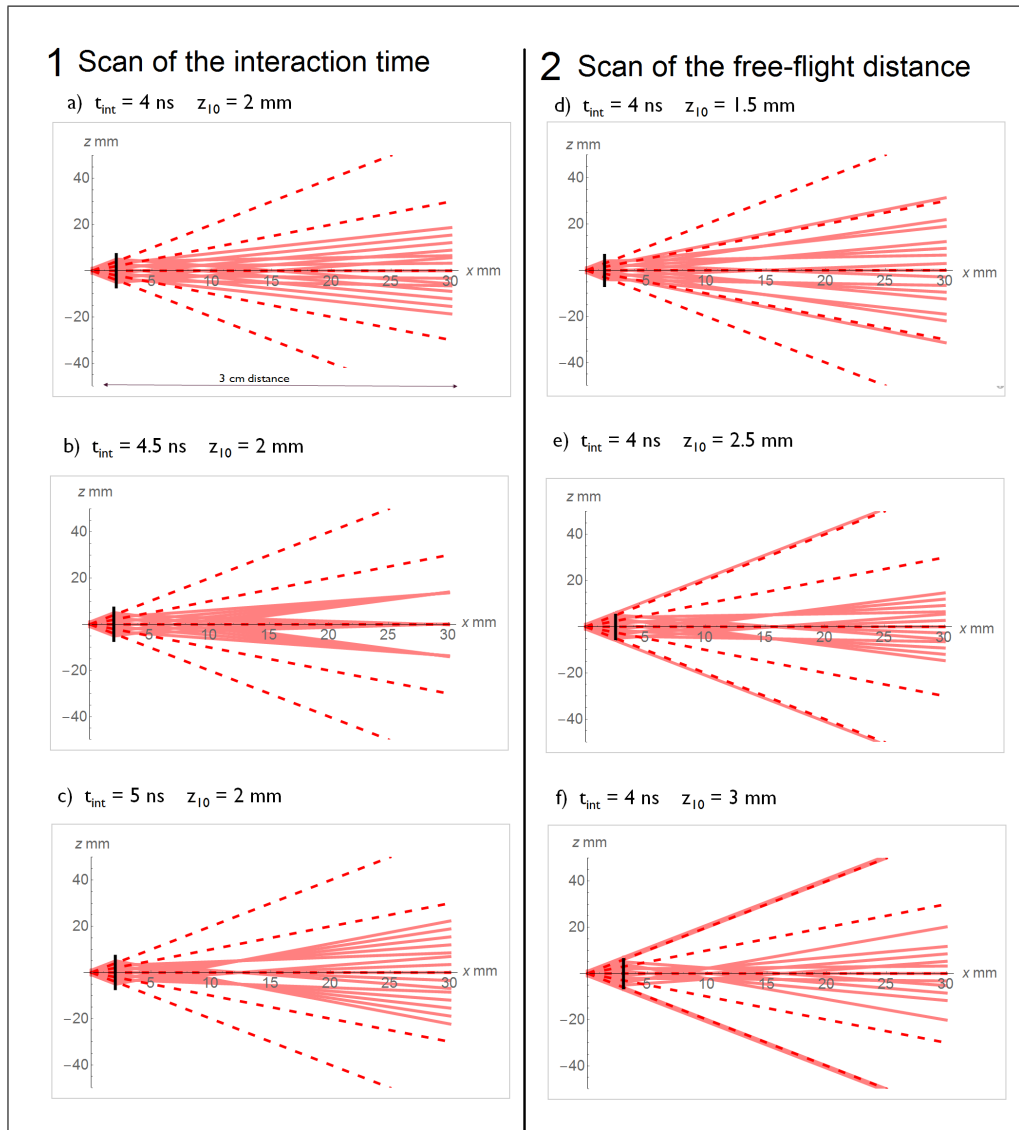


Figure 10.5: Scan results of the interaction parameters (time $t_{21}=t_{int}$) and distance x_{10}). The simulations are done for a Ps cloud initially at 30 K and over 2 mm spread (along z). The 1 column shows results for a fixed position of the laser ($x_{10} = 2$ mm), and a varied interaction time. The 2 column gives results of the scan of the laser position x_{10} , for a fixed interaction time (4 ns). The antiproton target is located at 3 cm far from the Ps emission target. Without laser interaction, the Ps cloud would have expanded to 12 cm after the 3 cm of free-flight (red dashed line). In all the graphs, the Ps atoms paths in interaction with the dipolar force are in pink, and the laser position is given by the black line. We can remark that in f), the extreme Ps trajectories are not deflected by the laser: the free-flight propagation during 3 mm lets the Ps cloud extend too much, and the extreme Ps atoms are out of the laser spot. The laser spot's size in x is represented by a black line.

$$\begin{cases} \mu_0 &= \begin{pmatrix} 0 \\ 0 \end{pmatrix} \\ \Sigma_0 &= \begin{pmatrix} \sigma_{Z_0}^2 & 0 \\ 0 & \sigma_{V_{z,0}} \end{pmatrix} \end{cases} \quad (10.10)$$

In the case of the point-source model, we have seen in Eq. (10.8) that $Z(t)$ follows an affine transformation $Z(t)=M_{tot}Z_0$. **For the spread-source case, the $Z(t)$ random variable then also undergoes this affine transformation.** This is valid in the harmonic hypothesis where all the atoms feel a constant field. In other words, we consider here that the Ps atoms are in the center of the laser spot, and that the laser spot is bigger than the Ps cloud. In this case, the spread-source $Z(t)$ of all the atoms follows the normal distribution:

$$\boxed{\mathcal{N}(M_{tot} \mu_0, M_{tot} \Sigma_0 {}^t M_{tot})} \quad (10.11)$$

We finally obtained the variance $\Sigma = M_{tot} \Sigma_0 {}^t M_{tot}$ expression of the Ps cloud that has experienced a first free-flight during t_{10} time, then a dipolar interaction during t_{21} and finally a second free-flight of t_{32} to reach the antiproton target:

$$\boxed{\begin{aligned} \sigma_x^2 &= \sigma_{x,0}^2 \times \{\cos(\omega_{trap} t_{21}) - \omega_{trap} t_{32} \sin(\omega_{trap} t_{21})\}^2 + \\ &\sigma_{V_{z,0}}^2 \left\{ (t_{10} + t_{32}) \cos(\omega_{trap} t_{21}) + \left(\frac{1}{\omega_{trap}} - t_{32} \times \omega_T \right) \sin(\omega_{trap} t_{21}) \right\}^2 \end{aligned}} \quad (10.12)$$

$$\boxed{\sigma_{V_z}^2 = \sigma_{z,0}^2 \omega_{trap}^2 \times \sin(\omega_{trap} t_{21})^2 + \sigma_{V_{z,0}}^2 \times \{\cos(\omega_{trap} t_{21}) - t_{10} \omega_{trap} \sin(\omega_{trap} t_{21})\}^2} \quad (10.13)$$

The dipolar force implies rotation in the phase-space of the position and velocity distribution spreads ; the rms value σ_z and thus the spatial size of the Ps cloud are alternatively focused or defocused, as shown in Fig. 10.6, a).

Optimum traveling and interaction times can be found to focus the spatial distribution in the antiproton target area. In Fig. 10.6 b) and c) are plotted the ratio $\frac{\sigma_z}{\sigma_{z,0}}$ of the spatial distribution of a Ps cloud initially at 30 K, as a function of the interaction time t_{21} . Without any laser interaction,

the free propagation for a flight of 3 cm leads to a spread of the Ps cloud of $\sigma_z = 15 \times \sigma_{z,0}$. In b) The Ps cloud first travels $x_{10}=2$ mm before the laser interaction ; the antiproton target area is located at 3 cm distance from the Ps emission initial region (along the x axis). With a dipolar interaction of 2.5 ns, the spatial distribution is focused to reach a final variance value $\sigma_z = 10 \times \sigma_{z,0}$ at the \bar{p} region.

In c) The Ps cloud propagates longer before the dipolar interaction ($x_{10}= 5$ mm), and the final squeezing of the Ps cloud in the target region becomes $\sigma_z = 5 \times \sigma_{z,0}$ for an interaction time of 2 ns.

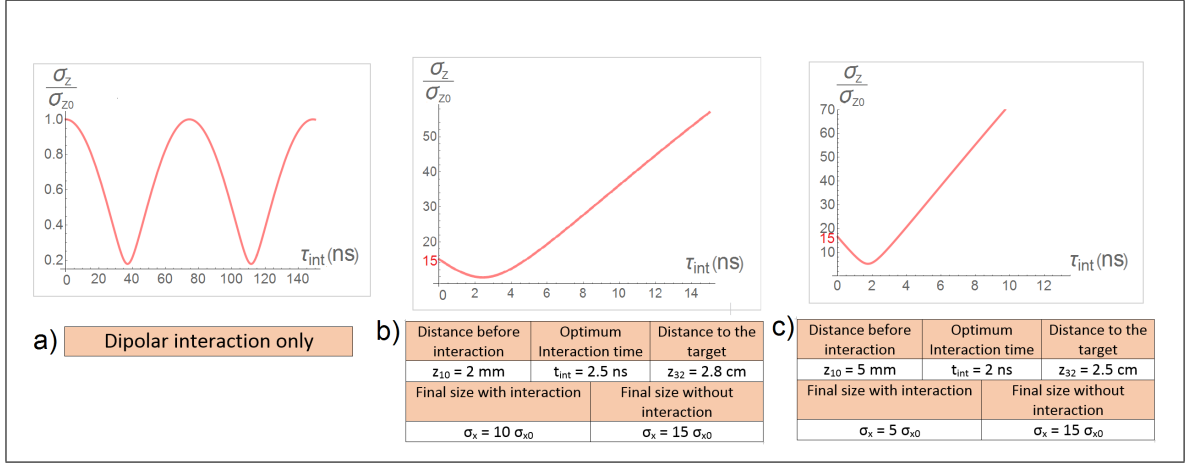


Figure 10.6: The evolution of the variance of the spatial distribution of the Ps cloud, depending of the first free-flight distance z_{10} and the interaction time $t_{21}=t_{int}$. The notations are given in Fig. 10.2. Fig. a) presents the ratio $\frac{\sigma_z}{\sigma_{z,0}}$, for the case where the dipolar interaction is only considered. No free-flight contribution is taken into account ($t_{10} = t_{32} = 0$), the variance σ_z is thus plotted just after the Ps emission ($x_{10} = x_{32} = 0$). This illustrates the rotation effect of the dipolar force on the space-phase distribution of the cloud: $\frac{\sigma_z}{\sigma_{z,0}}$ varies sinusoidally as a function of the interaction time. Whereas, in Fig b) and c), the variance of the Ps cloud's spatial distribution is measured at the antiproton target. In these two graphs, both the traveling distance before the interaction z_{12} and the interaction time t_{int} are chosen to focus the Ps cloud at the antiproton target, located at 3 cm distance from the Ps emission source. Optimum interaction times can be found to focus the spatial distribution in the antiproton target area.

Theses results confirm the simulations performed in Sec. 10.3, which consider only the ballistic paths of few atoms. For cold atoms, the dipolar trap acts like a focusing lens on the Ps cloud, for chosen traveling and interaction times.

However, in the present state, the dipolar focusing technique seems not to be adapted for the AEGIS purposes ; mainly because of the small capture range. Indeed, as shown in the simulations Fig. 10.6, in order to have a good focusing effect, the Ps cloud needs first to extend a bit before the laser interaction: a better focusing is reached for a first free-journey of $z_{10} = 5 \text{ mm}$

than for $z_{10} = 2$ mm. As a consequence, the laser spot needs to be big enough to cover the Ps cloud and a huge power would be needed to have a strong laser intensity to keep a good capture range.

Unfortunately, the depth trap is limited by the reachable laser intensity, and the capture range doesn't exceed few tens of Kelvins. Technical solutions could be studied to increase the capture range of the dipolar interaction: for instance, the potential depth could be enhanced using a cavity to build a more intense laser. Further studies and laser developments would be required to adapt the dipolar focusing force to our purposes.

Chapter 11

Short summary of the Ps studies and prospective

In the parts I and II, I presented the studies I have done on the positronium physics and the experimental works. In 2015 in the test chamber setup, we obtained the first laser excitation results for AEGIS, that was a milestone toward the formation of antihydrogen by charge exchange. The excitation of Ps atom to Rydberg states is now planned to be performed during the beam-time of 2016. This will be a crucial step toward the formation of antihydrogen via charge-exchange for us.

In parallel to this, the possibility of Doppler laser cooling the Ps atoms seems promising in theory and has to be tested. The experimental solution to built an adequate laser is under development. We aim to conceive a UV pulse, lengthened to 50 ns - 80 ns, with a minimum power of 300 μJ - 500 μJ . Currently, both the beam splitter R=35%/ T=65% and the polarization cube have been ordered. Once delivered, Olga and I would like to perform the first trials to align the loss cavity. We think that the biggest problem will be the stability of the cavity shot by shot, and hope that we will be able to match the cavity to produce at least 4 secondary pulses. Moreover, we have just ordered two fiber dividers 1 \leftrightarrow 5 from the IDIL company. They have been looking for technical solutions to avoid to burn the divider when injecting 500 μJ to 1 mJ of UV light. The fiber solution will have the advantage to provide a stable stretching system. This will be a first setup to demonstrate the laser cooling, inside the test chamber in the absence of magnetic field, where no strict control of the polarization is required.

Moreover, we have to tackle the problem of the narrow bandwidth of the 243 nm generated from the dye-laser technique. The laser bandwidth is de-

fined by the inner-cavity grating that limits the spectral width. We may consider to change our setup and use solid crystals to generate the 243nm, using optical parametric generator (OPG)/ optical parametric amplifier techniques as it is the case in the Milano laser system of AEgIS. Anyway, a commercial solution would be to buy a solid-state laser based on Alexandrite, that could provide a long pulse at 243 nm of 200 ns, with a tunable bandwidth from 50 GHz to 1 THz. This would be the ideal - and expensive - solution. If performed, the Ps laser cooling would have a great impact on the \bar{H} formation efficiency, by focusing the solid angle of the Ps cloud and improving the overlap between trapped antiprotons and the incoming Ps atoms.

As mentioned in the introduction of the Part.II, another way to enhance the charge exchange process is to cool the antiproton plasma. In the AEgIS proposal, a 100 mK antiproton plasma is required to perform the gravity test within a precision of 1%. In the next Part III, I will present the works on antiprotons I took part in order to try to fulfill this condition.

Part III

Antiprotons manipulations and cooling studies

As the unique source of cold antiprotons in the world, the Antiproton Decelerator (AD) facility at CERN delivered bunches of $3 \cdot 10^7$ antiprotons since 2001. The cycling rate of the AD is a \bar{p} bunch every ~ 120 s, provided at an energy of 5.3 MeV.

During the beam-time period, the \bar{p} beam time is divided in slices of 8 hours, sent to the 5 experiments currently settled in the hall: AEGIS [15], Alpha [69], Asacusa [70], Atrap [71], and Base [72]. The 5 experiments share their working-time in 3 periods or shifts: the morning shift, from 7 am to 3 pm, the afternoon shift from 3 pm to 11 pm, and the night shift to complete the day from 11 pm to 7 am. A weekly rotation of the attributed shifts is done. Typically an experiment has 3 weeks of antiprotons beams, and one-two weeks off to work during these periods.

Most of the experimental setups use degrader foils (thin foils, generally in aluminum or silicon) to decelerate antiprotons down to around few keV that is a suitable energy for trapping. This process leads to the loss of most (99%) of the antiprotons. An upgrade of the AD ring is currently under construction to slow further down the antiproton bunches to 100 keV. This new ring is called ELENA[73] for Extra Low ENergy Antiproton ring, and would be able to provide antiproton to all experiments at the same time, canceling the need for the 8 hours shifts division. The first commissioning of ELENA is planned for end of the 2016 beam time. The new Gbar[13] experiment - approved in 2012 - should start its commissioning in the AD hall at the end of 2016 and take beam during the 2017 beam time from the ELENA facility.

Approved in 2008, AEGIS experiment has started to be installed in 2010 and took its first beam-time in 2012. In the first chapter of this last part (Chap. 12), I would like to give a quick overview of the AEGIS main apparatus and the non-neutral plasma trapping scheme used in AEGIS. For more details, the reader could report to the thesis of Daniel Krasnický [74], currently post-doc in the collaboration, who worked during its Ph.D on the commissioning of the two traps.

In the chapter 13, I will present some of the results of antiproton plasma manipulations and cooling we obtained during the 2015 beam-time. During this period of my Ph.D, my time was mainly dedicated to the \bar{p} shifts.

The idea of sympathetically cool antiproton plasma with laser cooled atomic anions has been studied for years by the group of Alban Kellerbauer of the Heidelberg university [75], in AEGIS. During my thesis, I took an ac-

tively part in the studies to rather use cold molecular anions than atomic anions. The study of different possible laser schemes to cool the molecular anion C_2^- will be presented in the chapter 14.

Chapter 12

The AEgIS main apparatus - the traps description and plasma behaviors

The AEgIS apparatus is illustrated in Fig. 12.1. In the AD experimental zone, it is composed of the positron system, traps system, the data acquisitions (DAQ) and detectors systems (not indicated in Fig. 12.1), and the lasers systems (not indicated in Fig. 12.1). The description of the positron system is given in the first part of this thesis, Chap. 3, and the descriptions of the laser systems can be found in Sec. 4.3 and Chap. 9. Here, we will focus on the short review of the two Penning-Malmberg traps, referred as 4.5 T and 1 T traps (main traps) that form the core of the trapping system.

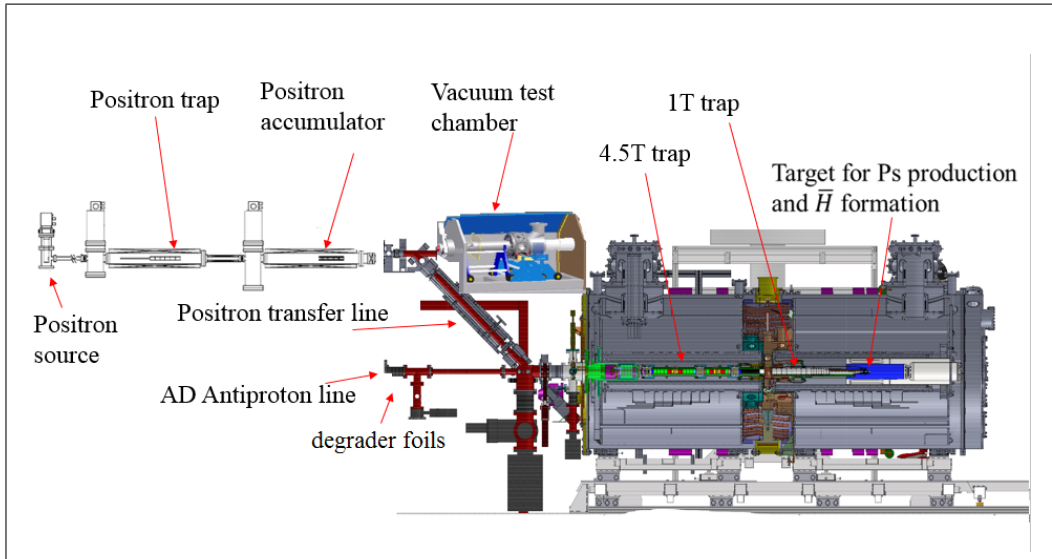


Figure 12.1: Schematic of the AEGIS apparatus. The AD arm provides antiprotons that are trapped into the main apparatus composed of two Penning-Malmberg traps at 4.5 T and 1 T. On the second floor, the positron system is installed. A transfer line has been built to transport e^+ from the accumulator traps into the main traps, where the antihydrogen formation is planned to occur in the 1 T trap's production region.

12.1 The choice of Penning-Malmberg traps

As for the other experiments in the AD Hall, AEGIS has chosen to use the so-called linear Penning traps in order to catch and manipulate the antiprotons from the AD facility. In this section, I would like to remind quickly some properties of this type of trap, and the possibility of plasma manipulations and compressions that a Penning trap offers ; before presenting more specifically the AEGIS apparatus.

12.1.1 The ideal Penning trap

A Penning trap is composed of a superposition of a static electric potential that ensures the axial confinement, and of a homogeneous magnetic field that confines radially the charged particles. The ideal electrostatic potential of a Penning trap is quadratic:

$$\Psi(x, y, z) = \frac{V_0}{2D} \left(z^2 - \frac{x^2}{2} - \frac{y^2}{2} \right) \quad (12.1)$$

where V_0 and D are the constant of the traps: V_0 is the potential difference between the ring electrode and the end-cap electrodes, and D is the characteristic size of the trap.

In order to conceive an ideal harmonic field, the electrodes have to be hyperbolic shaped, as illustrated in Fig. 12.2 a). This experimental trap setup is mainly limited by the purity of the field-lines: since the charged particles need to be loaded into the trap, usually a hole is made in the center of one of the end-caps that perturbs the field lines and thus the trap stability. Besides, machining electrodes following hyperbolic curves is rather difficult to obtain, and default in curvature would induce perturbations too.

12.1.2 The cylindrical-shape Penning trap alternative

For these practical reasons, the open-ended cylindrical-type Penning traps geometry are widely used as an alternative setup in ion trap physics. Fig. 12.2 b) presents the concept idea: any cylindrically symmetric electrode structure that creates a saddle point also generates a harmonic potential of the form of Eq. (12.1) in a small region around its center. Adding correction electrodes to reach the ideal electrostatic field has been studied in detail, as in [76] where a total of 7 electrodes compensate the trap's field to reach a perfect quadratic-like field.

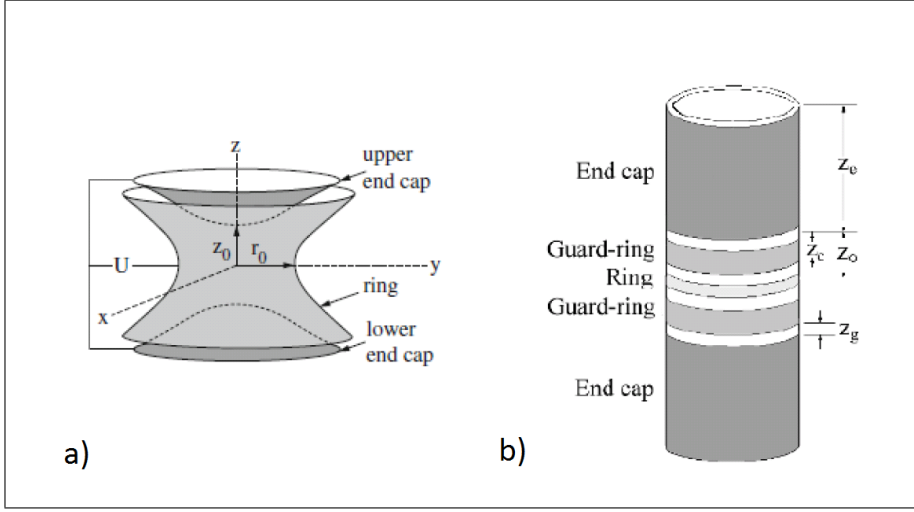


Figure 12.2: Different Penning trap designs: a) the ideal Penning trap geometry - hyperbolic shape b) The open-ended cylindrical Penning trap. The magnetic field axis is along the cylindrical electrodes. *Pictures taken from [74]*

In a Penning trap, the dynamics of a plasma differs from the motion of non-interacting particles. We consider here the plasma dynamics for $\lambda_{Debye} = \sqrt{\frac{\epsilon_0 k_B T_{plasma}}{n^* e^2}} \ll \text{size}_{plasma}$, where n^* is the plasma density. A cloud of particles presents the collective behavior of a plasma for a low temperature and a high density. Some derivations on the plasma dynamics are given in [74]. In short, the plasma rotates around the magnetic axis at the rotation frequency $\omega_r = \frac{\omega_c}{2} \pm \sqrt{\frac{\omega_c^2}{4} - \frac{\omega_p^2}{2}}$, where $\omega_c = \frac{qB}{m}$ is the cyclotron frequency and $\omega_p = \frac{q^2 n_0}{\epsilon_0 m}$ is the plasma frequency, proportional to the plasma density n_0 .

The rotation of the plasma is caused by the cross field product $\mathbf{E} \times \mathbf{B}$. The radial component of the electric field comes both from trap's radial electric field components and the space charge of the plasma that creates an electric field. This rotation drift pushes inward the particles, due to the generated Lorentz force $q\vec{v} \times \vec{B}$, and thus compensate the combined repulsion effect (space charge, default of the trap, etc), and makes the trap stable.

Remark: In the following, we use the "plasma" word to refer to "non-neutral plasma", composed only of particles of the same sign of charge. In plasma physics in general, a plasma is usually defined by the property of quasi-neutrality, which does not hold in our case. By "plasma", I indicate either cloud of positrons, electrons or antiprotons or even both species together that do exhibit collective phenomena similar to neutral plasma, but do have substantial space-charge, which is the main difference compared to neutral plasma.

12.1.3 The Penning-Malmberg trap

An alternative trap is to generate a square-like potential rather than a harmonic trap. Fig.12.3 shows a schematic of a typical Malmberg trap, that is a easier-to-build version of the Penning trap. This trap is composed of a set of concentric cylindrical electrodes which form a flat potential well. Usually, the central electrode is grounded and designed to be longer than the end-caps electrodes where the trapping voltage is applied.

The particle motion in a Malmberg trap differs from a pure Penning trap (harmonic well), since the particle doesn't feel any electric field in most of its travels (in the center of the trap) except at the edges, close to the end-cap regions. Thus, the particles undergo cyclotron oscillation in the magnetic field and bounce back and forth between the end-caps. Only in the end-cap regions, the particles feel the drift rotation $E \times B$ from the external electric field.

However, we can note that due to the radial electric field of the non-neutral plasma (generated by the space-charge effect), the particles out of axis rotate even though there is no radial trap field in the middle of the trap. This is the main difference between single particle and many particle behavior: the non-neutral plasma with homogeneous density rotates at a defined frequency (collective behavior).

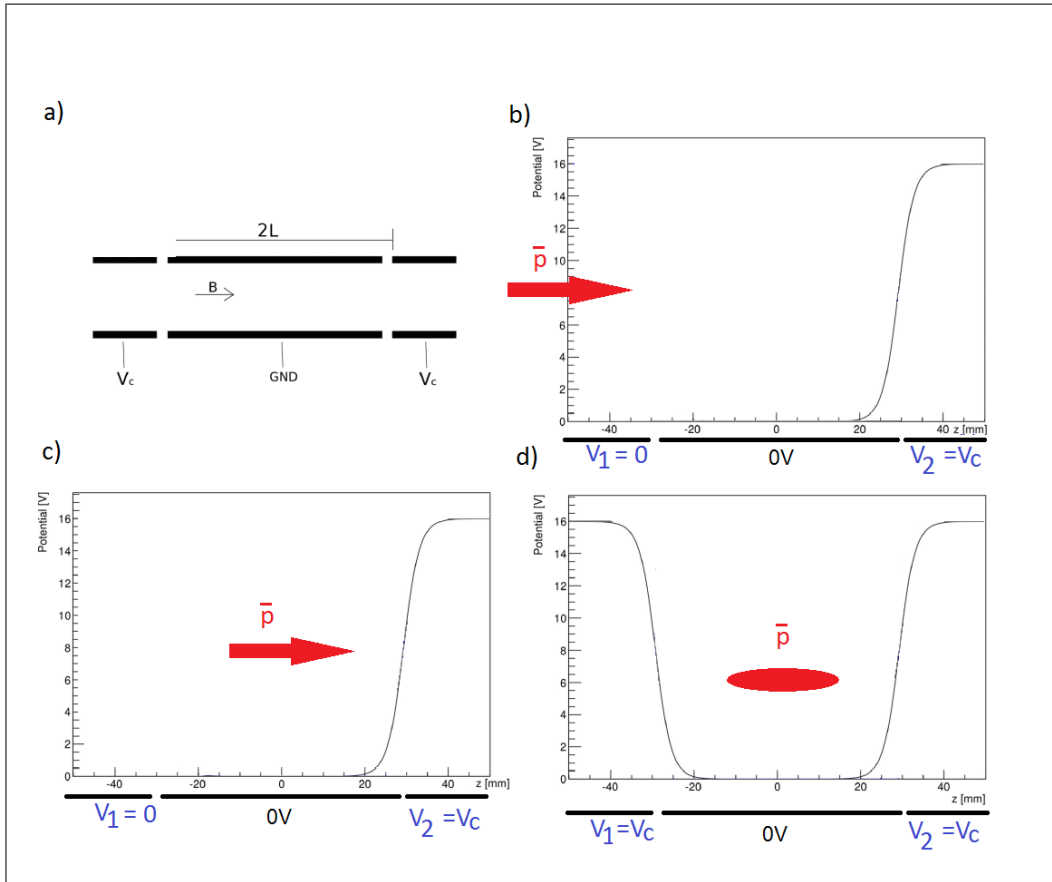


Figure 12.3: Penning-Malmberg trap. a) schematic of the linear Penning-Malmberg trap: two ends caps ensure the axis confinement. b), c) and d): the loading procedures. The end caps V_1 plays the role of the door for the charge particles to enter. For the loading, the V_1 electrode is grounded to let enter the particles (b), while the end-caps electrode V_2 is set at $V_c=9\text{kV}$ for catching the antiprotons. Once entered (c), the V_1 electrode is raised to V_c (d). Once caught, the electrons cooling procedure can start.

12.1.4 The AEgIS apparatus

AEgIS has chosen to use the so-called Multi-Ring Trap geometry, that is a cylindrical Penning-Malmberg trap composed of many short cylindrical electrodes of the same length. One of the advantages of a multi-ring trap is that the length of the harmonic region can be tuned or its spatial position can be moved along the axis by just changing the voltages applied to

trap's electrodes [74], and then shift the position of the plasma inside under certain conditions of trap stability (usually, we proceed of an adiabatic transfer to reshape the trap). We also can use this trap is a non-harmonic trap configuration (Malmberg-type) that gives more freedom for the plasma manipulations.

12.2 The 4.5 T Penning-Malmberg trap - the catching system

As shown in Fig. 3.5, the Penning-Malmberg trap referred as the 4.5 T trap is the first system that is responsible for catching the antiprotons coming from the AD arm¹⁷.

The 4.5 T catching system consists of a 1 m long stack of cylindrical electrodes with inner electrode radius of $r_0 = 15$ mm. The Fig. 12.4 is a drawing of the catching system, where three types of electrodes are mounted:

- the standard gold-plated aluminum low voltage (± 200 V) electrodes, with different lengths of 13.5 mm, 30 mm and 40 mm. They constitute the core of the parts called "antiproton trap", "positron trap" and "transfer region" in the global trap. See Fig. 12.4 for the notations.
- the divided electrodes (gold-plated aluminum) for rotating wall compression, split azimuthally into 4 equivalent sectors 13.5 mm long each. They are placed in the "antiproton trap" and "positron trap".
- the high voltage electro-polished Titanium electrodes, that can sustained up to -20 kV at maximum for the \bar{p} catching, and up to +1 kV for positron catching. They are used as the end-caps of the trap. In Fig. 12.4, they are marked as HV1, HV2 and HV3.

¹⁷The capture range of these traps in the order of few keV, but the AD delivers bunches of 5.3 MeV \bar{p} . Before catching, the incoming antiprotons are first slowed down passing through thin aluminum foils of $\approx 150 \mu\text{m}$, that are called degrader foils.

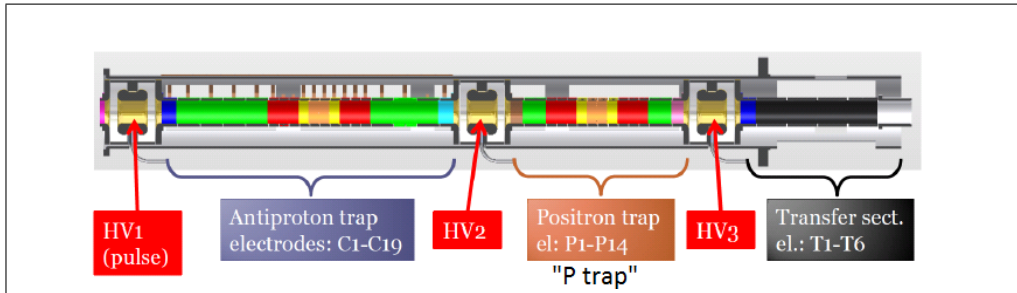


Figure 12.4: 4.5 T trap design, with the different trap regions indicated. Drawing taken from [74]

The role of this first trap is multiple:

- the catching of antiproton bunches, compression (via the rotating wall technique), stacking and cooling. Typical potentials applied to the trap for a loading procedure are illustrated in Fig. 12.3 b).
- the catching of positrons, accumulation and compression.
- the transfer to the 1 T trapping system.

Started during the beam-time of 2014 and continued during the beam-time of 2015, we mostly characterized the 4.5 T catching system. For instance, systematic studies have been carried out to determine procedures and parameters to cool and compress at best the antiproton plasma. I will present some of our recent results in the chapter 13

12.3 The 1 T Penning-Malmberg trap

The 1 T trapping system has been conceived to match both:

- the exigence of having a low magnetic environment to avoid as much as possible the Zeeman mixing of the different energy levels of the \bar{H}^* , produced in Rydberg states. The idea of the AEGIS proposal is to perform Stark acceleration of the antihydrogen atoms, and a good control of the energy levels is needed to accelerate the \bar{H} toward the trap exit.
- the necessity of having a high enough magnetic field to be able to trap and manipulate antiproton and positron plasmas.

The 1 T trapping system is complex since it has to comply with a lot of requirements. Fig. 12.5 is a schematic of the different parts of the 1 T traps.

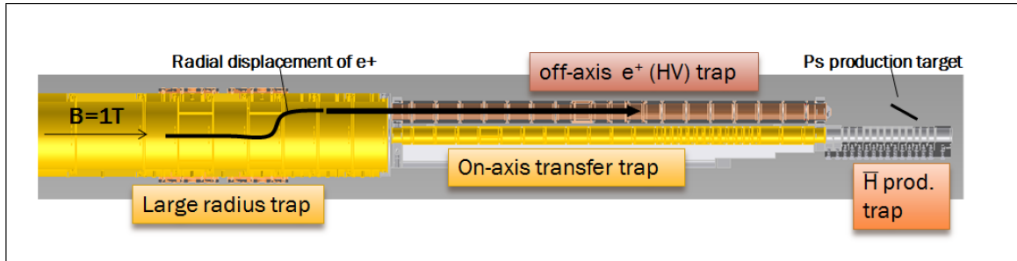


Figure 12.5: 1 Tesla trap schematic, with the different trap regions indicated. *Drawing taken from [74]*

First, since the plasma radius depends on the confinement of magnetic field, the transfer from 4.5 T trapping environment to 1 T will induce a drastic increase of the plasma radius such as $r_{1T} = r_{4.5T} \times \sqrt{\frac{4.5T}{1}} \approx 2.1 \times r_{4.5T}$. This plasma expansion is not really desirable for an efficient transfer without losing antiprotons during the process. However, the needs of having a moderate catching magnetic field in order to limit the Zeeman splitting effects on \bar{H} didn't let much choice. That's why a so-called "Large radius trap", with large radius electrodes ($r=22$ mm), was designed to catch and recompress the antiprotons coming from the 4.5 T trap. Then, the "ON-axis" trap ($r=5$ mm) is made for stacking and cooling the antiprotons before being loaded to the "production trap" region. The "OFF-axis" ($r=5$ mm) trap has been conceived to accumulate positron plasma, loaded by diocotron motion. From there, the positrons are accelerated to be implanted into the positronium target converter, placed at about 2 cm away from the antiproton plasma trapped into the production area.

Note that the electrodes of the ON-axis trap have a grid in the top, in order to let pass through the Ps^* from the Ps target converter placed above. The transparency of the grid is estimated to be 50 %. Because of the grid, the stability of the plasma confined inside the ON-axis trap is perturbed. We aim to have a plasma as compressed as possible before the transfer toward the ON-axis trap, in order to limit the disturbance of the grid.

More details about all the procedures of trapping and loading can be

found in [74]. In the next chapter, I will present some typical procedures of antiprotons catching, cooling and compressions we performed in the 4.5 T trap, during the beam-times of 2014 and 2015.

Chapter 13

The 2014 and 2015 beamtimes - some results about the cooling and compression of the \bar{p} plasma

During the beam-times of 2014 and 2015, AEGIS spent a great amount of time characterizing the trap behaviors to obtain the coolest and most compressed plasma of antiprotons reachable in our apparatus. An article is under process that would analyze deeply the physics behind our last results. It is out of the context of this chapter to enter into the details of the dynamics of the plasma and its modes, or to review the detailed physics theory behind the rotating walls and electrons cooling techniques. This chapter is more to focus on the results obtained.

The INFN Genova group, led by Gemma Testera, is responsible for the trap operation. In addition to the installation and maintenance of the traps, part of their mission is to optimize the catching procedure of antiprotons but also to develop manipulation protocols on electron, positron and antiproton plasmas, to compress and cool the plasmas to prepare the antihydrogen production.

During the beam-time periods, all the laboratories of the collaboration have to take their share in providing participants for the runs, called "shift operators". Although the Genova group settles down the main physics objectives for a session of shifts, the shift operator takes an active part in the data acquisition and decisions about further measurements to carry on in the shifts.

During the beam-times 2014 and 2015, I dedicated a major part of my

time participating in the trap missions as a "shift operator". Part of the time was dedicated to the trap calibrations:

- catching efficiency of antiprotons - depending on the degrader foils. In AEGIS, different degrader foils can be placed on path of the AD bunch to adjust the reduction of energy on the antiprotons. We found the optimum for a combination of 40 μm (thickness from the tunable degrader) + the other degrader systems ($\approx 100 \mu\text{m}$).
- sympathetic cooling efficiency - depending on the electron plasma loaded (number of electrons, compression and overlap of the two plasmas). Typically, we load about $10^8 e^-$, and reduce the antiproton energy in 30 - 50 s of about 55% - 65 % of the caught \bar{p} .
- transfer efficiency - depending on the compression and cooling, detectors calibrations (MCP), etc. Typically, a total efficiency of 10 - 15 % of the total among of caught antiprotons from the AD bunch can be transferred and trapped into the ON-axis trap inside (1 T region), after cooling and compression.

In the following, the second point will be mainly discussed. In addition to this task, I was involved in the series of measurements to optimize the compression and cooling of the antiproton plasma in the 4.5 T Penning-Malmberg trap. Reaching a compressed plasma is crucial for an efficient transfer from the 4.5 T catching trap to the production trap in the 1 T trap (see Chap. 12), since the plasma blows up during its travel from a high magnetic field to a lower one. It is also of the first important to compress the antiproton plasma to re-catch the antiprotons in the center of the ON-axis trap with a small radius. Indeed, the grids pierced in the ON-axis electrodes disturb the symmetry of the trap. Then, in order limit the disturbance on the confinement efficiency, the antiprotons should be compressed to be far from the default of the trap (the grids). Some of the best results obtained are presented here.

Section 13.1 provides some definitions of the techniques we used to compress and cool the antiproton plasma. A quick review of the experimental setup and diagnostics we used is given in section 13.2. In Sec. 13.3, the best procedures and the results obtained are presented.

13.1 Electron cooling and rotating walls techniques

As mentioned before in Chap.12, the results of compression presented here rely on the so-called Rotating Wall (RW) technique, that compresses non-neutral plasmas in a Penning-trap. Since this process generates heat, a cooling mechanism needs to be present in the trap. The electrode has to be at least sectorized into 4 sectors to apply the rotating electric field. The rotating field injects an angular momentum to the plasma (production of a torque on the plasma), and thereby compresses the plasma radially. More details can be found in [34, 74]

Originally, the rotating wall technique operates only at the frequencies of the plasma radial modes. In 2005, Danielson and Surko used a 5 T Penning-Malmberg trap and demonstrated a new regime of rotating wall process called the "strong drive" regime [77] that "permits a novel high-density regime" to be reached, where the RW frequency corresponds to the rotation frequency of the plasma.

It is worth noticing that the RW technique is really efficient for electrons and positrons. Indeed, the cooling mechanism required to maintain the stability of the plasma during the RW process comes directly from the particles themselves that are cooled by cyclotron radiation in a high magnetic field Penning-Malmberg trap (See. Chap. 14). Applying RW drive on antiprotons directly seems less efficient, because the particles are heavier than electrons. In 2008, the experiment ASACUSA has performed direct RW on \bar{p} plasma, and the speed and efficiency of compression appear to be relatively low [78]: a time of 200s was needed to compress roughly 40% of the caught antiprotons. They don't seem to indicate the cooling mechanism that ensures the stability of the antiproton plasma during the RW drive. One explanation could be that some electrons remain in the trap after the removal of the e^- plasma, too few to be easily detected but still playing a role of cooler.

An indirect compression of the antiprotons can be achieved, as first presented by the collaboration Alpha [79] in 2008. The electrons and antiprotons are confined in the same trap, and the compression of antiprotons is driven by the electron plasma on which the RW is applied. The results presented below use this indirect technique.

13.2 The diagnostics

During the 2014 and 2015 beamtimes, we carried out several systematic measurements to test procedures that implement various numbers of rotating walls (RW) stages on electrons, for different numbers of the e^- in the trap. We aimed to determine the best procedure that provides a good compromise between reaching a high cooling rate on the antiprotons caught and obtaining a good compression of the plasma, in relatively short times.

The procedures tested and presented here were carried out in the 4.5 T trap, in the so-called P trap (defined in Sec. 12.2, Fig. 12.4). In order to image the radial profile of the plasma (electron, antiproton or positron), we used the MCP coupled to a phosphor screen and a CCD located after the "on-axis" trap at the end of the 1 T trap (defined in Sec. 12.3, Fig. 12.5), far from the location where the procedures took place. The plasma blows up during its flight from the 4.5 T to the 1 T region (radius 2.1 times bigger), the sizes of the plasma have then to be rescaled during the analysis process. Because of a slight misalignment between the 4.5 T and 1 T electrodes, the images of the MCP presented in this chapter appear to be partially cut.

The Fig. 13.1 illustrates the setup used here. In order to obtain the number of electrons/positrons, a Faraday cup is used in the left of the P trap. Several external scintillators placed all around the P trap estimate the number of antiprotons released from the trap, by comparing with Monte Carlo simulations.

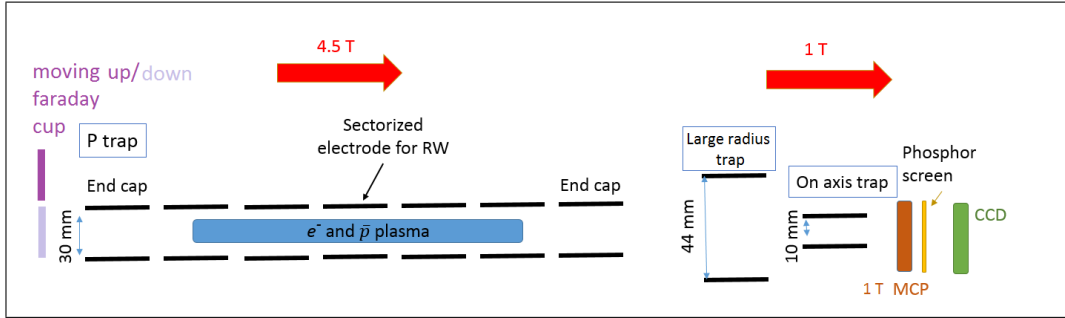


Figure 13.1: Schematic of the experimental setup. The antiprotons and electrons are confined in the P trap of the 4.5 T apparatus. The plasma imaging is realized by dropping the particles to the right through the 1 T traps (large radius trap and on-axis trap with smaller radius) toward an MCP coupled to a phosphor screen and a CCD camera. To measure the electron number, the e^- are pulsed to the Faraday cup on the left hand-side of the P trap. External scintillators located all around the P trap estimate the number of antiprotons released, thanks to comparison to Monte Carlo simulations.

During the procedures of cooling and compression of antiprotons, we usually get rid of the electrons by applying series of short 80 ns pulses on one of the endcap. By opening the trap for a short time, we allow the electrons (that move $\sqrt{\frac{m_{\bar{p}}}{m_{e^-}}} = 42$ times faster than the antiprotons) to leave the trap. More than 90% of the antiprotons stay inside the trap during this process. The electrons can be sent either toward the Faraday cup to be counted (left side of the P trap), or toward the 1 T MCP on the right side. Again, either the number of antiprotons is measured (dump recorded by the scintillators) or the radial profile is recorded (dump toward the 1 T MCP).

Remark : Because we can't distinguish the signal coming from an antiproton or from an electron in the MCP detector, we can't measure in a single run the two radial profiles of the electron and antiproton plasmas. We have to repeat twice the procedure to obtain both information. This requires a high repeatability of each run, and then stable trap conditions. This is obtained by a stable loading condition of the electrons (density varying of 2% at most) and a fast and reliable "real-time" electronics system that controls the traps. A 10 MHz clocked homemade FPGA system drives the potentials

of traps and triggers the motion of the pistons for the diagnostics tools - MCP/mirrors/Faraday cups/etc.

However, we must also rely on the stability of the AD that should deliver identical \bar{p} bunches (with approximately the same steering position and intensity for each bunch). Unfortunately, this can vary in time, and this is so far the biggest instability we encounter. A good 8 hours- shift would be for an AD intensity above $3 \cdot 10^7 \bar{p}$, with fluctuations shot by shot of the order of 10-15 %.

13.3 Results on \bar{p} plasma compression

In this section, I only present some selected procedures to illustrate the cooling and compression standards we can reach in AEGIS. The first two procedures in Sec. 13.3.1 and Sec. 13.3.2 describe the preliminary actions on electron and antiproton plasmas required to prepare the plasmas in good conditions to be able to start compressing the \bar{p} : the electrons need to be pre-loaded, cooled, compressed by rotating walls to reach stable conditions, before catching the antiprotons (procedure 0). Afterward, the antiprotons are caught at 9kV (end-caps voltage), and sympathetically cool with electrons for tens of seconds (procedure 1). The following studies and procedures described in Sec. 13.3.3, Sec. 13.3.4 and Sec. 13.3.5 are protocols to compress the cold antiprotons, with different stages of sophistication.

13.3.1 Procedure 0: loading and cooling of electrons - Study: RW applied on electron plasma only.

Before catching any antiproton, the procedure 0 in AEGIS consists in loading electrons and letting them radiatively cool: in a 4.5 T environment, the electron plasma cools by cyclotron radiation within 1 second. We can apply a RW drive on the e^- plasma, in order to have a good control on the electron plasma's dimensions and density.

In a first study, we then apply a RW drive and characterize the e^- plasma response, for different frequencies and amplitudes of the drive - without antiprotons present in the trap. In Fig. 13.2 is plotted the electron density as a function of the frequency of the RW. For each frequency data point, the electron plasma is first dump toward the Faraday cup to determine the numbers of e^- . Then a second run is performed with the same RW conditions, where the electrons are dumped toward the MCP. The FWHM is extracted

from the radial profile measured, and the density is then calculated from these two measurements. From Fig. 13.2, we can note that we don't reach the strong-drive regime (indicated in dashed blue curve) where the plasma frequency follows the frequency of the RW (see Sec. 13.1). Anyhow, for slow frequencies applied, the compression of the electrons follows a linear regime.

When the RW is switched on directly with a high frequency (above 3 MHz), we have noted that the tails of the plasma are not driven and not compressed. It seems that if the difference between the plasma rotation frequency itself and the RW frequency is too high, the electrons far from the center of the plasma don't follow the RW drive. This tends to explain the break in compression for a frequency above 3 MHz, in Fig. 13.2. In addition to this, the RW implies heating (losses) is quite important for high amplitude of the RW drive (fast compression).

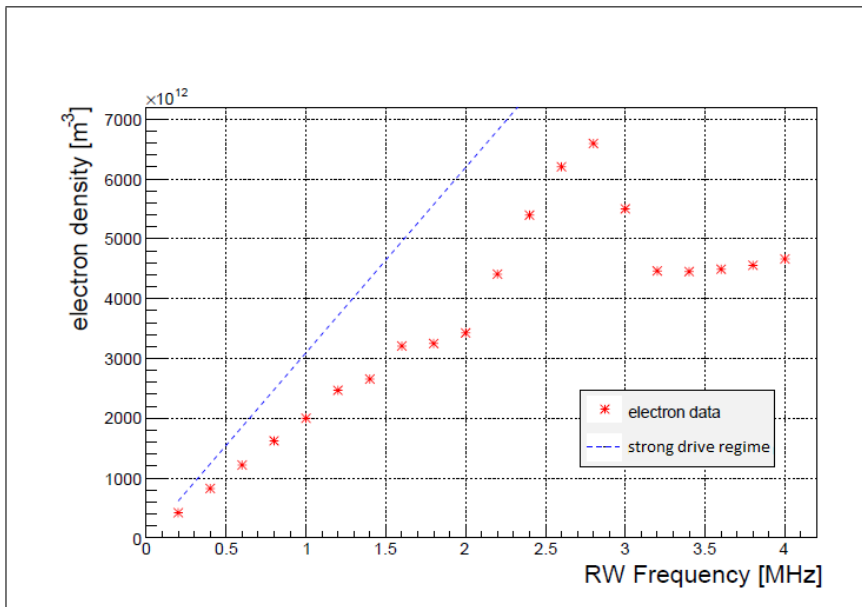


Figure 13.2: RW compression of electrons: scan of the response of the electron plasma under rotating wall drive, varying the frequency of the RW applied, for a fixed amplitude. The blue curve represents the strong drive regime. The red crosses are the density of the electron plasma achieved for different RW frequency.

Remark: The final size (compression) of the plasma is determined by

the frequency of the RW, whereas the speed of the RW drive is given by the amplitude (voltage applied). We did note that if we switch on the RW drive too fast (too high amplitude), the outer electrons seem not to be dragged and not compressed.

13.3.2 Procedure 1: catching and cooling of antiprotons - Study: centrifugal separation vs heating plasmas by RW drive.

In AEGIS, the starting point for any antiproton trapping and manipulation procedures begins with a pre-loading of electrons before the antiproton arrival. The antiprotons are caught at 9kV (end-caps voltage), and sympathetically cooled by the electron plasma. In the following, I call these two steps (loading electrons + catching antiprotons and cooling) the procedure 1. We studied two settings to maximize the fraction of antiprotons cooled by electrons.

- without any RW drive applied on electrons neither before the catching of \bar{p} nor during the sympathetic cooling the process.
- with RW drive active on electrons during all the procedure.

The motivation was to obtain as much as possible antiprotons, cooled and compressed before being transferred the production trap (ON-axis trap), and we had to determine which configuration was the most interesting for this purpose.

The procedure 1 begins with the loading of electrons ten seconds before the antiproton bunch arrival. The number of electrons loaded by our electron gun in the trap is typically $4 - 6.5 \times 10^8$. As seen in Sec. 13.3.1, the electrons are caught in the P trap (see Fig. 13.1), and thermalize by cyclotron radiation.

The antiprotons are caught in the 4.5 T trap, with the end-caps voltage set at 9kV. We typically confine about 1 - 1.3% of the antiproton bunch from the AD, corresponding roughly to $3 \cdot 10^5$ antiprotons. The overlap between the antiproton and the electron plasmas determines the fraction of antiprotons sympathetically cooled. The number of electrons loaded determines also the time needed for cooling. Typically, for $4 - 6.5 \times 10^8$ electrons, all the antiprotons that overlap with the e^- cloud are cooled within a cooling time of 40 s or 50 s: their axial energy, initially mostly of the order of keV, has decreased below 150 eV. The fraction of the remaining hot antiprotons is

released in a dump (I might refer as the "hot dump"), by reshaping the P trap to set the end-caps voltage at -150 V.

Using the electrodes located in the middle of the trap, we can create a deeper well to ensure that the cooled fraction of antiprotons remains in the trap, when applying RW drives. We typically used a 300 V depth after the hot dump: the cold antiprotons have then an axial energy of less than 300 eV.

Depending on the experimental settings, we can select if we apply a first RW (RW1) on electrons before catching antiprotons, or not. Then, we can either maintain it or switch it off during the antiproton cooling.

No RW drive on electrons before and during the cooling of antiprotons.

Without any RW applied to e^- neither before the antiprotons catching and nor during the cooling, the electron plasma is large, and the overlap between the \bar{p} and e^- plasmas is more consequent than if the case where a RW drive is first applied on the electrons. At best, we obtained an efficiency of 80% of cooled antiprotons in 50 s.

However, because of some instability with the electron gun, the loading of electrons (numbers, size of the plasma, tails) fluctuates, and induces changes in the efficiency of cooling of the antiprotons. Applying a RW drive tends to allow us to have a better control on the electrons ensuring the cooling (the compressed core).

Moreover, in the absence of any heating system to limit the sympathetic cooling, the antiprotons tend to centrifugally separate outward from the electrons. The cold and heavier antiprotons are repulsed from the center of the trap. This separation is expected for two cold species plasmas in equilibrium ([80]). The Fig. 13.3 gives an example of the centrifugal separation of the antiproton and electron plasmas in our trap.

When the antiprotons and electrons are centrifugally separated, the indirect compression of \bar{p} by the RW drive on electrons becomes difficult. We have noted that once the two cold plasmas are separated, when we want to apply a RW drive on electrons, only the antiprotons at the edges of the electron plasma are dragged with the electrons during the compression; the outer antiprotons don't follow the compression (tails effect).

Since we want to reach a dense plasma of antiprotons in order to enhance the formation rate of antihydrogen by charge exchange, we need to avoid the

centrifugal separation of cold antiprotons and electrons.

With a RW drive active before and during the cooling process

As seen in Sec. 13.3.1, a first RW can be applied to the electron plasma to compress it before the antiprotons arrive, in order to have a good control on the shape and density of the e^- plasma. It can be kept active once the antiprotons are caught to provide heats on both the \bar{p} and e^- plasmas, to avoid the centrifugal separation.

Indeed, it is important to note that if we kept the first RW active during the sympathetic cooling of the antiprotons, this RW drive does not induce compression on the antiprotons. Indeed, the electrons are typically loaded 10s before the antiprotons arrival. The first RW is applied just after the loading, and is then active for a long enough time to let the electron plasma reach its equilibrium and be compressed at the maximal density imposed by the frequency of the RW1. Once the antiprotons are caught, the RW1 doesn't imply compression on electrons anymore and thus there is no indirectly compression on antiprotons. This RW1 only generates heat to both plasmas and blocks the centrifugal separation during the cooling stage.

In AEgIS, we use the RW drive to apply a constant heating on the plasmas and thereby avoid the centrifugal separation.

The usual fraction of antiprotons caught that gets cooled by electrons in 50s is 55% up to 65%, depending on the RW1 frequency and amplitude chosen. We usually choose 0.3 MHz and 0.2 V for the first RW stage, and obtain about 60-62 % cooling efficiency, meaning that we obtained $2 \cdot 10^5$ cold antiprotons trapped into our system.

In our apparatus, the RW drive has to be active to prevent the centrifugal separation. In order to illustrate the importance of keeping the heating of the RW drive active during all the antiproton manipulation procedures, the Fig. 13.3 gives an example of the images, of both the antiproton and the electron plasmas, when the RW drive has been switched off one second before dumping the plasma toward the MCP. This leads to centrifugal separation.

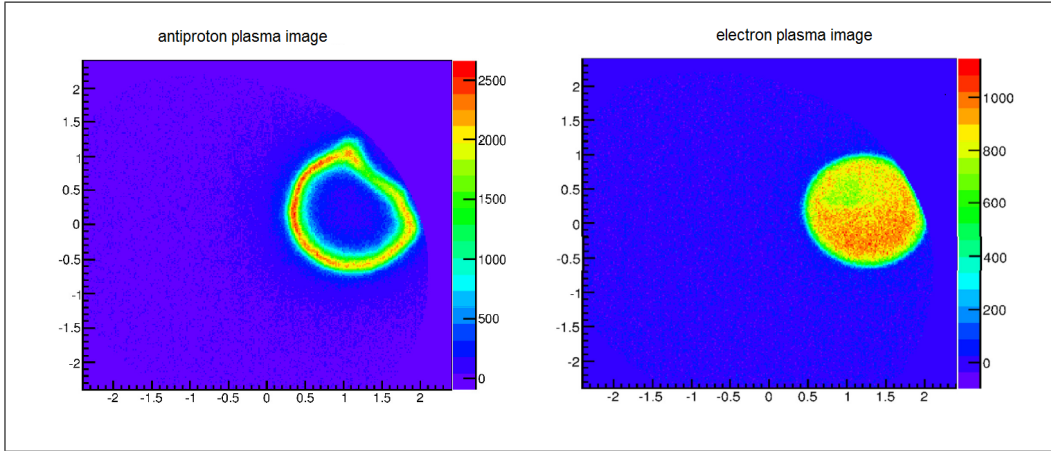


Figure 13.3: An example of the images of the antiproton (left image) and the electron plasmas (right image) on the MCP, in case of centrifugal separation. To obtain these images, the RW drive that was active during the cooling process is stopped 1 s before the electrons are first dumped, followed by the antiprotons after a delay of $250\mu\text{s}$.

However, in order to have a wide plasma and a large overlap between antiprotons and electrons, and thereby to a better cooling ratio, one could think about applying a RW drive on the electrons at a lower frequency than 0.3 MHz. Indeed, the final density of the electron plasma is determined by the frequency of the RW drive. A frequency <0.3 MHz would lead to a wider plasma and a bigger overlap between antiprotons and electrons. However, during our scans, we noted that if we used a lower frequency (<0.3 MHz), we observed a "boiling-off" effect on the antiprotons caught. The external scintillators counts, recording the annihilation of antiprotons, increase during the cooling procedure when the RW drive is active for low frequencies. These losses appeared to be radial losses of the antiprotons. A RW frequency lower than 0.3 MHz seems to induce some coupling with the radial modes of the \bar{p} plasma and provoke losses. That's why, we typically used 0.3 MHz as the RW frequency for the first RW drive in all our procedures.

We can note in Fig. 13.3 in the electrons image (right image) that the two traps are misaligned: electrodes in the 1 T trap obliterate the plasma from the 4.5 T trap projected onto the MCP ("tiger-eyes" phenomenon), we see an image "cut". However, for the antiprotons (right image), the deformation of the image observed comes from an additional phenomenon. The deformation

is due to $E \times B$ drift: during their flight from the 4.5 T trap toward the MCP, the antiprotons (much slower than the electrons) have time to interact with their own charge image of the (cutting) electrode. Since they travel close to this electrode (misalignment of the 4.5 T and 1 T axis), they actually feel their charge image and a change in the confinement E field compared to the center position of the trap (gradient), that cause a shift and also a deformation of the ring.

13.3.3 Procedure 2: a second faster RW applied once the antiprotons are cooled.

The second procedure we tested on antiprotons was developed to compress the antiprotons, after the electron cooling. A second RW drive (RW2) is applied just after the dump of the hot antiprotons.

As the procedure 1, this procedure starts with the compression of electrons with a slow frequency and amplitude (default value 0.3 MHz and 0.2 V). This first RW is kept active during the whole cooling process for 40 s or 50 s, once the antiprotons are caught. After the hot dump has been released, we apply a second RW stage (RW2) at a higher frequency to start compressing both plasmas. The antiprotons are dragged with the RW drive on electrons. Fig. 13.4 shows several images of the antiproton plasma obtained for different frequencies of the second stage of the RW, and for about 6.5×10^8 electrons loaded. The second column shows the reconstruction analysis tool, to compensate the tiger-eyes effect observed on the MCP due to misalignment of the 4.5 T and on-axis 1 T traps.

During these scans, we varied the number of electrons loaded into the trap. We observed that the maximum compression achieved depends on the density of the e^- : a lower number of electrons appears to allow a stronger compression, for the same RW frequency and amplitude values. This phenomenon is illustrated in Fig. 13.5. In the first row, the compressed images of the antiproton plasma is shown for different frequencies of the second RW stage, with 6.5×10^8 electrons loaded in the trap (case 1). In the second line, the number of loaded electrons is reduced to 4×10^8 (case 2).

For all the compressions scans presented in Fig. 13.5, the first RW stage was applied for 50 s (cooling time) at a frequency of 0.8 MHz and an amplitude of 0.2 V. The second RW stage was applied for 20 s.

Besides, it is worth noticing that the number of cooled antiprotons we

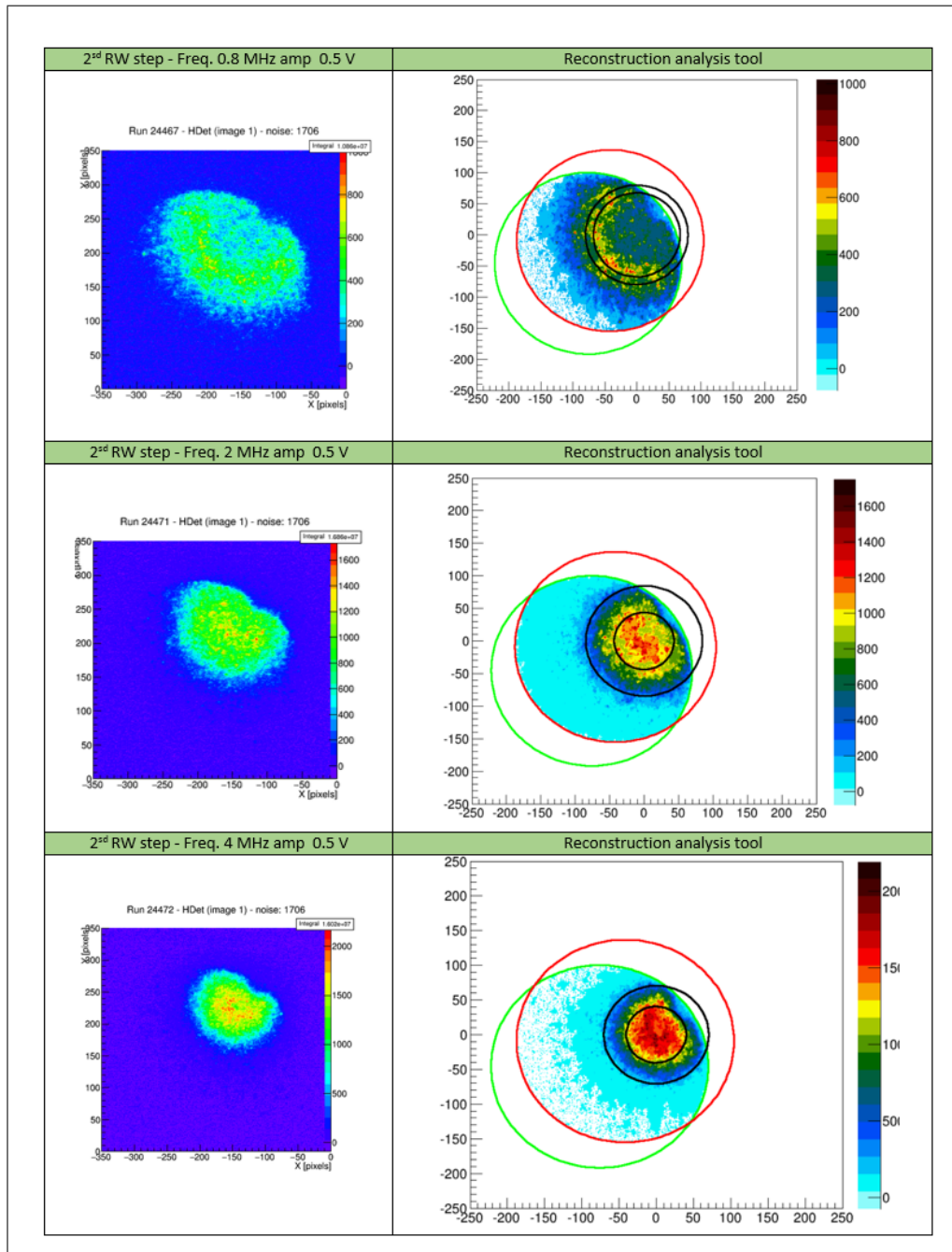


Figure 13.4: Example of MCP images of the antiproton plasma, for different frequencies of the second RW stage. An increase of the frequency of the RW enhances the compression of the plasma. The first column gives in false-color the images of the MCP without analysis treatment, whereas the second column shows a reconstruction fit of the cut plasma to obtain a value for the radii of interest. The black circles delimit the plasma FWHM and the intensity of the signal at about 3 sigma above the background. We applied a radial symmetry to determine the profile of the plasma. The green and red circles delimit the electrodes inner diameter of the 4.5 T and 1 T traps that are misaligned.

measured for the case 2 where $4 \times 10^8 e^-$ are loaded in the trap seem to be roughly in the order of the number of the cold \bar{p} obtained with the larger number of electrons 6.5×10^8 (case 1). Indeed, in the second case, about 55-60 % of the caught antiprotons are sympathetically cooled, whereas for the case 1, with a larger number of electrons, the cold fraction is about 60 - 65 %. The fluctuations of the AD facility, shot by shot, makes it difficult to carry out a precise comparison for the two loading electron cases, and we will need to accumulate more data on this procedure. However, it seems that the number of antiprotons for the case 2 is only slightly lower than for the case 1, whereas the compression of the antiproton plasma, for the same frequency and amplitude of the RW drive appears to be much bigger for the case 2 than the case 1 (see Fig. 13.5). This would imply that for the same frequency of the RW2, a better compression on the antiprotons can be achieved if the number of loaded electrons is lower.

In the Fig. 13.5, we only present results for two typical numbers of electrons (6.5×10^8 and $4 \times 10^8 e^-$). However, we did continue to decrease the number of electrons loaded before the antiprotons catching, and carried on the frequency scan. The final compression on \bar{p} appeared to be even better for lower number of electrons, for the same frequency of the second RW applied.

Anyhow, the choice of the ideal number of electrons to be loaded is not that easy. A compromise has to be done between the final compression achieved on antiproton plasma (low number of electrons in the trap) and the fraction of cooled \bar{p} obtained (high number of electrons). Indeed, if the number of electrons first loaded is too small, the compression at the first stage of the RW will lead to a small compressed e^- plasma. Then, the overlap between the electron plasma and antiprotons caught that get sympathetically cooled will decrease. Moreover, the time needed to cool the antiprotons has to be also considered: by reducing the number of electrons, the cooling time is extended (less collisions), and we aim to have relatively fast procedures to use as much as possible the antiproton bunches from the AD, deliver every ≈ 120 s.

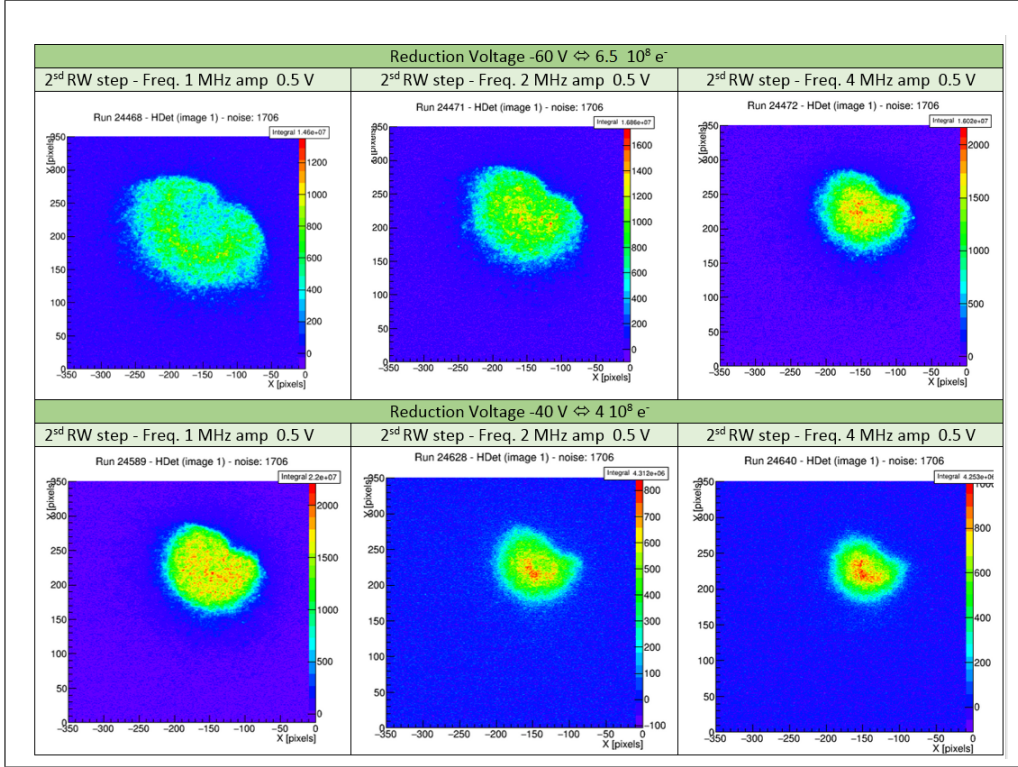


Figure 13.5: MCP images of the antiproton plasma - scan of the second RW stage frequency, for two electron loading conditions: the first row presents the results of compression on antiproton plasma, with 6.5×10^8 electrons loaded into the trap (case 1), for three different RW2 frequencies. The second row gives the image of the antiprotons for the same three RW frequencies, with an initial cloud of 4×10^8 electrons (case 2). The maximum compression achieved seems to be reachable for a reduced number of electrons, and this, only for a slight trade-off in the number of cold and compressed antiprotons - see discussion above.

At the end of these scans, we decided that a good compromise was to load $4 \cdot 10^8$ electrons into the trap before the antiproton catching.

13.3.4 Procedure 3: a third RW stage, with a reduced number of electrons

After the conclusion of the previous scans, we came up with the idea of applying the compression RW stages, with a reduced number of electrons,

after the cooling process. The idea is then to keep a large number of electrons for the phase of cooling (before the release of the hot dump) in order to have a big overlap between antiprotons caught and electrons to quickly cool a maximum of \bar{p} . Then, since we have seen that a better compression is achieved with a lower number of electrons, we remove a fraction of them and start the RW compression.

In other words: the third procedure presented here consists of following the standard loading and compression of electrons before the antiprotons arrival, and keeping it active during 40 s of cooling (first RW stage). We typically load 4×10^8 electrons into the trap, in order to reach a fraction of 55-60 % cold antiprotons. Then, the remaining fraction of hot antiprotons is dumped by reshaping the trap (procedure 1). A second stage of RW is applied during 20 s or 40 s (RW2) to start the compression of the electrons (procedure 2). The innovation of this third procedure resides in removing one fifth of the electrons in fast kicked. During the process, more than 90% of the antiprotons ($\sqrt{\frac{m_{\bar{p}}}{m_{e^-}}} = 42$ times slower) stay in the reshaped trap. A third RW stage is applied afterward, with a higher frequency or amplitude, during 20 s or 40 s and a further compression is achieved on the antiprotons.

Fig. 13.6 shows the FWHM of the antiproton plasma radial profile as a function of the third RW frequency. As the image of the plasma is obtained in a 1 T magnetic field region and the procedure is developed into the 4.5 T trap, a correction on the size of the plasma has been applied (factor 2.1 smaller in the higher magnetic field region).

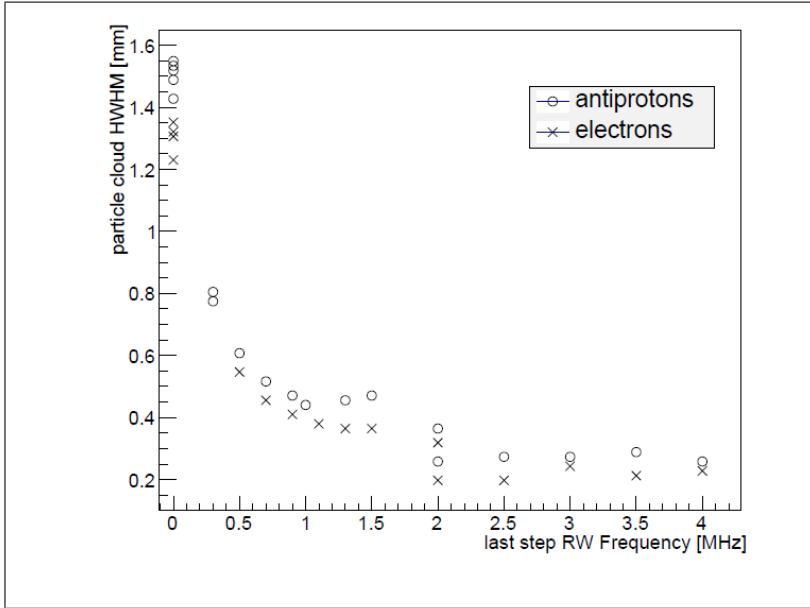


Figure 13.6: Results of the third RW stage applied on a reduced electron plasma: the FWHM of the antiproton plasma’s radial profile in the 4.5 T is plotted as a function of the third RW frequency.

For the results plotted here, the two first RW frequencies were set at 0.3 MHz, for 0.1 V, and for a number of $4 \cdot 10^8$ electrons. Our best compression results are obtained for a third RW frequency above 2 MHz with 0.5 V and a compression during 20 s, where the FWHM is below 0.4 mm, for typically $2 \cdot 10^5$ antiprotons.

Some antiprotons losses are observable during the third RW process, when the frequency applied higher than 4 MHz, probably due to an excessive heating of the plasma.

13.3.5 Procedure 4: toward a fourth RW stage and higher compressions of e^- and \bar{p}

Finally, we implemented a procedure that adds a fourth RW stage, on even more reduced electron plasma compared to the procedure 3. After the third RW compression, a second fast removal of electrons is performed whereas the trap is reshaped to be smaller. Even if a full scan of this procedure hasn’t been carried out because of some vacuum issues and lack of time, this technique looks promising. In Fig. 13.7 is gives one of the best compression

results we obtained for a fourth RW frequency of 2 MHz, with 0.5 V applied during 20 s of compression. The radial profile of the antiproton plasma is presented in two cases: without any compression stage (blue dots) and with the four RW drives applied to the plasma (procedure 4). The size correction (from 1 T to 4.5 T environment) has been applied to the data. The FWHM radius is found to be $170\mu\text{m}$.

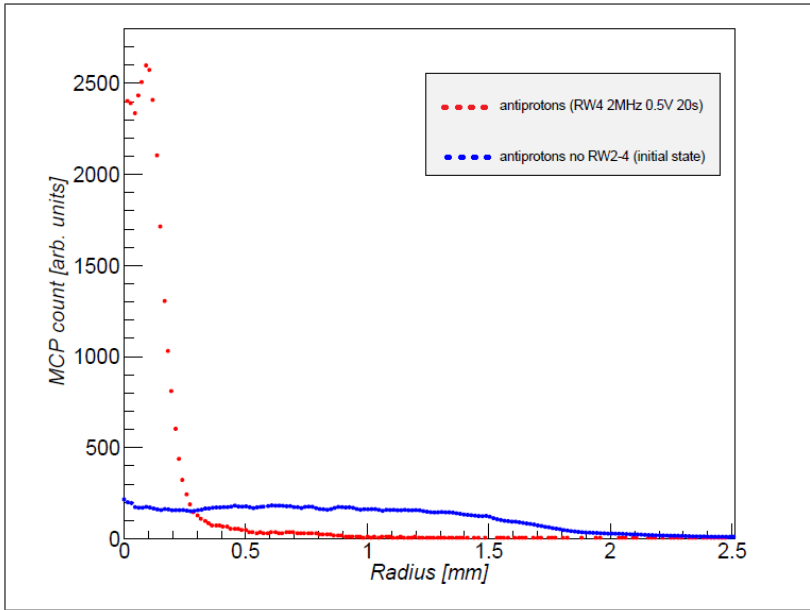


Figure 13.7: Radial profile of the antiproton plasma without compression (blue dots) and with (red dots) the procedure 4 where four RW stages are applied.

We can note the hole in the radial profile of the compressed antiprotons (red dotted curve) in Fig. 13.7, that results from a partial centrifugal separation of the electron and antiproton plasma.

13.4 Summary

Typically, from a good AD bunch (intensity $3 \cdot 10^7 \bar{p}$), we are able to catch $3 \cdot 10^5$ antiprotons into our trap at 4.5 T and 9 kV end-caps voltage. Then, within 150 s, up to $2 \cdot 10^5$ antiprotons are sympathetically cooled by electrons. Thanks to several stages of RW on electrons, the antiprotons are driven to a highly compressed plasma: from the procedures we developed,

we are able to reach \bar{p} plasma of radius below 0.4 mm, into a 10 cm long trap, with a 4.5 T magnetic field confinement.

During the last beamtimes, we rather focused on improving the compression procedures, since a high density of the antiproton plasma is required for an efficient transfer toward the production region trap, at 1 T. However, we could easily increase the number of caught antiprotons by improving our trap control electronics in order to extend the end-cap voltage from 9kV to 12kV (no hardware limitation). This could increase drastically the number of antiprotons in our trap. Moreover, each step of the procedures described above could be optimized further more to enhance the number of \bar{p} cooled and compressed.

Because of some vacuum issues during the beamtime of 2015 and consequent bad lifetime of the antiprotons in the trap, the full characterization of the procedures hasn't been carried out, and more systematic measurements for procedure 4 need to be done. The behavior of the tails of both the electrons and antiproton plasmas needs to be fully characterized for the procedures 3 and 4, as well as the possible losses when the RW applied is too fast or too strong. Typically, we load $4 \cdot 10^8$ electrons into the trap before catching antiprotons, and apply a slow RW of 0.3 MHz and 0.2 V for few tens of second. This first compression on electrons leads to an overlap of the two plasmas that results in a cooling efficiency of 55-65 % for the sympathetic cooling: about $2 \cdot 10^5$ antiprotons are cooled after being caught. This rotating wall is usually kept active in order to produce some heat on both plasmas to avoid centrifugal separation, during the 40 -50 s of the cooling process. Then, several stages of RW can be applied. We observed that reducing the number of electrons allow for better compression of the antiproton plasma, for a fixed RW frequency. We developed further procedures that alternatively use RW stages and electron removals. Final compression of the \bar{p} plasma, down to 400 μm (FWHM of the radial profile) were achieved.

These nice preliminary results indicate that our trap system provides highly repeatable conditions and great compression results, necessary for an efficient production of antihydrogen. As mentioned in the description of the ON-axis trap in Sec. 12.3, where the production of antihydrogen is planned to occur, the presence of grid in the top of the electrodes perturbs the stability of the antiproton confinement. In order to limit this effect, the plasma needs to be compressed in the center of the trap, far from the grid default.

Chapter 14

Toward a sympathetic cooling of antiprotons - the laser cooling of molecular anions

As mentioned previously in the introduction of the Part II, a key element to increase the antihydrogen formation via charge-exchange is to use a cold antiproton plasma, since the cross section of the reaction depends on the relative velocity between the antiproton, the center of mass of the Ps and the orbital velocity of the positron [15]. Moreover, AEGIS aims to form a cold beam of 100 mK antihydrogen atoms. The temperature of the antihydrogen atoms depends mainly of the temperature of the antiprotons in the charge-exchange process. Several techniques can be use to cool ion plasma in a Penning trap, among them are:

- The buffer gas cooling [81]. This consists of the exchange of energy between the trapped ions and the particles of a low-pressure gas that undergo elastic collisions. This gas is usually chosen to be light and inert, as for instance the He gas. This technique works for cyclotron and axial but not for the magnetron motion ; the temperature limit is the apparatus temperature. This technique is for instance used in AEGIS for the positron system in the Surko and Accumulator traps (See Chap. 3)
- The resistive cooling [81]. For this technique, a resistor is connected between the two end-caps electrodes. The ions moving in the trap induce a charge image in the electrodes. This charge image follows the motions of center of mass of the ions, and then leads to a movement of electric charges through the resistor system that dissipates energy.

This energy comes from the motional energy of the ions in the axial direction. This technique leads to an exponential decrease of the axial motion of the center of mass of the ions, down to the temperature of the apparatus.

- The radiative cooling [81]. This technique is based on the fact that charged particles radiate when they don't undergo a constant motion. For non-relativistic energies, in magnetic fields, this phenomenon is generally called synchrotron radiation, and this leads to the thermalization of the particles with the environment. This specially works well for light charged particles (electron/positron) since the radiation rate γ_{rad} is inversely proportional to the cube of the mass. The radiation rate

for the cyclotron motion (radial) is derived in [74]: $\gamma_{rad} = \frac{q^4 B^2}{3\pi, \epsilon_0 c^3 m^3}$.

For electron (or positron), the thermalization time $t_{th} = \frac{1}{\gamma_{rad}}$ is then 2.6 s in a 1 T environment, and about 0.13 s in a 4.5 T environment. However, for antiprotons 1800 times heavier than electrons, the thermalization time is too long to be considered, in comparison for instance to the stability of the trap (heating process).

- The electron cooling. Sympathetic cooling of ions can be performed using electrons cooled by cyclotron radiation. For cations, this technique can use the so-called nested Penning traps, as first performed by D. Hall and G. Gabrielse in 1996 [82]. This consists of an M shaped trap: the electrons are loaded and cooled in the central part of the M. The positive ions are confined in the inverted part of the potential well, on both sides of the central region, where they can interact with the electrons and get cooled. Applying this technique to antiprotons has the great advantage that the electrons and \bar{p} can be caught in the same trapping well. Usually, the electrons are pre-loaded to be cooled before the antiprotons arrival and improve the cooling efficiency. In AEgIS, from the centrifugal separation we measured during standard catching/cooling procedure, we estimate the cold fraction of the antiprotons trapped and cooled in the 4.5 T apparatus to be around 80 K when the RW drive is kept active. In Chap. 13, the procedures presented to compress the antiproton plasma use electron cooling to first cool antiprotons but also to compensate the heating coming from the rotating wall drive.
- The adiabatic cooling [74]. This consists of opening the trap's walls slowly. By this action, the ions cool down due to the volumetric expansion.

sion. To stay adiabatic, the changes of the electric and magnetic fields of the trap has to be slower than the time-scale of the ions motions and slower than the collisions time. Under these conditions, the ion cloud stays at equilibrium and can be described by a Maxwell-Boltzmann distribution. In this technique, the antiprotons density decreases.

- The evaporative cooling, that consists of elastic collisions that scatter high energy particles out of the confining trap, decreasing then the temperature of the remaining particles. In 2010, the Alpha collaboration performed an evaporative cooling on antiprotons [83], to reach with the remaining \bar{p} a cooled plasma of about 9 K.
- Direct laser cooling. The first demonstrations of laser cooling on trapped ions have been performed in 1978 [84, 85], on Ba^+ and Mg^{2+} ions. The theoretical analysis of laser cooling for both free and trapped atoms can be found in [86]. In this chapter, I will more specifically deal with the possibility of a laser cooling on the molecular anion C_2^- , that is even more tricky for several reasons I discuss later in Sec. 14.1. The direct laser cooling requires that the charged particle has at least two internal bound states ; e.g. this technique is then irrelevant for cooling antiprotons.
- **The sympathetic cooling using another (laser cooled) species.** Demonstrated in 1980 [87] on isotopes of Mg^+ ions, the sympathetic cooling by directly laser-cooled species on a simultaneously trapped second species can be powerful. The trap stability has to be carefully checked for both trapped species, for the ions to reach a common equilibrium temperature. For instance, the Gbar experiment plans to sympathetic cool a single antihydrogen ion \bar{H}^+ with laser cooled Be^+ ions [88]. The use of a third species with an intermediate mass as the hydrogen-deuterium ion HD^+ has been considered to play the role of a buffer species to increase the sympathetic cooling efficiency. I studied the possibility to sympathetic cool the antiproton plasma with anions (see Sec. 14.1). This chapter is specially dedicated to the study of the cooling of the molecular anion C_2^- .

More details for all the techniques mentioned above could be found for instance in [34, 81] where most of the trap techniques, plasma manipulations, cooling and detections are reviewed. In the thesis of D. Krasnický [74], results of the radiative, adiabatic and resistive cooling techniques can be found for the AEgIS apparatus.

14.1 A possible laser cooling of anions to sympathetically cool antiprotons in AEgIS

In the AEgIS proposal [15], a temperature of 100 mK is assumed to efficiently form a cold beam of antihydrogen atoms to perform gravity tests. To reach such a cold plasma, a possibility is to use cold anions to sympathetically cool the antiprotons. Indeed, most of the standard cooling techniques I reviewed above lead to a final temperature close to the ambient temperature of the apparatus. Even if AEgIS setup is cooled at cryogenics liquid helium temperature (4.2 K), the antiproton plasma, cooled by electrons, is far above the 100 mK foreseen for the gravity measurement.

That's why the laser cooling of anions is under study in AEgIS. The choice of atomic anions is limited, since the excess electron is only weakly bound by quantum-mechanical correlation effects. As a result, only a few atomic anions are known to exhibit electric-dipole transitions between bound states: Os^- , La^- and Ce^- [89, 90, 91]. The group of A. Kellerbauer has studied the spectroscopy of atomic anions, as Os^- [92] and La^- [93] to find the proper candidate, and a laser cooling scheme is under development for La^- .

For molecules, the situation is quite different because their electric dipole can bind an extra electron, and even di-anions have been found to exist [94].

That's why a parallel study plans to use molecular anions instead of atomic anions, since the number of potential suitable candidates for a laser cooling seems larger. One major problem for applying laser cooling to molecules is to find a closed cycle of transitions, in order to avoid to populate dark states that would stop the cooling process. Although it has already been successfully performed for neutral diatomic molecules [95], it has never been done so far for anions. Some challenges of the laser-cooling molecular ions have been described in [96]. For direct laser cooling of diatomic molecules, a key ingredient is a good branching ratio, i.e. Franck-Condon factor, between vibrational levels in order to close the absorption/emission cycle of the cooling scheme with only few levels involved.

In this chapter, I will deal more specifically with one molecule selected during our reviewing of the possible candidates: the C_2^- anion. It presents a well known spectroscopy as well as good Franck Condon coefficients to close with a few lasers the transition $X \leftrightarrow B$ (see Fig. 14.1 where the green arrows indicate the cooling scheme), repumping the vibrational ground states up to $v''=4$. This implies that Doppler laser cooling could be possibly considered,

the details of the cooling scheme and some results are presented in Sec. 14.3.

Besides, I studied a scheme to apply a Sisyphus cooling on the transition $X \leftrightarrow A$, in a Penning-like trap with a gradient of magnetic potential for the C_2^- molecule, and I develop this idea in the Sec. 14.4 - see Fig. 14.1 with the transition indicated by the red arrows.

The results presented here are published in Ref. [18].

14.2 The C_2^- molecule

In order to find a proper cooling scheme, it seems appropriate to select a molecule with good FC factor. However, the choice of the most suitable candidate is not obvious since a compromise has to be found between using fast electronic transitions and choosing extremely good FC factors. A list of possible candidates is given in our article [18]. This necessary preliminary research has been performed mainly by D. Comparat. I focused my studies on the C_2^- anion physics and simulations, presented here. This molecule presents the great advantage that its spectroscopy is very well-known. The C_2^- molecule exhibits a $B^2\Sigma_u(v' = 0) \leftrightarrow X^2\Sigma_g(v'' = 0)$ system and a $A^2\Pi_{1/2,u}(v' = 0) \leftrightarrow X^2\Sigma_g(v'' = 0)$ system with 72% and 96 % branching ratio, respectively. As an homonuclear molecule, C_2^- doesn't present a decay channel through $B^2\Sigma \rightarrow A^2\Pi$, as heteronuclear molecule does, that is also a great benefit. Finally, this anion has the notable advantage of not presenting any hyperfine structure.

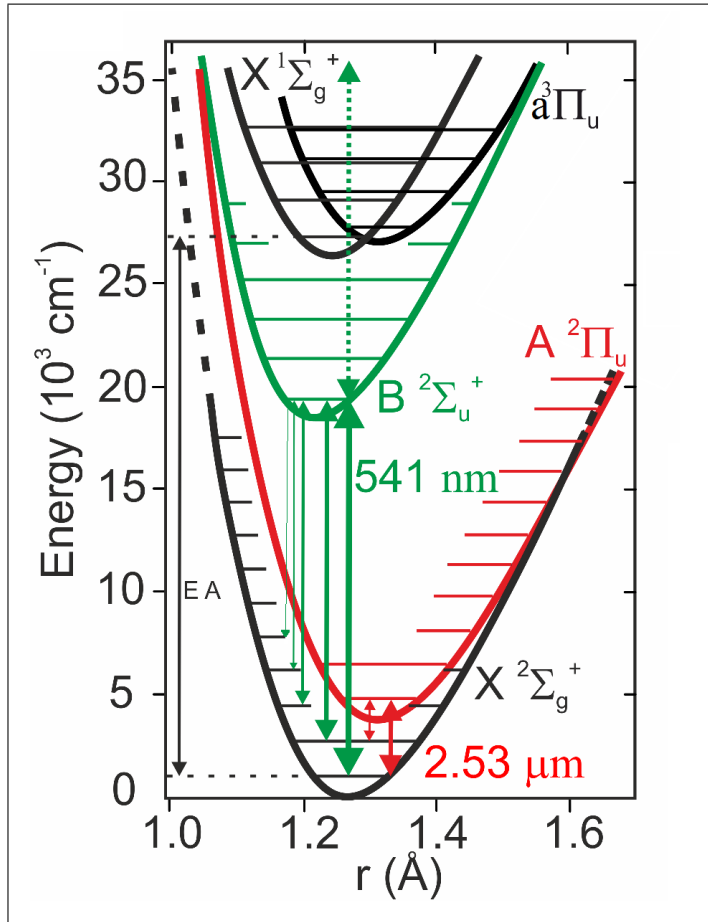


Figure 14.1: C_2^- level structure. Electronic and vibrational levels, as well as the optical transitions potential laser cooling are drawn, in the absence of magnetic field. The green arrows show the Doppler cooling scheme on the $X \leftrightarrow B$ transition, with a possible photodetachment (dashed green line). The red arrows point out the transitions that could be used for a Sisyphus cooling on the $X \leftrightarrow A$ transition. The widths of the arrows are proportional to the transition strengths given by the Franck Condon coefficients. Besides, the two fundamental electronics levels of the neutral molecule the C_2 are presented: the $X^1\Sigma_g^+$ and $a^3\Pi_u$ states.

In Fig. 14.1 is presented the electronic and vibrational levels of C_2^- . Its three electronic levels are shown: the ground state $X^2\Sigma_g^+$ (in black), and the two excited states $A^2\Pi_u$ (in red) and $B^2\Sigma_u^+$ (in green). The green arrows present the Doppler scheme studied on the $X \leftrightarrow B$ transition, that I develop in Sec. 14.3 ; the red arrows show the transitions over $X \leftrightarrow A$ to try to perform a Sisyphus-type laser cooling - see Sec. 14.4. To illustrate the possibility

of a photodetachment of the electron, two fundamental electronics levels of the neutral molecule the C_2 are presented too: the $X\ ^1\Sigma_g^+$ and $a^3\Pi_u$ states.

14.3 The first scheme: Doppler cooling over $X \leftrightarrow B$ transition

The first cooling scheme I studied was a Doppler cooling on the transition $X(v''=0) \leftrightarrow B(v'=0)$. For a 3D laser cooling, 6 counter-propagating lasers are set on the $X(v'' = 0, N'' = 2) \leftrightarrow B(v' = 0, N' = 0)$ transition and 2 repumping counter-propagating lasers are needed on the $X(v'' = 0, N'' = 0) \leftrightarrow B(v' = 0, N' = 0)$. Besides, because of a FC factor of only 72% between the $X(v''=0)$ and $B(v'=0)$ states, an optical repumping is needed to close the cooling circuit. 8 counter-propagating (on the direction $\pm z$) repumper lasers have been considered to pump the higher vibrational ground states $X(v''=1,2,3$ and 4). The widths of the green arrows in Fig. 14.1 indicate the weight of the FC factors and the transitions involved in the cooling scheme. The dotted green arrow illustrated the possibility of a two-photon absorption and a photoionization of C_2^- , that has been taken into account in our simulations.

14.3.1 The 3D optical molasses

We first studied the possibility of cooling C_2^- without external field to capture the particles. When looking for a possible cooling scheme for ions, it is common to confine them with external fields before applying any laser cooling. That's why at first glance, this study may appear like a simple exercise in style. However, we considered interesting to investigate the possibility of removing the strong external trapping field, in the same spirit of what it was realized for the first laser cooling of neutral molecules (YO [97] and SrF [95]), which was performed in a magnetic optical trap (MOT). Besides, removing the external trapping field would allow to get rid of the micro motion that perturbs the cooling in Paul and Penning traps: for instance, the group of Ch. Schneider, T. Schaetz and coworkers [98] succeeded in cooling Ba^+ cloud by dipolar force in 2010.

Before considering an optical molasses for ions, it is worth noting that an anionic beam can be brought close to standstill very easily by an electric field [99] unlike for neutral molecules which are difficult to produce at low velocity, despite the development of techniques such as velocity filtering or

buffer gas cooling (see detailed list in [100]).

If we consider a typical beam of C_2^- is produced with a current of 1 nA and emitted at 1000 eV with an energy dispersion of 1 eV [101], then a 1000 volt potential electrode can decelerate such a beam. Moreover, due to the energy dispersion of the beam, the stability of this voltage power supply is not critical. Typically 1/100000 of the anions (i.e. 0.01 pA current) will be decelerated inside the box to below an energy of 0.01 mV. This corresponds roughly to 0.1 K, which is within the capture range of molasses cooling.

We first studied the possibility of laser cooling in free space: we simulate a 3D molasses cooling on a cloud of 150 particles at an initial temperature of 80 mK, with a spherical Gaussian distribution ($\sigma_{rms} = 4$ mm). All the lasers are CW lasers, with a power of 0.5 W, a 2 cm waist and a red detuning of 10 MHz from the transition. The laser parameters values have been determined and optimized after a scan of each different parameters around theoretical values, in order to obtain .

Indeed, it is worth noticing that the $X(v''=0, N''=2) \leftrightarrow B(v'=0, N'=0)$ transition corresponds to the usual Doppler cooling over a broad-line case:

$$E_{recoil} = \frac{\hbar^2 k_L^2}{2 m_{C_2^-}} = \frac{\hbar^2 \left(\frac{2\pi}{541 \text{ nm}} \right)^2}{2 \times 2 \times 12 \text{ a.u.}} = 1.9 \cdot 10^{-29} \text{ J} \quad (14.1)$$

$$\hbar \Gamma_s = 1.38 \cdot 10^{-27} \text{ J} \gg E_{recoil}$$

where *a.u.* is the atomic mass. In this case, the radiation pressure force can be used to roughly determined the cooling strength of the interaction, as function of the laser power, detuning and bandwidth - see Append. D.

In Fig. 14.2(a) is presented the evolution of the kinetic energy of the cloud over time (black), that corresponds to the $T_{3D,50\%}$ defined in Chap. 8. We can note a first increase in temperature at 1 ms. This is explained due to the conversion of the Coulomb potential (repulsions) energy into kinetic energy: for the initialization parameters of the particles, we have arbitrary chosen a density of the cloud that leads to a Coulomb repulsion force stronger than the confinement force of the trap. That's why, at the first instants of the simulations, the charged particle cloud extends, that is translated by the increase of the kinetic energy. Then, a fast cooling down to 1 mK is observed, even if most of the molecules escape from the laser waist interaction area (dashed red curves). The molecules that leave the laser interaction zone are

lost for the cooling process, I refer to them as "losses".

During the optimization of the cooling parameters, we observed that the final temperature and losses depend on the initial density (defined by the σ_{rms} of the Gaussian distribution of the cloud) because of space charge effects that counter the cooling. In these first simulations, we didn't attempt trapping in a MOT configuration (Optical Molasses trapping). Indeed, the Zeeman effect of $B(v' = 0, N' = 0)$ is weak (quadratic behavior [102]), and realizing a MOT would require a magnetic-field gradient that produces a Lorentz force stronger than the laser trapping one.

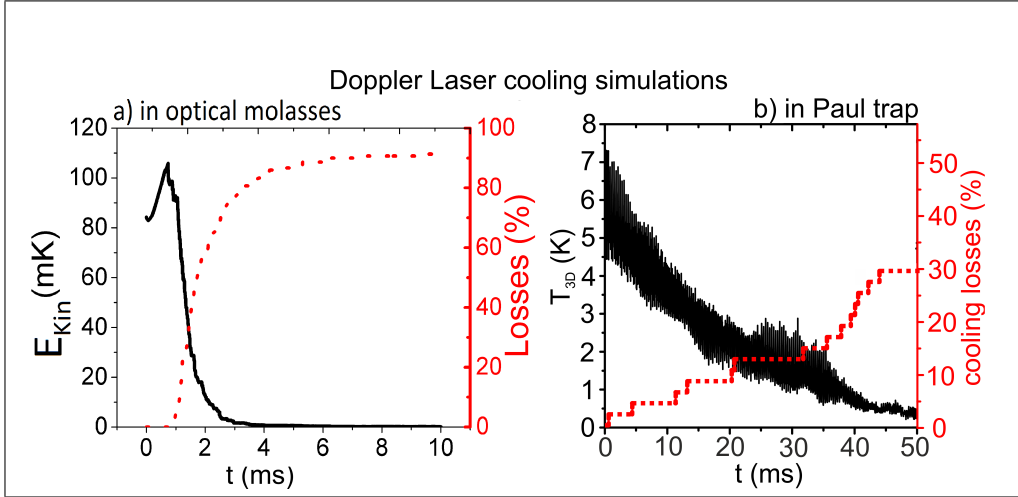


Figure 14.2: Doppler laser cooling results, cycled on the $X \leftrightarrow B$ transition of the C_2^- molecule. (a): the 3D molasses cooling. Result of the 3D laser cooling simulation of an initial bunch of 150 anions at 80 mK. The red dashed curve gives the population losses, corresponding to molecules which escape from the laser interaction area. The kinetic energy evolution (in temperature unit) of the remaining particles is plotted in black. (b): The Doppler cooling in a Paul trap. In black, evolution of the temperature initially at 5K in a Paul trap. The red dashed curve gives the population losses, through photo-ionization or decays into high vibrational ground states that are non repumped ($v > 4$).

This 3D free-cooling appears to work for diluted cloud of particles (to limit the Coulomb interaction and fast expansion of the cloud that escapes from the laser interaction area), and for initial temperatures below the hundreds of mK.

14.3.2 In a Paul trap

We then simulated the Doppler cooling over the transition $X \leftrightarrow B$ in a Paul trap. For simplicity, we only considered the motion in a harmonic pseudo-potential well $V(\mathbf{r}) = 1/2 m \omega_r(x^2 + y^2) + 1/2 m \omega_z^2$. That consists of averaging the RF micro-motion, as done in [103].

We considered here 5 K as an initial temperature for the C_2^- cloud. This could correspond to a pre-cooling, using for instance a buffer gas (Helium). The lasers are set with a 600 MHz red detuning, and a spectral laser bandwidth of $\sigma_L=35$ MHz, values coming from an optimization scan of each parameter to find the best laser cooling efficiency. We also set the repumping lasers for the different vibrational levels of the ground state X up to $X(v'' = 4)$, as shown in Fig. 14.1(a). But since the particles are trapped, the repumping lasers are only along the $+z$ direction, and we use only 4 repumpers.

In Fig. 14.2(b), the simulation result is presented where a cooling down to 60 mK is achieved within 50 ms. The photo-detachment process has been taken into account. Because the photo-detachment cross-section of C_2^- for the B-state is unknown, we used the order of magnitude of the photo-detachment cross section of C_2 , $\sigma_{ph,C_2} \sim 10^{-17} \text{ cm}^2$ [104] as a typical value.

For a laser intensity of $I = 0.16 \text{ W/cm}^2$, the photo-detachment rate for the B-state is then $I\sigma_{ph}/h\nu = 4.3 \text{ s}^{-1}$. For our simulation parameters that define the excitation rate ($X \leftrightarrow B$), within 50 ms of interaction, only 3 % of the molecules are lost by photo-detachment ($X \rightarrow B \rightarrow \text{Continuum}$).

In addition to the photo-detachment losses, we considered that the molecules decaying into the high vibrational ground states $X(v'' > 4)$ are lost for the cooling process (dark states). The total losses' evolution over time is shown in Fig. 14.2(b) in the red dotted curve.

The Doppler cooling in the Paul trap gives promising results (a temperature of less than 100 mK can be reached within 50 ms), with 12 lasers to close the cooling cycle (2 cooling laser on the transition $|X, v'' = 0, j'' = 3/2\rangle \leftrightarrow |B, v' = 0, j' = 1/2\rangle$ along $\pm z$, 2 repumping laser on $|X, v'' = 0, j'' = 1/2\rangle \leftrightarrow |B, v' = 0, j' = 1/2\rangle$ on $\pm z$, and 1 laser along $+z$ for each transition $|X, v'' = 1, 2, 3, 4, j = 1/2, 3/2\rangle \leftrightarrow |B, v' = 0, j' = 1/2\rangle$).

. Even if we need 12 lasers are required here, we believe that this sketch could be experimentally implemented, using for instance fiber laser technology.

We note that for these simulations, the trap is loaded using an initial (non thermalized) Gaussian velocity distribution. The evolution of this non equilibrium system leads to the high frequency velocity variations and thus to the instantaneous temperature fluctuations visible in Fig.14.2(b), due to the oscillations of the particles in the trap. Indeed, when a particle oscillates into a trap, the kinetic energy is exchanged into potential energy, then back to kinetic energy. At the beginning of the simulations, each particle of the cloud is randomly attributed an initial velocity v picked from a Maxwell-Boltzmann distribution at T_0 ($p(v) = \left(\frac{m}{2\pi k_B T_0}\right)^{3/2} \exp\left(-\frac{m v^2}{2 k_B T_0}\right) d^3v$). The contribution of every particle that oscillate in the trap with different maximal kinetic energy, leads to the fluctuations of the global temperature at each time t , $T_{instantaneous} = \langle T_{inst,i} \rangle_{i \in \{x,y,z\}} = \sqrt{\frac{1}{3} \sum_{i \in x,y,z} T_{inst,i}^2}$, with $T_{inst,t}$ defined below.

In order to try to reduce the instantaneous temperature fluctuations in our simulations, I started to investigate a way to force the thermalization of the cloud of particles in motion inside the trap, before we start the laser cooling.

An idea proposed by Berendsen and coworkers [105] is to couple the molecules to an external bath to force the thermal equilibrium. Coupling the particles to a thermostat makes the instantaneous temperature of the cloud converge toward T_0 (enhanced thermalization). To do so, their algorithm proposes to apply a correcting factor λ to the velocity of each particle of the cloud, at every time evolution step Δt . The λ factor models the coupling to an external bath at T_0 .

For a given time t , we determine the factor $\lambda(t)$ to apply to the velocity of each atom at the time $t + \Delta t$. The velocity at $t + \Delta t$ is modified by $\forall i \in \{x, y, z\}$, $v_i(t + \Delta t) = \lambda(t)v_i(t)$, where $\lambda(t)$ is determined by [105]:

$$\lambda(t) = \left(1 + \alpha \left[\frac{T_{inst,i}}{T_0} - 1 \right] \right) \quad (14.2)$$

with α the coupling strength of the particle cloud to the thermostat; and $T_{inst,i}$ the "instantaneous equivalent temperature" along the i axis for the entire cloud of the N particles, such as $T_{inst,i} = \frac{2}{k_B} \frac{1}{N} \sum_{j \leq N} \frac{1}{2} \times m \times (\bar{v}_i - v_{i,j})^2$ (see Eq (8.1)).

The strength of the coupling α determines the time required to reach the equilibrium. This parameter has to be carefully tuned, to find a compromise between a fast thermalization process and smooth changes in the velocity distribution to avoid any numerical artifact error. Typically, Berendsen and coworkers considered a coupling time $\tau = \alpha \Delta t = 0.4$ ps, where Δt is evolution time step taken for the calculations of the dynamics evolutions. I have updated the optical pumping C++ code to implement this enhanced thermalization, before we start the laser cooling. The full study of this algorithm hasn't been yet carried out for our C_2^- simulations, but its effectiveness seems to be mostly linked to the strength of the coupling. Besides, since the laser cooling wipes out the thermal equilibrium, the instantaneous fluctuations the global cloud temperature, due to the motion of particles with different velocities, continues to be present during the cooling process. Since the laser cooling of a diluted C_2^- cloud in trap would probably lead experimentally to a non thermal equilibrium condition, we consider that forcing the thermalization in our simulations was not crucial for our purposes.

14.4 The second scheme: Sisyphus cooling over $X \leftrightarrow A$ transition

A solution to avoid the losses of C_2^- through photo-detachment or decays into high vibrational levels of the ground-state is to cool through the A-state. This cooling has very similar characteristics (linewidth, wavelength) to those of La^- [91] but with a lighter particle and no photo-detachment in the case of C_2^- . The cooling over the transition $X \leftrightarrow A$ is slow $\tau_{spont,A(v'=0)} \approx 50 \mu s$ ([106]) compared to the usual lifetime of the transitions used in the laser cooling of the Alkali atoms. This corresponds to a Doppler cooling over a narrow-line case: $E_{recoil} = \frac{\hbar^2 k_L^2}{2 m_{C_2^-}} = 1.8 \cdot 10^{-30} J \sim \hbar \Gamma_s = 2.1 \cdot 10^{-30} J$. The particularities of this kind of transition have been seen for the Ps atom cooling case (See Chap. 7).

Anyhow, the cooling scheme considered in this third simulation is new. It consists of performing a Sisyphus-type laser cooling [57], on the $X \leftrightarrow A$ transition. We call "Sisyphus" cooling any cooling scheme that makes a particle climb again and again a potential hill. During the process, the particle losses energy. The trick is then to find a way to place back the particle at the beginning of the potential hill, just after its has reached the top of the

hill, without gaining back the same amount of energy lost.

In the scheme we developed, the particles are trapped into a modified Penning trap, where the magnetic field has a gradient from 0.2 T to 2 T - see Fig. 14.3 a). This gradient creates the potential hill needed for the Sisyphus cooling process, indicated in Fig. 14.3 b). Due to the axial motion induced by the electric trapping potential (300 μ s oscillation time in the simulation), particles move between the high (2 T) and low (0.2 T) magnetic fields at both ends of their axial range.

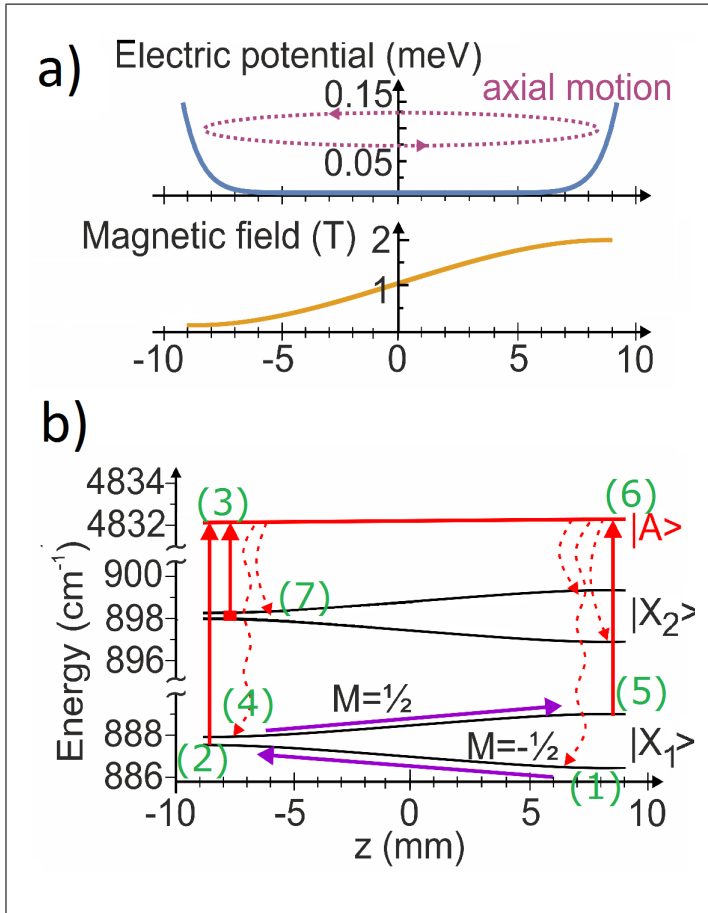


Figure 14.3: Detail of the Sisyphus cooling principle. a) Schematic of the trapping potentials. The trap considered here is a Penning-like trap, with a harmonic electric potential to confine the axial motion (upper graph). The confinement of the radial motion is insured by a magnetic field varying from 0.2 T to 2 T, in ~ 1.5 cm long. This magnetic gradient field creates the Sisyphus potential hill. b). A zoom on the $X \leftrightarrow A$ energies: $|X_1\rangle = X(v'' = 0, N'' = 0)$ and $|X_2\rangle = X(v'' = 0, N'' = 2)$ $|A\rangle = A(v' = 0, N' = 1, J' = 1/2)$. From the magnetic field gradient, the corresponding Zeeman effect on the C_2^- internal level states is represented. Laser excitations and spontaneous decays are illustrated with red solid line and red dashed line respectively. The different steps of the cooling cycle are indicated by the green numbers in parenthesis - see description in the text.

The sisyphus cooling cycle is explained in Fig. 14.3 b), with the different steps of the cycle indicated by the green numbers in parenthesis. A useful cooling cycle can be described by the following steps: a given particle ini-

tially in the ground state $|X_1\rangle, M_1 = -\frac{1}{2}$ in position 1 oscillates in the trap, climbs the potential hill before getting excited in position 2 toward $|A\rangle$ state (position 3). There, the particle is spontaneously emitted to the $|X_1, M = \frac{1}{2}\rangle$ in position 4. The particle oscillates and climbs the potential hill and gets excited in position 5 to the state A (position 6). There, the particle spontaneously decays to position 1. The cooling cycle is closed.

The repumper laser on the transition $|X_2\rangle \leftrightarrow |A\rangle$ in position 7, excites the atoms that spontaneously decay from the position 3 and 5 of the cooling cycle in the $|X_2\rangle$ states, in order to allow the deexcitation toward $|X_1\rangle$ and continue the cooling process.

The energy gaps between the $|X_1\rangle, M_1 = -\frac{1}{2}$ and $|X_1\rangle, M_1 = \frac{1}{2}$ states, due to the Zeeman splitting, leads to a huge amount of energy removed for each useful cooling cycle. More than 1 K is removed for each closed absorption-emission cycle, as the molecule continuously climbs the magnetic potential hill.

14.4.1 The simplest scheme with 3 lasers

Here, we studied the evolution of the axial temperature, set initially at 60 K for a cloud of 200 anions. For our low density plasma there is no coupling between radial and axial motions. The radial shape of the plasma follows the inhomogeneous magnetic field, thus the plasma is more compressed in the 2T field region, and has a larger radius in the 0.2 T region.

For the first simulations, two cooling lasers for the transitions $|X_1\rangle \leftrightarrow |A\rangle$ are detuned at $2.5351 \mu\text{m}$ and $2.5358 \mu\text{m}$ to be respectively resonant at 0.2 T and 2 T, along the $X(v'' = 0, N'' = 0, M'' = -1/2)_{0.2T} \leftrightarrow A(v' = 0, N' = 1, J' = 1/2)_{0.2T}$ and $X(v'' = 0, N'' = 0, M'' = 1/2)_{2T} \leftrightarrow A(v' = 0, N' = 1, J' = 1/2)_{2T}$ transitions. The laser power is set at 0.05 W for a 1 mm waist, and a spectral bandwidth of 100 MHz.

In order to reduce the number of lasers, the repumping of the losses in the $X(v'' = 0, N'' = 2)$ states is performed ($|X_2\rangle \leftrightarrow |A\rangle$ transition) with only one single broadband ($\sigma_L = 6000$ MHz, $P_L = 0.05$ W) laser which addresses all the Zeeman-split sub-levels, resonant at 0.2 T. The transitions pumped by laser are indicated in Fig. 14.3 b).

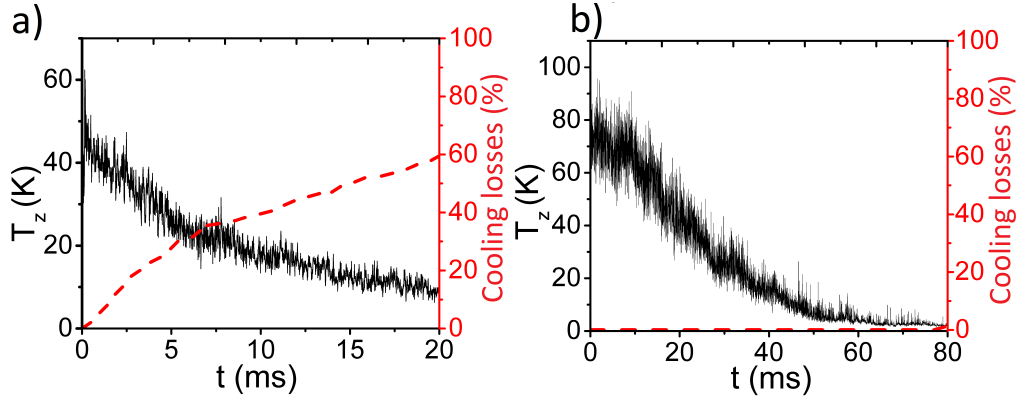


Figure 14.4: Sisyphus cooling results. The black curves correspond to the evolution of the axial temperature of the cloud, the red dashed curves indicate the number of C_2^- lost during the cooling process. Sisyphus cooling performed in an inhomogeneous Penning trap and cooled on the $X \leftrightarrow A$ transition, without (a) or with (b) repumping the $X(v'' = 1)$ state. The initial temperatures of the cloud are respectively 60 K and 100 K.

The simulation result is presented in Fig.14.4(a). In tens of ms, the axial temperature is cooled down from 60 K to few K. The lost population indicated in dashed red reached 60 %. This is mainly due to the spontaneous decay to $X(v'' = 1)$.

14.4.2 With repumping lasers on the vibrational state $X(v''=1)$

We then studied the same cooling scheme, repumping the $X(v'' = 1)$ states. In Fig. 14.4(b) is presented an alternative simulation where the decays in the vibrational $X(v'' = 1)$ states are repumped by two lasers at $4.574 \mu\text{m}$ and $4.593 \mu\text{m}$. These lasers address the $X(v'' = 1, N'' = 0) \leftrightarrow A(v' = 0, N' = 1, J' = 1/2)$ and $X(v'' = 1, N'' = 2) \leftrightarrow A(v' = 0, N' = 1, J' = 1/2)$ to be both resonant at 0.2 T, with a spectral bandwidth of 6 GHz and a power of 0.1 W.

Although this simulation requires 2 more lasers, it has the clear advantage of cooling a greater part of the molecules, since less than 0.5% of anions fall in the $X(v'' = 2)$ black levels within 80 ms. This has to be compared with

the first case without repumpers, where 60% of the C_2^- decay into the black states $X(v'' = 1)$ within 20 ms. These encouraging results seem they tend to indicate that a powerful cooling could be realized on molecular anions, without populating dark states too fast.

As for the Doppler cooling in the Paul trap, we load the trap using an initially non thermalized Gaussian velocity distribution. The evolution of this system toward the equilibrium leads to the instantaneous temperature fluctuations observed in the results in Fig.14.4.

14.5 Conclusion

In this chapter, I have presented three possible deceleration and laser cooling schemes for anionic molecules, either in free space or trapped, by using Doppler or Sisyphus cooling. The Sisyphus cooling scheme proposed here on the transition $X \leftrightarrow A$ has the great benefit of getting rid of the problem of photo-detachment.

Finally, among these three cooling schemes studied, the Sisyphus cooling appears to be the most promising for the AEGIS apparatus. The project Borealis, led by Sebastian Gerber, within the AEGIS collaboration has started in 2015 to commission and develop the test-setup at CERN. The experimental construction of the C_2^- source has started in the summer 2016, as well as the mass spectrometer. Since the first studies published in 2015, we have considered other cooling schemes to cool the C_2^- molecules, such as a possible laser evaporative cooling, on the transition $X \leftrightarrow A$: this will consists of exciting the hottest particles by Doppler selection, then photoionizing the selected anions. A foreseen problem is that the hot electrons removed will probably stay trapped in the Penning trap where the C_2^- are confined, heating up the cold remaining particles.

We have also tried to find out technical solutions to build a trap complying with the Sisyphus cooling scheme. In addition to the difficulties to build with permanent magnets a stable Penning-like trap with a strong gradient of field, it seems that collective effects of the plasma will affect the motion inside the Sisyphus trap if the gradient of magnetic field is too steep ([107]). An idea will be then to build a standard Penning trap, and locally create a potential hill generated by dipolar force (strong detuned laser). The depth of a dipolar well will be quite limited, and the amount of energy lost at every cooling cycle will be smaller (≈ 1 mK) than for the potential hill created by Zeeman splitting as presented in Sec. 14.4. However, with many oscillations

in the trap, this cooling alternative could be efficient. This is one of the many solutions currently studied by the group of S. Gerber in AEGIS, in which D. Comparat and I still take an active part.

We could note that if successful, the production of a cold C_2^- plasma would be more suitable for the AEGIS purposes than the La^- cold plasma. Indeed, the small mass ratio between C_2^- atoms and \bar{p} seems to be promising for an efficient sympathetic cooling of the antiprotons, as studied in [88], if compared with the La^- mass difference with the antiproton.

Chapter 15

Conclusion and perspective

During these three years of my Ph.D, we obtained significant results that paved the way for the antihydrogen formation in AEGIS. As for instance the first Ps laser excitation to the $n=3$ level [19], used as an intermediate state to reach the Rydberg states $n=15 - 17$. These measurements were performed in the test chamber, in low electro-magnetic field environment (600 V/cm and 200 G). The next step is then to carry out the laser excitation of Ps inside the 1 T magnetic field environment of the main apparatus. This is one of the big objectives for the beam times of 2016 and 2017.

During the previous beam times of 2014 and 2015, we have developed reliable and efficient procedures to manipulate the electron and antiproton plasmas. On average, about 1% of the antiprotons provided by the AD ring are caught, and between 55% to 65% are cooled sympathetically by electrons ; meaning that for a typical run, we have 2×10^5 cold antiprotons. Compression procedures, using several rotating walls stages have been tested, leading to a maximal radial compression of the plasma down to 200 μm (radius of the FWHM) for the best results inside the 4.5 T magnetic field trap. A good compression is mandatory to be able to transfer the \bar{p} plasma toward the production trap inside the 1 T magnet. Besides, a compressed antiproton plasma is required to enhance the stability of confinement of the production trap (whose electrodes have grids on the top to let pass through the Ps* cloud), and then increase the production rate of the antihydrogen atoms.

In parallel to the experimental results obtained, I worked on future projects to enhance the antihydrogen formation:

- The sympathetic cooling of the antiproton plasma, using laser cooled molecular anions. The theoretical studies to determine the most suitable candidate and the best laser cooling schemes have been carried out

[18]. It appears that the C_2^- molecule is a good candidate, with its spectroscopy well-known and good Franck Condon coefficients. For instance, I found that a 100 K C_2^- cloud can potentially be cooled down to few Kelvin in tens of ms, using a Sisyphus-type laser cooling scheme, on the transition $X \leftrightarrow A$, where very few molecules are lost into dark states. The simulation results are promising, and the experimental setup is under development at CERN. The C_2^- source should be operational within the end of 2016.

- The direct laser cooling of Ps. The studies of both Doppler cooling and Dipolar focusing have been performed, and the simulations indicate that a 243 nm pulse of 50 ns long would already have a significant impact on the velocities distribution of the Ps cloud. However, building the suitable laser system still requires more work. The laser system based on dye-laser that I have installed at CERN generates a UV pulse of 4-8 ns, depending on the NdYAG pump used. A few ideas have been studied to stretch the UV pulse up to 50 ns, limiting the loss of energy during the process. But this needs now to be implemented, and some solutions still need to be found to ensure the stability of the laser, and the detuning of the spectral bandwidth. In addition to the development of the laser itself, the test chamber needs to be modified to prepare the cooling (two counter-propagating lasers are required) and install diagnostics.

These works represent some of the future improvements of the AEGIS apparatus, to prepare the gravity measurements in the best conditions.

Appendix A

Hydrogenoid atoms: scaling relations between Hydrogen and Positronium atom

The hydrogen atom is a simple two-body problem system, and its physics in quantum mechanics is analytically well-known. The Ps atom, as the bound state of an electron and an antiproton is also a two-body system, and its physics can be deduced from the hydrogen atom up to a certain point. This appendix is dedicated to derive some scaling relations between the hydrogen and the positronium atoms. The reader may refer to the ref [108], in whose spirit this annex was written.

A.1 General description

A hydrogenic atom consists of two charged particles (of respective mass m_1 and m_2), in Coulomb potential interaction.

In the Galilean laboratory frame, the total energy of the system is given by:

$$H_{tot} = \frac{p_1^2}{2m_1} + \frac{p_2^2}{2m_2} + V_{interaction} = \frac{p_1^2}{2m_1} + \frac{p_2^2}{2m_2} + \frac{q^2}{|\vec{r}_1 - \vec{r}_2|} \quad (\text{A.1})$$

Where: $q^2 = e^2/4\pi\epsilon_0$; $\vec{r}_1 = \overrightarrow{OM_1}$, $\vec{r}_2 = \overrightarrow{OM_2}$ are the respective positions of the two particles in the laboratory frame (O is the center of this frame, M_1 and M_2 the positions of the real particles), and \vec{p}_1 , \vec{p}_2 their momentum.

If the system of our two particles is isolated, we generally solve the problem introducing two fictitious particles: the center of mass (CM) particle and the reduced particle. The CM particle has the total mass of the system, $M_{CM} = m_1 + m_2$, and its motion ($\{\vec{R}_{CM}, \vec{P}_{CM}\}$) is given by the classical motion equation. We denote G the point position of the CM particle.

$$\vec{R}_{CM} = \overrightarrow{OG} = \frac{m_1 \vec{r}_1 + m_2 \vec{r}_2}{m_1 + m_2} \Rightarrow \vec{P}_{CM} = \vec{p}_1 + \vec{p}_2$$

It is then more practical to resolve the Schrödinger equation motion for the reduced particle into the center of mass frame, which is Galilean ($\ddot{\vec{R}}_{CM} = \vec{0}$). **In this frame, we consider only the relative motion of (real or reduced) particles with respect to the position of the center of mass particle (point G).** For the real particles M_1 and M_2 we have then the following relations:

$$\begin{cases} \vec{r}'_i = \overrightarrow{GM}_i = \overrightarrow{GO} + \overrightarrow{OM}_i = -\vec{R}_{CM} + \vec{r}_i \\ \vec{p}'_i = m_i \dot{\vec{r}}'_i = m_i (-\dot{\vec{R}}_{CM} + \dot{\vec{r}}_i) = -m_i \dot{\vec{R}}_{CM} + \vec{p}_i \end{cases}$$

Then, we obtain the following relations:

$$\vec{r}'_1 - \vec{r}'_2 = \vec{r}_1 - \vec{r}_2$$

We introduce then a vector \vec{r} as $\vec{r} = \vec{r}'_1 - \vec{r}'_2 = \vec{r}_1 - \vec{r}_2$, and introduce the notion of the reduced particle that is defined by the position vector \vec{r} . Reciprocally, in the CM frame, the real particle motion can be expressed thanks to the motion of the reduced particles:

$$\begin{cases} \vec{r}'_1 = -\frac{m_2}{m_1 + m_2} \vec{r} \\ \vec{r}'_2 = \frac{m_1}{m_1 + m_2} \vec{r} \end{cases}$$

and:

$$\begin{cases} \vec{p}'_1 = m_1 \dot{\vec{r}}'_1 = m_1 \left(-\frac{m_2}{m_1 + m_2}\right) \dot{\vec{r}} = -\mu \dot{\vec{r}} = -\vec{p} \\ \vec{p}'_2 = m_2 \dot{\vec{r}}'_2 = m_2 \left(\frac{m_1}{m_1 + m_2}\right) \dot{\vec{r}} = \mu \dot{\vec{r}} = \vec{p} \end{cases}$$

The reduced particle has then a mass of $\mu = \frac{m_1 m_2}{m_1 + m_2}$, and its motion vector is $\{\vec{r}, \vec{p}\}$ in the CM frame.

Now, we want to derive the total energy of the system (*cf.*(A.1)) in the CM frame. For that, we inject the following relation for a real particle i : $\vec{p}_i = \vec{p}'_i + m_i \dot{\vec{R}}_{CM}$ into the following sum:

$$\begin{aligned} \frac{p_1^2}{2m_1} + \frac{p_2^2}{2m_2} &= \frac{p_1'^2}{2m_1} + \frac{p_2'^2}{2m_2} + \frac{m_1^2 \dot{R}_{CM}^2}{2m_1} + \frac{m_2^2 \dot{R}_{CM}^2}{2m_2} + \frac{m_1 \dot{\vec{R}}_{CM} \cdot \vec{p}'_1}{m_1} + \frac{m_2 \dot{\vec{R}}_{CM} \cdot \vec{p}'_2}{m_2} \\ &\stackrel{\vec{p}'_1 = -\vec{p}'_2}{=} \frac{(m_2 + m_1)}{2m_1 m_2} p^2 + \frac{(m_1 + m_2)}{2} \dot{R}_{CM}^2 + 0 \\ &\Rightarrow \boxed{\frac{p_1^2}{2m_1} + \frac{p_2^2}{2m_2} = \frac{p^2}{2\mu} + \frac{P_{CM}^2}{2M_{CM}}} \end{aligned}$$

A.1.1 The positronium model

In this annexe, we focus on the Positronium atom, which is made of an electron coupled with its antiparticle, a positron. This atom is the lightest leptonic atom possible: the masses of the two particles are the same, $m_1 = m_2 = m_e = 9.109 \cdot 10^{-31}$ kg. Thus, we have the following reduced system:

$$\begin{cases} M_{CM}^{(Ps)} &= 2m_e \\ \mu^{(Ps)} &= \frac{m_e}{2} \end{cases}$$

We note that the reduced mass of the Hydrogen is

$$\boxed{\mu^{(H)} = m_e = 2 \mu^{(Ps)}} \quad (\text{A.2})$$

Here we want to scale some usual parameters from the Hydrogen's ones, such as the internal energy, the Bohr radius, and the photo-ionization cross section.

A.2 The time independent Schrödinger equation

A.2.1 For a reduced particle μ

We derive here the time independent Schrödinger equation in the reduced/center of mass particles' frame, by identifying the classical total energy

H of the Eq. (A.1) with the Hamiltonian operator of our global system. *This is possible because all the transformation done are linear operations.*

Thus, we obtain the following equation:

$$\left\{ \begin{array}{l} \hat{H}_{tot}\psi^{tot} = E\psi^{tot} \\ \Leftrightarrow \\ \left(\frac{\hat{p}^2}{2\mu} + \frac{\hat{P}_{CM}^2}{2M_{CM}} + \frac{q^2}{\hat{r}}\right)\psi^{tot} = E\psi^{tot} \\ \Leftrightarrow \\ \left(-\frac{\hbar^2\nabla_r^2}{2\mu} - \frac{\hbar^2\nabla_{R_{CM}}^2}{2M_{CM}} + \frac{q^2}{r}\right)\psi^{tot} = E\psi^{tot} \end{array} \right. \quad (\text{A.3})$$

Where ψ^{tot} is the eigenstate of the total system. Then, since we are placed in the CM frame, we can separate the eigen function of the total system into the product of the two partial wave functions describing the reduced particle and the CM particle:

$$\psi^{tot} = \psi^{(\mu)}\psi^{(CM)}$$

The only operator acting on the wavefunction of the CM particle, in the sub-system of the CM is $-\hbar^2\frac{\nabla_{R_{CM}}^2}{2M_{CM}}$. Thus, $\psi^{(CM)}$ has the following solution form:

$$\boxed{\psi^{(CM)} = \exp(-i\vec{k}\cdot\vec{R}_{CM})} \quad (\text{A.4})$$

Where the wavevector \vec{k} such as $E = \hbar c k$.

In the following, we simply refer to the wavefunction of the reduced particle by $\psi^{(\mu)} = \psi$. And finally, without any interaction with an external field, for the reduced particle for any hydrogenic atom, the time independent Schrödinger equation can be expressed as:

$$\left(-\frac{\hbar^2}{2\mu}\vec{\nabla}_{\vec{r}}^2 - \frac{e^2}{4\pi\epsilon_0 r}\right)\psi(\vec{r}) = E\psi(\vec{r}) \quad (\text{A.5})$$

It is well known ([109]) that the solutions are:

$$\psi(\vec{r}) = \psi_{n,l,m}(r, \theta, \phi) = R_{n,l}(r)Y_{l,m}(\theta, \phi)$$

We denote $\psi_{n,l,m}$ the eigenstates for the bound states, and by extension $\psi_{k,l,m}$ becomes the solutions for the continuum.

We usually denote the Hartree Energy as the following quantity:

$$E_{Ha}^{(\mu)} = \frac{\mu e^4}{(4\pi\epsilon_0\hbar)^2} \quad (\text{A.6})$$

Thus, the internal energy for a state ψ_n of a hydrogenic atom is given by:

$$E_n^{(\mu)} = \frac{E_{Ha}^{(\mu)}}{2n^2}$$

Thus, because of the $\frac{1}{2}$ factor between the reduced mass of the Ps and that of the H, the non-relativistic energy of Ps can be expressed by:

$$\boxed{E_n^{(Ps)} = \frac{1}{2} E_n^{(H)}} \quad (\text{A.7})$$

In other words, the whole well-known non-relativistic internal structure of the Hydrogen can be transposed to the Ps atom, by dividing each energy by 2 (See Fig. 2.1).

In a same way, we define the Bohr radius as:

$$a_0^{(\mu)} = \frac{4\pi\epsilon_0\hbar^2}{\mu e^2}$$

Thus, we obtain the following scaling for the Ps Bohr radius:

$$\boxed{a_0^{(Ps)} = 2 a_0^{(H)}} \quad (\text{A.8})$$

A.2.2 The 1D-Schrödinger equation

From the previous 3 dimensional equation A.5, the 1D-Schrödinger equation only depending on r can be derived ([61, 59]):

$$\boxed{\frac{\partial^2}{\partial r^2}(r R_l(r)) - \frac{l(l+1)}{r^2} r R_l(r) - \frac{2\mu}{\hbar^2 4\pi\epsilon_0} r U_l(r) = -\frac{2\mu}{\hbar^2} r R_l(r)} \quad (\text{A.9})$$

The solution of the equation (A.9) is well-known. The reader could refer to [109] or [61], and the normalized radial function can be expressed as:

$$R_{n,l}^{(\mu)}(r) = \left(\frac{2}{n a_0^{(\mu)}} \right)^{3/2} \left[\frac{(n-l-1)!}{2n(n+l)!} \right]^{1/2} e^{-Zr/(n a_0^{(\mu)})} \left(\frac{2Zr}{n a_0^{(\mu)}} \right)^l L_{n-l-1}^{2l+1} \left(\frac{2Zr}{n a_0^{(\mu)}} \right) \quad (\text{A.10})$$

This expression is helpful to study the scaling relation between the hydrogen and the positronium atom.

A.2.3 Scaling relation between Ps and H atoms

From the solutions given in Eq. (A.10) of the Eq. (A.9), we can derive the scaling relation between the Ps and the hydrogen wavefunctions:

$$\begin{aligned} R_{n,l}^{(Ps)}(r) &= \left(\frac{2}{n a_0^{(Ps)}} \right)^{3/2} \left[\frac{(n-l-1)!}{2n(n+l)!} \right]^{1/2} e^{-Zr/(n a_0^{(Ps)})} \left(\frac{2Zr}{n a_0^{(Ps)}} \right)^l L_{n-l-1}^{2l+1} \left(\frac{2Zr}{n a_0^{(Ps)}} \right) \\ &= \left(\frac{2}{n 2 \times a_0^{(H)}} \right)^{3/2} \left[\frac{(n-l-1)!}{2n(n+l)!} \right]^{1/2} e^{-Zr/(n 2 \times a_0^{(H)})} \left(\frac{2Zr}{n 2 \times a_0^{(H)}} \right)^l L_{n-l-1}^{2l+1} \left(\frac{2Zr}{n 2 \times a_0^{(H)}} \right) \\ &= \frac{1}{2}^{3/2} \times R_{n,l}^{(H)}\left(\frac{1}{2}r\right) \end{aligned} \quad (\text{A.11})$$

Since $\psi_{n,l,m}^{(\mu)}(r, R) = R_{n,l}^{(\mu)}(r, E) \times Y_{l,m}$, we finally obtained the following relation scale for the wavefunctions of Ps and Hydrogen atoms:

$$\boxed{\psi_{n,l}^{(Ps)}(r, E_n) = \frac{1}{2\sqrt{2}} \times \psi_{n,l}^{(H)}\left(\frac{1}{2} \times r, 2 \times E_n\right)} \quad (\text{A.12})$$

From this relation scale can be derived more complex relations, as for instance the electric dipole scaling relation between two states $|1\rangle$ and $|2\rangle$:

$$d_{|1\rangle,|2\rangle}^{(\mu)} = \langle 2|\hat{d}_{1,2}|1\rangle \quad (\text{A.13})$$

This leads then to:

$$\begin{aligned}
d_{|1\rangle,|2\rangle}^{(Ps)} &= \langle \psi_2^{(Ps)}(r) | q_e r | \psi_2^{(Ps)} \rangle \\
&= \int r^2 dr d\theta \sin(\phi) d\phi \psi_2^{(Ps)}(r) \times q_e r \times \psi_2^{(Ps)}(r) \\
&= q_e \frac{1}{2\sqrt{2}}^2 \times \int r^2 dr d\theta \sin(\phi) d\phi \psi_2^{(H)}\left(\frac{1}{2}r\right) \times q_e r \times \psi_2^{(H)}\left(\frac{1}{2}r\right) \\
&= q_e \frac{1}{2\sqrt{2}}^2 \times \int 2^3 r'^2 dr' d\theta \sin(\phi) d\phi \psi_2^{(H)}(r') \times q_e 2r' \times \psi_2^{(H)}(r') \\
&= q_e \frac{2^4}{2^3} \int r'^2 dr' d\theta \sin(\phi) d\phi \psi_2^{(H)}(r') \times q_e r' \times \psi_2^{(H)}(r') \\
&= 2d_{|1\rangle,|2\rangle}^{(H)}
\end{aligned} \tag{A.14}$$

$$\boxed{d_{|1\rangle,|2\rangle}^{(Ps)} = 2d_{|1\rangle,|2\rangle}^{(H)}} \tag{A.15}$$

A.3 Scaling relations - prospective

In this Appendix are given some of the most useful scaling relations between Ps and Hydrogen. This approach is powerful since it helps to predict and derive the Ps atomic physics properties of the Coulomb interaction (no QED and hyperfine structure energy correction). For instance, the internal energy for the state n for a positronium atom is half the internal energy of the corresponding level for the hydrogen atom ($E_n^{(Ps)} = E_n^{(H)}$), the lifetime of an excited state n of Ps is twice the spontaneous time of the corresponding level for the hydrogen: $\tau_{n=2}^{(Ps)} = 3.2 \text{ ns} = 2 \times \tau_{n=2}^{(H)} = 2 \times 1.6 \text{ ns}$. Moreover, from these scaling considerations, the photoionization cross section value can be numerically calculated [62], as well as the branching ratio between two states.

These relations were used for many simulation works on Ps I carried out during my thesis.

Appendix B

Photoionization probability for a 3-level system

Here, we want to derive an exact solution of the number of atoms photoionized, from the simple 3-level system described in Part.I Sec.6. The notation can be found in the Fig. 6.1. The ground state population is noted N_0 , the excited state one N_1 and the "continuum" fictive level is N_2 . This model is considered for a high photoionization regime, meaning that the spontaneous decay has been neglected in comparison to the photoionization process ($\Gamma_{spont} \ll \Gamma_{photo}, \Gamma_e$).

$$\begin{cases} \frac{dN_0}{dt} = \Gamma_e(N_1 - N_0) \\ \frac{dN_1}{dt} = -\Gamma_e(N_1 - N_0) - \Gamma_{photo}N_1 \\ \frac{dN_2}{dt} = \Gamma_{photo}N_1 \end{cases} \quad (\text{B.1})$$

where $\Gamma_{photo} = \Gamma_p$ the photoionization rate and Γ_e the, stimulated excitation rate.

B.1 An exact solution

The Eq. B.1 are linear equations, that can be easily solved when diagonalizing the matrix M such as $\frac{d}{dt} \begin{pmatrix} N_0 \\ N_1 \\ N_2 \end{pmatrix} = M \begin{pmatrix} N_0 \\ N_1 \\ N_2 \end{pmatrix}$. This leads to the solutions:

$$N_2(T) = N \left(1 - \frac{1}{2B} \exp\left(-\frac{1}{2}(A+B)T\right) \{ (A+B) \exp(BT) + (A-B) \} \right) \quad (\text{B.2})$$

where I considered the initial conditions $N_1(t=0) = N$ and $N_2(t=0) = 0$. We note $A = (2\Gamma_e + \Gamma_p)$ and $B = \sqrt{\Delta} = (\sqrt{4\Gamma_e^2 + \Gamma_p^2})$.

B.2 The high saturation hypothesis to simplify the formula

Since we worked in the high saturation regime for the photoionization laser, we can consider that $\Gamma_p T \gg 1$. That implies $(A-B) \ll (A+B) \exp(BT)$. We then approximate N_2 with:

$$N_2(T) \approx N \left(1 - \frac{A+B}{2B} \exp\left(-\frac{(A-B)}{2}T\right) \right) \quad (\text{B.3})$$

We introduce the factor α :

$$\alpha = \frac{\Gamma_e}{\Gamma_p} \quad (\text{B.4})$$

We can rewrite the factors:

$$\begin{aligned} A+B &= 2\Gamma_e + \Gamma_p + \sqrt{4\Gamma_e^2 + \Gamma_p^2} = \Gamma_p(1 + 2\alpha + \sqrt{1 + 4\alpha^2}) \\ A-B &= \Gamma_p(1 + 2\alpha - \sqrt{1 + 4\alpha^2}) \end{aligned}$$

And finally, for a ratio $\Gamma_p \times T \gg 1$, the photoionization probability for an excitation time T is :

$$\begin{aligned} P_{photo}(T) &= \frac{N_2(T)}{N} \\ P_{photo}(T) &\approx 1 - \frac{1 + 2\alpha + \sqrt{1 + 4\alpha^2}}{2\sqrt{1 + 4\alpha^2}} \exp(\Gamma_p T (\sqrt{1 + 4\alpha^2} - 1 + 2\alpha)) \end{aligned} \quad (\text{B.5})$$

B.3 Approximations formula - determination of the validity conditions

We want now to determine in which conditions the probability of photoionization can be approximated by:

$$\boxed{P_{photo}(T) \approx 1 - \exp(-\Gamma_e T)} \quad (\text{B.6})$$

as it has been done in the section (Part I Sec.6) analyzing the measurements results in the core of this thesis. These approximation conditions are defined by studying the value of the characteristic product $\frac{1}{\Gamma_p \times T}$.

For this, in Fig. B.1 we plotted in Mathematica the 3 different formula found for the photoionization probability:

- the Eq. (B.2): is the exact solution of the rate equations. The only approximation: the spontaneous decay has been neglected in comparison to the photoionization process - curve in blue
- the Eq. (B.5): gives an approximated solution, under the condition $\frac{1}{\Gamma_p \times T} \gg 1$ - curve in red
- the Eq. (B.6): is an intuitive solution derived from the 3-level system in case of high saturation regime, ($\frac{1}{\Gamma_p \times T} \gg 1$) - curve in green.

In Fig. B.1 are presented three sets of plots, for $\frac{1}{\Gamma_p \times T} = 5$, $\frac{1}{\Gamma_p \times T} = 10$ and $\frac{1}{\Gamma_p \times T} = 20$, as a function of α . We can note that for $\Gamma_p \times T = 20$, the three formula correctly match for any α , meaning for any excitation rate $\Gamma_e(\Omega, \delta) = \alpha \times \Gamma_p$. We conclude that for $\Gamma_p \times T \geq 20$, the approximated formula for the photoionization probability given in Eq. (B.6) is valid.

B.4 Verification of the approximation's validity made for our measurements analysis

We want here to justify the validity of the approximations we made in the chapter Chap. 6, where we considered the simple intuitive solution (in Sec. 6.1) to model the photoionization probability.

In order to verify in which regime we were for our measurements, we first have to express both Γ_p and Γ_e rates. To determine the stimulated excitation rate, we consider that the UV laser performing the transition $n=1 \leftrightarrow n=3$

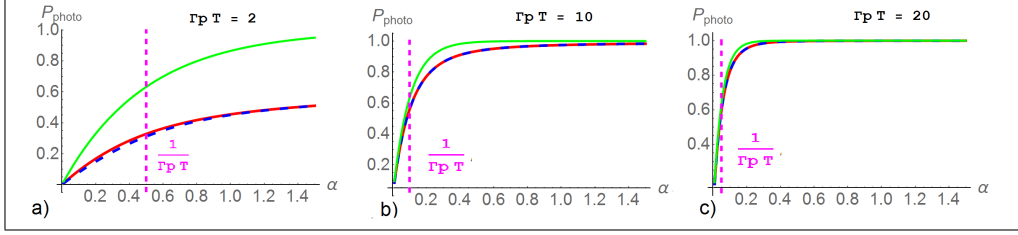


Figure B.1: Photoionization probabilities plots, for the 3 different formula: in dashed blue, the exact solution derived from the rate equation model Eq. (B.2) ; in red, the approximated solution Eq. (B.5), and in green, the simple solution intuited for the high saturation regime Eq. (B.6). a) $\Gamma_p \times T = 2$, b) $\Gamma_p \times T = 10$, c) $\Gamma_p \times T = 20$. Results are discussed in the text.

is a Gaussian with a spectral bandwidth (110 GHz) much larger than the natural bandwidth of the 3^3P excited level ($t_{lifetime} \approx 10$ ns) or the hyper-fine splitting (3 GHz). Then, the Lorentzian spectral distribution of the $n=3$ level can be approximated by a Dirac function centered on the wavelength λ_0 : $L_\omega = \delta(\omega_0)$.

Since the excitation rate Γ_e can be seen as the convolution of the laser irradiance spectrum (I_ω) and natural linewidth of the transition, with a normalization term ([58]. Appendix.B).

$$\Gamma_e(\delta, \Omega, \gamma_L) = [L_\omega \otimes I_\omega](\omega_0 - \mathbf{k}_L \cdot \mathbf{v}) \times \frac{\pi |d|^2}{\hbar^2 \epsilon_0 c} \quad (\text{B.7})$$

The convolution is then simplified by the Dirac function and gives:

$$\Gamma_e(\delta, \Omega, \gamma_L) = \frac{\Omega(r)^2 \pi}{2} \frac{1}{\sqrt{2\pi\gamma_L^2}} \exp\left(-\frac{\delta}{2\gamma_L^2}\right) \quad (\text{B.8})$$

with $\Omega(r) = \frac{|E_L d|}{\hbar}$ is the Rabi frequency norm of the laser-matter coupling, and σ_L the rms value of the laser bandwidth.

We calculated the value of photoionization rate Γ_p using the theoretical value of the photoionization cross section for the $n=3$ level $\sigma_{photo} = 3.48 \cdot 10^{-17} \text{ cm}^2$ [46], that leads to:

$$\Gamma_p = \sigma_{photo} \frac{I}{\hbar\nu} = 5.6 \times 10^9 \text{ s}^{-1} \quad (\text{B.9})$$

The laser intensity I is calculated for 60 mJ of 1064 nm, with a radius waist of 4 mm.

Here, we can verify the first approximation we made: the spontaneous decays has been neglected since we considered the photoionization process to be much faster to occur, i.e. we considered $\Gamma_p \gg \Gamma_{spont}$. This hypothesis is thus valid since the lifetime of the 3^3P level is about 10 ns. This leads to a spontaneous rate $\Gamma_{spont} = \frac{1}{10ns} = 0.1 \cdot 10^9 \text{ s}^{-1} \ll \Gamma_p = 5.5 \cdot 10^9 \text{ s}^{-1}$.

Besides, for an interaction time of 4ns, corresponding to the IR pulse time(FWHM), we find a parameter $\alpha_{crit} \approx \frac{1}{20} \approx 0.05 \ll 1$. In other terms, with our experimental settings, we have a factor $\Gamma_p \times T = 5.5 \cdot 10^9 \times 4 \text{ ns} = 22$. As we have seen in the previous section, this regime corresponds to the Fig. B.1 c). In this case, the probability of photoionization can be perfectly approximated by the simple formula Eq. (B.6).

In particular, for our measurements settings, the excitation rate Γ_e can be calculated considering the laser energy and detuning:

$$\Gamma_e = \text{function}(\Omega(r), \delta) = \text{function}(\Omega, \delta) \quad (\text{B.10})$$

We here neglect the r dependence of the Rabi frequency to only consider its peak value $\Omega = \Omega(0)$, and introduce instead a total spatial efficiency factor η . This approximation is discussed in the following section B.5. The transition electrical dipole strength d can be calculated theoretically using:

$$d = \sqrt{\Gamma_{spont} \frac{3 h 4\pi\epsilon_0 \lambda^3}{64\pi^4}} \approx 1.65 \text{ Debye} \quad (\text{B.11})$$

Leading to:

$$|\Omega| = \frac{d E_L}{\hbar} = \frac{d \sqrt{\frac{2 I_L}{\epsilon_0 c}}}{\hbar} = 5.24 \cdot 10^{10} \text{ s}^{-1} \quad (\text{B.12})$$

The excitation rate for a laser at resonance ($\delta = 0$) and 110 GHz (FWHM) large is then $\Gamma_e = 5.75 \cdot 10^9$. This gives a ratio $\alpha = \frac{\Gamma_e}{\Gamma_p} = \frac{5.75}{5.51} \approx 1.1$.

According to the Fig. B.1 c), when we are the case $\Gamma_p T = 20$, the three curves perfectly match for this α value. We have justified here our use of the

simple solution for the photoionization probability in Part.I Sec.6, in case of high saturation regime for the photoionization process:

$$P_{photo}(T, \Gamma_e) = 1 - \exp(-\Gamma_e T)$$

B.5 The geometrical factor η approximation

In the previous calculations and analysis, we decided to use a total geometrical factor η to take into account the lasers and Ps cloud overlap as well as the spatial dependence of the efficiency of the laser-matter coupling. Here, we discuss the validity of this approach.

In general, the excitation process and thus the photoionization probability depend on the spatial variation of the laser intensity $I(\mathbf{r})$, that defines the coupling strength or the Rabi frequency $\Omega(r)$ such as:

$$\Omega(r) = \frac{d E_L}{\hbar} = \frac{d}{\hbar} \times \sqrt{\frac{2 I(r)}{\epsilon_0 c}} \quad (\text{B.13})$$

Where the laser intensity profile $I(\mathbf{r})$ is taken to be Gaussian, with a variance $\sigma_{r,L}$. The spatial dependance of the Rabi frequency can be written as:

$$\Omega(r)^2 = \Omega(0)^2 \times e^{-\frac{x^2 + y^2}{2\sigma_{r,L}^2}} \quad (\text{B.14})$$

where, $\{x,y,z\}$ are the spacial coordinates in the test chamber, as indicated in Fig. 5.1. The z axis is the direction of the incoming e^+ pulses that are implanted in the target area. The $\{x,y\}$ plane is the parallel plane to the target converter where the lasers are shined, so $\{x, y\}$ is the transverse plane to the e^+ and Ps clouds propagation.

We want now to demonstrate that it is possible to remove this spatial dependance of the photoionization probability by introducing a global geometrical factor η , in case of a low saturation regime on the $n=1 \leftrightarrow n=3$ transition, and a high saturation of the photoionization process.

In this case, for a spatial localization \mathbf{r} in the laser spot, and a velocity \mathbf{v} of Ps, and for the laser set at the resonance, the probability of photoionization is given by:

$$\begin{aligned}
P_{photo,approx} &= 1 - \exp(\Gamma_e T_{int}) \\
&\approx \Gamma_e \times T_{int} \\
P_{photo,approx}(r, \delta_0, \mathbf{v}) &\approx \frac{\Omega(r)^2}{\sqrt{2\pi}\sigma_{r,L}} e^{-\frac{(\delta_0 - \mathbf{k}_L \cdot \mathbf{v})^2}{2\sigma_{r,L}^2}} \times T_{int} = P_{photo,r,v}(r, \delta_0, \mathbf{v})
\end{aligned} \tag{B.15}$$

The probability of photoionization for a fixed r integrated over the Ps cloud velocity distribution is then:

$$P_{photo,r}(r, \delta_0) = \int_{-\infty}^{+\infty} P_{photo,r,v}(r, \delta_0, \mathbf{v}) \times p_v dv \tag{B.16}$$

where p_v is the velocity distribution of the Ps, defined by a Boltzmann distribution of a cloud at a temperature T :

$$p_v = \frac{1}{2\pi\sigma_T^2} e^{-\frac{v^2}{2\sigma_T^2}} \text{ with } \sigma_T = \sqrt{\frac{k_B T}{m_{Ps}}} \tag{B.17}$$

We obtained:

$$\begin{aligned}
P_{photo,r}(r, \delta_0) &= \int_{-\infty}^{+\infty} P_{photo,r,v} \times p_v dv \\
&= \int_{-\infty}^{+\infty} T_{int} \times \Gamma_e (\delta_0 - \mathbf{k}_L \cdot \mathbf{v}) \times p_v dv \\
&= \int_{-\infty}^{+\infty} T_{int} \times \Omega(r)^2 \frac{1}{\sqrt{2\pi}\sigma_{r,L}} e^{-\frac{(\delta_0 - \mathbf{k}_L \cdot \mathbf{v})^2}{2\sigma_{r,L}^2}} \times \frac{1}{2\pi\sigma_T^2} e^{-\frac{v^2}{2\sigma_T^2}} dv
\end{aligned} \tag{B.18}$$

For a fixed \mathbf{r} , the probability of photoionization integrated over the Ps velocity distribution is thus the convolution of two Gaussians and leads to:

$$P_{photo,r}(r, \delta_0) = T_{int} \frac{\Omega(r)^2}{2} \pi \frac{1}{\sqrt{2\pi(\sigma_{r,L}^2 + k_L^2 \sigma_T^2)}} e^{-\frac{\delta_0^2}{2(\sigma_{r,L}^2 + k_L^2 \sigma_T^2)}} \tag{B.19}$$

Finally, the total probability of photoionization P_{photo} integrated over space is given by the 3D integral of $P_{photo,r}$ times the spatial distribution of the Ps cloud $n(\mathbf{r}) = \frac{1}{(2\pi\sigma_{r,Ps}^2)^{3/2}} e^{-\frac{r^2}{2\sigma_{r,Ps}^2}}$. This is an approximation since we consider an isotropic 4π emission, without any preferential direction.

$$\begin{aligned}
P_{photo} &= \int d^3r P_{photo,r}(\delta_0, \Omega(r)) \times n(r) \\
&= T_{int} \int dx dy \frac{\Omega(x,y)^2}{2} \int_0^\infty dz \pi \frac{1}{\sqrt{2\pi(\sigma_{r,L}^2 + k_L^2 \sigma_T^2)}} e^{-\frac{\delta_0^2}{2(\sigma_{r,L}^2 + k_L^2 \sigma_T^2)}} \\
&\quad \times \frac{1}{(2\pi\sigma_{r,Ps}^2)^{3/2}} e^{-\frac{x^2 + y^2 + z^2}{2\sigma_{r,Ps}^2}} \\
&= T_{int} \frac{\Omega(0)^2}{2} \pi \frac{1}{\sqrt{2\pi(\sigma_{r,L}^2 + k_L^2 \sigma_T^2)}} e^{-\frac{\delta_0^2}{2(\sigma_{r,L}^2 + k_L^2 \sigma_T^2)}} \\
&\quad \times \int d^2r \left(e^{-\frac{x^2 + y^2}{2\sigma_{r,L}^2}} \times \int_0^\infty dz \frac{1}{(2\pi\sigma_{r,Ps}^2)^{3/2}} e^{-\frac{x^2 + y^2 + z^2}{2\sigma_{r,Ps}^2}} \right)
\end{aligned} \tag{B.20}$$

We identify the factor $T_{int} \frac{\Omega(0)^2}{2} \pi \frac{1}{\sqrt{2\pi(\sigma_{r,L}^2 + k_L^2 \sigma_T^2)}} e^{-\frac{\delta_0^2}{2(\sigma_{r,L}^2 + k_L^2 \sigma_T^2)}} = P_{photo,r=0}(\Omega(0), \delta_0)$ to be the probability of photoionization at $r=0$, calculated in Eq. B.19. Then:

$$\begin{aligned}
P_{photo} &= P_{photo,r=0}(\Omega(0), \delta_0) \times \frac{\sqrt{2\pi\sigma_{r,Ps}^2}}{(2\pi\sigma_{r,Ps}^2)^{3/2}} \times \int dx dy e^{-\frac{x^2 + y^2}{2\sigma_{r,L}^2}} \times e^{-\frac{x^2 + y^2}{2\sigma_{r,Ps}^2}} \\
&= P_{photo,r=0}(\Omega(0), \delta_0) \times \frac{1}{2\pi\sigma_{r,Ps}^2} \times (2\pi \frac{\sigma_{r,L} 2\sigma_{r,Ps}^2}{\sigma_{r,L}^2 + \sigma_{r,Ps}^2}) \\
P_{photo} &= P_{photo,r=0}(\Omega(0), \delta_0) \times \frac{\sigma_{r,L}^2}{\sigma_{r,L}^2 + \sigma_{r,Ps}^2}
\end{aligned} \tag{B.21}$$

At the end, the total probability of photoionization, integrated over spatial and velocity distributions can be written as:

$$\boxed{P_{photo} = P_{photo,r=0}(\Omega_0, \delta_0) \times \eta} \tag{B.22}$$

where η is a geometrical factor of overlaps

$$\eta = \frac{\sigma_{r,L}^2}{\sigma_{r,L}^2 + \sigma_{r,Ps}^2} \quad (\text{B.23})$$

$P_{photo,r=0}$ is the probability of photoionization for a constant Rabi frequency taken at the peak value $\Omega_0 = \Omega(0)$, and a detuning $\delta_0 = \omega_0 - \omega_L$, integrated over the Ps velocity distribution.

This derivation is valid for a weak saturation of the $n=1 \leftrightarrow n=3$ transition and in high photoionization regime. To simplify the equations and analysis of the data, we decided to keep this approximation for the moderate saturation ($E_{UV} = 56\mu\text{J}$) regime we had during the measurements of the $n=3$ and Rydberg measurements we performed. The fit results are in good agreement with the theoretical values expected, we then decided that a higher refinement of the model would have been beyond the scope of our measurements analysis.

Appendix C

Derivation of the internal energies of an hydrogenoid atom

In this annex, I would like to briefly give the formula used in the Mathematica code to calculate the internal energies of the Ps, under the presence of external electric and magnetic fields. These calculations are based on the work of Fabio Villa [46]. In addition to the energies of the internal state, the code gives the dipole strengths of the transitions, and the excitation rate for a given transition of the Ps in interaction with a laser. We are under the semi-classical approach, where the atom is quantified but not the laser field.

The analytic formula that give the energetic corrections are generally given in the Clebsh-Gordan and 3J-6J symbols notations [110].

C.1 Q.E.D correction

The quantum electrodynamics (Q.E.D) correction Q.E.D is the shift in energy due to the electromagnetic interaction between the nucleus and the electrons or positrons. This leads to the fine structure of an atom without any external magnetic field. We only considered the Q.E.D correction in α^2 order, where α is the fine structure constant. $\alpha = \frac{e^2}{4\pi\epsilon_0 \hbar c}$, with e the electrical charge.

For a given state $|n, l, s, j, m\rangle$ of the Ps, where n is the principal quantum number, l the total orbital momentum, s the spin of the electron or positron and $j = l + s$, with m its projection on the quantification axis (the magnetic axis), the QED correction can be expressed as [109]:

$$\begin{aligned} \Delta E_{QED}(n, l, s, j, m) = & \frac{E_{ha} e \alpha^2}{4n^3} \times \left(\frac{11}{8n} - \frac{4}{2l+1} \right) + \\ & \frac{E_{ha} e \alpha^2}{4n^3} \times \frac{2}{l(2l+1)(l+1)} \left(\delta_{j,l+1} \frac{l(3l+4)}{2l+3} - \delta_{j,l} - \delta_{j,l-1} \frac{(l+1)(3l-1)}{2l-1} \right) \end{aligned} \quad (C.1)$$

This correction has to be applied on the level energy:

$$E_n = \frac{E_{Ha}(\mu)}{2n^2} \quad (C.2)$$

where $E_{Ha}(\mu)$ is the Hartree energy $E_{Ha}(\mu) = \frac{\mu \times e^4}{(4\pi\epsilon_0\hbar)^2}$.

Without any external field, the Ps energy fine structure can be derived using:

$$\boxed{E[n, l, s, j, m] = E_n + \Delta E_{QED}} \quad (C.3)$$

The derivation of the Ps level input file for the C++ code - in absence of magnetic field

As mentioned in Chap.8, Sec. 8.1.1, I used the formula (C.3) to calculate the energies of the sub-levels of the state $n=1$ and $n=2$ and then, I generate the levels file as input for the C++ code. I took the zero-energy reference to be the ground state 1^3S_1 energy. For instance, another possibility could have been to consider the continuum limit as the zero-energy reference.

The annihilation levels have been added with a negative arbitrary energy. The only relevant parameters for the annihilation levels are their quantum states (to allow the spontaneous decay from any ground state, following the selection rules) and the strength of the transition itself (given by the annihilation rate $\Gamma_{annih} = \frac{1}{\tau_{annih}}$).

The "continuum" levels have been set at the energetic limit that defines the continuum (i.e at the energy $+E_{n=1,l=0,s=1,j=1}$).

C.2 Zeeman effect

In the presence of a magnetic field, the Zeeman effect induces energy shifts. We note the magnetic dipoles for the total angular momentum $\hat{L} = \vec{r} \times \vec{p}$ and the spin of the electron and positron of the Ps as

$$\mu_{\vec{L},e^\pm} = \pm \frac{e}{2m_e} \vec{L}_{e^\pm} \quad \text{and} \quad \mu_{\vec{S},e^\pm} = \pm \frac{e}{2m_e} \vec{S}_{e^\pm} \quad (\text{C.4})$$

Under a magnetic field $\vec{B} = B\vec{u}_z$, the Zeeman effect can be expressed as:

$$\hat{H}_{Zeeman} = -(\vec{\mu}_{L,e^+} + \vec{\mu}_{L,e^-} + \vec{\mu}_{S,e^+} + \vec{\mu}_{S,e^-}) \cdot \vec{B} = \frac{2\mu_B B}{\hbar} (S_{e^-}^z - S_{e^+}^z) \quad (\text{C.5})$$

where μ_B is the Bohr magneton such that $\mu_B = \frac{e\hbar}{2m_e}$.

We can remark that for Ps, the Zeeman effect only couples sub-levels of same spin configurations. Indeed, the center of mass of the Ps (composed by an electron and its antiparticle of same mass, the positron) is at the center of the system, implying $\vec{L}_{e^+} = \vec{L}_{e^-}$. Thus, the angular orbital momenta compensate each other. Only the effect of the magnetic field on the spins lead to an energetic correction between two sub-levels $|n1, l1, s1, j1, m1\rangle$ and $|n1, l2, s2, j2, m2\rangle$:

$$\begin{aligned} \Delta E_{Zeeman} &= \langle n1, l2, s2, j2, m2 | \hat{H}_{Zeeman} | n1, l1, s1, j1, m1 \rangle \\ &= 2\mu_B B \times -\frac{((-1)^{s1+s2} - 1)}{2} \times \delta_{n1,n2} \delta_{l1,l2} \delta_{m1,m2} \times C_{s1,0,l1,m1}^{j1,m1} \times C_{s2,0,l2,m2}^{j2,m2} \end{aligned} \quad (\text{C.6})$$

where $(C_{a,\alpha,b,\beta}^{c,\gamma})$ are the Clebsh-Gordan coefficients (See. [110], chap. 8). For more details about the formula shown here. See e.g. [46], Chap 3.2

C.3 Stark and Motional Stark effects

If we want to perform laser cooling on Ps in the AEGIS apparatus, the presence of the huge magnetic field of 1 T has to be taken into account. Because the Ps is so light, its center of mass velocity \vec{v}_{CM} is important enough to induce a significant electric field $E_{induced} = \vec{v}_{CM} \cdot \vec{B}$ that can't be neglected. The Motional Stark effect has to be modeled, even if no important external electric field should be present in the AEGIS environment.

$$\vec{H}_{Motional\ Stark} = \vec{d}_{electrical} \cdot \vec{E}_{induced} = -e \vec{r} \cdot (\vec{v}_{CM} \wedge \vec{B}) \quad (C.7)$$

The Wigner-Ecart theorem gives the action of an irreducible tensor on a state $|n, l, s, j, m\rangle$. Because we want to study the effect of a field perpendicular to the quantization axis (the magnetic field), it is interesting to rotate the basis $\{x, y, z\}$, where z is the magnetic axis toward the new basis ([111], Chap. 2.):

$$\{\vec{u}_{-1}, \vec{u}_0, \vec{u}_{+1}\} = \left\{ \left(\frac{\vec{u}_x - i \vec{u}_y}{\sqrt{2}} \right), \vec{u}_z, \left(\frac{\vec{u}_x + i \vec{u}_y}{\sqrt{2}} \right) \right\} \quad (C.8)$$

In this basis, an external field \vec{F} is separated in a component parallel to the magnetic axis Z , and in two elements perpendicular to it. The Stark effect of the field \vec{F} is then expressed as :

$$\begin{aligned} \Delta E_{Stark} &= \langle n2, l2, s2, j2, m2 | \hat{H}_{MS} | n1, l1, s1, j1, m1 \rangle = e (2a_0) (\delta_{l1, l2-1} + \delta_{l1, l2+1}) \\ &\times (-1)^{s1+m2+1+l2} R_{n1, l1}^{n2, l2} \begin{Bmatrix} l2 & s1 & j2 \\ j1 & 1 & l1 \end{Bmatrix} \begin{pmatrix} l1 & 1 & l2 \\ 0 & 0 & 0 \end{pmatrix} \times \sum_{q=-1}^1 (E_q \times \begin{pmatrix} j2 & 1 & j1 \\ -m2 & q & m1 \end{pmatrix}) \end{aligned} \quad (C.9)$$

where a_0 is the Bohr radius of the Hydrogen (two times smaller than the one of the Ps) and $R_{n1, l1}^{n2, l2}$ is the matrix element of radial function such as $R_{n1, l1}^{n2, l2} = \int_0^{\text{inf}} R_{n1, l1} \times R_{n2, l2} \times r r^2 dr$. We note $R_{n, l}$ the radial function of the wavefunction of the Ps $|n, l, s, j, m\rangle = |\Psi_{n, l, s, j, m}\rangle$.

In the case of the Motional Stark effect, we note that the non-zero components are along \vec{u}_+ and \vec{u}_- and than the maximum energy shift is obtained for:

$$E_{induced, max}^{(+1)} = -E_{induced, max}^{(-1)} = \frac{|\vec{v}_{CM}| \cdot |\vec{B}|}{\sqrt{2}} \quad (C.10)$$

The derivation of the Ps level input file for the C++ code - in presence of magnetic field

In case of the 1 T field we wanted to simulate, I generated the levels file input of the Ps using the formula:

$$\boxed{E[n, l, s, j, m] = E_n + \Delta E_{QED} + E_{Zeeman} + E_{MotionalStark}} \quad (C.11)$$

C.4 The dipole strength of an optical transition

Without electric and magnetic fields, the dipole strength of a transition between two states $|1\rangle_0 = |n1_0, l1_0, s1_0, j1_0, m1_0\rangle$ and $|2\rangle_0 = |n2_0, l2_0, s2_0, j2_0, m2_0\rangle$ is given by ([46], Chap.3.):

$$d_{electrical,0} = \langle n2_0, l2_0, s2_0, j2_0, m2_0 | -e\vec{r} | n1_0, l1_0, s1_0, j1_0, m1_0 \rangle = {}_0 \langle j | \hat{d} | i \rangle_0 \quad (\text{C.12})$$

$$d_0 = e 2a_0 \times \delta_{s1_0, s2_0} (\delta_{l1_0, l2_0+1} + \delta_{l1_0, l2_0-1}) \times R_{n1_0, l1_0}^{n2_0, l2_0} \times (-1)^{j1_0 + s1_0 + l1_0 + 1 + m2_0 - m1_0} \\ \times \sqrt{2j1_0 + 1} \sqrt{2l2_0 + 1} \times C_{j1_0, m1_0, 1, (m2_0 - m1_0)}^{j2_0, m_0} \times C_{l2_0, 0, 1, 0}^{l1_0} \times \begin{Bmatrix} l2_0 & s1_0 & j2_0 \\ j1_0 & 1 & l1_0 \end{Bmatrix} \quad (\text{C.13})$$

In case of magnetic field, the eigen states of the total Hamiltonian are expressed in the perturbed basis $\{|n, l, s, j, m\rangle\} = \{|i\rangle\}$. The presence of a magnetic field induces Zeeman mixing of the states.

The electric or magnetic field induces a perturbation that affects the dipole value too. The dipole strength d_0 of the non-perturbed states are known (Eq. C.13). Then, in order to derive the new perturbed dipole strength d , we expressed the perturbed states into the non-perturbed states basis $\{|n_0, l_0, s_0, j_0, m_0\rangle\} = \{|i\rangle_0\}$. To do so, we performed the numerical diagonalization of the full-Hamiltonian, and obtained the coefficients a_{i,i_0} of basis exchanges:

$$|n1, l1, s1, j1, m1\rangle = |i\rangle = \sum_{i_0} a_{i,i_0} |i\rangle_0 \quad (\text{C.14})$$

Leading to:

$$d = \langle j | \vec{d} | i \rangle = \sum_{i_0} \sum_{j_0} a_{i,i_0} a_{j,j_0}^* \underbrace{\langle j_0 | d | i_0 \rangle}_{\text{known}} \quad (\text{C.15})$$

The derivation of the Ps lines input file for the C++ code

The dipole strengths formulas, derived in presence (see Eq. (C.15)) or absence of magnetic fields (see Eq. (C.13)) were used to generate the "lines" input file, of the C++ code Optical Pumping, described in Chap. (see Chap.8, Sec. 8.1).

Appendix D

Laser cooling on a broad-transition - the radiation pressure force

We want here to quickly remind some well-known results about the laser cooling over a broad transition $\hbar\Gamma_s \gg E_{recoil}$, in order to compare with the Ps case. I studied the possibility of performing the laser cooling of Ps over the transition $n=1 \leftrightarrow n=2$ in Chap. 7 and the hypothesis of the usual Doppler cooling over a broad-transition have to be checked carefully. In this appendix, I review quickly the derivation of the radiation pressure force, and uses it in first approximation to determine, with a Mathematica code, some parameters for the Ps cooling.

In this case, the absorption and emission of a photon leads to a small perturbation on the velocity of the atom, and the Brownian motion formalism can be applied to derive an averaged force from the laser-matter interaction. Due to random walk, the momentum coming from spontaneous emission is average zero, and consequently, we define the radiation pressure force to be:

$$\langle \vec{F}_{rad} \rangle = -\hbar\Gamma_{scat} \vec{\nabla}\psi_L \quad (D.1)$$

Where $\vec{\nabla}\psi_L$ is the gradient of phase the laser. For a plane-wave, we find:

$$\langle \vec{F}_{rad} \rangle = -\hbar\Gamma_{scat} \vec{k}_L = \hbar\vec{k}_L \Gamma_s \rho_{22,st} \quad (D.2)$$

For two counter-propagating lasers in a low saturation regime, the total force resulting is the sum of the two radiation pressure forces ([60]. Chap. 2).

$$\begin{aligned}
\langle F_{rad,tot} \rangle &= \langle F_{rad,1} \rangle + \langle F_{rad,2} \rangle \\
&= \hbar \vec{k}_L \frac{\Gamma_s}{2} \left(\frac{s_1}{s_1 + 1} - \frac{s_2}{s_2 + 1} \right) \\
&= \vec{k}_L \frac{\Gamma_s}{2} \left\{ \frac{(\Omega^2/2) \times (\Gamma_{tot}/\Gamma_s)}{(\delta_0 - k_L \cdot v)^2 + (\Gamma_{tot}^2/4) + (\Omega^2/2) \times (\Gamma_{tot}/\Gamma_s)} - \right. \\
&\quad \left. \frac{(\Omega^2/2) \times (\Gamma_{tot}/\Gamma_s)}{(\delta_0 + k_L \cdot v)^2 + (\Gamma_{tot}^2/4) + (\Omega^2/2) \times (\Gamma_{tot}/\Gamma_s)} \right\}
\end{aligned} \tag{D.3}$$

where s_1 and s_2 are the saturation parameter of each laser, depending on the detuning $\delta = \delta_0 \pm k_L \cdot v$. Γ_{tot} is the coherence rate, taking into all the decoherence contributions, such as $\Gamma_{tot} = \Gamma_s + \sigma_L + \Gamma_1 + \Gamma_2 + \gamma_{col}$. The definition of the rates are given in the Chap. 7.1 Fig. 7.1.

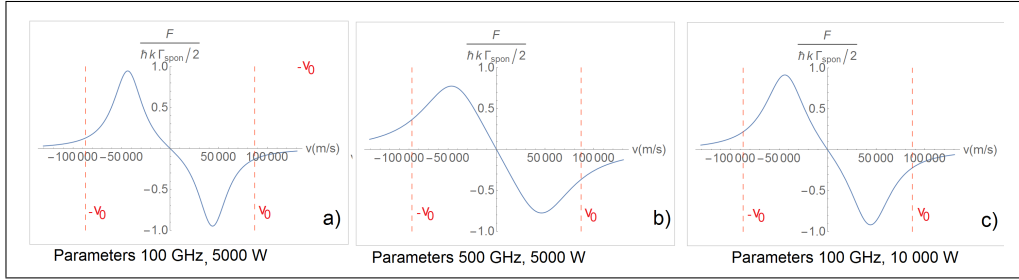


Figure D.1: Case of a broad-line transition: The radiation pressure force for two counter-propagating lasers - optimization of the cooling parameters. The normalized radiation pressure force is plotted for different power and bandwidth values, for a fixed detuning $\delta = \frac{\Gamma_{Doppler}}{2} = \frac{k v_0}{2}$. In abscissa is

the velocity of the Ps atom, between $\{-1.5 v_0, 1.5 v_0\}$, where $v_0 = \sqrt{\frac{k_B T}{m_{Ps}}}$.

The Ps cloud temperature is fixed at $T = 1000$ K. a) $P_L = 5000$ W ($E_L = 500 \mu\text{J}$, $t_{pulse,L} = 100$ ns) and $\sigma_L = 100$ GHz. b) $P_L = 5000$ W ($E_L = 500 \mu\text{J}$, $t_{pulse,L} = 100$ ns) and $\sigma_L = 500$ GHz. c) $P_L = 10\,000$ W ($E_L = 500 \mu\text{J}$, $t_{pulse,L} = 50$ ns), and $\sigma_L = 100$ GHz. Increasing the laser bandwidth implies a decrease of the radiation pressure force intensity but a longer capture range.

As mentioned in the introduction of this appendix, in a first approxima-

tion to model laser cooling on the Ps atom, we decided to use the radiation pressure force expression, that gives an empirical approach of the laser effect on the atom. Plotting this total force in a simple Mathematica code, allowed us to determine a rough estimate of the optimum parameters for a possible Doppler cooling of Ps.

Some results are shown in Fig. D.1. We can see that increasing the laser bandwidth implies a decrease of the radiation pressure force intensity but a longer capture range. I fixed $\delta \approx \frac{\Gamma_{Doppler}}{2} = \frac{k_L \times v_0}{2}$ that presents a good compromise between addressing the maximum of atoms and having an intense force, that is determined by the tangent of the force in the zero velocity range. We remind that v_0 is the mean velocity given by $v_0 = \sqrt{\frac{k_B T}{m_{Ps}}}$

Remark: to compensate the huge Doppler broadening of the Ps cloud, it would be ideal to have a laser as large as the broadening to excite all the Ps. Unfortunately, a large bandwidth of the laser implies a decrease in the force intensity, as shown in Fig. D.1 b). For a Ps cloud at 1000 K, the Doppler

broadening is in the order of $k_L \times \sqrt{\frac{k_B T}{2 m_e}} \approx 2\text{THz}$. For these simulations, we find that a laser power of 5000 W, for a bandwidth of 100 GHz seems to generate a decent cooling force, with a good capture range.

These preliminary studies given in this appendix were as a starting point for the simulations studies of the Doppler laser cooling of Ps, reported in Chap.8

D.0.1 The low saturation regime - $s \ll 1$

For low saturation regime, the radiation pressure force of $N \geq 2$ counter-propagating lasers is the sum of the different lasers contributions¹⁸, and can be written as:

¹⁸Since the cooling time scales with $1/s_0$, it could be interesting to increase the saturation. But for generic saturation parameter values, the derivation of the total force becomes more complex and we can't sum the forces of each laser. In practice, the optimum value for the saturation parameter tends to be $s \approx 1$, when the stimulated and spontaneous emissions are in the same order. On average, an excited atom will decay through the spontaneous process once over 2 cycles, that is a good compromise for efficient cooling (spontaneous decay preferred, meaning $s \ll 1$) and a fast cooling time (meaning transition strongly saturated).

$$\boxed{\begin{aligned}\mathbf{F} &\approx \hbar k_L^2 s_0 \frac{2\delta\Gamma_s}{\delta^2 + \Gamma_s^2/4} \times \mathbf{v} \\ \mathbf{F} &\approx -\alpha\mathbf{v}\end{aligned}} \quad (\text{D.5})$$

where we note the friction coefficient $\alpha(\delta, \Omega) = \hbar k_L^2 s_0(\delta, \Omega) \frac{2\delta\Gamma_s}{\delta^2 + \Gamma_s^2/4}$. We note that s_0 is the saturation parameter, for an atom at rest, that can be expressed in case of a Lorentzian laser as:

$$s_0 = \frac{2|\Omega|^2}{\Gamma_{tot}^2 + 4(\delta)^2} \frac{\Gamma_{tot}}{\Gamma_s} \quad (\text{D.6})$$

We finally derive a simple expression for the radiation pressure force to first-order of the atom velocity, that can be seen as a friction force. We note that α is positive for a negative detuning δ . As a consequence, the Ps velocity distribution experiences an exponential decay under the laser-light interaction:

$$\begin{aligned}m a &= m \frac{dv}{dt} = F = -\alpha v \\ v &= v_0 \exp(-\alpha t)\end{aligned} \quad (\text{D.7})$$

The maximum friction coefficient α_{max} is obtained for a detuning $\delta = \frac{\Gamma_s}{2}$:

$$\begin{aligned}\alpha_{max} &= 2 s_0(\delta = \frac{\Gamma_s}{2}) \times \hbar k_L^2 \\ \alpha_{max} &= 2\hbar k_L^2 \frac{\Omega^2}{\Gamma_s^2}\end{aligned} \quad (\text{D.8})$$

The strength of the total force is illustrated by the slope of the force plotted in Fig. D.1 (the steeper the slope is, the stronger the force is). The minimum temperature reachable with the Doppler cooling over a broad-line transition is given by the so-call Doppler limit:

In order to model the total radiation pressure force, it is usual to consider the atom is saturated by the 6 incoming lasers, and derive the saturation answer of the system. More information can be found in [112] that provides the following formula for the force for N plane-wave lasers interaction:

$$\mathbf{F}(v) = \sum_{j \leq N} \hbar \mathbf{k}_j \frac{\Gamma_s}{2} \frac{I_j/I_{sat}}{1 + 4(\delta - \mathbf{k}_j \cdot \mathbf{v}/\Gamma_s)^2 + N \frac{I_j}{I_{sat}}} \quad (\text{D.4})$$

$$T_{min} = \frac{\hbar\Gamma_s}{k_B} \quad (\text{D.9})$$

Hypothesis validity?

In this last part, I remind the hypothesis behind the derivation of the radiation pressure force. The averaged radiation pressure force comes from the Brownian motion approach. The validity limit is then $\hbar\Gamma_s \gg E_{recoil}$, that is not the case for the Ps atom for a monochromatic laser, as discussed in Chap. 7. We can translate this hypothesis by the following: any consequent effect of the radiation pressure force on the atom velocity is the result of many repeated absorption-spontaneous cycles. For one cycle of absorption and photon scattered, the change in velocity is considered to be a small perturbation that lets the radiation pressure force constant over a single cycle.

Besides, as explained in [60] lesson 2, in order to be able to apply the Brownian motion formalism, the atom velocities have to be small enough compared to the interval of resonant velocities for the laser $\delta v_{res} = \frac{\Gamma_s}{k_L}$. This condition comes from the competition between:

- the cooling process that is characterized by the friction coefficient α defined below
- and the warming up due to the random walk, that is translated by the diffusion coefficient in momentum $D_p \approx \hbar^2 k_L^2 \Gamma_s s_0$ (formula valid for the low saturation regime $s_0 \ll 1$).

Bibliography

- [1] Carl D. Anderson. The positive electron. *Phys. Rev.*, 43:491–494, Mar 1933.
- [2] Savely G. Karshenboim. Precision physics of simple atoms: {QED} tests, nuclear structure and fundamental constants. *Physics Reports*, 422(1 - 2):1 63, 2005.
- [3] E.G. Adelberger, J.H. Gundlach, B.R. Heckel, S. Hoedl, and S. Schlamminger. Torsion balance experiments: A low-energy frontier of particle physics. *Progress in Particle and Nuclear Physics*, 62(1):102 – 134, 2009.
- [4] Sandip Pakvasa, Walter A. Simmons, and Thomas J. Weiler. Test of equivalence principle for neutrinos and antineutrinos. *Phys. Rev. D*, 39:1761–1763, Mar 1989.
- [5] A Apostolakis, E Aslanides, G Backenstoss, P Bargassa, O Behnke, A Benelli, V Bertin, F Blanc, P Bloch, P Carlson, M Carroll, E Cawley, G Chardin, M.B Chertok, M Danielsson, M Dejardin, J Derre, A Ealet, C Eleftheriadis, L Faravel, W Fetscher, M Fidecaro, A Filipcic, D Francis, J Fry, E Gabathuler, R Gamet, H.-J Gerber, A Go, A Haselden, P.J Hayman, F Henry-Couannier, R.W Hollander, K Jon-And, P.-R Kettle, P Kokkas, R Kreuger, R Le Gac, F Leimgruber, I Mandić, N Manthos, G Marel, M Mikuz, J Miller, F Montanet, A Muller, T Nakada, B Pagels, I Papadopoulos, P Pavlopoulos, G Polivka, R Rickenbach, B.L Roberts, T Ruf, L Sakeliou, M SchÅœfer, L.A Schaller, T Schietinger, A Schopper, L Tauscher, C Thibault, F Touchard, C Touramanis, C.W.E Van Eijk, S Vlachos, P Weber, O Wigger, M Wolter, D Zavrtanik, D Zimmerman, John Ellis, N.E Mavromatos, and D.V Nanopoulos. Tests of the equivalence principle with neutral kaons. *Physics Letters B*, 452(3 4):425 433, 1999.

- [6] Michael Martin Nieto and T. Goldman. The arguments against anti-gravity and the gravitational acceleration of antimatter. *Physics Reports*, 205(5):221 – 281, 1991.
- [7] J. Ponce de Leon. Extra symmetry in the field equations in 5-D with spatial spherical symmetry. *Class. Quant. Grav.*, 23:3043–3052, 2006.
- [8] M. Amoretti et al. Production and detection of cold antihydrogen atoms. *Nat Lett*, 419:456–459, 2002.
- [9] G. Gabrielse, N. S. Bowden, P. Oxley, A. Speck, C. H. Storry, J. N. Tan, M. Wessels, D. Grzonka, W. Oelert, G. Schepers, T. Sefzick, J. Walz, H. Pittner, T. W. Hänsch, and E. A. Hessels. Driven production of cold antihydrogen and the first measured distribution of antihydrogen states. *Phys. Rev. Lett.*, 89:233401, Nov 2002.
- [10] G. B. Andresen et al. Trapped antihydrogen. *Nature*, 468:673–676, Oct 2010.
- [11] B.X.R. Alves and al. Alpha collaboration. Observation of the 1s-2s transition in trapped antihydrogen. *Nature*, 2016.
- [12] C. Amole, al. Alpha collaboration, and A.E. Charman. Description and first application of a new technique to measure the gravitational mass of antihydrogen. *Nature Communication*, 4:1785, 2013.
- [13] G. Dufour, D. B. Cassidy, P. Crivelli, P. Debu, A. Lambrecht, V. V. Nesvizhevsky, S. Reynaud, A. Yu. Voronin, and T. E. Wall. Prospects for studies of the free fall and gravitational quantum states of antimatter. *Advances in High Energy Physics*, 2015, 2015.
- [14] The ALPHA Collaboration and A. E. Charman. Description and first application of a new technique to measure the gravitational mass of antihydrogen. *Nature Comm.*, 4:1785, March 2013.
- [15] G. Dobrychev et al. Proposal for the AEGIS experiment at the CERN Antiproton Decelerator (Antimatter Experiment: Gravity, Interferometry, Spectroscopy). 2007.
- [16] C. H. Storry, A. Speck, D. Le Sage, N. Guise, G. Gabrielse, D. Grzonka, W. Oelert, G. Schepers, T. Sefzick, H. Pittner, M. Herrmann, J. Walz, T. W. Hänsch, D. Comeau, and E. A. Hessels. First laser-controlled antihydrogen production. *Phys. Rev. Lett.*, 93:263401, Dec 2004.

- [17] D. Krasnicky, R. Caravita, C. Canali, and G. Testera. Cross section for rydberg antihydrogen production via charge exchange between rydberg positroniums and antiprotons in a magnetic field. *Phys. Rev. A*, 94:022714, Aug 2016.
- [18] Pauline Yzombard, Mehdi Hamamda, Sebastian Gerber, Michael Doser, and Daniel Comparat. Laser cooling of molecular anions. *Phys. Rev. Lett.*, 114:213001, May 2015.
- [19] S. Aghion, C. Amsler, A. Ariga, T. Ariga, G. Bonomi, P. Bräunig, J. Bremer, R. S. Brusa, L. Cabaret, M. Caccia, R. Caravita, F. Castelli, G. Cerchiari, K. Chlouba, S. Cialdi, D. Comparat, G. Consolati, A. Demetrio, L. Di Noto, M. Doser, A. Dudarev, A. Ereditato, C. Evans, R. Ferragut, J. Fesel, A. Fontana, O. K. Forslund, S. Gerber, M. Giammarchi, A. Gligorova, S. Gninenko, F. Guatieri, S. Haider, H. Holmestad, T. Huse, I. L. Jernelv, E. Jordan, A. Kellerbauer, M. Kimura, T. Koettig, D. Krasnicky, V. Lagomarsino, P. Lansonneur, P. Lebrun, S. Lehner, J. Liberadzka, C. Malbrunot, S. Mariazzi, L. Marx, V. Matveev, Z. Mazzotta, G. Nebbia, P. Nedelec, M. Oberthaler, N. Pacifico, D. Pagano, L. Penasa, V. Petracek, C. Pistillo, F. Prelz, M. Prevedelli, L. Ravelli, L. Resch, B. Rienäcker, O. M. Røhne, A. Rotondi, M. Sacerdoti, H. Sandaker, R. Santoro, P. Scampoli, L. Smestad, F. Sorrentino, M. Spacek, J. Storey, I. M. Strojek, G. Testera, I. Tietje, S. Vamosi, E. Widmann, P. Yzombard, J. Zmeskal, and N. Zurlo. Laser excitation of the $n = 3$ level of positronium for antihydrogen production. *Phys. Rev. A*, 94:012507, Jul 2016.
- [20] S. Aghion, C. Amsler, A. Ariga, T. Ariga, A.S. Belov, G. Bonomi, P. Bräunig, J. Bremer, R.S. Brusa, L. Cabaret, M. Caccia, R. Caravita, F. Castelli, G. Cerchiari, K. Chlouba, S. Cialdi, D. Comparat, G. Consolati, A. Demetrio, L. Di Noto, M. Doser, A. Dudarev, A. Ereditato, C. Evans, J. Fesel, A. Fontana, O.K. Forslund, S. Gerber, M. Giammarchi, A. Gligorova, S. Gninenko, F. Guatieri, S. Haider, H. Holmestad, T. Huse, I.L. Jernelv, E. Jordan, T. Kaltenbacher, A. Kellerbauer, M. Kimura, T. Koetting, D. Krasnicky, V. Lagomarsino, P. Lebrun, P. Lansonneur, S. Lehner, J. Liberadzka, C. Malbrunot, S. Mariazzi, L. Marx, V. Matveev, Z. Mazzotta, G. Nebbia, P. Nedelec, M. Oberthaler, N. Pacifico, D. Pagano, L. Penasa, V. Petracek, C. Pistillo, F. Prelz, M. Prevedelli, L. Ravelli, B. Rienäcker, O.M. Røhne, S. Rosenberger, A. Rotondi, M. Sacerdoti, H. Sandaker, R. Santoro, P. Scampoli, F. Sorrentino, M. Spacek, J. Storey, I.M. Strojek, G. Testera, I. Tietje, S. Vamosi, E. Widmann, P. Yzombard,

- S. Zavatarelli, and J. Zmeskal. Positron bunching and electrostatic transport system for the production and emission of dense positronium clouds into vacuum. *Nuclear Instruments and Methods in Physics Research Section B: Beam Interactions with Materials and Atoms*, 362:86–92, 2015.
- [21] Martin Deutsch. Evidence for the formation of positronium in gases. *Phys. Rev.*, 82:455–456, May 1951.
- [22] Sebastiano Mariazzi, Paolo Bettotti, and Roberto S. Brusa. Positronium cooling and emission in vacuum from nanochannels at cryogenic temperature. *Phys. Rev. Lett.*, 104:243401, Jun 2010.
- [23] A. C. L. Jones, T. H. Hisakado, H. J. Goldman, H. W. K. Tom, A. P. Mills, and D. B. Cassidy. Doppler-corrected balmer spectroscopy of rydberg positronium. *Phys. Rev. A*, 90:012503, Jul 2014.
- [24] T. E. Wall, D. B. Cassidy, and S. D. Hogan. Single-color two-photon spectroscopy of rydberg states in electric fields. *Phys. Rev. A*, 90:053430, Nov 2014.
- [25] Savely G. Karshenboim. Precision study of positronium: Testing bound state qed theory. *International Journal of Modern Physics A*, 19(23):3879–3896, 2004.
- [26] Andrzej Czarnecki. Positronium and polyelectrons. *Nuclear Physics A*, 827(1 4):541c–543c, 2009. {PANIC08Proceedings} of the 18th Particles and Nuclei International Conference.
- [27] S Berko and H N Pendleton. Positronium. *Annual Review of Nuclear and Particle Science*, 30(1):543–581, 1980.
- [28] Hermann Marxer and Larry Spruch. Semiclassical estimation of the radiative mean lifetimes of hydrogenlike states. *Phys. Rev. A*, 43:1268–1274, Feb 1991.
- [29] M W Horbatsch, M Horbatsch, and E A Hessels. A universal formula for the accurate calculation of hydrogenic lifetimes. *Journal of Physics B: Atomic, Molecular and Optical Physics*, 38(11):1765, 2005.
- [30] S. Van Petegem, C. Dauwe, T. Van Hoecke, J. De Baerdemaeker, and D. Segers. Diffusion length of positrons and positronium investigated using a positron beam with longitudinal geometry. *Phys. Rev. B*, 70:115410, Sep 2004.

- [31] S. Mariuzzi, P. Bettotti, S. Larcheri, L. Toniutti, and R. S. Brusa. High positronium yield and emission into the vacuum from oxidized tunable nanochannels in silicon. *Phys. Rev. B*, 81:235418, Jun 2010.
- [32] T. J. Murphy and C. M. Surko. Positron trapping in an electrostatic well by inelastic collisions with nitrogen molecules. *Phys. Rev. A*, 46:5696–5705, Nov 1992.
- [33] J. R. Danielson, D. H. E. Dubin, R. G. Greaves, and C. M. Surko. Plasma and trap-based techniques for science with positrons. *Rev. Mod. Phys.*, 87:247–306, Mar 2015.
- [34] N Madsen RC Thompson, M Knoop. Physics with trapped charged particles, lectures from the les houches winter school. *Imperial College Press.*, 2014.
- [35] Ine Larsen Jernelv. *Master Thesis - Optimising Positron-Positronium Conversion in Preparation of Positronium Laser Excitation*. Norwegian University of Science and Technology., 2015.
- [36] D. B. Cassidy, S. H. M. Deng, H. K. M. Tanaka, and A. P. Mills. Single shot positron annihilation lifetime spectroscopy. *Applied Physics Letters*, 88(19), 2006.
- [37] Steven Chu and Allen P. Mills. Excitation of the positronium $1^3s_1 \rightarrow 2^3s_1$ two-photon transition. *Phys. Rev. Lett.*, 48:1333–1337, May 1982.
- [38] K P Ziock, C D Dermer, R H Howell, F Magnotta, and K M Jones. Optical saturation of the $1\ 3\ s\text{-}2\ 3\ p$ transition in positronium. *J. Phys. B: At., Mol. Opt. Phys.*, 23(2):329, 1990.
- [39] K. P. Ziock, R. H. Howell, F. Magnotta, R. A. Failor, and K. M. Jones. First observation of resonant excitation of high n states in positronium. *Phys. Rev. Lett.*, 64:2366–2369, May 1990.
- [40] D. B. Cassidy, T. H. Hisakado, H. W. K. Tom, and A. P. Mills. Efficient production of rydberg positronium. *Phys. Rev. Lett.*, 108:043401, Jan 2012.
- [41] T. E. Wall, A. M. Alonso, B. S. Cooper, A. Deller, S. D. Hogan, and D. B. Cassidy. Selective production of rydberg-stark states of positronium. *Phys. Rev. Lett.*, 114:173001, Apr 2015.

- [42] D. B. Cassidy and S. D. Hogan. Atom control and gravity measurements using rydberg positronium. *International Journal of Modern Physics: Conference Series*, 30:1460259, 2014.
- [43] M. L. Wall, C. S. Norton, and F. Robicheaux. Two-stage rydberg charge exchange in a strong magnetic field. *Phys. Rev. A*, 72:052702, Nov 2005.
- [44] W A Bertsche, E Butler, M Charlton, and N Madsen. Physics with antihydrogen. *Journal of Physics B: Atomic, Molecular and Optical Physics*, 48(23):232001, 2015.
- [45] F. Castelli, I. Boscolo, S. Cialdi, M. G. Giammarchi, and D. Comparat. *Phys. Rev. A*, 78:052512, Nov 2008.
- [46] F. Villa. Laser system for positronium excitation to Rydberg levels for Aegis experiment. *Laser system for positronium excitation to Rydberg levels for Aegis experiment, PhD thesis, Milano*, 2011.
- [47] K C Harvey. Slow metastable atomic hydrogen beam by optical pumping. *J. Appl. Phys.*, 53(5):3383–3386, 1982.
- [48] M. K. Oberthaler. Anti-matter wave interferometry with positronium. *Nuclear Instruments and Methods in Physics Research B*, 192:129–134, May 2002.
- [49] R. Caravita. *Laser apparatus for exciting Positronium in AEGIS Positronium spectroscopy experiment*. Master thesis, University of Milano-Italy, 2012.
- [50] D. B. Cassidy, K. T. Yokoyama, S. H. M. Deng, D. L. Griscom, H. Miyadera, H. W. K. Tom, C. M. Varma, and A. P. Mills. Positronium as a probe of transient paramagnetic centers in α - SiO_2 . *Phys. Rev. B*, 75:085415, Feb 2007.
- [51] Pauline Yzombard. *Master Thesis - rapport de stage : refroidissement laser de l'antimatière*. Institut d'Optique Graduate School, Univerté Paris XI, 2013.
- [52] M. H. Anderson, J. R. Ensher, M. R. Matthews, C. E. Wieman, and E. A. Cornell. Observation of bose-einstein condensation in a dilute atomic vapor. *Science*, 269(5221):198–201, 1995.
- [53] Edison P. Liang and Charles D. Dermer. Laser cooling of positronium. *Optics Communications*, 65(6):419 – 424, 1988.

- [54] H Iijima, T Asonuma, T Hirose, M Irako, T Kumita, M Kajita, K Matsuzawa, and K Wada. Laser cooling system of ortho-positronium. *Nucl. Instru. Meth. Phys. Res. A*, 455:104–108, 2000.
- [55] T. Kumita, T. Hirose, M. Irako, K. Kadoya, B. Matsumoto, K. Wada, N.N. Mondal, H. Yabu, K. Kobayashi, and M. Kajita. Study on laser cooling of ortho-positronium. *Nucl. Instru. Meth. Phys. Res. B*, 192:171–175, 2002.
- [56] K Shu, X Fan, T Yamazaki, T Namba, S Asai, K Yoshioka, and M Kuwata-Gonokami. Study on cooling of positronium for bose einstein condensation. *J. Phys. B*, 49(10):104001, 2016.
- [57] Daniel Comparat. Molecular cooling via sisyphus processes. *Phys. Rev. A*, 89:043410, Apr 2014.
- [58] Daniel Comparat. Molecular cooling via sisyphus processes. *Phys. Rev. A*, 89:043410, Apr 2014.
- [59] Gilbert Grynberg Alain Aspect, Claude Fabre. *Optique Quantique: lasers*. Ecole Polytechnique, 2006.
- [60] Jean Dalibard. *Une brève histoire des atomes froids, Lessons at the Collège de France*. Collège de France, 2015.
- [61] H. A. Bethe and E. E. Salpeter. Quantum Mechanics of One- and Two-Electron Atoms. 1977.
- [62] J. J. Yeh and I. Lindau. Atomic Subshell Photoionization Cross Sections and Asymmetry Parameters: $1 \leq Z \leq 103$. *Atomic Data and Nuclear Data Tables*, 32:1, 1985.
- [63] S. Mariazzi, A. Salemi, and R. S. Brusa. Positronium cooling into nanopores and nanochannels by phonon scattering. *Phys. Rev. B*, 78:085428, Aug 2008.
- [64] Margaret K. Brown. Long-pulse broadband 243-nm source based on a cr:lisa laser operating at 972 nm, 1999.
- [65] Hori, M., Sôtér, A., and Dax, A. Development of narrowband lasers for spectroscopy of antiprotonic atoms. *EPJ Web of Conferences*, 66:05006, 2014.

- [66] Rajeev Khare and Paritosh K. Shukla. *Temporal Stretching of Laser Pulses, Coherence and Ultrashort Pulse Laser Emission*. Number ISBN 978-953-307-242-5. InTech, 2010.
- [67] A I Bishop, L Wang, and P F Barker. Creating cold stationary molecular gases by optical stark deceleration. *New Journal of Physics*, 12(7):073028, 2010.
- [68] Daniel Comparat. *Atoms Photons interaction, Master lessons*. University of Paris XI, 2012.
- [69] Jeffrey S Hangst and Paul Bove. ALPHA Proposal. Technical Report CERN-SPSC-2005-006. SPSC-P-325, CERN, Geneva, Jan 2005.
- [70] Ryugo Hayano and Eberhard Widmann. Atomic Spectroscopy And Collisions Using Slow Antiprotons (ASACUSA). Technical Report CERN-SPSC-2005-002. SPSC-97-19-ADD-2, CERN, Geneva, Jan 2005. revised version submitted on 2005-01-11 03:56:36.
- [71] G Gabrielse, T Roach, and J K Estrada. Proposal presented to the SPSLC: The production and study of cold antihydrogen. Technical Report CERN-SPSC-97-8. SPSC-P-306, CERN, Geneva, 1997.
- [72] S Ulmer, Y Yamazaki, C Smorra, K Blaum, K Franke, Y Matsuda, H Nagahama, W Quint, J Walz, A Mooser, and G Schneider. Technical Design Report BASE. Technical Report CERN-SPSC-2013-002. SPSC-TDR-002, CERN, Geneva, Jan 2013.
- [73] H Herr. A small deceleration ring for extra low energy antiprotons (ELENA). *Ettore Majorana Int. Sci. Ser., Phys. Sci.*, 17(CERN-SPSC-82-3. SPSC-P-52-Add-1):633–642. 14 p, 1982.
- [74] Daniel Krasnicky. *PhD. Thesis: Antiproton Capture and Cooling for Production of Cold Antihydrogen*. Number ISBN 978-953-307-242-5. Universtá di Genova, 2013.
- [75] A. Kellerbauer, A. Fischer, and U. Warring. Measurement of the zee-man effect in an atomic anion: Prospects for laser cooling of os^- . *Phys. Rev. A*, 89:043430, Apr 2014.
- [76] H. Raimbault-Hartmann, D. Beck, G. Bollen, M. König, H.-J. Kluge, E. Schark, J. Stein, S. Schwarz, and J. Szerypo. A cylindrical Penning trap for capture, mass selective cooling, and bunching of radioactive ion beams. *Nuclear Instruments and Methods in Physics Research B*, 126:378–382, 1997.

- [77] J. R. Danielson and C. M. Surko. Torque-balanced high-density steady states of single-component plasmas. *Phys. Rev. Lett.*, 94:035001, Jan 2005.
- [78] N. Kuroda, H. A. Torii, M. Shibata, Y. Nagata, D. Barna, M. Hori, D. Horváth, A. Mohri, J. Eades, K. Komaki, and Y. Yamazaki. Radial compression of an antiproton cloud for production of intense antiproton beams. *Phys. Rev. Lett.*, 100:203402, May 2008.
- [79] G. B. Andresen, W. Bertsche, P. D. Bowe, C. C. Bray, E. Butler, C. L. Cesar, S. Chapman, M. Charlton, J. Fajans, M. C. Fujiwara, R. Funakoshi, D. R. Gill, J. S. Hangst, W. N. Hardy, R. S. Hayano, M. E. Hayden, R. Hydomako, M. J. Jenkins, L. V. Jørgensen, L. Kurchaninov, R. Lambo, N. Madsen, P. Nolan, K. Olchanski, A. Olin, A. Povilus, P. Pusa, F. Robicheaux, E. Sarid, S. Seif El Nasr, D. M. Silveira, J. W. Storey, R. I. Thompson, D. P. van der Werf, J. S. Wurtele, and Y. Yamazaki. Compression of antiproton clouds for antihydrogen trapping. *Phys. Rev. Lett.*, 100:203401, May 2008.
- [80] T. M. O’Neil. Centrifugal separation of a multispecies pure ion plasma. *Physics of Fluids*, 24(8):1447–1451, 1981.
- [81] F. G. Major, V. N. Gheorghe, and G. Werth. *Charged Particle Trap: Physics and Techniques of Charged Particle Field Confinement*, volume 37. Springer Berlin Heidelberg, 2005.
- [82] D. S. Hall and G. Gabrielse. Electron cooling of protons in a nested penning trap. *Phys. Rev. Lett.*, 77:1962–1965, Sep 1996.
- [83] G. B. Andresen, M. D. Ashkezari, M. Baquero-Ruiz, W. Bertsche, P. D. Bowe, E. Butler, C. L. Cesar, S. Chapman, M. Charlton, J. Fajans, T. Friesen, M. C. Fujiwara, D. R. Gill, J. S. Hangst, W. N. Hardy, R. S. Hayano, M. E. Hayden, A. Humphries, R. Hydomako, S. Jonesell, L. Kurchaninov, R. Lambo, N. Madsen, S. Menary, P. Nolan, K. Olchanski, A. Olin, A. Povilus, P. Pusa, F. Robicheaux, E. Sarid, D. M. Silveira, C. So, J. W. Storey, R. I. Thompson, D. P. van der Werf, D. Wilding, J. S. Wurtele, and Y. Yamazaki. Evaporative cooling of antiprotons to cryogenic temperatures. *Phys. Rev. Lett.*, 105:013003, Jul 2010.
- [84] W. Neuhauser, M. Hohenstatt, P. Toschek, and H. Dehmelt. Optical-sideband cooling of visible atom cloud confined in parabolic well. *Phys. Rev. Lett.*, 41:233–236, Jul 1978.

- [85] D. J. Wineland, R. E. Drullinger, and F. L. Walls. Radiation-pressure cooling of bound resonant absorbers. *Phys. Rev. Lett.*, 40:1639–1642, Jun 1978.
- [86] D. J. Wineland and Wayne M. Itano. Laser cooling of atoms. *Phys. Rev. A*, 20:1521–1540, Oct 1979.
- [87] R. E. Drullinger, D. J. Wineland, and J. C. Bergquist. High-resolution optical spectra of laser cooled ions. *Applied physics*, 22(4):365–368, 1980.
- [88] L. Hilico, J.-P. Karr, A. Douillet, P. Indelicato, S. Wolf, and F. Schmidt Kaler. Cooling antihydrogen ions for the free-fall experiment GBAR. *ArXiv e-prints*, February 2014.
- [89] L Pan and D. R. Beck. Candidates for laser cooling of atomic anions: L^- versus Os^- . *Phys. Rev. A*, 82(1):14501, 2010.
- [90] C. W. Walter, N. D. Gibson, Y.-G. Li, D. J. Matyas, R. M. Alton, S. E. Lou, R. L. Field, III, D. Hanstorp, L. Pan, and D. R. Beck. Experimental and theoretical study of bound and quasibound states of Ce^- . *Phys. Rev. A*, 84(3):032514, September 2011.
- [91] C. W. Walter, N. D. Gibson, D. J. Matyas, C. Crocker, K. A. Dungan, B. R. Matola, and J. Rohlén. Candidate for Laser Cooling of a Negative Ion: Observations of Bound-Bound Transitions in La^- . *Physical Review Letters*, 113(6):063001, August 2014.
- [92] Alban Kellerbauer and Stephan Fritzsche. High-resolution optical spectroscopy of os^- with a view to laser cooling of atomic anions. *Journal of Physics: Conference Series*, 388(1):012023, 2012.
- [93] E. Jordan, G. Cerchiari, S. Fritzsche, and A. Kellerbauer. High-resolution spectroscopy on the laser-cooling candidate la^- . *Phys. Rev. Lett.*, 115:113001, Sep 2015.
- [94] Stephen N Schauer, Peter Williams, and R N Compton. Production of small doubly charged negative carbon cluster ions by sputtering. *Physical review letters*, 65(5):625, 1990.
- [95] E. S. Shuman, J. F. Barry, and D. DeMille. Laser cooling of a diatomic molecule. *Nature*, 467:820–823, 2010.

- [96] J. H. V. Nguyen, C. R. Viteri, E. G. Hohenstein, C. D. Sherrill, K. R. Brown, and B Odom. Challenges of laser-cooling molecular ions. *New Journal of Physics*, 13(6):63023, 2011.
- [97] Matthew T. Hummon, Mark Yeo, Benjamin K. Stuhl, Alejandra L. Collopy, Yong Xia, and Jun Ye. 2d magneto-optical trapping of diatomic molecules. *Phys. Rev. Lett.*, 110:143001, Apr 2013.
- [98] T. Huber Ch. Schneider, M. Enderlein and T. Schaetz. Optical trapping of an ion. *Nat. Phot.*, 4:772, 2010.
- [99] V Rudnev and A González Ureña. Discharge source coupled to a deceleration unit for anion beam generation: Application to H_2^- photodetachment. *Review of Scientific Instruments*, 84(12):–, 2013.
- [100] D Comparat. Molecular cooling via Sisyphus processes. *Phys. Rev. A*, 89(4):43410, 2014.
- [101] U Hefter, Roy D Mead, P A Schulz, and W C Lineberger. Ultrahigh-resolution study of autodetachment in C_2^- . *Phys. Rev. A*, 28(3):1429–1439, September 1983.
- [102] M. R. Tarbutt. Magneto-optical trapping forces for atoms and molecules with complex level structures. *New Journal of Physics*, 17(1):015007, January 2015.
- [103] C. B. Zhang, D. Offenbergl, B. Roth, M. A. Wilson, and S. Schiller. Molecular-dynamics simulations of cold single-species and multispecies ion ensembles in a linear paul trap. *Phys. Rev. A*, 76:012719, Jul 2007.
- [104] S.S. Kumar, D Hauser, R Jindra, T Best, S Roucka, W.D. Geppert, T.J. Millar, and R Wester. Photodetachment as a Destruction Mechanism for CN^- and C_3N^- Anions in Circumstellar Envelopes. *Astrophysical Journal*, 776:25, 2013.
- [105] H. J. C. Berendsen, J. P. M. Postma, W. F. van Gunsteren, A. DiNola, and J. R. Haak. Molecular dynamics with coupling to an external bath. *The Journal of Chemical Physics*, 81(8):3684–3690, 1984.
- [106] Rosmus Pavel and Werner Hans–Joachim. Multireference –ci calculations of radiative transition probabilities in c_2^- . *The Journal of Chemical Physics*, 80(10):5085–5088, 1984.

- [107] K. Gomberoff, J. Fajans, J. Wurtele, A. Friedman, D. P. Grote, R. H. Cohen, and J.-L. Vay. Simulation studies of non-neutral plasma equilibria in an electrostatic trap with a magnetic mirror. *Physics of Plasmas*, 14(5), 2007.
- [108] P Lambropoulos L.B.Madsen. Scaling of hydrogenic atoms and ions interacting with lasers field: Positronium in a laser field. *PRA*, 59:6, 1999.
- [109] Claude Cohen-Tannoudji Bernard Diu Franck Laloë. *Tome I, Quantum Mechanics*. Wiley 1st edition, 1991.
- [110] D.A. Varshalovich; A.N. Moskalev; V.K. Khersoniskii. *Qmoment theory of angular momentum*. World Scientific, 1988.
- [111] Paul Huillery. *Few and Many-body Physics in cold Rydberg Gases*. PhD thesis, Université Paris-Sud, Laboratoire Aimé Cotton, Università di Studi di Pisa, dipartimento di Fisica E.Fermo, 2013.
- [112] P. D. Lett, W. D. Phillips, S. L. Rolston, C. E. Tanner, R. N. Watts, and C. I. Westbrook. Optical molasses. *J. Opt. Soc. Am. B*, 6(11):2084–2107, Nov 1989.

Court résumé de la thèse :

Refroidissement laser et manipulation d'antimatière, au sein de l'expérience AEgIS

Par : Pauline Yzombard

Novembre 2016

Université Paris-Sud, Paris XI, Paris-Saclay

Laboratoire Aimé Cotton (Orsay, France)

CERN (Meyrin, Switzerland)

Cette thèse s'est déroulée en collaboration avec le laboratoire Aimé Cotton et l'expérience AEgIS : Antihydrogen experiment : gravity, interferometry, spectroscopy) du CERN (Suisse). Cette collaboration qui rassemble les compétences diverses de plus de 15 laboratoires à travers l'Europe, a pour objectif final de mesurer la déflexion d'un faisceau froid d'antihydrogènes soumis au champ gravitationnel terrestre.

A cette fin, plusieurs étapes importantes doivent être réalisées pour préparer tous les ingrédients pour cette mesure de précision inédite. Durant les trois années écoulées à travailler dans AEgIS, j'ai pu prendre part à plusieurs de ces réalisations, et également participer à la conception et l'étude de futures améliorations. Ce bref résumé se propose de donner un aperçu des différentes problématiques en jeu et de quelques résultats obtenus. *Cette thèse traite des sujets tels que l'excitation par laser d'atomes de positronium, de plusieurs schémas de refroidissements par lasers envisagés pour améliorer la formation d'antihydrogène ou encore de manipulations de plasma d'antiprotons.*

1. L'antimatière et le Décélérateur d'antiprotons au CERN

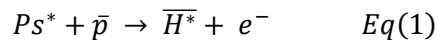
L'antimatière dont l'existence a été prédite par Dirac au début du 20^{ème} siècle, et pour la première fois observée en 1933 by Anderson [Anderson], est par définition le symétrique de la matière par rapport aux charges électriques. Si les antiélectrons, appelés positrons (e^+) sont produits sur Terre naturellement par radiation β^+ , les seules sources naturelles d'antiprotons (\bar{p}) observées proviennent des raies cosmiques. C'est pourquoi au pays des accélérateurs de particules, le CERN, a été construit l'unique source d'antiprotons froids à ce jour : un faisceau de protons accéléré par le Synchrotron à protons (PS) est bombardé contre une cible métallique. Les énergies libérées sont telles qu'une collision sur un million produit une paire de protons-antiprotons. Les antiprotons ainsi formés sont trop énergétiques et les trajectoires trop désordonnées pour que le faisceau de \bar{p} puisse être utilisé directement. Les antiprotons produits sont ainsi injectés dans le Décélérateur d'Antiproton (AD), qui collimate et refroidit les \bar{p} jusqu'à réduire leur énergie à 5.3 MeV avant de les distribuer aux cinq expériences présentes dans le hall de l'AD.

AEgIS [aegis] est l'une de ces expériences, et comme ses voisines, piège les antiprotons utilisant des pièges de Penning-Malmberg (piège de Penning linéaire) à haut champ magnétique (1 T et 4.5 T), en environnement cryogénique (≈ 4 K). Malgré les grandes capacités de confinement de tels pièges, seuls les antiprotons ayant une énergie autour de 100keV sont attrapés, et AEgIS utilise de fines feuilles de métal pour réduire la puissance du faisceau d'antiprotons entrant. Environ 1% des antiprotons fournis par l'AD sont capturés et refroidis dans nos pièges, soit environ $2-3 \cdot 10^5 \bar{p}$ par cycle du décélérateur (≈ 2 minutes)

2. L'antihydrogène dans AEgIS

AEgIS prévoit donc de pratiquer la première mesure directe de l'effet de la gravité sur un faisceau d'antihydrogène froid (\bar{H}). L'antihydrogène est le plus simple atome d'antimatière réalisable, puisqu'il lie un antiproton avec un positron.

AEgIS prévoit d'utiliser la technique d'échange de charges entre un plasma d'antiprotons plasma et des atomes de positronium excités par laser dans leurs états de Rydberg pour créer un faisceau d'antihydrogène.



Un positronium (Ps) est un atome exotique qui lie un électron à son antiparticule, le positron. Cette combinaison instable entre matière et antimatière peut se former dans un état de spin singlet ($s=0$), le positronium alors formé est appelé para-positronium (p-Ps) et a un temps de vie extrêmement court (125 ps). L'état de spin triplet ($s=1$) donne lieu à un atome d'ortho-positronium (o-Ps), de temps de vie plus long (142ns) ; c'est cet état métastable que nous considérons dans AEgIS.

Dans AEgIS, nous voulons utiliser des atomes de Ps excités vers des états de hautes énergies, dits de Rydberg. L'intérêt de l'excitation par laser est double :

- augmenter la section efficace du Ps pour accroître le taux de formation d'antihydrogènes par échange de charges. En effet, la section efficace de collision qui détermine l'efficacité de la recombinaison des antiprotons avec les Ps, augmente avec la section efficace des particules en jeu. La section efficace du Ps croît quadratiquement avec le niveau d'excitation n : $\sigma_{Ps} \propto n^2$.

- augmenter le temps de vie du nuage de Ps. En effet, les o-Ps formés dans leur niveau fondamental ont un temps de vie de 142 ns dans le vide, un temps trop court pour que le nuage de Ps puisse traverser les 2 cm nécessaire pour atteindre le plasma des antiprotons piégés.

3. Excitation laser du Ps

AEgIS possède deux systèmes lasers pour exciter le positronium jusqu'à ses niveaux de Rydberg. Un premier système génère un pulse d'UV à 205 nm pour exciter la transition $n=1 \leftrightarrow n=3$, puis un second pulse d'infra-rouge autour de 1700 nm réalise la transition $n=3 \leftrightarrow n=15-18$ (Rydberg). Ce système, basé sur des cristaux non-linéaires, est pompé à partir d'une source laser NdYAG. Il a été conçu par le groupe de Milan (INFN) d'AEgIS, pour générer des pulses lasers larges spectralement (largeur spectrale $\sigma_{rms} \approx 110$ GHz) afin de couvrir l'important élargissement spectral induit par effet Zeeman à 1 T. En effet, ce système a pour but d'exciter les atomes de Ps jusqu'à leur état de Rydberg pour préparer la formation des antihydrogènes, et cela doit se faire à l'intérieur du piège de Penning à 1 T.

Le second système laser, installé par D. Comparat et moi-même au CERN, excite quant à lui les transitions $n=1 \leftrightarrow n=2$ et $n=2 \leftrightarrow n=Rydberg$ du Ps, en générant des pulses à 243 nm et 730 nm. Ces longueurs d'ondes sont obtenues en pompant des lasers à colorant, par une même source laser NdYAG. Ce second système a été pensé lui pour être fin spectralement afin de pouvoir pratiquer une

spectroscopie des états de Rydberg du Ps en champ nul. En effet, une chambre de test à température ambiante est installée dans AEgIS et permet de produire des Ps dans un environnement électromagnétique faible.

Lors de ma thèse, nous avons obtenus les premiers résultats de production de Ps dans la chambre de test (Voir. [Ps1]) et ainsi pu tester le premier système laser pour exciter les positronium. Nous avons ainsi obtenu les premiers résultats d'excitation par laser du Ps dans son niveau $n=3$, et prouvé que l'excitation jusqu'au niveau de Rydberg utilisant le niveau $n=3$ comme intermédiaire était efficace. Ces résultats ont été également publiés dans [Ps2].

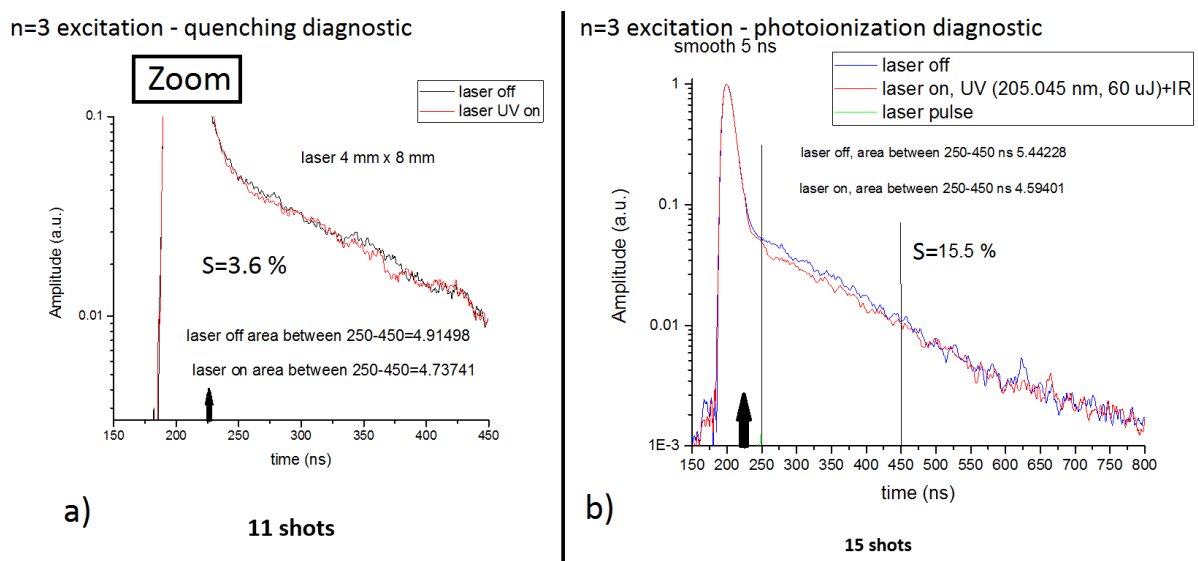


Fig. 1 : Résultats expérimentaux d'excitation du Ps dans le niveau excité $n=3$. Mesures du signal d'annihilation des positrons et positronium, au court du temps. Le pic d'annihilation visible à partir de 150 ns correspond à l'implantation des positrons dans la cible nano-poreuse pour former les positroniums. La queue du signal correspond à l'annihilation des o-Ps émis dans le vide, qui ont un temps de vie de 142 ns.

Deux techniques de détection ont été utilisées pour prouver l'excitation laser : a) La technique dite du « Quenching » : en présence d'un champ magnétique, les niveaux excités triplets du Ps sont mélangés par effet Zeeman avec les niveaux singlets. Ceci autorise la désexcitation vers le niveau fondamental du p-Ps, de très court temps de vie (125 ps). Les atomes excités par laser vers le niveau $n=3$ ont ainsi une probabilité de se désexciter vers le fondamental p-Ps et s'annihiler immédiatement. Le résultat sur le signal est une diminution des comptes d'annihilation sur les temps longs (queue du signal), ce qu'on observe sur la courbe rouge (laser envoyé) par rapport à la courbe bleue (pas de laser). b) la technique de photoionisation, qui consiste à envoyer un laser intense pour dissocier les Ps excités dans le niveau $n=3$. Comme la technique précédente, ceci se traduit par une diminution des comptes d'annihilation des Ps dans le temps (courbe rouge) par rapport au cas sans laser (courbe bleue). Les flèches noires indiquent le temps où les lasers pulsés excitateurs ont été envoyés.

Ces bons résultats sont les premiers pas vers la formation de l'antihydrogène via échange de charges, comme prévu dans AEgIS. Les beamtimes de 2016 et 2017 doivent maintenant confirmer que nous sommes capables d'exciter le Ps dans des états de Rydberg contrôlés en champ magnétique élevé, et ainsi pratiquer les premiers essais pour former l'antihydrogène.

4. L'étude d'un possible refroidissement laser

Par la configuration même du système de piégeage d'AEgIS, le taux de formation d'antihydrogène par échanges de charges apparaît comme insuffisant. En effet, comme illustré dans la figure 2, la cible permettant la création des Ps se trouve à 2 cm, le recouvrement entre le nuage de Ps et le plasma d'antiprotons confinés est faible. Ainsi, même si les atomes de Ps seront excités vers des niveaux à hautes énergies autour de $n = 15 - 20$, afin d'augmenter drastiquement la section efficace de collision, le taux de formation d'antihydrogènes reste faible.

Une des idées que j'ai étudiées pendant ma thèse afin de palier à ce problème de recouvrement, est la possibilité d'un refroidissement laser des positronium. La Fig. 2, b) montre le principe : si un refroidissement laser est pratiqué sur les vitesses transverses des atomes de Ps, le nuage sera focalisé et un plus grand nombre de Ps atteindra les antiprotons.

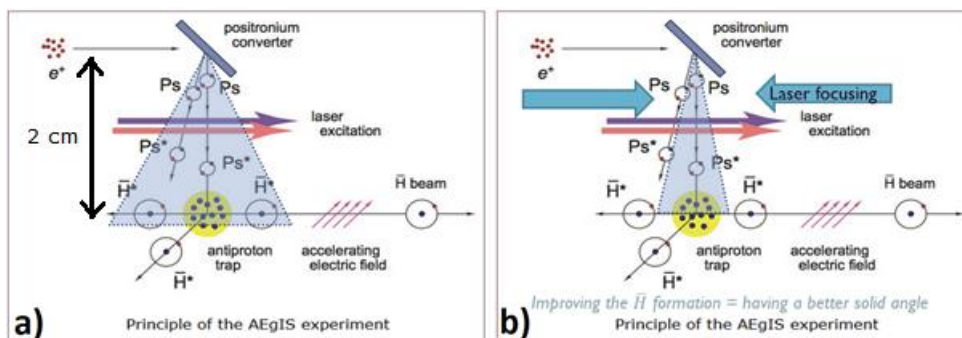


Fig. 2 : a) Schéma de la formation des antihydrogènes dans AEgIS, dans l'enceinte du piège à 1 T. Les antiprotons sont confinés au centre du piège, les atomes de positronium sont formés hors axe, à 2 cm de distance. b) un refroidissement laser appliqué sur les vitesses transverses à la propagation du nuage de Ps vers les antiprotons conduit à une focalisation des Ps sur le plasma de \bar{p} , et à un meilleur recouvrement donc à une meilleure production d'antihydrogène.

Le refroidissement Doppler

J'ai étudié la possibilité d'un refroidissement laser sur la transition $1S \leftrightarrow 3P$ de l'ortho-positronium, transition déjà envisagée dans des travaux antérieurs [Pscool1] ou plus récemment dans [Pscool2].

Le refroidissement du Ps est spécial et nécessite d'être réalisé dans un temps assez court, comparable au temps de vie moyen des Ps, de 142 ns. Les temps typiques de refroidissement Doppler des atomes alcalins sont de plusieurs ms.

Pour autant, le Ps est l'atome le plus léger qu'il soit (2 fois la masse de l'électron !), ce qui conduit à une énergie de recul conséquente. Tout photon absorbé ou émit sur la transition $n=1 \leftrightarrow n=2$ conduit

à une variation de la vitesse de l'atome de 1500 m/s. Face à une si forte énergie de recul, la modélisation de la force moyenne de refroidissement devient subtile. Nous avons eu recours aux équations de taux pour calculer l'évolution temporelle d'un nuage de Ps, soumis à des lasers excitateurs. Le code C++, écrit par Daniel Comparat, que j'ai aidé à améliorer, calcule l'évolution des états internes et externes de chaque particule. Ce code étudie l'excitation laser et le mouvement de N particules, sous l'effet de forces extérieures (diffusion, force dipolaire, champ magnétique et électrique, gravité), et prend en compte l'interaction Coulombienne à N corps et la force de Lorentz en cas de particules chargés. Le moment de recul est aussi implémenté. Une description complète du code peut être trouvée dans l'article [Comparat1].r

Quelques résultats : En Fig. 3, sont donnés l'évolution de la température d'un ensemble mésoscopique (200 Ps) sans champ magnétique, soumis à un refroidissement laser 1D (deux lasers contra-propageant) ou 3D (6 lasers contra-propageant deux à deux).

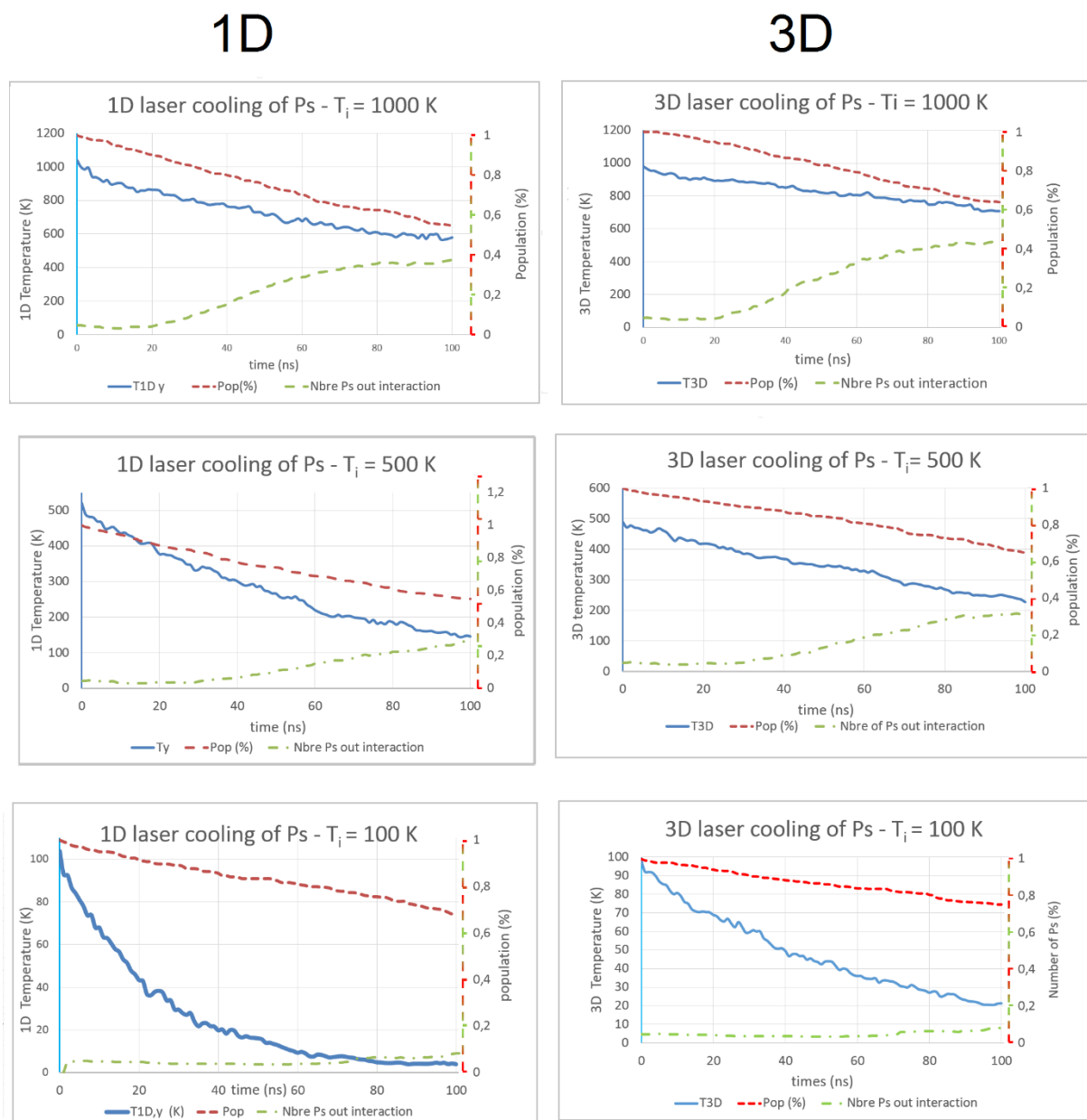


Fig. 3. Résultat d'un refroidissement Doppler appliqué à un ensemble de 200 Ps, en l'absence de champ magnétique. La température initiale des Ps, suivant une distribution de Boltzmann, est

choisie à 1000 K (première ligne), 500 K (deuxième ligne), et 100 K (troisième ligne). L'évolution de la température est donnée en bleu, la courbe en vert pointillée donne le pourcentage d'atomes quittant la zone d'interaction laser. L'annihilation des Ps est prise en compte et la courbe en tiret rouge présente l'évolution du nombre de Ps dans le temps.

Après 100 ns d'interaction laser, un refroidissement conséquent de la température moyenne des atomes est visible, en 1D et 3D.

Une étude similaire a été faite dans le cas de la présence d'un fort champ magnétique. L'effet Zeeman conduisant aux mélanges d'états triplets et singlets du Ps donnent lieu à des subtilités pour éviter d'augmenter l'annihilation des Ps. Pour autant, un refroidissement 1D semble envisageable, si effectué le long de l'axe de quantification qui correspond à l'axe magnétique. La prochaine étape est maintenant de procéder aux premiers tests expérimentaux. Les développements lasers nécessaires pour construire le système laser adapté (long pulse, énergétique à 243 nm) sont aussi discutés dans ma thèse.

5. Refroidissement et compression du plasma d'antiprotons

Dans AEGIS, nous utilisons deux séries de pièges de Penning-Malmberg à 4.5 T et 1 T pour confiner les plasmas d'antiprotons, électrons et positrons. De fines feuilles d'aluminium (dites « degraders ») sont placées à l'entrée du premier piège à 4.5 T afin de décélérer le faisceau d'antiprotons à 5 MeV et piégés les antiparticules restant à quelques keV. Typiquement, nous piégeons les antiprotons traversant les degraders, en appliquant une tension de 9kV aux électrodes dites « end-caps » qui servent à former les murs du puits de potentiel axial. Pour chaque paquet d'antiprotons délivrés par l'AD, nous capturons environ 1 % des particules, soit $3 \cdot 10^5 \bar{p}$.

Pour former des antihydrogènes, nous devons refroidir les antiprotons (diminuer leur énergie cinétique et donc potentielle de piégeage). Grâce à la technique dite « de refroidissement par électrons », nous sommes capables de refroidir environ $2 \cdot 10^5$ antiprotons en dessous de la centaine d'électrons voltes.

Cette technique consiste à utiliser un bain d'électrons froids qui va servir d'espèce tampon (« buffer ») pour refroidir les antiprotons par collisions : on appelle ce procédé un refroidissement sympathique. Les électrons sont refroidis grâce au rayonnement cyclotron, dans un champ de 4.5 T, les électrons thermalisent avec leur environnement en environ 1 s.

Tous nos pièges sont à des températures cryogéniques : les aimants supraconducteurs utilisés pour générer les forts champs magnétiques de 1 T et 4.5 T sont refroidis aux températures de l'hélium liquide – 4.2 K. Ainsi, en une seconde environ, un bain de 10^8 électrons sont refroidis à quelques dizaines de Kelvin, et confinés dans le même piège que le plasma d'antiprotons, permet de refroidir sympathiquement les \bar{p} .

Pendant les périodes de faisceaux de 2014 et 2015, j'ai travaillé à l'optimisation des procédures pour capturer, refroidir et compression les antiprotons. Grâce à la technique dite du « rotating walls », appliquée au plasma d'électrons, nous sommes en mesure de compresser le plasma des e^- . Les

antiprotons mélangés aux électrons peuvent suivre cette compression dans certaines conditions et être compresser à leur tour. Les détails de nos plus prometteurs résultats sont discutés dans ma thèse.

6. Le refroidissement par laser d'anions moléculaires -l'étude du cas du C_2^-

L'idée de cette dernière étude était de trouver une solution pour refroidir les antiprotons en dessous du Kelvin. Nous avons ainsi étudié la possibilité d'utiliser des ions négatifs, au préalable refroidit par laser, pour effectuer un refroidissement sympathique du plasma d'antiprotons.

Le groupe d'Alban Kellerbauer à Heidelberg, membre de la collaboration AEGIS, étudie depuis des années la possibilité de refroidir des anions atomiques : après l'étude de la spectroscopie de O^- et La^- , le candidat qui pourrait prétendre à un refroidissement laser semble être le La^- . Actuellement, leur groupe développe l'expérience pour les premiers essais, en piège de Paul.

Durant ma thèse, j'ai étudié la possibilité d'utiliser des anions moléculaires. Bien que le refroidissement laser ait été réalisé pour les molécules neutres, aucun refroidissement laser n'a jamais été montré pour les anions, atomiques ou moléculaires. Ce projet est ambitieux, mais présente l'avantage d'avoir plus de candidats à étudier parmi les molécules ! Nous avons sélectionné l'anion C_2^- , dont la spectroscopie est connue (grand avantage !) et propose de bons coefficients de Franck-Condon. Ces coefficients donnent le couplage entre les différents états internes de la molécule, et nous appelons « bons coefficients » des coefficients qui indiquent une nette préférence pour la particule de se désexciter vers un seul état. Ceci est très important afin de trouver un cycle de refroidissement qui nécessite qu'un nombre restreint de niveaux internes. Si la particule se désexcite vers des niveaux non excités par laser, les niveaux dits « noirs » accumulent des particules jusqu'à ce que le processus de refroidissement s'arrête, faute de particules restantes à exciter.

Fig. 4 présente la structure des niveaux internes de C_2^- , ainsi que les niveaux X et A de la molécule C_2 (pour montrer le risque de photoionisation). Les flèches vertes et rouges indiquent les transitions optiques sur lesquelles nous avons étudié la possibilité d'un refroidissement Doppler ou d'un refroidissement de type Sisyphus.

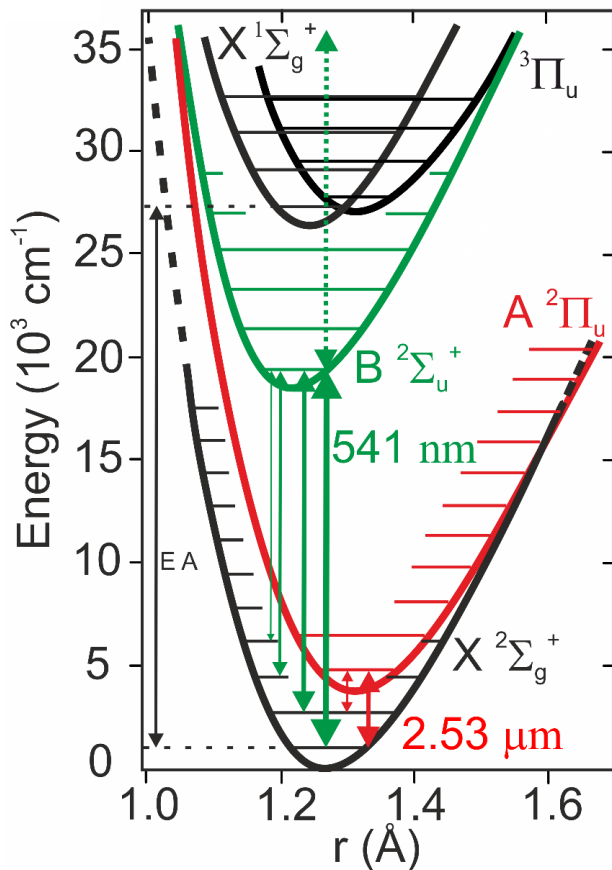


Fig. 4. Structure des énergies internes de l'anion C_2^- et de la molécule C_2 . Les flèches indiquent les transitions optiques étudiées pour un refroidissement Doppler (flèches vertes), sur la transition $X \leftrightarrow B$, ou un refroidissement Sisyphes (flèches rouges) sur la transition $X \leftrightarrow A$.

De cette étude théorique, nous avons publié un article [PRL_C2Minus]. Par exemple, nous avons étudié la possibilité d'un refroidissement de type Sisyphes sur la transition $X \leftrightarrow A$. L'idée est de générer un piège de Penning adapté avec un gradient de champ pour générer la colline de potentiel. L'effet Zeeman sépare les états $X \ |m=\pm 1/2\rangle$ (levée de dégénérescence), dont les énergies suivent (au premier ordre) linéairement le gradient du champ B. Les particules piégées oscillent, et ressentent cette colline de potentiel, et perdent de l'énergie à chaque fois qu'elles « montent ». Par des lasers astucieusement placés, on ramène les particules « en bas de la colline », comme le fameux mythe Sisyphes. Plus de détails sont donnés dans [PRL_C2Minus], ainsi que dans la thèse. La Fig.5 présente deux résultats de simulations du refroidissement Sisyphes. La température axiale d'un nuage de 200 C_2^- est tracé en fonction du temps, lors de l'interaction laser. En quelques dizaines de ms, l'effet du refroidissement se fait ressentir, et la température décroît jusqu'à quelques Kelvin. La Fig. 5, a) présente une simulation sans lasers « repompeurs » qui excitent les états « sombres » ($X, v''=1$), dans lesquels les particules peuvent se désexciter, alors que la Fig. 5) b) utilise deux lasers repompeurs, afin de pouvoir continuer le refroidissement plus longtemps, en limitant les états « sombres ».

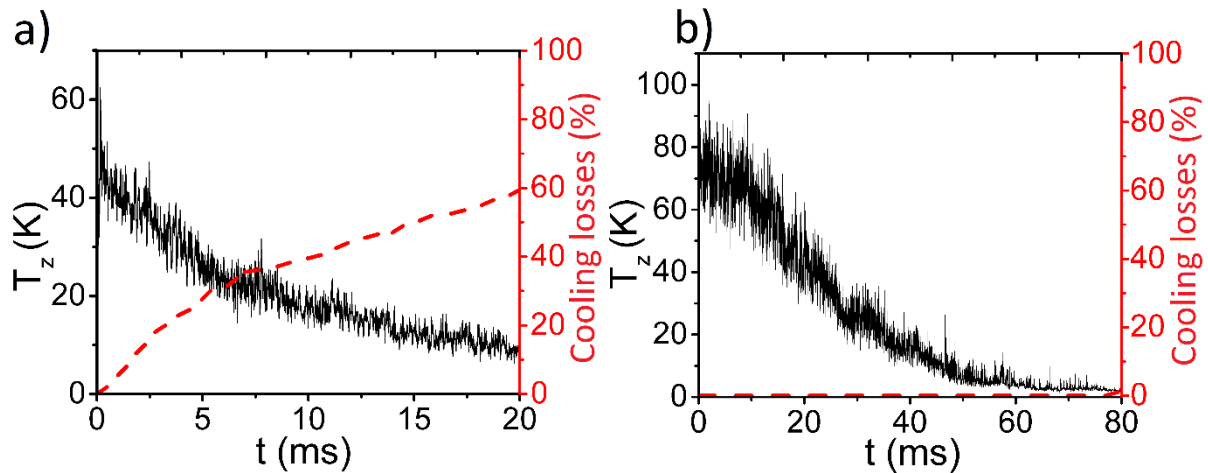


Fig. 5. Résultats de simulation du refroidissement Sisyphus, d'un nuage de 200 $C2^-$. Fig. a) n'utilise pas de lasers repompeurs, et b) présente des lasers repompeurs sur la transition $X v''=1 \leftrightarrow A$.

Ces simulations sont prometteuses, et nous ont permis de commencer à développer un système expérimental au CERN. Le Projet Borealis, au sein d'AEgIS, conduit par Sebastian Gerber, a pour but de développer une source de $C2^-$, et de tester différents schémas de refroidissement laser de ces anions, avant de l'implémenter dans AEgIS dans le futur.

7. Perspective

Cette thèse au sein de l'expérience AEgIS m'a permis d'être à l'interface de plusieurs domaines d'études : le développement d'un système laser et les simulations de physique atomique se sont alliés au travail quotidien pour maintenir l'expérience en état de fonctionnement (cryogénie, entretien du vide). J'ai pu prendre une part active dans l'acquisition de données lors des « shifts » d'antiprotons, et approfondir ma connaissance sur la physique des plasmas.

Cette thèse se divise en trois parties, présentant dans un premier temps mon travail expérimental effectué sur la physique des Positronium, dont l'excitation du niveau $n=3$ a été la plus grande avancée de notre travail. La deuxième partie présente plus mon travail théorique et de simulations, pour prévoir et développer un système laser adapté pour le refroidissement des atomes de positronium, et ainsi, améliorer le rendement de formation des antihydrogènes dans AEgIS.

Enfin, la troisième partie est consacrée à mon travail relatif aux antiprotons : la participation aux shifts, et l'optimisation de notre système de piégeage, pour compresser et refroidir par électrons les antiprotons. Mais aussi, l'étude d'un possible refroidissement sympathique des antiprotons, utilisant les anions moléculaires $C2^-$, au préalable refroidit par laser, a fait partie de mes sujets d'étude.

Bibliographie

[aegis] *AEgIS proposal* G. Drobychev *et al*, 2007 CERN-SPSC-2007017,
<http://cdsweb.cern.ch/record/1037532>

[Anderson] Anderson, Carl D. (1933). "The Positive Electron". *Physical Review*. **43** (6): 491–494.
[Bibcode:1933PhRv...43..491A](#). [doi:10.1103/PhysRev.43.491](#).

[PS1] *Positron bunching electrostatic transport system for the production emission of dense positronium clouds into vacuum*, S. Aghion, and al - **AEgIS Collaboration**, Nuclear Instruments Methods in Physics Research Section B: Beam Interactions with Materials Atoms **362**, 86-92, Published in November 2015

Doi : 10.1016/j.nimb.2015.08.097

[Ps2] *Laser excitation of the n=3 level of positronium for antihydrogen production*, Aghion, S. Amsler, and al - **AEgIS Collaboration**, Phys. Rev. A. **94** 012507, Published in July 2016

Doi: 10.1103/PhysRevA.94.012507

[Pscool1] Edison P. Liang and Charles D. Dermer. *Laser cooling of positronium*. Optics Communications, 65(6):419 _ 424, 1988.

[Pscool2] K Shu, X Fan, T Yamazaki, T Namba, S Asai, K Yoshioka, and M Kuwata-Gonokami. *Study on cooling of positronium for bose Einstein condensation*. J. Phys. B, **49**(10):104001, 2016.

[Comparat1] *Molecular cooling via Sisyphus processes*, Comparat, Daniel, Phys. Rev. A **89** 043410 (2014) - doi = 10.1103/PhysRevA.89.043410

[PRL_C2Minus] *Laser Cooling of Molecular Anions*, P. Yzombard, M. Hamamda S. Gerber, M. Doser, Michael D. Comparat Phys. Rev. Lett. **114** 213001, (2015)

Title : Laser cooling and manipulation of Antimatter in the AEGIS experiment

Keywords : laser cooling, positronium, anti-gravity, antihydrogen

My Ph.D project took place within the AEGIS collaboration, one of the antimatter experiments at the CERN. The final goal of the experiment is to perform a gravity test on a cold antihydrogen (\bar{H}) beam. AEGIS proposes to create such a cold \bar{H} beam based on a charge exchange reaction between excited Rydberg Positronium (Ps) and cold trapped antiprotons: $Ps^* + \bar{p} \rightarrow \bar{H}^* + e^-$.

Studying the Ps physics is crucial for the experiment, and requires adapted laser systems. During this Ph.D, my primary undertaking was the responsibility for the laser systems in AEGIS. To excite Ps atom up to its Rydberg states (≈ 20) in the presence of a high magnetic field (1T), two broadband pulsed lasers have been developed. We realized the first laser excitation of the Ps into the $n=3$ level, and demonstrated an efficient optical path to reach the Rydberg state $n=16-17$. These results, obtained in the vacuum test chamber and in the absence of strong magnetic field, reach a milestone toward the formation of antihydrogen in AEGIS, and the immediate next step for us is to excite Ps atoms inside our 1 T trapping apparatus, where the formation of antihydrogen will take place.

However, even once this next step will be successful, the production rate of antihydrogen atoms will nevertheless be very low, and their temperature much higher than could be wished. During my Ph.D, I have installed further excitation lasers, foreseen to perform fine spectroscopy on Ps atoms and that excite optical transitions suitable for a possible Doppler cooling.

I have carried out theoretical studies and simulations to determine the proper characteristics required for a cooling laser system. The transverse laser cooling of the Ps beam will enhance the overlap between the trapped antiprotons plasma and the Ps beam during the charge-exchange process, and therefore drastically improve the production rate of antihydrogen.

The control of the compression and cooling of the antiproton plasma is also crucial for the antihydrogen formation. During the beamtimes of 2014 and 2015, I participated in the characterization and optimization our catching and manipulation procedures to reach highly compressed antiproton plasma, in repeatable conditions. Another project in AEGIS I took part aims to improve the formation rate of ultracold antihydrogen, by studying the possibility of a sympathetically cooling of the antiprotons using a laser-cooled anion plasma. I investigated some laser cooling schemes on the C_2^- molecular anions, and the simulations are promising. I actively contribute to the commissioning of the test apparatus at CERN to carry on the trials of laser cooling on the C_2^- species. If successful, this result will not only be the first cooling of anions by laser, but will open the way to a highly efficient production of ultracold antihydrogen atoms.

Titre : manipulation et refroidissement laser de l'antimatière, au sein de l'expérience AEGIS

Mots clés : refroidissement laser, positronium, anti-gravité, antihydrogène

Ma thèse s'est déroulée dans le cadre de la collaboration AEGIS, une des expériences étudiant l'antimatière au CERN. L'objectif final est de mesurer l'effet de la gravité sur un faisceau froid d'antihydrogène (\bar{H}). AEGIS se propose de créer les \bar{H} froids par échange de charges entre un atome de Positronium (Ps) excité (état de Rydberg) et un antiproton piégé: $Ps^* + \bar{p} \rightarrow \bar{H}^* + e^-$.

L'étude de la physique du Ps est cruciale pour AEGIS, et demande des systèmes lasers adaptés. Pendant ma thèse, ma première tâche a été de veiller au bon fonctionnement des systèmes lasers de l'expérience. Afin d'exciter le positronium jusqu'à ses états de Rydberg (≈ 20) en présence d'un fort champ magnétique (1 T), deux lasers pulsés spectralement larges ont été spécialement conçu. Nous avons réalisé la première excitation par laser du Ps dans son niveau $n=3$, et prouvé une excitation efficace du nuage de Ps vers les niveaux de Rydberg $n=16-17$. Ces mesures, réalisées dans la chambre à vide de test d'AEGIS, à température ambiante et pour un faible champ magnétique environnant, sont la première étape vers la formation d'antihydrogène. Le prochain objectif est de répéter ces résultats dans l'enceinte du piège à 1 T, où les antihydrogènes seront formés. Pour autant, malgré l'excitation Rydberg des Ps pour accroître la section efficace de collision, la production d'antihydrogène restera faible, et la température des \bar{H} formés sera trop élevée pour toute mesure de gravité. Pendant ma thèse, j'ai installé au CERN un autre système laser prévu pour pratiquer une spectroscopie précise des niveaux de Rydberg du Ps. Ce système excite des transitions optiques qui pourraient convenir à un refroidissement Doppler : la transition $n = 1 \leftrightarrow n = 2$.

J'ai étudié la possibilité d'un tel refroidissement, en procédant à des simulations poussées pour déterminer les caractéristiques d'un système laser adapté. La focalisation du nuage de Ps grâce au refroidissement des vitesses transverses devrait accroître le recouvrement des positroniums avec les antiprotons piégés, et ainsi augmenter grandement la production d' \bar{H} .

Le contrôle du refroidissement et de la compression du plasma d'antiprotons est aussi essentiel pour la formation des antihydrogènes. Pendant les temps de faisceaux d'antiprotons de 2014 et 2015, j'ai contribué à la caractérisation et l'optimisation des procédures pour attraper et manipuler les antiprotons, afin d'atteindre des plasmas très denses, et ce, de façon reproductible.

Enfin, j'ai participé activement à l'élaboration d'autre projet à l'étude AEGIS, qui vise aussi à augmenter la production d'antihydrogène : le projet d'un refroidissement sympathique des antiprotons, en utilisant un plasma d'anions refroidis par laser. J'ai étudié la possibilité de refroidir l'ion moléculaire C_2^- , et les résultats de simulations sont encourageants. Nous sommes actuellement en train de développer au CERN le système expérimental qui nous permettra de faire les premiers tests de refroidissement sur le C_2^- . Si couronné de succès, ce projet ne sera pas seulement le premier résultat de refroidissement par laser d'anions, mais ouvrira aussi les portes à une production efficace d'antihydrogènes froids.

